RAPID DETERMINATION OF MASS AND STIFFNESS DISTRIBUTION ON PRIMARY SKIN-STIFFENER STRUCTURES

A Thesis
Presented to
The Academic Faculty

by

August Taylor Noevere

In Partial Fulfillment
of the Requirements for the Degree
Doctor of Philosophy in the
School of Aerospace Engineering

Georgia Institute of Technology
August 2016

RAPID DETERMINATION OF MASS AND STIFFNESS DISTRIBUTION ON PRIMARY SKIN-STIFFENER STRUCTURES

Approved by:

Dr. Alan Wilhite, Advisor
School of Aerospace Engineering
Georgia Institute of Technology

Jeffrey A Cerro
Vehicle Analysis Branch
NASA Langley Research Center

Dr. Graeme J Kennedy
School of Aerospace Engineering
Georgia Institute of Technology

Dr. Daniel P. Schrage
School of Aerospace Engineering
Georgia Institute of Technology

Dr. Mark Costello
School of Aerospace Engineering
Georgia Institute of Technology

Date Approved: 15 July 2016

To my wife Melody

ACKNOWLEDGEMENTS

If I have seen further, it is by standing on the shoulders of giants.
-Sir Isaac Newton

It was not until I began writing this section that I realized just how many people have helped me in so many ways to reach this point. An entirely separate document of equal length could be written to list the ways in which I have received support on the journey to my PhD. Consider this section to be a highlight reel of such a document.

I would first like to thank my family for being so inspirational and supportive. My dad gets credit for my interest in the aerospace field from digging through picture books of the Apollo program with me when I was young, and being able to answer all my ridiculous questions. I can still remember my first introduction to Newton's 3rd law (albeit somewhat of a confusing concept for a 10 year-old) after asking him "how do rockets work?" I have my mom to thank for inspiring me to become a distance athlete after seeing her take up marathoning and qualify for the Boston Marathon. The love of running I learned from her has helped keep me sane though the long hours of grad school. Also, thanks to my little brother for teaching me to strive to be a role model instead of just a sibling.

On the journey to completing this thesis, one of the things that have kept me going are distractions to clear my head and keep me fresh. For this, I owe the friends I have made along the way. Thanks for the companionship, pep talks, cookouts, bike trips, camping trips, kiteboarding excursions, and everything else that helped keep me going.

On the technical side, thanks to my advisor, Dr. Alan Wilhite, for contributing his vehicle design expertise to help build my methodology into a cohesive product. In addition to technical help, I owe Dr. Wilhite for keeping me on track conceptually despite my tendencies to get lost trying to perfect certain aspects of the product. Lastly, thanks for sticking with me for 1.5 years into retirement despite a promising career in professional car

racing.

Many thanks to Jeff Cerro (my mentor) and the Vehicle Analysis Branch (VAB) at NASA Langley for providing insightful ideas and critique to my methodology. I learned a lot about vehicle design in the two summers I spent sitting with the VAB.

I also owe the folks at Collier Research for teaching me a lot about stiffened panel analysis and optimization. They also provided software support for many of the unique tasks I performed in HyperSizer for this research.

Additionally, thanks to NASA for providing me with funding and support through the NASA Space Technology Research Fellowship.

Saving the best for last, I owe my wife, Melody, for providing unwavering support through my five years of grad school despite the occasional strains it put on both of us. Because of your support, I never had an opportunity to doubt myself or the path I pursued. I would have been hard-pressed to find the strength needed to complete this journey without you. I look forward to the next chapter of our lives and the excitement it holds. Sorry it took so long to get there.

TABLE OF CONTENTS

LIST OF TABLES

LIST OF FIGURES

NOMENCLATURE

α	Angle of Attack
β	Regression Coefficient for Failure Criteria (varying dimensions)
$\delta_{T,req}$	Required Wing Tip Deflection (in)
δ_T	Wing Tip Deflection (in)
κ	Regression Coefficient for Failure Criteria (varying dimensions)
μ	Mean Value of a Distribution
ν_{12}	Poisson's Ratio
ϕ	Continuous Prediction Metric for Failure Criteria RSE
ρ	Density
σ	Standard Deviation of a Distribution
σ_{actual}	Calculated Stress in Material for Applied Load (psi)
σ_{allow}	Stress Allowable for a Material (psi)
θ	Ply Angle
$[A]$	Matrix of Variable Coefficients for Simplex Optimization Constraints
$[A]$	Membrane Stiffness Matrix (lb/in)
A	Wing Area
a	Longitudinal Buckling Span of a Panel or Plate (in)
A_{11}	ABD Matrix Term: Longitudinal Stiffness (X-Axis) (lb/in)
A_{22}	ABD Matrix Term: Transverese Stiffness (Y-Axis) (lb/in)
A_{33}	ABD Matrix Term: Shear Stiffness (lb/in)
a_{ij}	Inverted [A] Matrix Terms
a_{ij}	Terms from $\mathbf{A}$ for Simplex Constraints
A_{panel}	Cross-Sectional Area of Stiffened Panel (in^2)
$A_{stiffener}$	Cross-Sectional Area of Stiffener (in^2)
AR	Aspect Ratio
$[B]$	Membrane-Bending Coupling Stiffness Matrix (lb/in)

$\vec{b}$	Vector of Maximum Constrain Values Allowed in Simplex Optimization
b	Transverse Buckling Span of a Panel or Plate (in)
b_i	Terms from $\vec{b}$ for Simplex Constraints
c	Wing Chord
C_D	Drag Coefficient
C_L	Lift Coefficient
C_M	Drag Coefficient
$C_{D,i}$	Induced Drag Coefficient
C_{ineq}	Scalar Representation of Inequality Constraint
C_i	Constant Terms in Failure Criteria RSEs (varying dimensions)
Cr_i	Set of Infeasible Points Defined by Failure Criteria i
$[D]$	Bending Stiffness Matrix (lb/in)
D	Drag Force (lb)
D_{11}	ABD Matrix Term: Bending Stiffness about Y-Axis (lb·in^2/in)
D_{22}	ABD Matrix Term: Bending Stiffness about X-Axis (lb·in^2/in)
D_{33}	ABD Matrix Term: Twisting Stiffness (lb·in^2/in)
$d_{[ABD]}$	Euclidean Distance Between Two Stiffness Designs
$\overline{e}$	Mean Value of Optimization Error
E	Young's Modulus (psi)
e	Span Efficiency Factor
e_{rms}	Root Mean Square of Optimization Error
$\vec{F}$	Vector of Forces Applied to FEM
f	Closed-Form Function of $\vec{x}$
G	Shear Modulus (psi)
H	Total Height of Stiffened Panel (in)
H_{wb}	Height of Stiffener Web (in)
$[K]$	Global Stiffness Matrix for a FEM
k	Fixity Factor for Column Buckling, in Buckling Context
k	Ply Index, in Laminated Plate Context

K_i	RSE Coefficients After Pre-Processing (varying dimensions)
L	Lift Force (lb)
M	Pitching Moment (in-lb)
m	Buckling Mode Number, in Buckling Context
m	Mass of Structure (lbm)
M_x	Bending Moment about Y-Axis (lb $\cdot$ in/in)
M_y	Bending Moment about X-Axis (lb $\cdot$ in/in)
M_{xy}	Twist Bending Moment about (lb $\cdot$ in/in)
MS	Margin of Safety for a Failure Criteria
n	Buckling Mode Number, in Buckling Context
n	G-Loading Factor, in Wing Load Design Context
n	Number of Plies, in Laminated Plate Context
n	Number of Stiffness Terms in Failure Criteria RSE
N_x	Axial Running Load (lb/in)
N_y	Transverse Running Load (lb/in)
$N_{x,crit}$	Critical Buckling Running Load (lb/in)
N_{xy}	Shear Running Load (lb/in)
$P()$	Probability of Obtaining a Given Value
P_{actual}	Calculated Buckling Load (lb)
P_{crit}	Critical Buckling Load for a Structure (lb)
$[\overline{Q}]$	Transformed Reduced Stiffness Matrix
$[Q]$	Reduced Stiffness Matrix
$\overline{Q}_{ij}$	Transformed Reduced Stiffness Matrix Term
Q_{ij}	Reduced Stiffness Matrix Term
r	Composite Laminate Design Paramter: 0^o-90^o Ply Balance
R^2	Coefficient of Determination
R_i	Polynomial Coefficient for A_{11} (lb/in^3)
R_{SA}	Ratio of Stiffener Cross-Section Area to Panel Cross-Section Area
R_{WFG}	Ratio of Stiffener Foot Width to Stiffener Cap Width

S	Stiffener Spacing (in)
s	Composite Laminate Design Paramter: $0^o/90^o$-45^o Ply Balance
t	Thickness of a Plate (in)
T_{fg}	Thickness of Stiffener Flange (in)
T_{ft}	Thickness of Stiffener Foot (in)
T_{sk}	Thickeness of Panel Skin (in)
T_{wb}	Thickness of Stiffener Web (in)
u	Stiffness Distribution Parameter for Chord-Wise Direction (in)
UM	Unit Mass (lbm)
v	Stiffness Distribution Parameter for Span-Wise Direction (in)
v	Vehicle Velocity, in Wing Load Design Context
W	Vehicle Weight (lb)
W_{fg}	Width of Stiffener Flange (in)
W_{ft}	Width of Stiffener Foot (in)
$\vec{x}$	Design Point in the Stiffness Domain
$\vec{x}$	General Set of Design Variables for Optimization
$\vec{x}$	Vector of Nodal Displacement, in FEM Context
$\vec{x}_{max}$	Maximum Design Variables Allowed in Optimization
$\vec{x}_{min}$	Minimum Design Variables Allowed in Optimization
X	Set of all Possible Design Points within the Min/Max Bounds
z_k	Vertical Location of k-th Ply in a Laminate (in)

ACRONYMS

AFP	Automated Fiber Placement
BWB	Blended Wing Body
CAD	Computer Aided Drafting
CFD	Computational Fluid Dynamics
CG	Center of Gravity
CLT	Classical Lamination Theory
DoE	Design of Experiments
EL	Effective Laminates
FAR	Federal Aviation Regulations
FEA	Finite Element Analysis
FEM	Finite Element Model
HSCT	High Speed Civil Transport
HWB	Hybrid Wing Body
LPa	Lamination Parameters
LPg	Linear Programming
MDO	Multi-Discipline Optimization
MER	Mass Estimating Relationship
MFA	Model Fit Accuracy
MRA	Model Representation Accuracy
OML	Outer Mold Line
RMS	Root Mean Square
RSE	Response Surface Equation

SUMMARY

Structural mass has always played an important role in design of aerospace vehicles, from the wood and cloth construction of the Wright Flyer to the titanium of the Lockheed SR-71 and Carbon/Epoxy of the Boeing 787. Mass of an aerospace vehicle can be reduced by advancements in three main areas: material selection, knowledge of flight loads, and efficient placement of material. The last area is the focus of the current research. This area is further sub-divided into two approaches. The first is determining placement of primary structural members, such as ribs, spars, frames, bulkheads, etc., referred to as internal arrangement. The second sub-division consists of finding detail dimensions (skin thickness, flange widths, etc.) that satisfy local material and buckling criteria. The two sub-divisions are coupled, but both present complex design challenges, thus making them difficult to consider simultaneously. Historically, designers have been forced to consider only a few possible internal arrangements for the sake of meeting time and efficiency constraints.

The objective of this research is to improve the efficiency of defining the structural design discussed above. In particular, emphasis is placed on structures with stringent stiffness constraints, as it is challenging to simultaneously optimize for mass and global stiffness. Most existing automated structural design tools are specialized for detailed final analysis and design, where the minute details of a structure are designed based on internal structure. In terms of detail, these tools have significant depth, but not enough breadth to be well-suited for studying a wide range of structural configurations. Thus, a tool is needed that captures most of the physics of a detailed design process, but still runs fast enough to be useful in an environment where many designs can be considered.

Initially, the research will apply basic, well-understood concepts to the detail design process to improve efficiency of stiffened panel optimization. Stiffened panels are found throughout aerospace structures and consist of a combination of skins and attached stiffeners. Optimization of these panels can be challenging because there can be many variables

related to the thicknesses and widths of the stiffener flanges and there are many failure criteria to satisfy such as material strength and buckling.

The first method applied to this optimization problem includes the use of a design of experiments, as well as third order response surface equations (curve-fits) to represent structural failure criteria. These concepts will make incremental improvements as demonstrated on an existing commercial structural design tool, HyperSizer. The resulting improvements in design efficiency will demonstrate the advantages of utilizing these existing techniques.

Next, the research will consider development of a new methodology to address the shortcomings of the approaches described above. Primarily, the methodology will provide significant improvements in stiffened panel design computational efficiency, as well as improved ability to handle local stiffness constraints. The methodology is based upon a change of variables, reformulating the design space from being a function of physical dimensions to being a function of stiffness terms. This change of variables enables a linearization of the design space which allows for very rapid structural mass optimization using first order response surface equations with the Simplex Algorithm. The change of variables also allows required local stiffness values to be directly specified at the panel level instead of having to impose additional constraints on the design space.

Additionally, application of the above methodology to composite structures will be considered. One advantage of a stiffness-based design space is that material variability does not increase the complexity of the design space. Variation of material stiffness, as found in composite design, can be developed as an integral part of the design space with the methodology described above. This allows for detailed structural design in conceptual vehicles to be performed much more quickly than with traditional design approaches for composites that are hampered by the greater number of variables that must be considered.

Finally, the developed methodology will be applied to a finite element model design environment to demonstrate its capability. Two examples are used; the first is a coarsely-meshed wing box that is similar to a Boeing 737 wing. A global stiffness constraint will be applied to the model in the form of a wing tip displacement limit. The objective of the demonstration is to use the developed methodology to optimize the upper and lower skins of

the wing box to simultaneously satisfy the global constraint and local failure criteria while providing a minimum overall structural mass. The second example uses a wing model similar to that of the F-86. This model is optimized with a composite laminate, simultaneously demonstrating applicability of the method to composites, as well as ability to couple with a finite element model.

The final product of this research will be a methodology for early trade studies with internal structure. The methodology will be able to determine optimum primary structure mass as well as stiffness distributions that satisfy global displacement requirements. Additionally, both metallic and composite structures can be considered because the methodology will be general enough to handle both in a similar manner.

CHAPTER I

INTRODUCTION

The purpose of this research is to develop a methodology which enables rapid structural design trade studies to be performed for aerospace systems. In this context, trade studies refer to the exploration of various structural layouts. This involves the placement of primary structural members, such as ribs, spars, frames, and bulkheads.

Of particular interest are structures with stringent stiffness constraints, such as those defined by global buckling or aeroelasticity. This chapter provides motivation for the research and presents research questions to be addressed by the developed methodology.

1.1 Motivation

In general terms, the presented research is motivated by a need for a capability to rapidly compute mass and stiffness distributions in structural trade studies. These trade studies typically arise within large Multi-Discipline Optimization (MDO) environments, which integrates many disciplines for aerospace vehicle design (structures, aerodynamics, propulsion, etc.) in an automated fashion [23],[24],[25],[26]. The goal is usually to optimize the vehicle at a system level considering multiple metrics such as cost and mass. Achieving this goal requires a significant number of iterations between each of the disciplines because the inputs of most disciplines are outputs from other disciplines (described in detail in Section 2.1). Thus, computational inefficiency in any of the disciplines will not only slow down the entire design process, but also make system-level global optimization nearly impossible.

Unfortunately, the coupled system-level MDO environment described above has proven to be elusive to engineers and researchers. The best that has been achieved to date for global system optimization are MDO environments that use simplistic analyses to provide high computational efficiency within each discipline. The drawback of using these kinds of analyses is that they are not suited for unconventional vehicle concepts (such as the Blended Wing Body (BWB) or High Speed Civil Transport (HSCT)), which require

physics-based design tools rather than scaled data from existing vehicles. Structural design for all aerospace vehicles, including unconventional configurations, requires studying a variety of internal structural arrangements (discussed in Section 2.3) and performing detailed design on each. Thus, one way to handle MDO for aerospace systems is to improve the computational efficiency of higher-fidelity design tools.

The intent of the research is to improve the efficiency of the design studies within the structures discipline to ensure that it can respond to a rapidly evolving design at the system level. Each of the disciplines mentioned above has a set of analyses and tools that trade accuracy for speed. Structures in particular, however, has a distinct gap between very coarse mass estimation and detailed design approaches that is to be addressed with the current research. This will be introduced next with four categories of structural design that describe where the research supplements and revolutionizes existing approaches. Each category is described by drawing upon existing literature and discussing the merits and drawbacks of approaches within the category. Figure 1 summarizes the fidelity and efficiency characteristics of each category.

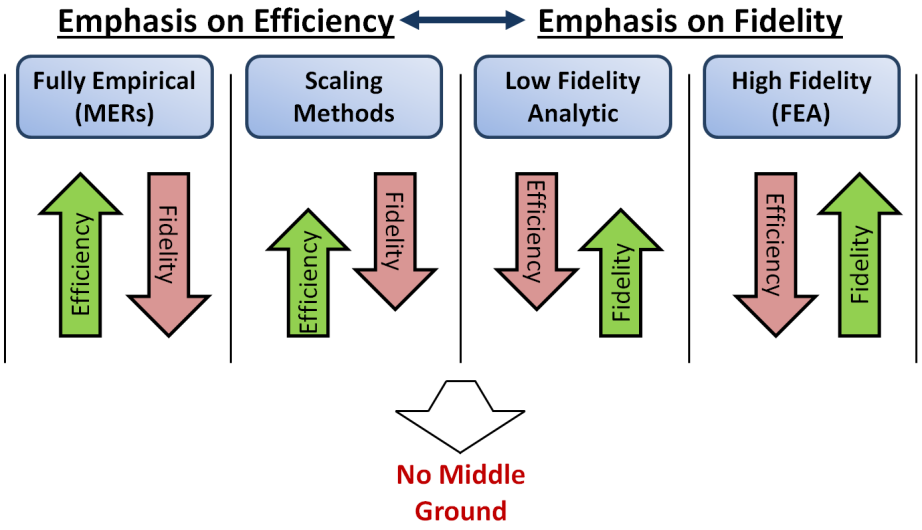

Figure 1: Characteristics of the Four Categories of Structural Design Tools

The four categories are found in a paper from 2013 by Chaussée [27] of Bombardier

Aerospace, which contains a concise summary of current structural mass estimation approaches. Starting with the lowest fidelity approaches, the first method is the "Fully Empirical" approach. This method is characterized by use of historical-based mass data of current and past systems to predict the mass of a new structure. This prediction is typically done on a large-scale basis, such as predicting the mass of an entire wing or fuselage based on the overall dimensions and loads of the structure. The mass is estimated by fitting a regression curve through historical data of masses for similar vehicles, usually as a function of several variables (wing span, thickness, design load, etc.) One advantage this provides is that the as-manufactured mass is estimated, including bolts, fittings, etc which may be more than half of the total structural mass.

The approach described above is often referred to as a Mass Estimating Relationship (MER). Because MERs are a simple regression, usually in the form of a polynomial, evaluating the mass of a structure is quick and simple. The primary advantage and also drawback of MERs is that the resulting mass estimation is not physics-based. While this makes MERs easy to evaluate, it also means that they are limited to evaluating designs that would be considered an "interpolation" of the existing vehicles used to generate the MER. Often, vehicles which require a MDO environment are much unlike any existing vehicles [28] and are therefore invalid to be used with a historical-based MER. Doing so could potentially require extrapolation of mass trends which is not considered a sound design practice. Thus, MERs do not contain the physics-based design processes needed to explore design points outside the envelope of existing designs. As a result, MERs are not useful for anything beyond very early system-level trade studies and cannot be used for trading various internal structure arrangements.

The next level of fidelity described by by Chaussée is the "Scaling Method." In this approach, several reference structural models are constructed that are somewhat similar to the anticipated final design. The primary structures of the reference models are analyzed and optimized in detail to get accurate structural masses. As the vehicle optimization proceeds, the reference masses are then scaled based on general parameters for the structure, such as wing span and area. The advantage of this method is that it is not reliant on

data of existing vehicles, making it useful for studying revolutionary configurations. By interpolating between reference designs, mass trades can be considered without spending time performing detail design of many structures. However, this approach can become prohibitively time-consuming if the desire is to simultaneously explore variations in external geometry and internal structure. This is because a large number of reference structural models would be needed and a rigorous optimization is required for each.

A classic application of the Scaling Method is given in Reference [29]. This paper from 1974 is a study of the application of composites to high-performance aircraft, when composite structures were much more of a conceptual notion than current applications. The study in Reference [29] determines a baseline structural mass breakdown for aluminum construction and then estimates the mass savings in each major component based on the stiffness, strength, and density relative to the baseline aluminum design.

In Reference [27], Chaussée identifies that the Fully Empirical approach and Scaling Method described above have unsatisfactory characteristics for application to challenging, unconventional structures and multi-discipline design environments. Primarily, the two approaches above give a lumped value of mass rather than a defined optimal structure with a distribution of mass and stiffness over the structure.

The next highest level of fidelity from Reference [27] can be found in "Low Fidelity Analytical Methods." Structural sizing approaches in this category are based on analytic structural analyses that often do not use Finite Element Analysis (FEA) [30],[31],[32]. One example of a non-FEA approach can be found in the ELAPS tool created by G. Giles [33],[34],. This tool uses an equivalent laminated plate representation to analytically solve for global displacement and load distribution for simple wing and fuselage models. In the approaches that do use a simplified FEA [23],[35],[36], the structure is usually sized as a simple shell without considering details such as internal stiffener dimensions or ply angles (in the case of composites).

The advantage of approaches in the "Low Fidelity Analytic" category over the previous category is that internal loads can be derived, so that any sizing performed will give a distribution of mass and stiffness over the structure as opposed to a single lumped value.

This information allows for preliminary multi-disciplinary studies, such as investigating aeroelastic performance. However, yet an even higher level of fidelity is needed to perform trade studies on the internal configuration of the structure.

The final category of conceptual structure sizing described in Reference [27] is "High Fidelity Analytical Methods." This category is characterized by advanced analyses similar to those used for final design of a vehicle. The majority of studies in this category implement a Finite Element Model (FEM) to derive accurate internal loads for sizing the structure and determining the stiffness distribution [37]. Additionally, this category is where multi-disciplinary studies of main structural components begin to show up, such as aeroelastic studies of a wing; some examples of this are shown in References [38] and [39].

There are several existing commercial tools to perform detail design of structures [1],[40],[41] in this category. In this context, "detail design" refers to determining parameters such as skin thicknesses, stiffener heights, and ply angles (for composites). These tools excel at finding a low-mass solution for given load cases while also accommodating global requirements such as wing tip deflection [42]. However, these tools are inappropriate for conceptual design studies that require run-times approaching several minutes rather than hours, days, or weeks. Significantly lower run times are needed when performing MDO that requires a large number of design variables to be evaluated. Additionally, any design process that has a human in the loop becomes burdensome if run times of the sizing tool are greater than a few minutes for each analysis.

Another factor that must be considered when applying detail design tools to conceptual design is that they often require a well-defined starting point to achieve a good design. In terms of "depth versus breadth," these tools excel at finding a minimum mass, but are difficult to apply to a design space with broad bounds. Tools for design of conceptual structures must be sufficiently robust against unexpected combinations of internal loads and be able to generate a design which can support those loads. Any vehicle configuration which is significantly different than existing configurations will likely have internal loads and stiffness requirements that require a new and unique internal design [28],[43],[8].

These challenges are compounded by the fact that the global performance of the structure can have significant dependance on the finer details of the structure. For example, the aeroelastic performance of a composite wing is highly dependent on the layup of the upper and lower skins [44]. In turn, the layup of the skin is coupled with the design of the stiffeners to ensure that the skin/stiffener combination passes all failure criteria for the internal structural loads. This environment is referred to as a "panel-level" sizing, discussed in detail in the next chapter. Panel-level sizing is typically only adequately handled by the detailed design tools described above. Unfortunately, these are difficult to incorporate into closely-coupled MDO due to poor efficiency.

To resolve the issues facing MDO for detailed structural design, it is necessary to advance the computational efficiency of existing high fidelity tools. This will allow for the tools to be used earlier in the design process where MDO studies are found. As shown in Figure 2 , the desire is to push structures tools from the high fidelity categories into conceptual design.

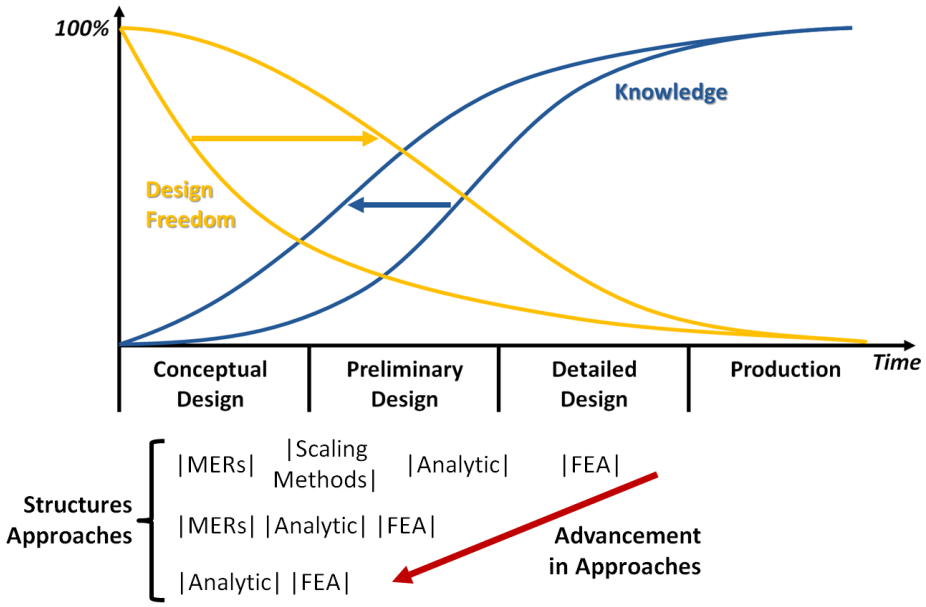

Figure 2: Notional Progression of Vehicle Design [2] and Associated Tools

Figure 2 shows the progression of design knowledge and design freedom over the conceptual, preliminary, detailed design, and production of a vehicle. Traditional design environments are characterized by a low level of design knowledge until the detail design phase, and a steep drop in design freedom during the conceptual phase. For future design environments, it is desirable to shift the knowledge curve to the left, such that vehicle design is well understood in the conceptual and preliminary phases. Additionally, the design freedom curve should be shifted to the right, such that large portions of the design space are not eliminated in early conceptual design. These two curve shifts can be facilitated by pushing detailed design tools into the conceptual phase, thereby allowing more concepts to be studied and ultimately improving understanding of the vehicle design.

The focus of this thesis is to develop a structural sizing methodology that serves as an intermediate conceptual sizing tool between simplistic mass estimation and detailed structural design. Existing design tools are either too simplistic or too inefficient to be useful for achieving the goals described above for system-level MDO integration. In developing this methodology, four key features are considered:

1. **Efficiency:** paramount to usefulness in an MDO environment.
2. **Fidelity:** necessary to analyze unique, unconventional vehicle configurations.
3. **Generality:** must be able to consider a variety of materials and structural concepts.
4. **Global Interface Capability:** necessary for coupling and iterating with a MDO environment.

These desired features become a part of the objectives of this research, which are discussed in the next section.

1.2 Research Goals and Objectives

The objective of this research is to explore approaches for structural design which are efficient enough to be useful in a large-scale multi-discipline environment, but which also retain the accuracy of physics-based analyses. The research will consider existing approaches

for simplifying structural optimization and also present a new panel-based optimization methodology to improve upon existing approaches. The goal of the new panel methodology is to explore a gap in existing techniques, exploiting a change of optimization variables to linearize the design space and improve optimization efficiency. In doing so, the new methodology must retain the generality of existing tools by being applicable to multiple material systems (metallics and composites) as well as multiple panel concepts. Additionally, the methodology must be capable of interfacing with FEM -based design environments, which have become a standard part of aerospace vehicle design. The following objectives address these points in more detail. These were developed as a result of the literature search performed in Sections 2.7 through 2.9.

1. **Use a design of experiments and response surface equations to expedite stiffened panel design.**

Panel optimization is often the most cumbersome part of the conceptual design of a structure. The first objective of this research is to apply existing combinatorial approaches to the panel optimization problem to improve efficiency and compare to the optimization tool HyperSizer as a baseline. HyperSizer uses a full-factorial optimization approach to perform broad studies of the design space. Compared to a full-factorial exploration of the stiffened panel design space, a design of experiments can provide a set of design points with similar breadth but with fewer total points. Further improvement in efficiency can be achieved using regression to generate response surface equations which represent stiffened panel failure criteria as a function of panel dimensions. These equations can provide a more simple form when evaluating constraints and also improve compatibility with optimization algorithms.

2. **Perform linearization of the panel design environment to improve efficiency beyond existing approaches.**

Linearization of the stiffened panel failure criteria used in optimization can be achieved

through a change of variables, from physical variables to smeared stiffness terms. The linearization is not closed-form, but can be achieved through the use of response surface equations to represent the panel failure criteria as a function of panel stiffness terms. Linearization allows the optimization to be solved with the very simple Simplex Algorithm, greatly improving efficiency. The challenge to overcome is that the linearization must be developed in such a way that the panel design environment retains substantial accuracy.

3. **Apply linearized panel design methodology to composite panels to demonstrate generality of the approach.**

Composite materials allow the stiffness of a structure to be customized with a small impact on mass. Although this is a highly useful trait, it also introduces significant complexity to structural design. Due to the increased proliferation of composites into aerospace vehicles in recent years, it is important for the linearized panel design environment to be capable of handling this increased complexity. The methodology must be able to account for total ply angle counts in the composite, as well as distribution of the ply angles through the thickness of the composite.

4. **Couple linearized panel methodology with a FEM -based design environment.**

The vast majority of modern aerospace vehicle design process use a FEM -based design environment, even in early stages of design. Thus, it is critical for any panel optimization methodology to be well-suited for integration with a FEM and FEA results. Primarily, this means having the ability to handle constraints imposed at the FEM (global) level, ability to execute quickly so that iterations can be performed with the FEM , and ability to handle multiple load cases during optimization.

1.3 Dissertation Outline

This chapter (1) introduced the motivation behind the methodology developed in this research and presented the goals and objectives used as the framework for the dissertation.

The four distinct objectives from the previous section provide requirements for the content developed in Chapters 3 through 8.

Chapter 2 provides the background (literature review) needed to understand the methodology presented in this research, as well as its role in aerospace vehicle design. This background includes an overview of multi-discipline design and the role the structures discipline plays. Following the high-level content, the chapter delves into the details of internal structural arrangement and stiffened panel design.

Chapter 3 directly addresses the first two research objectives presented in the previous section. First, the chapter considers application of existing techniques (design of experiments and response surface equations) to improve run time of stiffened panel optimization. Additionally, the chapter contains the primary development made in this research, linearization of the stiffened panel design space performed via a change of variables. The remainder of the chapter contains a thorough development of the methodology, providing justification for each step. This includes the change of optimization variables, reformulation (linearization) of the panel failure criteria, and constraints needed to map between the two variable domains. The last chapter presents a method for the reverse-mapping that is needed at the completion of conceptual sizing with the stiffness-based approach developed in this research. This reverse-mapping is needed to produce physical panel designs to provide a starting point for preliminary design.

Chapter 4 focuses on performing a validation of the methodology developed in Chapter 3. The metallic I-stiffened panel is used for three different types of validation. The first validation determines how accurately the linearized failure criteria represent the original analyses. This is done by comparing failure predictions from the linearized analyses with the original analyses for a large number of panel designs and loads. In the next validation, the overall accuracy of the optimization is assessed by comparing results from the new methodology to a high-resolution optimization performed with present state-of-the-practice methods. The final validation performed in this chapter verifies a key aspect of the methodology that is needed to interface with a FEM , which is the ability to handle stiffness constraints specified on the FEM .

Chapter 5 addresses the third research objective presented in the previous section by showing that the new methodology is fully applicable to composite panels. The chapter develops two composite panels in parallel, an unstiffened laminate (flat plate) and an I-stiffened panel. The demonstration goals are slightly different for the two panels. The flat plate uses a high level of fidelity by capturing effects of ply stacking sequence as well as ply stacking rules. The I-stiffened panel uses a higher level of abstraction to represent the composite material (via effective stiffness) to demonstrate ability to handle a large design space. The optimization methodology for these panels is developed in a similar pattern to Chapter 3, providing a step-by-step application of the linearization methodology to the composite panels.

Chapter 6 provides the methods used to couple the panel optimization methodology from Chapter 3 with a FEM -based environment. First, the concept of bi-level optimization is presented, which is a common approach for handling such environments. Next, an approach is developed to control the FEM stiffness at the global level using a relatively small number of control points. The final part of this chapter presents the methodology needed to update the FEM based on results from the linear panel optimization. This is necessary because the linear panel optimization uses only a subset of panel stiffness terms, so the remainder must be estimated to correctly update the FEM .

Chapter 7 presents the first of two FEM -based demonstrations using the methodology developed in this research, addressing the fourth research objective. The optimization is performed on a metallic wing box from a 737-similar aircraft and focuses on the skins of the wing box, which use a metallic I-stiffened concept. Longitudinal stiffness of the wing box skins is controlled at the global level of the optimization to meet a required wing tip deflection while simultaneously minimizing the mass of the upper and lower skins. The result from this optimization is compared to a baseline optimization using an existing commercial software, HyperSizer, to determine viability of the approach, and establish the improvement in efficiency.

Chapter 8 contains the second FEM -based demonstration, a composite wing for an F-86-similar aircraft. The wing uses the unstiffened composite laminate optimization methodology from Chapter 5. The F-86 wing optimization does not include a global stiffness constraint like the previous example in order to simplify the FEA iteration process. However, properties of the composite are controlled at the global level to enforce continuous (manufacturable) distributions of ply thickness and ply angles. This also simultaneously demonstrates two key objectives for the current research: applicability to composites and ability to couple with a FEM . The results are compared to a baseline design developed in HyperSizer to determine viability of the approach.

Finally, Chapter 9 provides conclusions about the linear panel optimization methodology and its ability to meet the demands of a multi-disciplinary conceptual design environment. The chapter also includes recommendations for future work to further improve the efficiency and accuracy of the methodology, as well as further examination of the generality of the approach.

CHAPTER II

BACKGROUND

The sections presented in this chapter are focused on providing the background for the developments made in the current research.

The first section frames the general multi-discipline environment in which the research is focused and introduces the role of the structures discipline. From here, the sections provide increasingly specific background information on the structural design approaches considered in the current research. This starts with an example of external load application, a step required to initiate any conceptual structure design.

The second section studies internal structural arrangement, which is is a complex 3-dimensional problem with few analytic solutions. This section emphasizes the need to have a fast stiffened panel design tool to be suitable for conceptual studies because a significant number of structural arrangements must be considered to find one which is mass efficient.

The next section provides a description of Finite Element Modeling (FEM) and Finite Element Analysis (FEA), tools frequently used in structural design.

Following the introduction to FEA , the next two sections provide details of the structural design process considered in this research. A high-level outline of the process is given, followed by a detailed description of stiffened panel design. This includes the approach of a commercial tool (HyperSizer) as well as a review of several other stiffened panel tools.

The last three sections are focused on literature directly relevant to the methodology developed within the current research. Of these three, the first is a review of applying regression (curve-fitting) to stiffened panel design in order to improve efficiency. The next section reviews how stiffened panel design environments are efficiently coupled to a FEM - based design process with global constraints. The final section is a review of approaches used to simplify composite laminate design to be more suitable for conceptual panel sizing.

Each section in this chapter provides the background needed to build the methodology

and meet the objectives of the current research. Along the way, gaps in existing research are identified to demonstrate the overall contribution of the research.

2.1 General Multi-Discipline Design Environment for Aerospace Vehicles

This section contains a broad discussion of multi-discipline design environments for aerospace vehicles and includes the majority of disciplines found in aerospace vehicle design.

The first step to providing background for the current research is to introduce the structures discipline within vehicle design environment. This is done in Figure 3, which describes the general flow used to design a new aerospace vehicle for a given mission. Note that the diagram only considers a fixed Outer Mold Line (OML), meaning it does not include variation in external geometry. The final output of this flow chart is a vehicle structure and propulsion system which is consistent with the specified OML and meets the mission requirements. The vehicle design is closed when each of the disciplines can meet all specified requirements.

In Figure 3, the data transferred between each discipline is numbered and corresponds to the descriptions shown below. In the paragraphs below, the feed-forward loops (upper-right arrows) are described first for each individual discipline. Next, the feedback loops (lower-left arrows) are described.

Feed-Forward: Aerodynamics

1. The vehicle OML is passed to the aerodynamic analysis tool.

This input is used to evaluate overall aerodynamic performance for the configuration and generate surface pressure distributions.

Feed-Forward: Propulsion

2. The flight profile dictates the general type of propulsion system needed for the vehicle (e.g. air-breathing vs rockets).

Feed-Forward: Mission Trajectory

3. The flight profile provides a target for trajectory design.

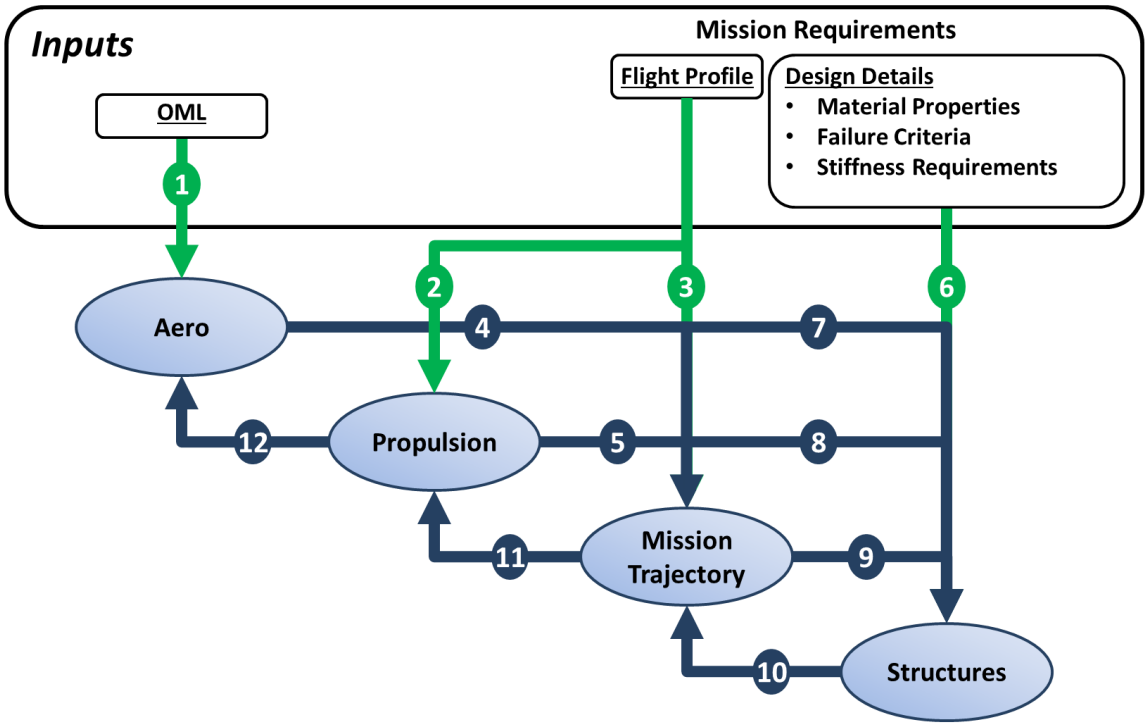

Figure 3: General System-Level MDO Flow Chart

4. The aerodynamic characteristics are passed to the mission trajectory discipline to be used in trajectory design.

5. Characteristics of the propulsion system (thrust, efficiency) are also passed in to be used for trajectory design.

With these inputs, trajectory design can be performed. This consists of determining time-varying parameters such as angle of attack or thrust vector integrated along the specified flight profile.

Feed-Forward: Structures

6. Many high-level requirements feed into the structures discipline. Materials are selected at the system level according to cost, manufacturing, temperature limits, etc. Failure criteria are dictated by FAA, EASA, and customer requirements, as well as by similar previous vehicles. Additionally, stiffness requirements for the structure are often dictated at the system level (discussed in detail later).

7. Pressure distributions determined in the aerodynamics analysis provide external loads.

8. The mass of the propulsion system selected for the mission is input to the analysis to determine resulting internal loads.

9. Inertial loads are passed in based on the trajectory designed for the mission.

The structures discipline uses these inputs to determine an appropriate structural design (internal arrangement and detail designs) to support the given requirements and loads. The design produces a distribution of mass throughout the structure. Note that the structural masses determined here are of the primary load-bearing structure. Non-optimum masses such as bolts, welds, fittings, interface pad-ups, etc. are not considered in this research.

The processes used to achieve the objectives of the structures discipline are the focus of the current research and are described in detail in the remaining sections of this chapter.

Feedback Loops

The final parts of Figure 3 to identify are the feedback loops, identified by the lower-left arrows on the figure. These data transfers occur after the first pass through the flow chart when the disciplines update each other with new design information.

10. Mass properties of the vehicle (mass, Center of Gravity (CG), moments of inertia) are passed back to the mission trajectory discipline for trajectory design and optimization.

11. New propulsion requirements are passed back to the propulsion discipline for reasons such as improving efficiency or closing the design (meeting thrust-to-mass requirements).

12. Geometry of the propulsion system is passed back to the aerodynamics discipline to account for changes in propulsion nacelles and struts.

2.2 Load Case Development for Conceptual Structure Design

As discussed in Section 1.1 of the Introduction, fully integrated vehicle design environments, such as the one described in Section 2.1, are ideal but difficult to use in practice. Thus, the structures discipline is often required to resort to more simplistic methods to get the external

loads acting on a structure instead of relying on the trajectory and aerodynamics discipline for initial loads. This is often required at the very start of a vehicle design because of the "chicken-and-egg" problem that exists between the disciplines. Each discipline requires inputs from other disciplines to function, meaning rough estimations of these inputs are needed to initiate the feed-forward and feed-back loops described in Section 2.1.

This section discusses how load cases are selected for conceptual design and how approximations of these loads are derived to initiate the structural design.

2.2.1 Critical Flight Conditions

The structures of production aerospace vehicles are usually designed considering thousands of load cases to cover every conceivable flight and ground loading scenario. Among these, typically only a small number of cases drive the design of the majority of the structure. This small subset of loads is often used in conceptual design under the assumption that doing so will capture the majority of the structural mass.

2.2.1.1 Aircraft

For the wing structures used as the examples in this research, the prevalent critical loads are the pull-up and pull-down maneuver. Thus, determining loads for conceptual sizing primarily consists of estimating lift distributions over the surface of the wing for these flight conditions. The severity of the pull-up and pull-down maneuver is typically established by the type of aircraft. Most commercial aircraft are designed to a FAA-required 2.5g pull-up maneuver [45], whereas fighter jets are usually designed for a pull-up maneuver greater than 6g's [46] depending on customer requirements.

The pull-up and pull-down design limits for the aircraft help define the maneuver envelope, or V-n diagram for the aircraft. An example of a typical V-n diagram for a jet trainer aircraft is shown in Figure 4 [3]. Lines BC and ED on the diagram define the pull-up and pull-down limits respectively. The two curves on the figure are the maximum possible load factor (n_{max}) that can be achieved at a given free stream velocity (v). This relationship is given in Equation 1. Equation 1 also uses free-stream density (ρ), maximum lift coefficient

of the vehicle ($C_{L,max}$), weight of the vehicle (W), and wing area (A).

$$n_{max} = \frac{1}{2}\rho v^2 \frac{C_{L,max}}{W/A} \tag{1}$$

If the pilot attempts to maneuver the aircraft at a higher load factor, aircraft will enter a stall. Beyond points B and E, the aircraft cannot be flown at n_{max} without risk of incurring structural damage. The vertical line CD represents the maximum velocity allowed for the aircraft. This limit is always higher than the aircraft's maximum velocity in level flight and thus can only be reached in a dive. This maximum dive velocity is usually dictated by flutter, aileron reversal, or wing divergence, which are all aeroelastic phenomena [47]. These constraints are often neglected for conceptual sizing due to complexity.

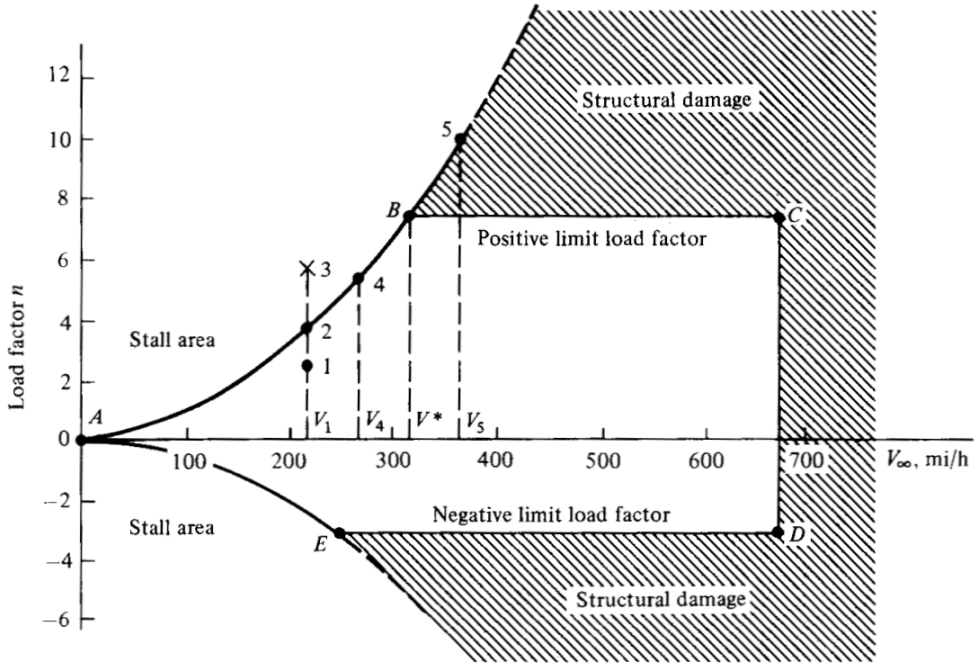

Figure 4: V-n Diagram for a Typical Jet Trainer Aircraft [3]

A similar diagram exists for commercial transport aircraft. The FAA Federal Aviation Regulations (FAR) Part 25.333 provides the minimum required flight envelope for these aircraft [4]. The envelope, given in Figure 5, shows a maximum pull-up maneuver of +2.5gs and a maximum pull-down maneuver of -1.0g. There is an additional allowance for the flaps-down condition because transport aircraft often have large flaps and thus a much higher maximum lift coefficient when extended.

The air speeds indicated in Figure 5 are unique to each aircraft. However, the FAA specifies the required ratios between each airspeed appearing on Figure 5 in the FAR Part 25.335.

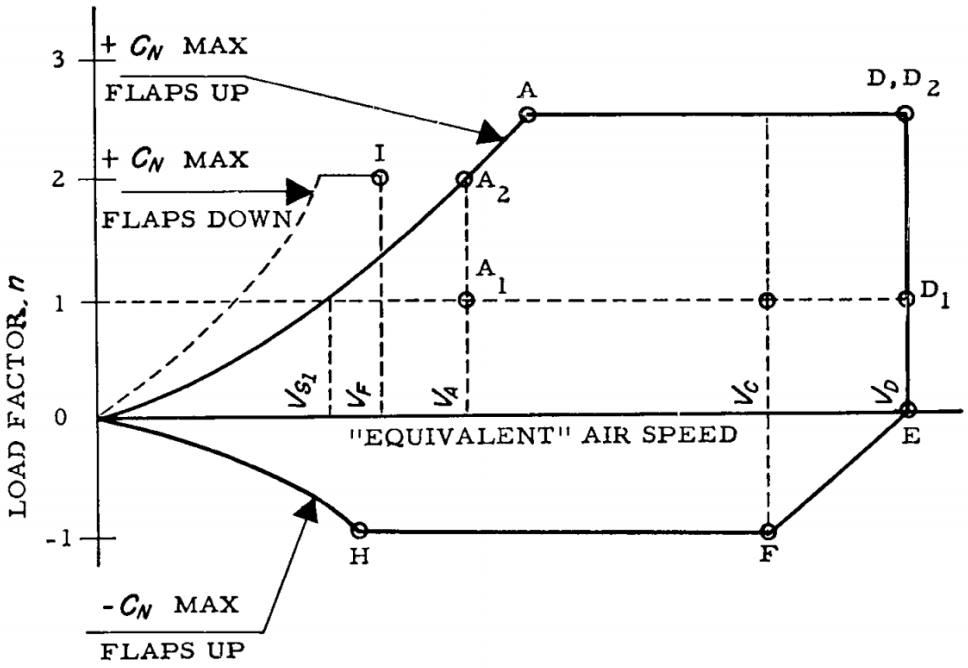

Figure 5: V-n Diagram for Commercial Aircraft [4]

A final note to make about the maneuver limits is that a 1.5 safety factor is usually included on top of the requirements. This is usually accounted for by scaling the internal loads when stress analysis is performed.

2.2.2 Approaches for Aerodynamic Load Development

Now that the premise of load case selection has been introduced, this section will provide a discussion on how aerodynamic load cases are developed. There are three common approaches for deriving a pressure distribution (thus providing lift and drag) over a structure, listed below in order of increasing fidelity.

1. A combination of 2D airfoil aerodynamics and approximations of 3D aerodynamics. 2D analysis can be used to determine the local performance of an airfoil, but must be scaled according to span-wise location to account for 3D circulation (vortexes). An

elliptical distribution is typically used to account for this effect, as discussed in the next section. This approach only works for long slender structures, such as wings and struts, but is simple to perform.

2. The discrete linear vortex lattice method [48]. This analysis requires some rough geometric modeling of the vehicle, but is very computationally efficient. This approach is able to determine 3D wing phenomena such as induced drag and pressure coefficient distribution. However, the analysis is limited to simple geometries.

3. Use of Computational Fluid Dynamics (CFD) [49],[50]. This approach can provide highly accurate results, but requires a precise geometric model. The advantage of CFD over the vortex lattice method is that it can produce a pressure distribution over any arbitrary geometry. This is necessary for later stages of design to determine the aerodynamic loading unique to the vehicle OML.

Of the approaches listed above, only the first is considered in this research. As stated previously, only simple approximations are needed to initialize the structural design process. The more advanced approaches would be used as the structures discipline becomes more integrated with the aerodynamics discipline.

2.2.3 Approximate Method for Determining Load Distribution Over a Wing

This section contains the details of the first approach presented in Section 2.2.2 for determining lift, drag, and moment distributions. The calculations in this section were identified by D. Raymer [51] as an approach to determine a load distribution on a wing for conceptual design. References [3] and [52] provide additional calculations needed to complete the process. The approach described in this section was applied to the wing structure examples presented in Chapters 7 and 8.

The first step of developing an approximate load distribution for a wing is to select critical load case(s) as described in Section 2.2.1. Once the level of the load factor (n) is set, the weight (W) of the aircraft must be estimated to determine the load on the wings.

For a n-g maneuver, the wing loading (L) is calculated by Equation 2 [51].

$$L = n \cdot W \tag{2}$$

The next step is to determine the lift coefficient of the wings during the maneuver. Lift coefficient is calculated from the relation for wing lift shown in Equation 3 [51]. The calculation requires knowing the velocity of the vehicle during the maneuver (v), density of the air (ρ), and wing area (A). The value of L determined by Equation 2 is also used.

$$L = \frac{1}{2}\rho v^2 A C_L \tag{3}$$

Once the lift coefficient has been calculated, the angle of attack of the wing can be approximated from a C_L-α plot for the wing's airfoil. These plots can be determined by experimental data or from 2D airfoil analysis codes such as XFOIL [53]. This resulting angle of attack is necessary to determine the lift, drag, and moment distributions described below.

The next step is to approximate 3D wing effects with an estimated load distribution in the span-wise direction. It is common to approximate this distribution as having an elliptical shape [3], pictured in Figure 6. However, the span-wise lift distribution is influenced by wing taper ratio, twist, and sweep. Schrenk's approximation can be used to account for the effect of wing sweep and taper [52].

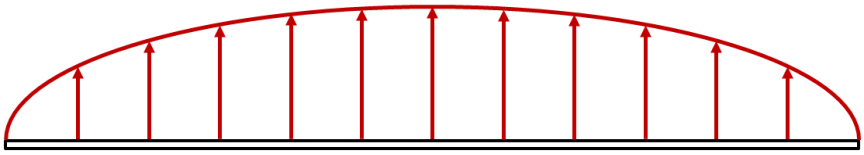

Figure 6: Example Elliptical Lift Distribution Over the Span of a Wing

Another 3D wing effect that must be approximated is induced drag. A subsonic 2D airfoil analysis can only capture skin friction drag and pressure drag (referred to together as profile drag). Induced drag is caused by the same 3D circulation (vortexes) that reduces lift at the tips of a 3D wing. The induced drag coefficient ($C_{D,i}$) can be calculated from Equation 4 [3] based on the wing lift coefficient (C_L), span efficiency factor (e), and wing

aspect ratio (AR). The value of e was assumed to be 0.9 for the wings considered in this research.

$$C_{D,i} = \frac{C_L^2}{\pi e AR} \tag{4}$$

From this point, there are two possible routes to apply the load distribution to the structural model. The first is to apply the lift load to the model at discrete points along the wing, which is more simplistic from a FEM modeling standpoint. The second approach applies the lift load via a continuous pressure distribution over the upper and lower skins of the wing, which provides more accurate loads but requires greater modeling effort. These two approaches are described in the sections below.

2.2.3.1 Equivalent Discrete Load Distribution

This approach approximates the wing as a series of segments, each with a constant chord. The total load on the wing is achieved by calculating lift, drag, and pitching moment on each segment and applying these loads to the centroids of the segments. This is depicted in Figure 7. The span-wise distribution described above dictates how these loads are scaled from root to tip.

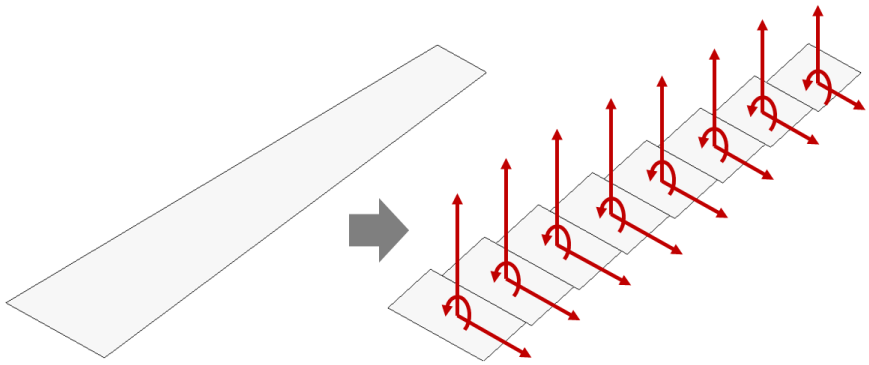

Figure 7: Application of Discrete Loads to Wing Segments

The loads on each segment are calculated from the geometry of the segment. Lift is determined by Equation 3, where A is the segment area instead of half the wing area. Drag (D) is determined by a similar calculation, given in Equation 5. Pitching moment (M) of

the segment is determined by Equation 6, which also includes the segment chord c.

$$D = \frac{1}{2}\rho v^2 A C_D \tag{5}$$

$$M = \frac{1}{2}\rho v^2 A c C_M \tag{6}$$

The final loads (force and moment) are applied to the FEM at the centroid of each wing segment. This is done by rotating the lift and drag force components to align with the local airfoil normal vector (for each segment). Additionally, moving the lift and drag force vectors from the center of pressure to the geometric centroid of each segment requires the addition of a pitching moment.

2.2.3.2 Continuous Pressure Distribution Approximation

The second method for applying the loads to the wing uses a continuous pressure distribution to produce lift and drag forces, as well as pitching moment. Deriving loads with a continuous pressure approximation is similar to the discrete approach described above, but also incorporates the pressure distribution over the airfoil. Instead of applying discrete loads to the wing structure, the aerodynamic forces are applied to the structural model as a pressure on every element of the wetted surface of the wing. This results in a smoother load introduction for the structural model than the discrete load approach.

The chord-wise pressure distribution can be calculated by 2D airfoil analysis codes for subsonic, non-stalled conditions [53] at a specified angle of attack. An example of such a distribution is shown in Figure 8. As discussed in Reference [3], a continuous pressure distribution can be integrated over the curvature of the airfoil to derive the net lift, drag, and pitching moment of the section. Thus, the continuous approach produces the same total load on the structure as the discrete approach described above.

The information shown in Figure 8 establishes the chord-wise variation in wing pressure. Next, the span-wise variation in pressure must be determined. This is done in a manner identical to what was described in the previous section, by applying an elliptical scaling to the pressure distribution in the span-wise direction. The final result of this process is a continuous distribution that defines the magnitude of pressure on the lower and upper

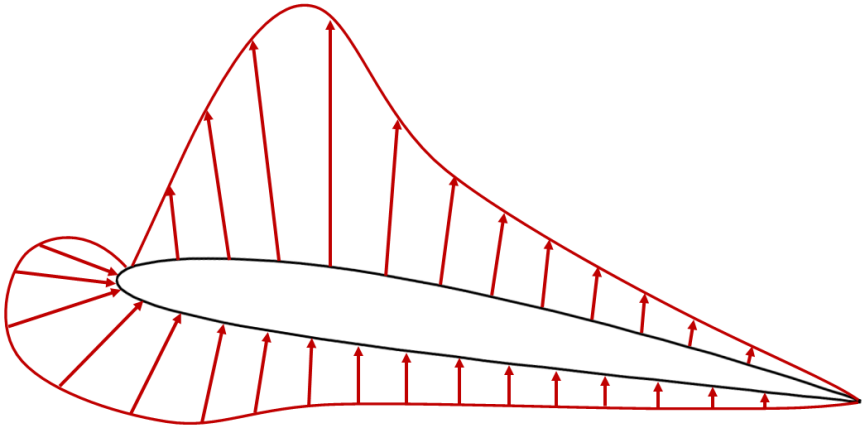

Figure 8: Example Pressure Distribution on an Airfoil

surface of the wing at every point over the area of the wing. An example of the resulting pressure coefficient (C_p) distribution is shown in Figure 9. This pressure distribution can be mapped to the mesh of a FEM based on the location of the centroid of each element in the upper and lower skins of the wing (many commercial FEA pre-processors can perform this mapping).

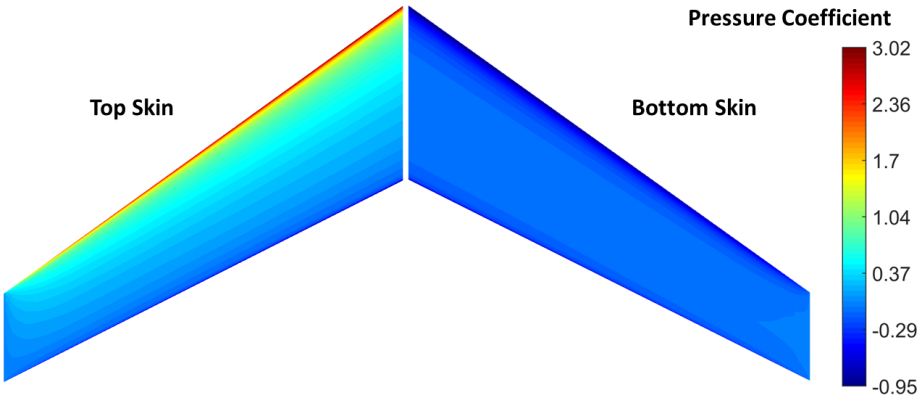

Figure 9: Example Pressure Distribution on a 3D Wing

2.3 Overview of Internal Structure Arrangement

Internal structure arrangement pertains to the placement of primary structural members within a given OML. These structural members are often described as frames, bulkheads, ribs, and spars. Placement of these structures must provide a favorable internal load path

and sufficient overall vehicle stiffness. This topic is of high relevance to the current research because it defines where stiffened panels are located in a structure. Figure 10 shows an example of frame and stiffened panel placement in a Boeing 777 fuselage. Stiffened panels are described in detail in Section 2.6.

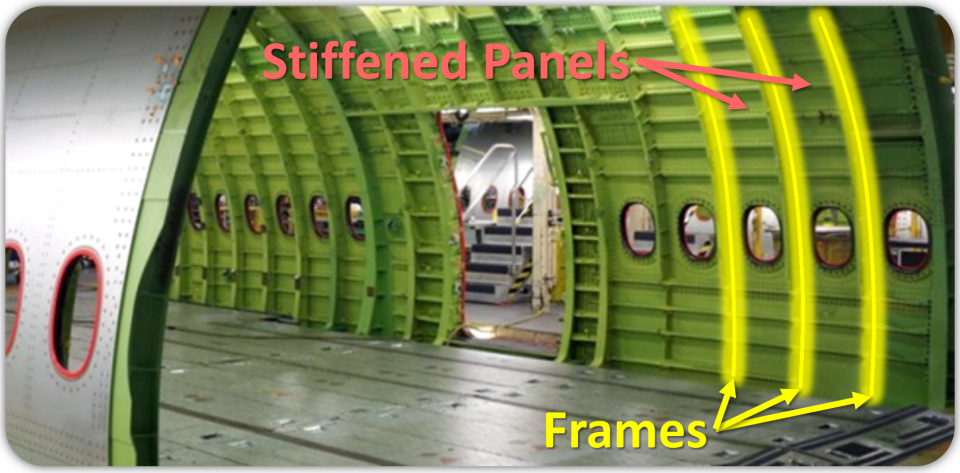

Figure 10: Frame and Stiffened Panel Placement in Boeing 777 Fuselage [5]

The intent of the current section is to provide background information on how the internal arrangement of a structure is determined and to highlight how it is closely coupled with stiffened panel design. A brief description of each type of structural member is provided below. Figure 11 identifies these four structural members.

- **Frame:** commonly found in fuselage structures and barrel sections of launch vehicles. Primary usage is to break up un-supported spans of structure to prevent buckling. In general, they are oriented perpendicular to the skin they support. Additionally, frames are usually open structures and do not significantly intrude on the internal volume of a vehicle.

- **Bulkhead:** also found primarily in fuselages, but are usually heavier than frames and carry more load. Characterized by providing closure on an internal volume, either to maintain internal pressure or to support subsystems and other fixtures.

- **Rib:** commonly found in wings, but serve a similar purpose to frames. These structures are usually aligned with the chord-wise direction of a wing.

- **Spar:** also found in wings, oriented perpendicular to ribs. These structures are substantially heavier and stiffer than ribs, and are designed to carry significant shear load when the wing is loaded in bending.

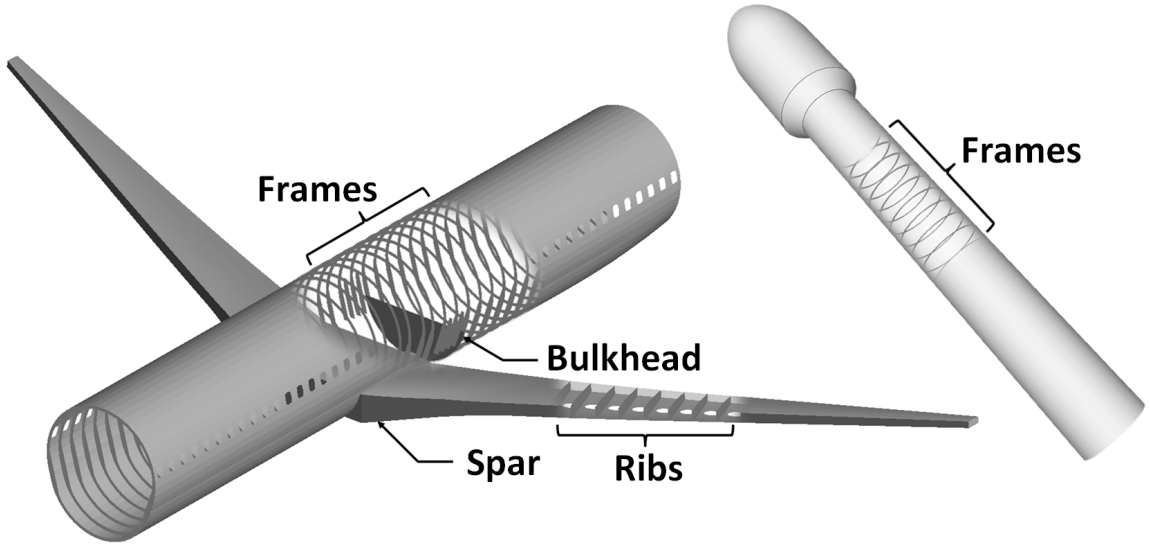

Figure 11: Primary Components of an Internal Arrangement for a Commercial Aircraft and Launch Vehicle Barrel

The external loads and overall OML geometry are usually what dictate the complexity of the internal arrangement of a structure. The simplest internal arrangement is usually found in the barrel of a launch vehicle or a commercial aircraft fuselage or wing (see Figure 11). These structures often have a uniform overall geometry and a significant amount of structural acreage to bear the internal loads. These characteristics result in simple internal structure with the arrangement varying in just one direction. This characteristic makes it very straight-forward to study a large number of different configurations.

Structural arrangement is more complex for vehicles that are subject to high loads, complex OML geometry, or a combination of the two. One structure that falls in this category is that of a fighter jet. Most fighter jets have a slender OML optimized for high-speed flight. Within the OML, a significant portion of internal volume is usually taken up by

large jet engine(s). Thus, there is not much volume available for the primary structure in both the wings and the fuselage. Additionally, fighter jets are designed to have a large flight envelope, able to withstand as much as 9g's (estimated, this information is not generally published by the DoD). The resulting internal structure is usually irregular throughout the vehicle (see Figure 12). These structures are at the opposite end of the design complexity spectrum from the barrel sections shown above. As shown in Figure 12, the internal arrangement varies in three dimensions, whereas the barrel section arrangement varies in only one direction. The challenge of designing and performing trade studies with such a structure is modifying the internal geometry.

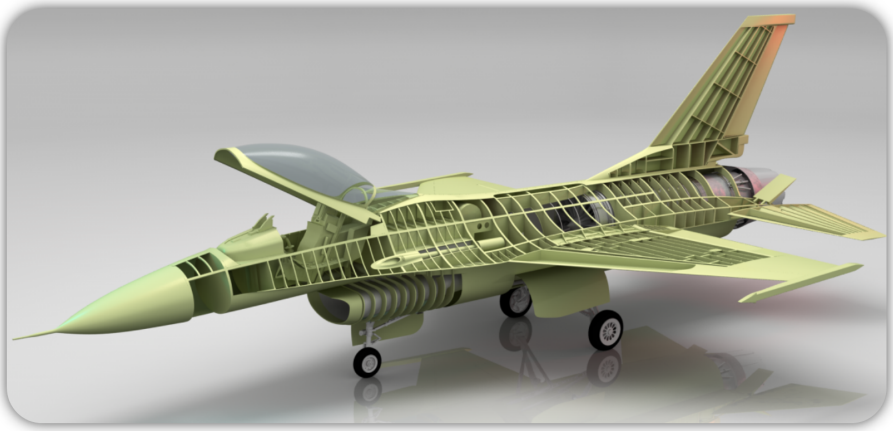

Figure 12: Cutaway View of Internal Arrangement for F-16 Fighter Jet [6]

Drawing on the discussion above, studies of internal structure can vary from just a few arrangements to 10 or more. Below is a description of several different studies that perform trades with different internal arrangements. Each one highlights the unique challenges posed by coupling between internal arrangement and stiffened panel design that are unique to the vehicle.

The first case study was performed with the Ares V interstage by C. Collier et al. [7]. The primary challenge of designing this structure was global buckling caused by the compression loading from the second stage and payload. Global buckling of the interstage is dependent on the combined stiffness of different parts of the internal structure. By definition, global buckling has a mode shape that spans across multiple components of the

structure, as opposed to local buckling which occurs only in small unsupported portions of the structure. Local buckling can be mitigated by small design changes, such as increasing the thickness of a skin or increasing the depth of a honeycomb core, both of which are easy to modify. Global buckling is much more complicated to resolve while obtaining a mass-optimum solution because it requires simultaneously rearranging internal structure and adjusting the stiffness of the structure by changing the thickness of the parts.

For the Ares V interstage, global buckling was evaluated with a linear static buckling solution in a FEA package. The requirements were that global buckling of the interstage could not occur at a loading less than 2.15 times the flight load and that the buckling mode shapes were be bounded by the frames in the interstage. The approach taken to meet this requirements while minimizing mass was to perform a study on spacing of the frames. For each frame spacing, the frame and skin were optimized. The frame was optimized to provide sufficient stiffness to force the buckling mode to fall in between frames, and the skin was optimized to prevent buckling between frames. The For the skin, several stiffening concepts were considered, including honeycomb sandwich and hat stiffened panels. Figure 13 summarizes the findings from Reference [7]. This study demonstrates the importance of the coupling between internal arrangement and stiffened panel design.

Another internal arrangement study to consider is that of the BWB (also known as a Hybrid Wing Body (HWB)) fuselage. A unique design challenge in the BWB is that the passenger compartment is flat and wide, making it non-ideal to handle pressurization than traditional cylindrical fuselages. The flat top and bottom of the passenger compartment have a tendency to pillow outward when the fuselage is pressurized. The primary solution for this problem is the use of longitudinal bulkheads to hold the top and bottom of the fuselage together.

An additional complication is that the passenger compartment must sustain loads induced by the fuselage and wing simultaneously. Because the wing and fuselage are integrated, the center body structure receives lateral loads from the wing and longitudinal loads from the fuselage.

Considering the challenges described above, the approach taken by T. Laughlin et al.

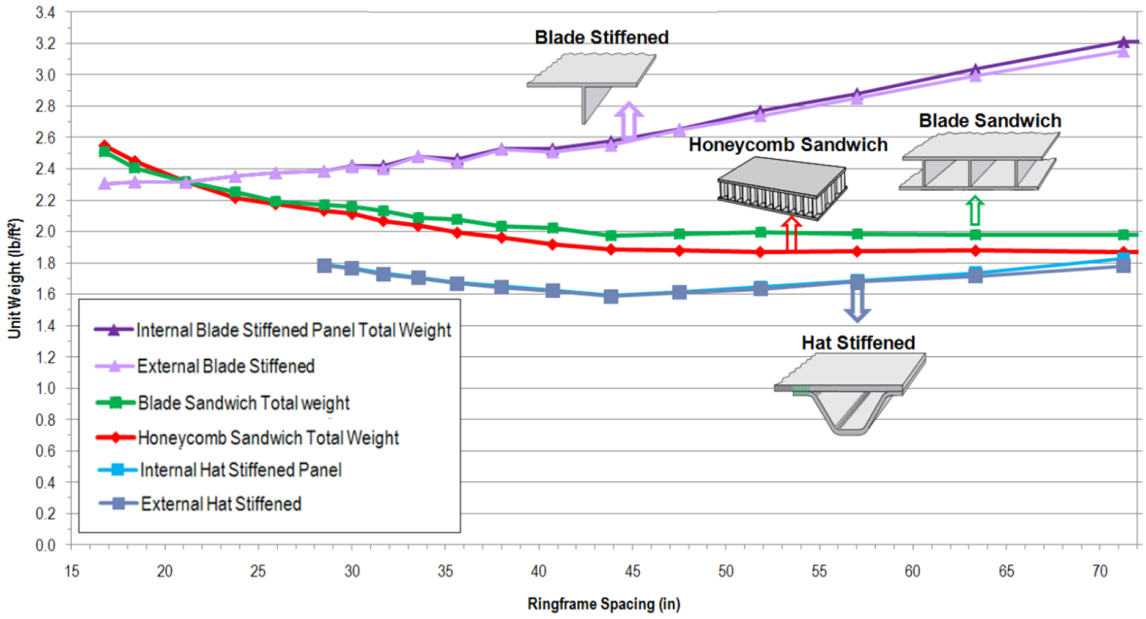

Figure 13: Trade Study of Frame Spacing for Ares V Interstage [7]

[8] was to consider various arrangements of bulkheads in the passenger compartment. In conjunction with the study of internal arrangement, the authors also explored how the optimum internal configuration varied for different scales of the BWB. To perform these studies, an automated FEM generation tool was used to generate variations of internal structure. Stiffened panel sizing was then performed for each internal arrangement variation to determine the mass of the primary structure. It was found that different numbers of bulkheads were needed for the various scales of BWB. These different bulkhead configurations are shown in Figure 14.

The final internal arrangement study considered in this section is the rib layout of a wing box structure. Two similar studies were performed by M. Harmin et al. [9] and G. Francois et al. [10]. The focus of these two studies was to determine if the stiffness of a metallic wing box can be tailored to improve aeroelastic performance without a significant mass penalty. The stiffness was tailored by varying the number and orientation of the ribs and then sizing the thickness of the skins, ribs, and spars. The sized thicknesses of the skins, spars, and ribs are dependent on the internal arrangement because the load path varies with different arrangements. This again highlights the coupling between internal arrangement and panel

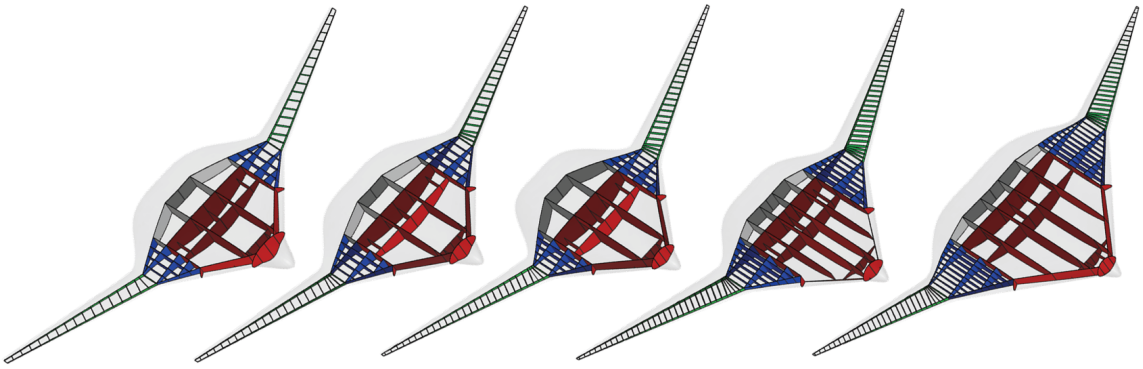

Figure 14: Internal Arrangement of 98, 160, 216, 301, 400 Passenger BWB (Left to Right) Reproduced from Reference [8]

sizing.

Both Reference [9] and [10] considered static aeroelasticity, analyzing the wing tip and twist for each arrangement and determining sensitivity of these responses to rib spacing and orientation. Static aeroelasticity considers the ability to influence wing bending and twist to improve the aerodynamics of the wing. Additionally, Reference [10] considered dynamic stability by evaluating natural frequency and velocity of first aeroelastic instability for each internal arrangement. Both authors concluded that significant aeroelastic tailoring can be achieved from rib placement and orientation alone. Figure 15 displays the geometry considered by the two studies on rib placement.

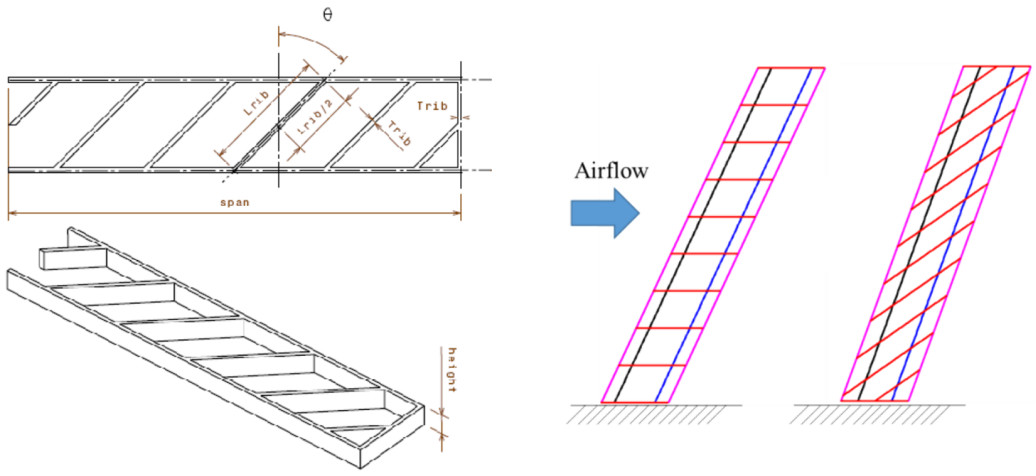

Figure 15: Studies of Rib Placement and Orientation Reproduced from References [9] (Left) and [10] (Right)

In summary, variations of internal arrangement cannot be studied independent of local stiffened panel design. The speed of the stiffened panel design is especially critical if a large number of arrangements is to be considered. Similarly, rapid panel design is needed when global stiffness constraints are applied because iterations must be performed for each internal arrangement.

The next section provides detailed information on existing stiffened panel design and considers applicability to conceptual design.

2.4 Introduction to Finite Element Analysis

Before discussing the details of general structural design it is necessary to first introduce Finite Element Analysis (FEA), which is a core component of modern structural design. FEA is a numerical technique for determining the load path through a complex geometry. FEA determines the displacement of nodes ($\vec{x}$) based on the applied loads ($\vec{F}$) and stiffness of elements connecting the nodes. In its most basic form, FEA solves Equation 7 for $\vec{x}$. This requires inverting the global stiffness matrix ($[K]$) which is built from the stiffness of all the elements in the model. Once the nodal displacements have been solved for, internal element loads can be calculated to define the load path in the structure [54].

$$\vec{F} = [K]\vec{x} \tag{7}$$

To perform FEA , the part must first be drawn in a Computer Aided Drafting (CAD) package to create a representation of the geometry. Next, the part is meshed in a pre-processor. Then the elements of the mesh are grouped into "properties." These property definitions include a reference to a material definition as well as information about the part design. For example, a FEM property could be used to define a 1/4" aluminum plate. Next, loads and boundary conditions are applied to the mesh in the pre-processor. The resulting model is usually referred to as a Finite Element Model (FEM). Next, the FEM is submitted to an FEA solver to solve for internal loads as described above. Finally, a post-processor is used to extract and examine the displacements and internal loads. Figure 16 depicts this entire process and identifies the tools related to each.

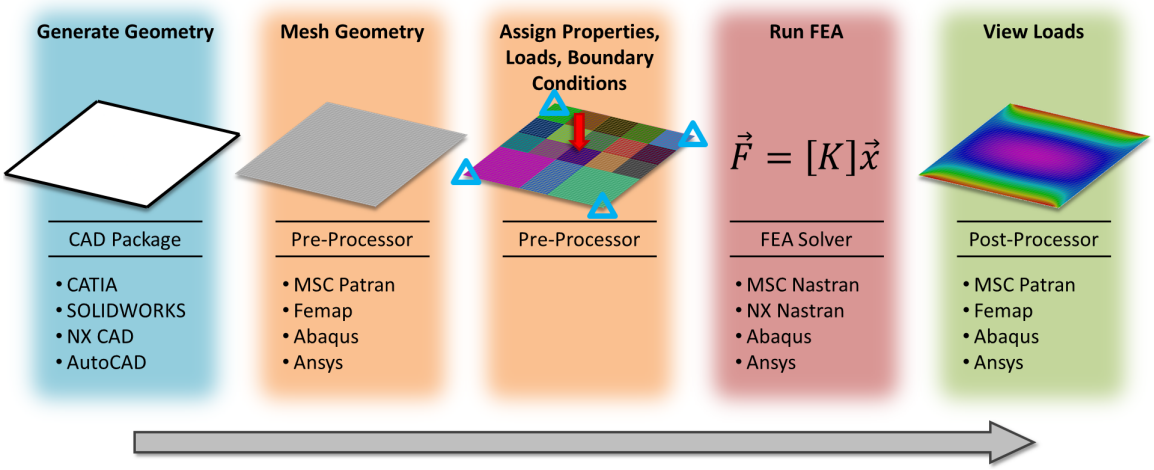

Figure 16: Process for Developing a FEM and Running FEA

There are a variety of solution types available in most FEA packages. These are described in the list below.

- **Linear Static:** This is the most simple and computationally efficient solution type. The primary assumptions are that deformations are small relative to the model scale, and the materials are not strained enough to leave the elastic regime. Most commercial aircraft manufacturers use linear static FEA in their global loads FEM , also known as a GFEM. This solution type is also very common for conceptual design.

- **Static Geometric Nonlinearity:** The next step up in complexity is to include the effects of geometric non-linearity. This allows for large deformations caused by the applied loads to be accurately modeled. However, this solution type is significantly slower than linear static.

- **Static Geometric and Material Non-linearity:** This solution type is similar to the previous, but allows for accurate representation of materials that begin to yield.

- **Eigenvalue Buckling:** Although buckling mode shapes can be captured with a geometric nonlinear solution, the eigenvalue buckling solution type is more computationally efficient and also captures all possible buckling mode shapes. This solution type is often used to determine where stiffness must be added in a structure to prevent

buckling.

- **Normal Modes:** This analysis type is also eigenvalue-based, but is used to evaluate the natural frequencies of a structure. This analysis type is commonly used for space launch vehicles and payloads subjected to significant vibration. It is necessary to ensure that the lowest natural frequency of the structure is higher than the frequency of the harmonic excitation to avoid unbounded growth of the structural vibration amplitude.

The FEA solution types listed above are common in aerospace vehicle design. In the present research, only the linear static analysis type is used. In addition to the analysis types listed above, there are several more advanced solution types used to solve specific problems. These are mostly related to dynamic events, such as impact simulation, transient harmonic excitation, and dynamic aeroelasticity (flutter).

Another distinction to be made for FEA applications is the type of model used. The majority of FEMs used in aerospace vehicle design fall into two categories: global FEMs and detail FEMs (also known as break-out FEMs). An example of each is shown in Figure 17. As the name indicates, global FEMs typically include the majority of the vehicle or at least all parts that contribute to the overall vehicle stiffness (parts such as small aerodynamic fairings are often left out). The global FEM is necessary to accurately capture the indeterminate load interaction between various parts of the vehicle (wing, fuselage, tail, etc). Once the FEA is complete, the global FEM is usually broken up and distributed to stress analysis groups to determine the detail dimensions (such as skin thickness) for all parts of the vehicle. A distinguishing feature of global FEMs is that they are often modeled mostly with 2D shell elements. The wing FEMs used in Chapters 7 and 8 of this research are considered to be members of a global FEM .

Detail FEMs are needed for parts of the vehicle where the global FEM is not accurate enough for parts with complicated geometry or loads, or for small parts. As shown in Figure 17, the global FEM has a fairly coarse mesh to ensure that there are no modeling mistakes. However, this mesh is too coarse to accurately design small parts such as brackets or fittings.

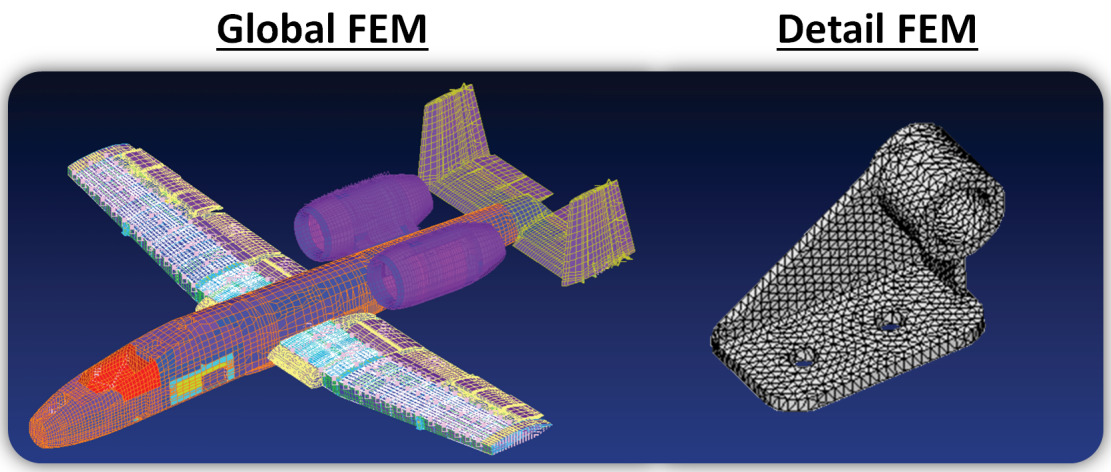

Figure 17: Examples of a Global FEM [11] and Detail FEM [12]

For these design scenarios, loads are extracted from the global FEM and applied to a detail FEM to design the part. An example of a detailed FEM is shown on the right side of Figure 17. Unlike global FEMs , detail FEMs are often composed of 3D solid elements.

2.5 General Structural Design Process

Having introduced the use of FEA in the previous section, the next step is to describe how a typical FEA -based structures design environment functions.

In most conceptual design environments, each internal arrangement considered for the vehicle (described in Section 2.3) is represented with a FEM that must be analyzed and sized. This requires applying external and inertial loads, running a FEA solver, and extracting the internal structural loads. The FEM is then broken down into panels and each panel is sized independently to determine the detail designs of the structure (part dimensions and thicknesses). These panels are the smallest design construct of a structure. The material properties and dimensions of the panel are assumed to be constant over the area of a panel. In a FEM, the elements within a panel all have the same property definition. Usually, multiple panels are used to create a structural assembly, such as a wing skin or spar. An example of this breakdown is shown in Figure 18. Additionally, the panels considered in this research are a combination of skin and stringer. They are modeled with a "smeared" technique [55], which uses an equivalent stiffness matrix ([ABD]) to represent

the stiffness of the skin and stiffener combined. The equivalent smeared stiffness matrix is built up from the stiffness of the panel objects (skin, web, flanges). The smeared panel technique is useful for conceptual design because it reduces FEM modeling effort. More details of the equivalent smeared stiffness representation are given in Section 3.2.3.

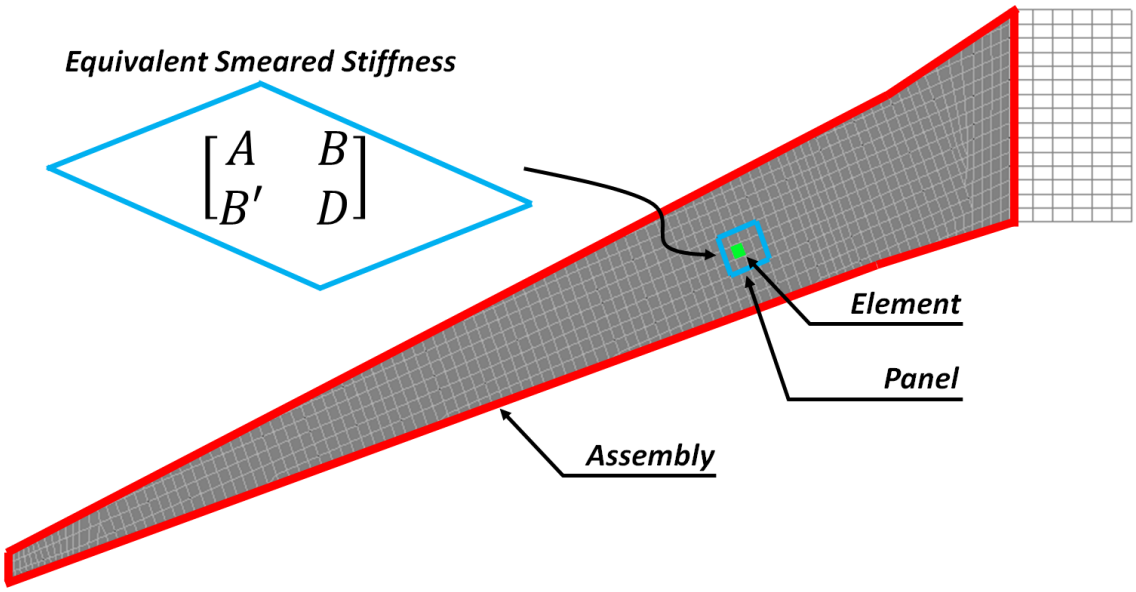

Figure 18: Breakdown of Structural Design Entities

The number of panels within a structural assembly depends on how refined the panel designs must be over the assembly. An example panel breakdown for a wing skin is shown in Figure 19. A structure can be defined in this manner to allow panel geometry to vary across the area of the part, which provides a more mass-optimum solution if the loads in the structure are non-uniform. In the example given in Figure 19, the panel definition allows the structural design to vary in the span-wise and chord-wise directions.

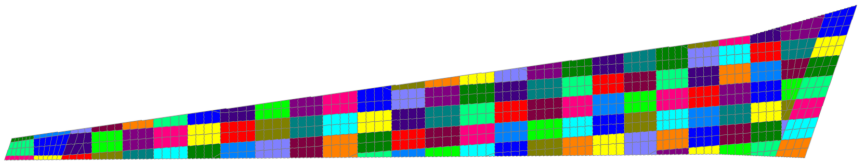

Figure 19: Panel Breakdown on an Upper Wing Skin

Once the panels are defined, a typical FEM-based conceptual sizing environment requires iteration to converge on a final design. Iteration occurs with the local panel design, global

stiffness distribution, and internal loads, all of which are coupled. These early FEMs often have external loads and geometry that are frequently updated. Thus, it is desirable to not spend a lot of time determining local panel designs that are eventually discarded as the model matures. A coarsely-meshed FEM for conceptual design with 5,000 elements or less can easily be run in a minute or less on a modern computer with linear static FEA . Thus, it is desirable for large trade studies to have a fast local design environment so that the run time for each configuration will still be 1-2 minutes including FEA plus optimization time. However, having to optimize all of the variables associated with the local design of skin and stiffeners can be burdensome. For example, a composite I-stiffened panel has 8 variables associated with the dimensions of the skin and stiffener, plus the variables associated with the composite laminate of the skin and stiffener. Assuming the skin and stiffener laminates were simplified to just a representation of the percentage of 0° , +/-45° , and 90° plies, the skin/stiffener combination would have a total of 14 variables. If a structure is represented by even as few as 100 panels (a very simplistic model), there would be a total of 1400 variables to consider. This is a significant number of variables for conceptual design, especially considering that the optimum combination of variables will be updated multiple times as the structure matures.

The discussion above reveals that finding suitable detail dimensions for each panel is usually the most cumbersome part of the process. Figure 20 illustrates the details of the general process described previously and indicates where the detailed panel design occurs (also known as local optimization). Note that the entire process described in Figure 20 fits within the "Structures" box shown in the system-level flow chart in Figure 3. The numbered data exchanges shown in the figure are described below. The process iterates until a design is found which meets the global stiffness requirements and also satisfies all of the failure criteria at the local level. The process outlined in Figure 20 is is very similar to that used by the commercial tool HyperSizer [1].

The starting point to the process in Figure 20 is a coarsely meshed preliminary FEM with an initial smeared stiffness distribution (1). This initial stiffness distribution is typically defined by "boiler plate" properties. This initial stiffness distribution is usually achieved by

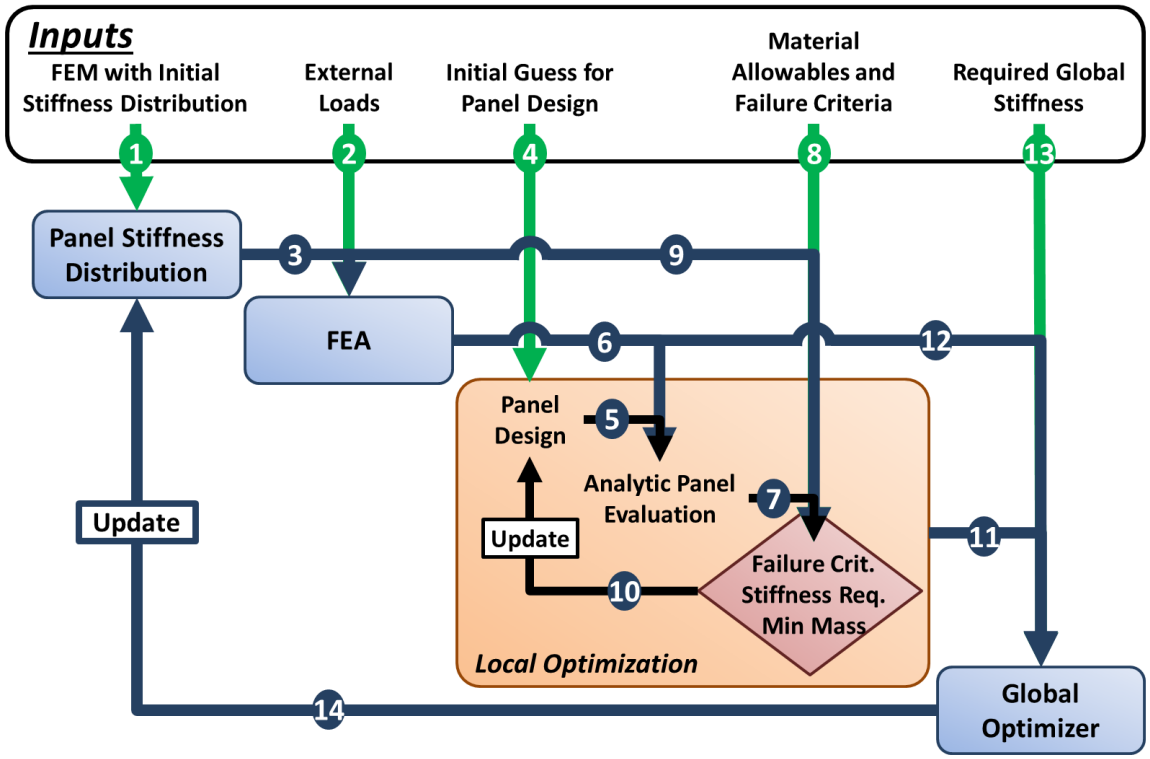

Figure 20: Outline of Iteration Process for Structural Optimization with a FEM

assigning a uniform thickness of an isotropic material to the entire FEM . Next, the external loads (2) are applied to the FEM (3) and submitted to the FEA solver. The FEA solver computes internal loads in the structure. Because the initial stiffness distribution was assumed to be uniform, the initial load distribution is not biased towards any particular part of the structure.

From here, the process enters into local optimization for each panel. Local optimization starts with an initial guess for the design of each panel (4), which consists of a combination of skin and stiffener thickness and geometry. The panel design is then passed to the panel analysis environment (5), where the internal loads from FEA (6) are used to derive the stresses in each object of the stiffener (skin, web, flanges) as well as critical buckling loads for the panel. The panel evaluation data (7) is then used to check requirements for the panel. First, the failure criteria (described in detail in Section 2.6.1.5) specified for the vehicle (8) are checked to determine if the structure will survive the flight loads. Next, the stiffness of the panel is checked against the required stiffness specified from the global level

(9). The local stiffness of the panel must match the global level to ensure consistency in the optimization. The final check in the local optimization is to determine if minimum mass has been achieved for the panel. If any of these three panel requirements are not met, the panel design is updated (10) and the local optimization iterates again.

Once the local optimization completes, the final mass and stiffness of each panel (11) is output to the global optimizer. The global optimizer checks two criteria. First, the global stiffness of the structure as determined from FEA (12) is compared against the required global stiffness (13) to determine if the requirement is met. Next, the global optimizer checks to determine if minimum mass has been achieved for the overall structure. If either criteria are not met, the global optimizer updates the panel stiffness distribution (14) over the structure and repeats the process until converged. This concludes the process described in Figure 20. Global optimization with a FEM is discussed more in Section 6.1 to introduce the algorithms and methodology needed to execute the optimization.

2.6 Review of Modern Stiffened Panel Design

This subsection is focused on the details of the local optimization presented above within Figure 20. In the current research, stiffened panels are optimized at the local level. The term "stiffened panel" is a subset of the general "panel" introduced previously and refers to the combination of the skin and stiffener, either bolted or bonded together.

Stiffened panels are frequently found in the "acreage" portion of aerospace structures. Acreage structure is characterized by large continuous shell sections (no complex curvature or kinks), where loads are well distributed and continuous. Some examples are the skins of an aircraft fuselage or wing (Figure 21) or the barrel section of a launch vehicle (Figure 22). These are in contrast to heavily loaded portions of a structure, such as the bulkheads where landing gear attach.

This section introduces the general inputs and outputs of a stiffened panel analysis, describes the details of the analysis performed with the panel failure criteria, and discusses previous tools that have been developed to perform stiffened panel analysis and optimization.

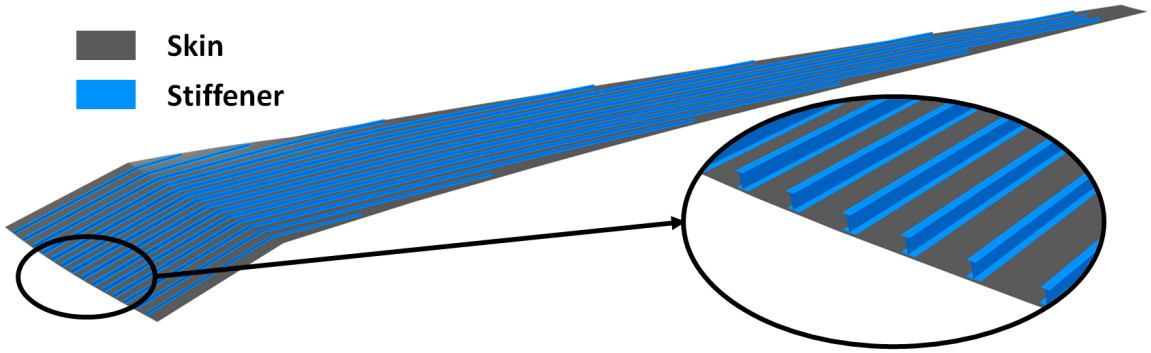

Figure 21: I-Stiffened Panels in a Wing Box Upper Skin

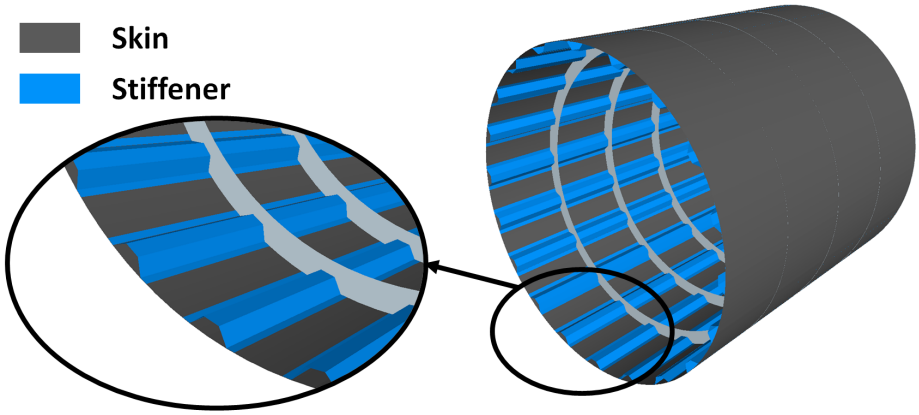

Figure 22: Hat-Stiffened Panels in a Launch Vehicle Barrel Section

2.6.1 Overview of Stiffened Panels

This section provides details on the inputs and outputs to a stiffened panel analysis. Although the FEM defines where panels are located, the stiffened panel analysis and design is performed entirely analytically and is a separate process from FEA . This gives the method generality, allowing various stiffener geometry to be considered. The only information used from the FEM and FEA are the buckling spans of the panel and the internal loads. Other inputs to stiffened panel design are the material selection, panel concept, and required stiffnesses. The outputs are mass, optimum panel geometry, and optimum ply orientations (if composite). These are summarized in Figure 23 and the inputs are described in subsections below.

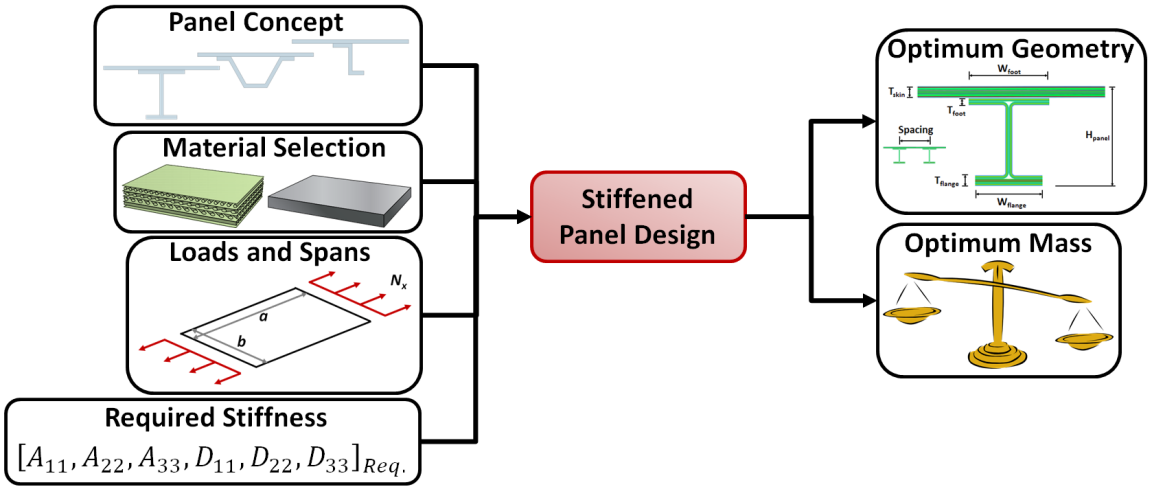

Figure 23: Inputs and Outputs for Stiffened Panel Design

2.6.1.1 Loads

Panel loads are determined by the internal forces of the FEM elements that make up the panel. The challenge is resolving a distribution of element loads from the FEM into a single load for the panel. This must be addressed any time FEA is used to derive internal structural loads. Figure 25 shows an example of an element N_x distribution over a panel that is resolved into a single panel load value. This operation is necessary to perform stress analysis at the panel level.

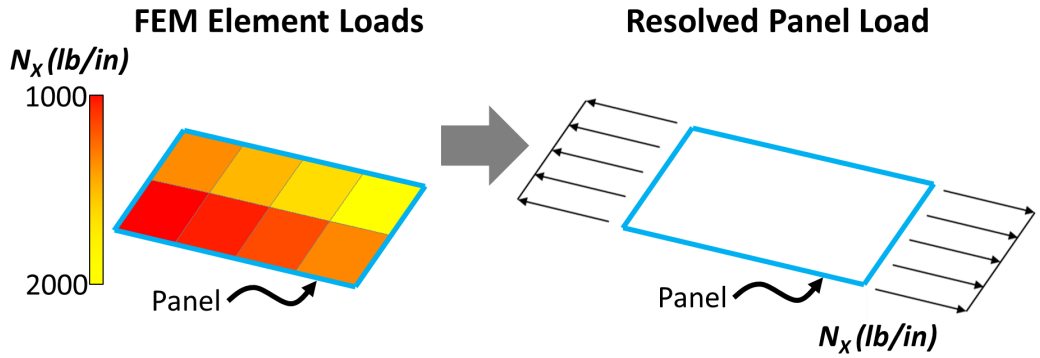

Figure 24: Resolving FEM Loads into Panel Loads

The most conservative approach of resolving the loads is to treat the load in each element as a separate load case. However, this process can be computationally inefficient if there

are many elements and/or many load cases. Additionally, this approach can result in an excessively heavy design if there is a spurious load in a single element. This is especially detrimental for conceptual design because the FEM is at a low maturity level and can potentially have a few elements with spurious high loads.

An alternative load resolution approach is to treat the element forces as a normal distribution and use the standard deviation of the distribution to define the rigor of the design loads [56]. This approach produces just a single load for the panel and is thus much faster. Due to its efficiency, this approach is favorable for conceptual design.

Figure 25 shows an example distribution formed from the N_x values of the 8 elements shown in 25. The first step to determine the N_x load to be used for stress analysis is to calculate the mean of the distribution, μ. Next, the standard deviation (σ) if the distribution is calculated, assuming a normal distribution. Finally, a severity factor (s) is selected; typical values are 0, 1, 2, and 3. Using these values, Equation 8 demonstrates how the N_x for panel sizing is calculated.

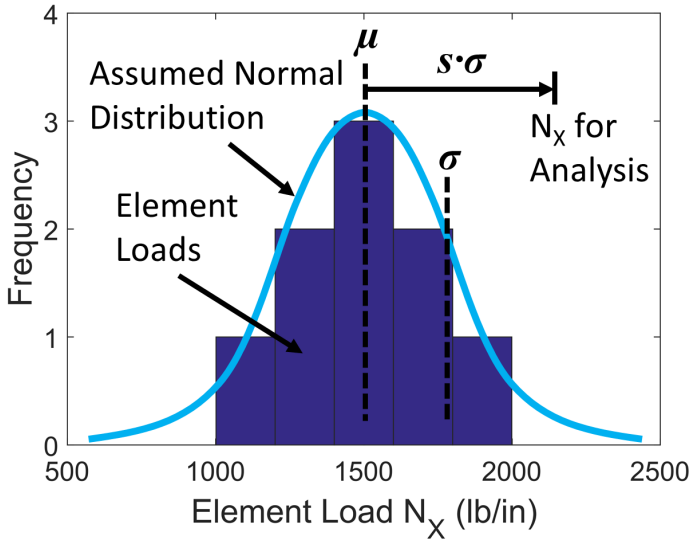

Figure 25: Statistical Approach for Determining Panel Optimization Loads

$$N_x = \mu + s \cdot \sigma \tag{8}$$

From Equation 8, it is evident that higher values of s provide more conservative loads for stress analysis. Note that $s = 0$ gives the element-average load value. In this case, N_x for

the panel would simply be equal to the average of the N_x values from all of the elements in the panel. The value of s used for optimization is ultimately up to the designer and usually depends on the maturity of the FEM .

2.6.1.2 Buckling Spans

The second piece of panel optimization input that comes from the FEM are buckling spans. These are simply extracted from the FEM geometry based on the outer dimensions of the panel. The orientation of these dimensions depends on the orientation of the stiffeners. Longitudinal buckling span (a) is aligned with the stiffeners, and lateral buckling span (b) is oriented perpendicular to the stiffeners. These are shown in Figure 26.

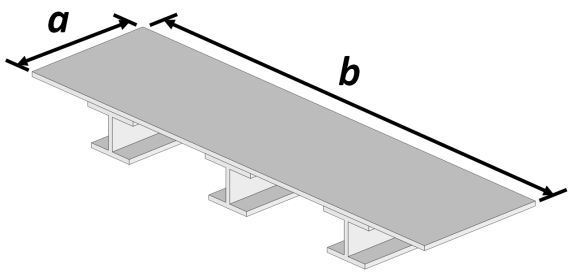

Figure 26: Panel Buckling Spans

2.6.1.3 Material

A variety of material properties are needed to perform stiffened panel design [57]. These include stiffness, stress allowables, strain allowables, laminate-based damage tolerance allowables, and thermal properties. The required material properties depend on the failure criteria selected for the panel, discussed in Section 2.6.1.5.

2.6.1.4 Panel Concepts

The selected panel concept varies greatly depending on the application. A comprehensive list of these concepts is shown in Figure 27. Note that each of the two-piece concepts usually comes in either a bolted or bonded variety, depending on the material system (usually bolted for metallic and bonded for composite). Some examples of stiffened panels on existing vehicles are the external hat stiffeners on the inter-tank sections of the Saturn

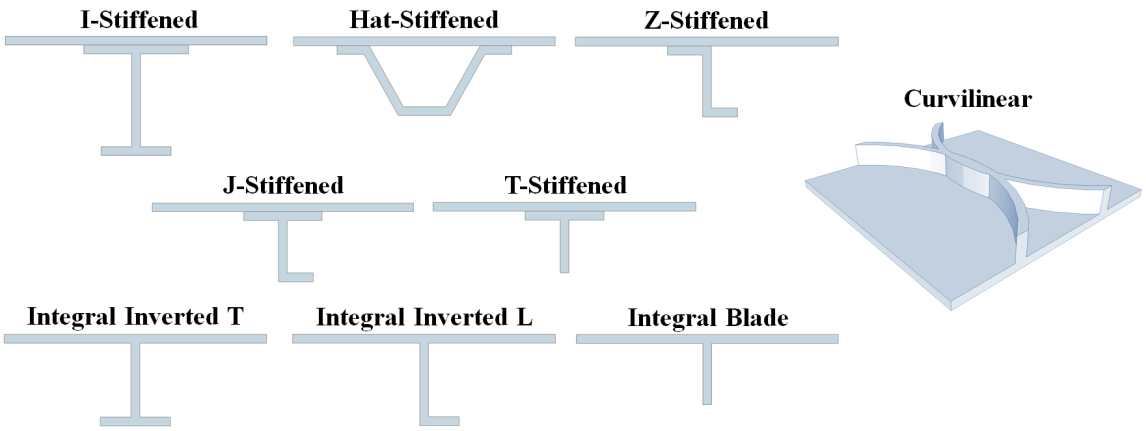

Figure 27: List of Panel Concepts Used in Aerospace Design Applications

V and the integral blade stiffeners on the wing skin of the A350, as shown in Figure 28.

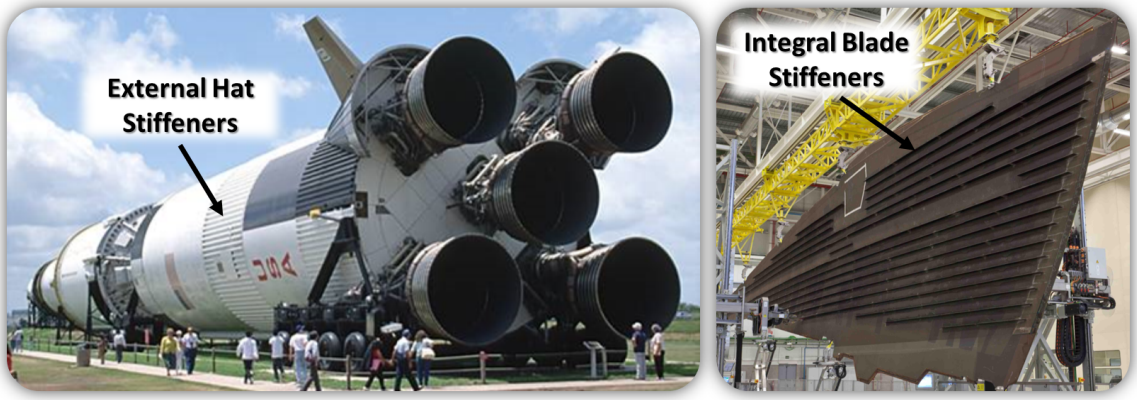

Figure 28: Stiffened Panel Examples on Saturn V Inter-tanks [13] and A350 Wing Skin [14]

Another common concept is the I-stiffened panel. This panel concept was selected for development of the methodology presented in this research. The advantage of using this concept is that many of the other concepts are geometrical subsets and can be created by removing flanges or parts of flanges from the I-stiffened panel.

Table 1: Failure Criteria Used for Metallic Stiffened Panel Optimization

Object	Type	Analysis Name
Panel	Buckling	Uniaxial and Biaxial, Simple BC Shear, Simple BC Uniaxial and Biaxial with Shear Interaction, Simple BC Curved and Flat, All BC Column with Transverse Shear Flexibility, Simple BC
Stiffener	Buckling	Argyris, Flexural Torsional
Panel	Crippling	Niu, Isotropic LTV, Isotropic Johnson-Euler Buckling Interaction
Facesheet	Local Buckling	Biaxial Shear Biaxial and Shear Interaction
Facesheet	Material	Strength, Longitudinal Load Strength, Transverse Load Strength, Shear Load Strength, Von Mises Interaction Yield Criterion
Bonded Combo	Material	Strength, Longitudinal Load Strength, Transverse Load Strength, Shear Load Strength, Von Mises Interaction Yield Criterion
Spacing Span	Local Buckling	Biaxial Shear Biaxial and Shear Interaction
Web	Material	Strength, Longitudinal Load Strength, Shear Load Strength, Von Mises Interaction Yield Criterion
Web	Local Buckling	Biaxial Biaxial and Shear Interaction
Bottom Flange	Material	Strength, Longitudinal Load Strength, Shear Load Strength, Von Mises Interaction Yield Criterion
Bottom Flange	Local Buckling	Biaxial Biaxial and Shear Interaction

2.6.1.5 Failure Criteria

Selection of failure criteria depends on the rigor of the design phase. Conceptual design typically uses a small set of failure criteria such as simple strength analysis and panel buckling [8]. Many more failure criteria are used for detail design and analysis for certification, including more advanced criteria such as crippling, post-buckling, damage tolerance, etc. Incorporating more of these advanced failure criteria in earlier phases of design provides a

more accurate mass estimate for preliminary sizing. An example of such a failure criteria set is given in Table 1.

Stiffened panels are usually subdivided into separate entities for various analyses, as shown in Figure 29 and described below.

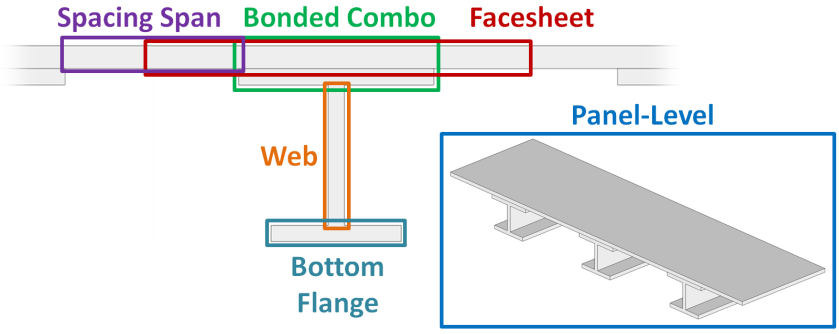

Figure 29: Analysis Objects in I-Stiffened Panel

- **Panel-Level:** Pertains to stiffness of the panel as a whole (usually for buckling).
- **Facesheet:** Length of the skin beginning and ending halfway between the adjacent stiffeners.
- **Bonded Combo:** Combined portion of the top flange and the skin adjacent to the top flange.
- **Spacing Span:** Free span of unstiffened skin between flanges of adjacent stiffeners.
- **Web:** Vertical portion of stiffener connecting top and bottom flanges.
- **Bottom Flange:** Horizontal portion of stiffener at the bottom of the web.

The types of failure criteria used with these panel objects are described below.

Panel Buckling

This failure mode occurs when the compressive load or shear load on the overall panel exceeds the critical buckling value for the panel design. This results in unbounded deformation of the overall panel as shown in Figure 30. There are a variety of different methods used to determine the critical buckling load of the panel ranging from the simplistic column

buckling calculation [58] to a more sophisticated numerical energy-based approach that can handle panels with curvature [59].

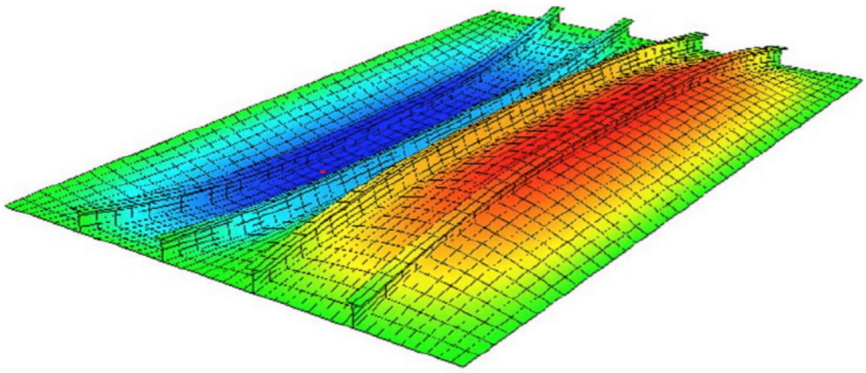

Figure 30: Panel Buckling of I-Stiffened Panel [15]

Stiffener Buckling

This buckling occurs when the stiffener reaches its critical buckling load before the entire panel buckles. Because the stiffener is supported by the skin, the stiffener usually "tips" over in the buckled mode shape, shown in Figure 31. This is known as flexural torsional buckling [60].

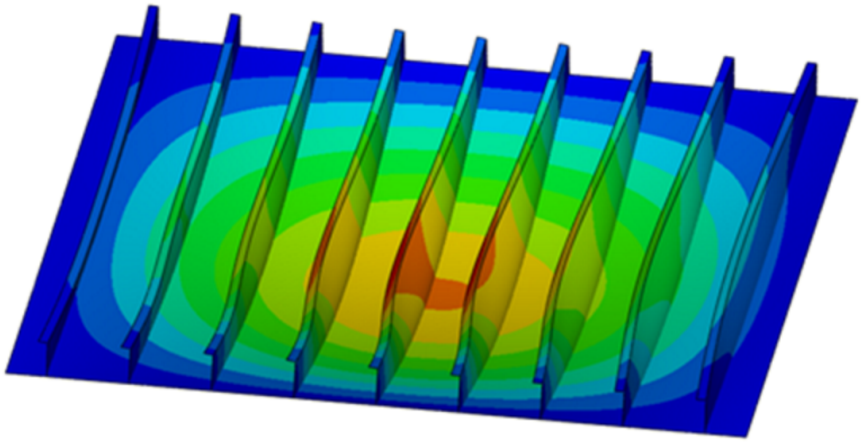

Figure 31: Stiffener Buckling of J-Stiffened Panel [16]

Local Buckling

This failure occurs when one of the parts of the panel buckle before the panel as a whole buckles. This can be in one of the flanges of the stiffener or in the skin between stiffeners.

Figure 32 shows an example of local buckling in the skin between two hat stiffeners. Local buckling can occur if a part of the panel was designed too thin relative to the rest of the panel. Analyses for this failure mode treat the segments of the panel as flat plates with boundary conditions that correspond to the flange location on the stiffener [61],[62],[63]. For example, the bottom flange of an I-stiffener would be analyzed as having a free edge.

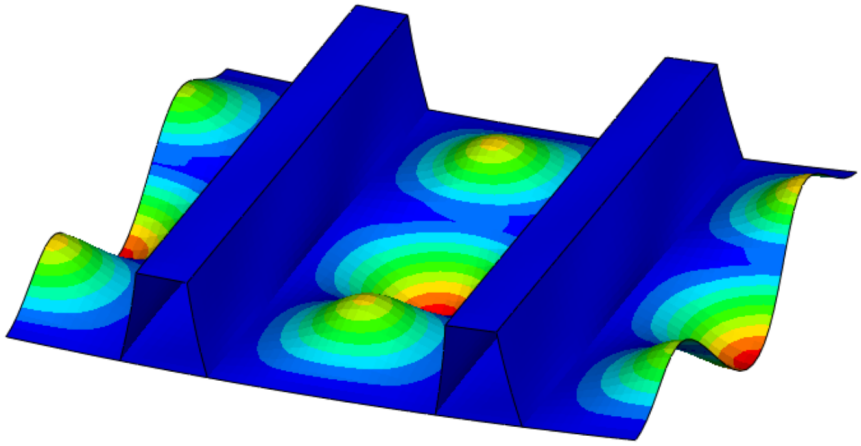

Figure 32: Local Buckling in the Skin of a Hat-Stiffened Panel [17]

Crippling

The analysis performed for this failure mode captures performance of the stiffener after the flanges of the stiffener have already locally buckled. At this point, the flanges are unable to carry any more load. However, the corners of the stiffener where the flanges intersect are inherently more stable and thus able to carry more load beyond the point where the flanges have buckled. The crippling analysis determines the point at which load in the stiffener corners is too great and the entire stiffener collapses [62].

Material Failure

The analyses for this failure mode are based on the stresses, strains, and curvatures found within each object of the stiffened panel. These are compared against material allowables with a variety of approaches ranging from simple longitudinal and transverse stress/strain checks to more advanced interaction criteria such as the Von Mises yield criterion [58]. There are also a number of criteria specific to composites, as discussed in Section 2.9 and Chapter 5.

2.6.1.6 Required Stiffnesses

Input stiffness values for each panel are necessary when there is a global stiffness-based objective to be met, such as a deflection limit or required global buckling eigenvalue. This requires a stiffness distribution to be specified at the global level. Thus, each panel will have a specific required stiffness value depending on its location in the structure. To satisfy global deflection limits, it is common to have a required panel *membrane* stiffness distribution. For global buckling limits, required panel *bending* stiffness distributions are common. The process of extracting required panel stiffnesses from a global stiffness distribution is a core part of bi-level optimization as described in Chapter 6.

2.6.2 Detailed Description of Stiffened Panel Analysis and Design

Inputs and outputs of the stiffened panel design environment were discussed in the previous section. This section describes the analysis that happens in-between the two. The described process encapsulates the details of the local optimization environment outlined within Figure 20 of Section 2.5.

The process presented here is intended for stiffened panels that are represented with a "smeared" modeling approach, which uses an equivalent stiffness (Equation 9) to represent the panel instead of discrete geometry. The smeared panel technique is used for conceptual design with FEMs because it gives the most design freedom and computational efficiency for a particular mesh. With the smeared panel analysis technique, stiffeners are not physically modeled in the FEM . Instead, the loads within the panel (web, flanges, etc.) must be calculated outside of FEA analytically, using the overall loads applied to the panel as derived from FEA. This process is outlined in Figure 33 and is typical for smeared panels [1]. The advantage of this approach is that the FEM mesh does not need to change every time the design is updated. Only the equivalent smeared stiffness (described below) in the FEM must be updated.

Figure 33 gives the step-by-step process for evaluating the failure criteria of a smeared stiffened panel. This is the process as used by HyperSizer, a commercial structural analysis tool [1]. The details to each step are described below.

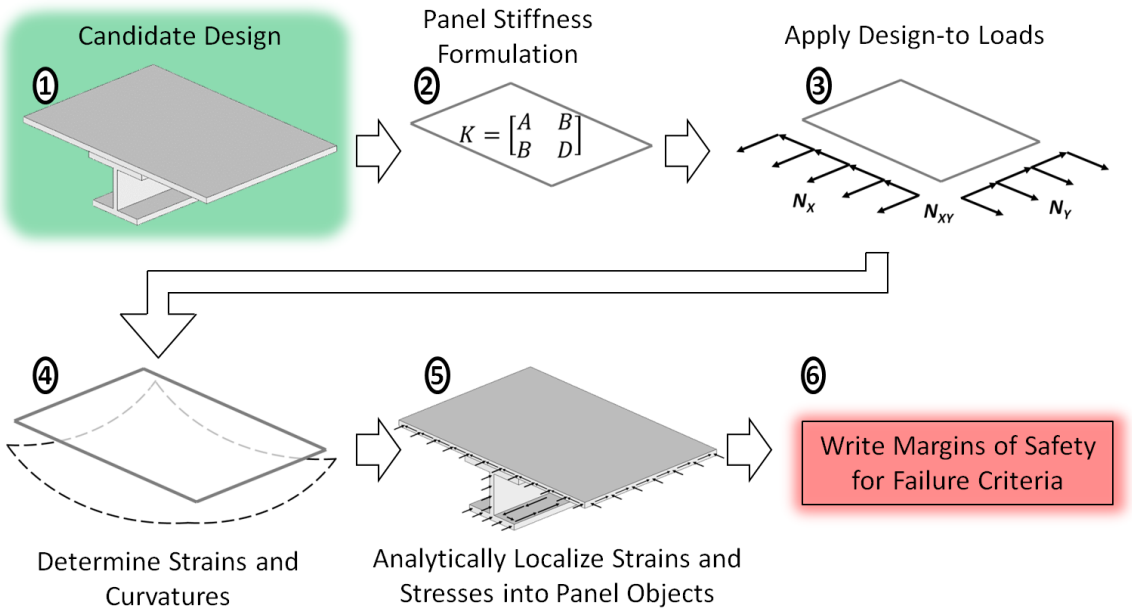

Figure 33: Evaluation of Candidate Design

1. The starting point for the analysis is a candidate design which consists of a selection of geometry and material.

2. A smeared stiffness representation of the panel is calculated in the form of the ABD matrix (Equation 9) for each candidate design. This stiffness calculation is done via an extension of Classical Lamination Theory (CLT) into stiffened panels [55].

3. Next, the design-to loads are applied. These loads are extracted from the elements that make up the panel (see description in previous section).

4. After applying loads, the overall deflection (strains and curvatures) of the panel is calculated using the smeared ABD matrix.

5. The final step of the internal load processing is to determine local strains and stresses of each part of the panel (skin, web, flanges) based on their relative stiffnesses (which depends on object dimensions and material properties).

6. With the local strains and stresses, failure criteria for the various panel objects can be evaluated. These failure criteria include material failure, local buckling, panel buckling, crippling, etc; a full list is given in the previous section.

To optimize the panel for minimum mass, the process described above is repeated numerous times until an optimum design is achieved. This requires that the process be connected to an optimizer, which determines the new candidate design for each iteration.

The ABD matrix shown in Equation 9 provides the equivalent smeared stiffness representation for the panel. Note that of the 36 terms shown, only 18 are unique because the sub-matrices [A], [B], and [D] are all symmetric. The [A] matrix represents the membrane (in-plane) stiffness of the stiffened panel. For this matrix, the 11, 22, and 33 terms represent longitudinal, transverse, and shear stiffness respectively. The [D] matrix represents the bending stiffness of the stiffened panel. For the [D] matrix, the 11 and 22 terms represent bending about the transverse and longitudinal axes. The D_{33} term represents twisting stiffness. Off-diagonal terms in both the [A] and [D] matrix give the interactions between the primary stiffnesses. Similarly, the entirety of the [B] matrix represents coupling between membrane stiffness and bending stiffness. If the [B] matrix is non-zero, the panel will bend when membrane load is applied and extend or contract when bending load is applied.

$$\begin{bmatrix} A & B \\ B & D \end{bmatrix} = \begin{bmatrix} A_{11} & A_{12} & A_{13} & B_{11} & B_{12} & B_{13} \\ A_{21} & A_{22} & A_{23} & B_{21} & B_{22} & B_{23} \\ A_{31} & A_{32} & A_{33} & B_{31} & B_{32} & B_{33} \\ B_{11} & B_{12} & B_{13} & D_{11} & D_{12} & D_{13} \\ B_{21} & B_{22} & B_{23} & D_{21} & D_{22} & D_{23} \\ B_{31} & B_{32} & B_{33} & D_{31} & D_{32} & D_{33} \end{bmatrix} \tag{9}$$

As mentioned above, the ABD matrix relates strains and curvatures to applied load. Calculation of the panel strains (ϵ_x, ϵ_y, ϵ_{xy}) and curvatures (κ_x, κ_y, κ_{xy}) is shown in Equation 10. These are determined by membrane load (N_x, N_y, N_{xy}) and bending load

(M_x, M_y, M_{xy}).

$$\begin{bmatrix} \epsilon_x \\ \epsilon_y \\ \epsilon_{xy} \\ \kappa_x \\ \kappa_y \\ \kappa_{xy} \end{bmatrix} = \begin{bmatrix} A & B \\ B & D \end{bmatrix}^{-1} \cdot \begin{bmatrix} N_x \\ N_y \\ N_{xy} \\ M_x \\ M_y \\ M_{xy} \end{bmatrix} \tag{10}$$

2.6.3 Existing Stiffened Panel Design Tools

There are a number of tools that have been developed in the last 30 years to perform stiffened panel sizing. The rise of modern computing has allowed for traditional structural analyses to be integrated with numerical optimization tools. Previously, structural optimization was performed by using a reduced set of analyses so that mass minimization could be done by hand as a function of one or two variables [64].

The majority of modern panel sizing tools were born in the 1980s and early 1990s. Several of these were developed by researchers at NASA and partner universities. Others were developed internally by commercial airframe manufacturers. By the early 2000s, most of these tools had either been adopted by commercial entities or fallen into disuse. This section describes the development and use prominent stiffened panel sizing tools. The intent is to provide background information on the maturity of stiffened panel design, as well as capabilities and limitations of existing tools. Additionally, it should be noted that none of the tools discussed below use a stiffness-based design space, which is unique to the current research.

2.6.3.1 HyperSizer

HyperSizer is the tool used for much of the data generation and validation for the current research, so it will be described first. The code base of HyperSizer was originally developed at NASA in 1988 under the name ST-SIZE for hypersonic vehicle research [65], [55]. The original concept of the software was to automate all of the standard structural analyses used by NASA engineers and couple them with FEA . This provided a tool that replaced the

manual process of finding stiffened panel designs that could withstand the loads derived in FEA . In 1996, the creators of the software obtained a commercial license through NASA's technology transfer program, and began to market the tool to commercial airframe manufacturers. What makes HyperSizer unique and more capable than the tools described below is the formulation with an equivalent stiffness matrix, as described in the previous section.

The only drawback to HyperSizer's core sizing capability (known as "Detailed Sizing") is the efficiency of the optimization. HyperSizer uses a full-factorial approach to optimize panels. The user inputs a min and max value for each dimension of the panel, and a number of increments to consider within this range. HyperSizer then builds a full factorial matrix of all possible combinations of the increments for each dimension. The panel failure criteria are then evaluated for each panel design, in order from lowest to highest panel mass. The first panel found that satisfies all of the failure criteria is selected as the optimum design.

Note that Collier Research Corporation has recently developed a new optimization capability called "Rapid Sizing" which uses a proprietary algorithm to size stiffened panels within about one second per panel. This is a substantial improvement over the older optimization methodology described above and makes it a promising tool for future studies as its capabilities are matured. To achieve the improvement in efficiency, there are some simplifications made in the Rapid Sizing tool compared to traditional Detail Sizing tool. Because of these simplifications, HyperSizer's Detail Sizing tool was used instead of the Rapid Sizing tool. The simplifications of Rapid Sizing compared to Detailed Sizing are listed below.

1. Currently only available for a few panel concepts: I-stiffened panels, honeycomb sandwiches, and flat plates.

2. Only a limited number of failure criteria are available with this tool.

3. Only membrane loads are considered in the analysis of stiffened panels.

4. Required stiffness values cannot be specified for stiffened panels, limiting ability to iterate with FEA.

2.6.3.2 PASCO

Another panel sizing tool was developed by W. J. Stroud and M. S. Anderson several years before ST-SIZE in 1981, referred to as PASCO [66]. This tool has many capabilities similar to HyperSizer, including ability to handle thermo-elastic effects and stiffness requirements. PASCO can also handle metallic and composite panels. Features that PASCO does not have is the ability to handle lateral bending loads or twisting loads. Additionally, only two panel concepts are available: blade stiffeners and hat stiffeners. PASCO has seen little use in more recent years but is occasionally run to verify newly developed design tools [67].

2.6.3.3 PANDA2

A similar approach was taken by D. Bushnell at Lockheed in the development of PANDA2, a panel sizing tool from 1987 [68]. This tool also uses standard structural analyses to evaluate strength and buckling failure in composite and metallic stiffened panels. Additionally, the tool performs optimization of the dimensions of the panel for a variety of stiffened panel concepts. Although it was conceptually similar to HyperSizer and PASCO, PANDA2 did not have the same generality. The panel loads were limited to membrane (N_x, N_y, N_{xy}) and out-of-plane pressure. Additionally, the tool did not have built-in ability to interface with FEA . PANDA2 was used by researchers on and off through 1998. Around this time, there was significant interest in using regression to represent local optimization tools, and several papers used both PANDA2 [69],[70] and PASCO [71],[72] to generate data points to get curve fits of optimum panel mass versus load. This topic is discussed in more detail in the next section.

2.6.3.4 VICONOPT

Yet another research-based stiffened panel optimization tool was developed in 1990 by R. Butler and F. Williams called VICONOPT. Unlike the tools described above, VICONOPT is focused mainly on optimizing the panel to handle natural frequency and buckling constraints. Thus, the optimization is driven much more by overall panel stiffness. VICONOPT

can handle several panel concepts including hat stiffeners and Z-stiffeners, making it relevant for trade studies with commercial aircraft. However, VICONOPT is not as general as the panel sizing tools described above, and has primarily been used for advanced panel-level studies such as for post-buckling [73],[74].

2.6.3.5 COSTADE

Another stiffened panel design tool which made it into the commercial world is COSTADE from 1993 [75]. This tool originated as a NASA initiative to promote cost and mass-efficient use of composite structures. The tool was a product of collaboration between several commercial and research entities, including Boeing, the University of Washington, Sikorsky, Northrop, MIT, and Dow/United Technologies. The goal was to develop a tool which combined the disciplines of cost estimating, structural analysis, and manufacturing to provide a comprehensive design tool for composite structures. Ultimately, the structural design portions of the tool have been incorporated into Boeing internal design processes.

2.6.3.6 ELAPS

This is a non-FEA tool that instead uses analytic structural analysis to derive an internal load distribution in wings and fuselages [33], [34]. This allows for rapid convergence on an optimum structural design. However, the tool does not provide much generality because it can only handle wing and fuselage configurations that are pre-programmed into the software. This means the tool has a significant lack of generality needed to handle unconventional structures.

2.6.3.7 Other Commercial Tools

In addition to the panel sizing tools adopted by commercial entities, there are many which were developed internally by commercial airframe manufacturers. Unfortunately, there is little published material on these tools because most of them are considered to be proprietary methods. Occasionally, studies are published for public consumption, such as for the Airbus wing sizing tool FAME-W by R. Kelm et al. [30]. This tool uses analytic methods to approximate internal loads from primary external load cases, without FEA . Basic strength

and buckling criteria are then used to size the structure and determine mass estimates for early preliminary design.

2.6.3.8 Summary

The characteristics described above for each tool are summarized in Figure 34. Each of these characteristics are described below, along with reasoning for how the ratings in Figure 34 were determined.

1. **Current Maintenance:** frequency of updates and bug fixes. Commercial software or software actively used for production design are given the highest rating in this category. Software with no references in literature in the last 10 years are given the lowest rating.

2. **Availability:** dependent on whether the software is commercial, proprietary, or a tool developed by an independent researcher. Free software hosted on a public website would receive the highest rating. Commercial software receives a slightly lower rating due to cost of acquisition. Software which is strictly a proprietary internal tool receives the lowest rating.

3. **Couples with FEA:** some software have built-in FEM and FEA interface tools, while others would require extra development to achieve this capability. Software with out-of-the-box FEA interface capability receive the highest rating in this category, and those which rely only on analytic methods for internal structural loads receive the lowest rating. Ratings in-between depend on estimated effort to write a script to couple the software with FEA .

4. **Fidelity of Analyses:** software with more advanced analyses such as crippling and post-buckling receive the highest rating. Those with only strength-based criteria receive the lowest rating. Software in-between the two are rated accordingly.

5. **Optimization Efficiency:** dependent on the optimization scheme used. Ratings are based on optimization times reported for similar problems in the references presented previously for each software.

6. **Material Selection:** ability to handle metallics and composites. All software reviewed are capable of optimizing both.

7. **Number of Panel Concepts:** ability to handle concepts listed in Section 2.6.1. The number of panel concepts available in the software determines the rating.

8. **Components of Load:** ability to include membrane, bending, and transverse load. The number of available components of load determines the rating.

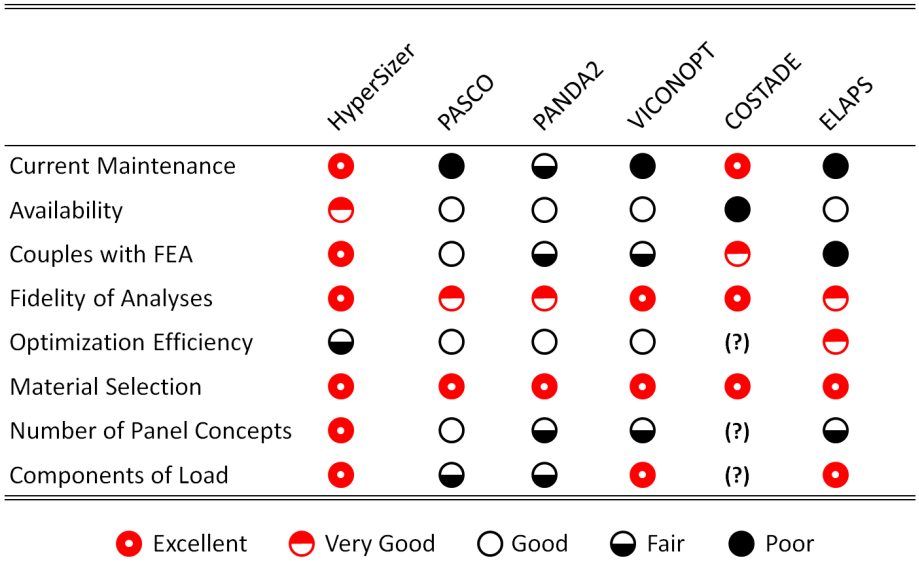

Figure 34: Summary of Characteristics for Existing Panel Optimization Software

Note that several of the categories in Figure 34 for COSTADE are unknown. This is because COSTADE is a Boeing proprietary internal tool and the current state of its capabilities is not published.

Drawing from the summary in Figure 34, HyperSizer dominates the majority of the categories and is selected for further consideration in the present research. The only two categories in which HyperSizer did not receive an "Excellent" rating are availability and optimization efficiency. The availability rating is due to the fact that it is available to the public, but is priced in the range of typical aerospace design tools. The optimization efficiency rating is due to the optimization approach based on full-factorial exploration, which is the target for improvement of the current research.

2.7 Regression for Panel Design

The intent of this section is to discuss literature that uses Response Surface Equation (RSE)s, either as a function of panel dimensions or panel stiffness. As discussed in the introduction, RSEs play a key role in the present research. Thus, it is necessary to understand current state-of-the-art applications in related areas. To this end, all known instances of RSEs used in panel sizing have been documented here. Each instance is summarized in Table 2, noting the dependent and independent variables as well as other features. The observations made in this literature review provide the framework of the logic used to develop the methodology in the current research.

2.7.1 Overview of Response Surface Equations

RSEs are surrogate functions used to represent complex analyses, thereby improving the efficiency of a design process [76]. They are typically simple functions, such as a 2nd or 3rd order polynomial. Before RSEs were introduced to aerospace vehicle design, the only way to gain an complete understanding of how a complex numerical analysis varies over the design space was to run a full-factorial exploration over the entire design space. However, this can be a substantially time-consuming task if the analysis is complex. For example, running a full-factorial exploration for five increments in five design variables with 15 minutes of analysis time for each point would take 33 days. Obviously, this is far too inefficient to be practical.

The alternative is to instead use RSEs to represent the complex analysis and explore the design space. Generation of RSEs requires evaluation of the complex numerical analysis at intelligently selected points in the design space. This collection of points is referred to as a Design of Experiments (DoE) and contains substantially fewer design points than a full-factorial evaluation of the design space. For example, only 46 design points would be needed to generate a 2nd order RSE with the five design variables described above [76]. This corresponds to a run time of 11.5 hours. Generation of these RSEs with a full-factorial data set would require 243 points, which is still five times more inefficient than the Design of Experiments (DoE) .

Once an RSE is generated, the design space can be explored with minimal computational expense. RSEs are generated with the steps listed below [76].

1. Generate a DoE to determine the settings for the design variables. The type of DoE chosen depends on the desired order of the RSE. There are several standardized DoE for 2nd order RSEs such as the Box Behnken and Central Composite Design DoE . For these type of DoE, a given number of design variables requires a specific number of DoE points. For higher order RSEs, "space-filling" DoE are often used such as the Latin Hypercube or Uniform Spacing DoE . Unlike the 2nd order DoE , these can have as many points as desired by the user. These DoE are characterized by points scattered throughout the design space. The location of each point is determined numerically to maximize regularity of spacing between points.

2. Evaluate each DoE point with the complex numerical analysis and record the response.

3. Perform regression to generate a polynomial (RSE) with the analysis response as the dependent variable and the design variables as the independent variables.

4. Use the RSE to evaluate the points in the DoE to determine the Model Fit Accuracy (MFA). This is based on the accuracy of the RSE in predicting the value of the response at each DoE point.

5. Perform a similar check with randomly-generated points in the design space to calculate Model Representation Accuracy (MRA). This is the RSE 's ability to accurately interpolate the response in within the design space.

6. If the MFA and MRA are not satisfactory, return to the first step and repeat the process with a higher order RSE to attempt to find a better fit. Note that the number of DoE points must be increased when the order of the RSE is increased. Additionally, the order of the RSE can only be increased up to a certain point before "over-fitting" begins to occur where the regression is attempting to fit the RSE to noise in the response.

2.7.2 Existing Literature Using Response Surface Equations

In most applications of RSEs in existing literature, the desire is to make stiffened panel design fast enough to be suitable for conceptual design. The intent of the current research is similar, so it is useful to draw upon techniques used previously. Table 2 lists references that use RSEs for stiffened panel optimization. The table identifies key features of the RSEs in each reference that are relevant to the present research. An explanation of each column heading is provided below.

2.7.2.1 Margin versus Mass

This category describes whether the RSE dependent variables are margins for the stiffened panel failure criteria, or a prediction of the optimum mass of the panel.

Margin: RSEs in this group are used to calculate the margins of the failure criteria for the stiffened panel. This type of RSE is most appropriate for design environments where it is necessary for physics-based design principles to be captured in the local optimization with a high amount of computational efficiency. These types of RSEs are needed when the panel design space is not well understood and significant design space exploration is needed.

Mass: Conversely, design environments that are better understood (a rough idea of the final design is known) often use RSEs that predict optimum mass for the stiffened panel. These RSEs are usually a function of panel load and one or two panel stiffness terms. Design environments that use these RSEs do not need to perform a local optimization because the dependent variable is the optimum mass for the given load. However, an offline optimization must be performed to generate the mass data points for the RSE regression. This can be a time-consuming task due to the required dimensionality of the regression data set. For example, if the three in-plane components of load (N_x , N_y , N_{xy}) and three stiffness terms are used as the independent variables, a minimum of 729 regression data points would be needed to generate a 2nd order polynomial ($(3\,points)^{6\,variables}$). If the optimization for each data point took 10 minutes to run, the total run time would be 122 hours.

2.7.2.2 Dimensions versus Stiffness

This category describes the form of the independent variables used in the stiffened panel RSEs. The selection usually depends on the intended use of the RSEs . Some studies are a combination of the two. For example, some studies that use composite materials will use physical variables to represent the panel geometry and stiffness terms to represent the laminate variables. The most common stiffness terms used to represent the laminates are Lamination Parameters (LPa)s [77]. These provide a representation of the ply angles and placement in a laminate without retaining information on the orientation of every single ply (discussed more in Section 2.9).

Dimensions: RSEs in this group are a function of the physical geometry of the panel and the applied panel loads. These types of RSEs are usually associated with the "Margin" group described above.

Stiffness: RSEs in this group are a function of panel stiffness terms and applied panel loads. The RSEs presented later in Chapter 3 fall into this category. The most common stiffness representation used for these RSEs are terms from the ABD matrix for smeared panels (described previously).

2.7.2.3 RSE Form

This category simply describes the mathematical form of the RSE, such as 2nd or 3rd order polynomial.

2.7.2.4 Material

All studies either fall under the metal or composite groups.

2.7.2.5 Smeared Panel Type

This category describes the general stiffened panel geometry, also known as panel "concept." These have been discussed in the previous section (see Figure 27).

2.7.2.6 Replace versus Correct

This category refers to how the RSE is applied in the panel design environment. Both types of RSE are used in Chapter 3 of this research.

Replace: In the majority of applications, the RSE is used to directly replace the panel failure criteria analyses performed during panel optimization. Some analyses, such as buckling, can be time-consuming to run and thus benefit from being replaced by an RSE.

Correct: There are a few applications where RSEs + low-fidelity analyses are used to replace high-fidelity analyses. The low-fidelity analysis is more computationally efficient but less accurate than the high-fidelity analysis. However, an RSE can be used to correct the error between the two with minimal impact on efficiency. The correction RSEs are generated from offline studies of high-fidelity and low-fidelity analyses for the problem. Usually, these studies use a local FEM as the high-fidelity analysis.

2.7.2.7 Tabulated Summaries

Table 2 represents the present collection of relevant references that implement RSEs in a panel-level optimization environment. In addition to this form of presentation, it is informative to regroup the references in a manner that reveals which combinations of approaches have yet to be considered. In Table 3, the rows represent the dependent variable of the RSE and the columns represent the independent variables of the RSE.

Table 3 forms four quadrants corresponding to the four primary ways in which RSEs can be used in the panel-level optimization. Starting with the upper-left corner, RSEs in this quadrant are not valuable. The relationship between panel mass and dimensions can be calculated with deterministic, closed-form equations just based on the cross-sectional area and material density of the panel. Thus, it does not make sense to generate RSEs that duplicate this relationship.

Moving to the lower-left corner, this quadrant represents a classical application of RSEs in a panel design environment. RSEs in this category are used to represent failure criteria as a function of the panel dimensions, essentially replacing complex analyses with simple polynomials. An optimization tool must still be used to determine the optimum

Table 2: Summary of RSE Usage in Stiffened Panel Design

Reference	Margin or Mass	Dimensions or Stiffness	RSE Form	Material	Panel Type	Replace or Correct
[72]	Mass	Stiffness (ABD)	2nd Order Poly.	Metal	Bonded J	Replacement
[69]	Margin	Dimensions and LPs	2nd Order Poly.	Comp.	Bonded Hat	Replacement
[78]	Margin	Dimensions	2nd Order Poly.	Metal	Curvilinear	Replacement
[71]	Margin	Dimensions	3rd Order Poly.	Comp.	Unstiffened	Replacement
[79]	Margin	Dimensions	Neural Network	Metal	Bolted T	Replacement
[80]	Mass	Stiffness (ABD)	3rd Order Poly.	Metal	J Stiffened	Replacement
[81]	Margin	Dimensions	3rd Order Poly.	Comp.	Integral Blade	Replacement
[82]	Margin	Dimensions	3rd Order Poly.	Comp.	Integral Blade	Replacement
[83]	Margin	Dimensions	Artificial Neural Network	Metal	Curvilinear	Replacement
[70]	Margin	Dimensions	2nd Order Poly.	Comp.	I stiffened	Correction
[84]	Margin	Dimensions	2nd Order Poly.	Comp.	Integral Blade	Correction
[85]	Margin	Dimensions	2nd Order Poly.	Comp.	Bonded Hat	Replacement

panel design, but it runs quickly because the analyses are simplified. The drawback to this approach is that the local-level optimization is in terms of panel dimensions, which do not interface well with the global portion of a two-level optimization. This is because requirements at the global (FEM) level are a direct function of stiffness, not panel dimensions. These FEM requirements are usually related to global buckling and deflection constraints.

The RSE application in the upper-right corner is intended to address the short-coming described for the previous quadrant. By having RSEs that represent panel optimum mass in terms of panel stiffness, the local design can be more closely coupled with the global design, which is also in terms of panel stiffness. The drawback of this approach is the offline

Table 3: Existing Literature Using RSEs in Stiffened Panel Design

		Independent Variables	
		Dimensions	Stiffness
Dependent Variable	Optimum Mass	[NA]	[72] [80]
	Failure Criteria	[69] [78] [71] [79] [81] [82] [83] [70] [84] [85]	[Gap]

computational expense needed to generate the data set for regression; each regression data point must be optimized with an independent panel sizing tool. It is evident from the number of references in this quadrant that this approach has been attempted but has not gained much popularity likely due to the required offline computational expense.

The final quadrant in the lower-right corner is the gap in the literature to be addressed by the current research. The approach of using RSEs to represent stiffened panel failure criteria as a function of panel stiffness terms has not been studied in existing literature. As discussed previously, the research presented here performs a change of variables to represent the stiffened panel failure criteria in terms of the smeared panel stiffness terms; specifically, using terms from the ABD matrix. Logistic regression is used to generate the failure criteria RSEs, resulting in a function that predicts pass/fail of the criteria for a given set of loads and panel stiffness. These RSEs are developed later in Section 3.3.

2.8 Coupling with a Finite Element Model

For modern conceptual design, an efficient method of optimization is required to couple stiffened panel optimization with FEM and FEA . This section reviews literature which connects stiffened panel design environments with FEM /FEA for the specific goal of promoting rapid iterations. In general, the literature reviewed here could be considered as geared towards conceptual design, where different internal layouts or OML configurations might be considered. Additionally, each of the references reviewed have a global stiffness-based constraint

in the form of either a displacement constraint or global buckling constraint. Thus, the literature contained in this section is relevant to the current research, providing insight on how to properly connect the new panel optimization methodology to a FEM /FEA environment. Such a process is usually handled with bi-level optimization, discussed below.

Bi-level optimization is a prominent approach for optimizing structures because the problem naturally decomposes into a global level (FEA and vehicle-level stiffness requirements) and a local level (selecting materials and detail dimensions that satisfy stress, strain, and local buckling failure criteria). Bi-level optimization has appeared numerous times in previous literature for wing boxes, using many different combinations of global and local optimization approaches. The following subsection discusses this literature.

2.8.1 Existing Literature on Bi-Level Optimization

Table 4 summarizes existing literature that applies a bi-level approach to wing box optimization. The table describes the optimization performed at the global and local level for each reference.

The commonality between all of the references listed in Table 4 is that mass is optimized at the global level, requiring iteration between the global and local level. Most of the references also have a constraint at the global level. Some of these are related to aeroelasticity, such as in [80], [86], and [87]. Other references have global buckling as a constraint. In a wing box, global buckling is the occurrence of buckling mode shapes that span across multiple bays (spaces between ribs). References [88] and [89] have no global constraints at all. These two references use the global level only for load convergence. This is necessary because each time the structural design at the local level changes, it has an impact on the global stiffness distribution and thus changes the internal load distribution.

The next feature to note in the references listed in Table 4 is the global level variable selection. Aside from defining the global design space, these variables form the interface between the global and local level. When the optimizer at the global level selects a particular combination of variables, these become constraints at the local level. For example, in Reference [87] the global variables are the number of 0° , 45° , and 90° plies distributed

Table 4: Relevant Works for Bi-Level Optimization of a Wing Box Structure

Reference	Global Optimization	Local Optimization
[80]	Distributions of A_{11} , A_{33} that satisfy wing tip deflection constraint with minimum mass	Optimum panel mass that satisfies buckling and strength criteria, given panel loads, A_{11} , and A_{33} from the global level
[86]	Cross-sectional stiffness distribution to meet flutter and deflection constraints with minimum mass	Optimum cross-section dimensions (skin thickness, stiffener geometry) to minimize mass and meet cross-section stiffness from the global level
[87]	Number of each ply orientation to satisfy bending stiffness requirements with minimum mass	Stacking sequence optimization to maximize local stiffness and satisfy failure criteria, using ply counts from global level
[88]	Iterate to converge load path and minimize mass; determine internal load distribution based on local designs	Size panels based on loads and deformation of panel determined at the global level
[89]	Skin thickness controlled by quadratic function to minimize mass	Stiffener dimensions optimized to minimum mass, accounting for the skin thickness determined at the global level
[90]	Distribution of equivalent ply thicknesses that represent the skin and stiffener, found to minimize mass and satisfy buckling and deflection constraints	Dimensions of hat stiffeners and skin that match the equivalent thicknesses defined at the ply level while satisfying panel failure criteria
[71]	Distribution of 0° , 45° , and 90° plies over the structure to minimize mass while satisfying global buckling constraints	Stacking sequence optimization to maximize local stiffness and satisfy strain allowables for the composite

over the structure. For each combination of ply counts chosen by the global optimizer, the local optimizer finds a stacking sequence that maximizes local bending stiffness while satisfying these ply counts. Reference [86] takes a slightly different approach by controlling cross section stiffness as the global-level design variable. Cross-section stiffness has a higher degree of control on the overall displacement of the wing box but less of a direct relationship to the physical design variables. In each step taken by the global optimizer, the local optimizer must determine a set of skin and stiffener dimensions that generate the cross-section stiffness defined at the global level.

Considering complexity of the references in Table 4, the local optimizations used in

Reference [86], [88], and [90] represent the most complex (and likely most time-intensive) approach of the group. In these references, the local optimization is a function of the skin and stiffener variables. For example, Reference [90] optimizes a composite hat-stiffened panel at the local level, which has four geometry variables and four thickness variables for the various parts of the stiffener. The next level down in complexity is found in References [87] and [71]. In these two references, the local panel is a composite flat plate without any attached stiffeners, meaning that there are not as many design variables. The lowest level of complexity found in Table 4 is in Reference [80], consisting of just the evaluation of an RSE. Such an operation takes a negligible amount of time on a modern computer, making this the fastest local optimization of the group. However, note that offline computational time required to generate the data for the RSE regression of optimized data points is extensive.

2.8.2 Summary of Existing Bi-Level Approaches

Considering the bi-level examples discussed above, it is evident that the run time of the local optimization can compound quickly in a bi-level optimization. In each iteration performed by the global optimizer, the local optimization must be performed for each panel. Depending on the structure, anywhere from 10 to several hundred panels might be used. Depending on the behavior of the global design environment and the optimization algorithm used, the number of global iterations can reach into the 100s. Thus, the total number of local optimizations that must be performed can easily be 1,000 or greater. Even a local optimization run time of as short as three or four seconds will cause the total run time to be substantial.

Another note to make about the bi-level examples above is that several trade-offs exist in current bi-level optimization techniques. Existing approaches do well at including either high panel design complexity (many variables), low local optimization time, or low offline data processing time, but not all three features simultaneously. Thus, improving upon current bi-level optimization techniques would require having all three characteristics. This is represented in the Venn diagram in Figure 35.

Of the references listed in Table 4, most fall within the overlap of only two circles shown

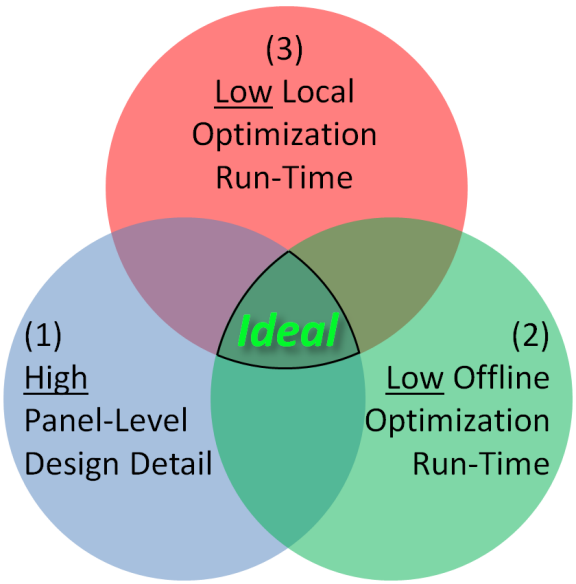

Figure 35: Venn Diagram of Key Features of Local Optimizations in Existing Bi-Level Wing Box Design Environments

in Figure 35. Any of the optimizations that do not use a RSE fall within the "low offline optimization run-time" circle (2). Of these, References [86], [88], [89], [90] overlap with the "high panel-level design detail" circle (1) because they have variables for stiffener geometry. References [87], [71] use a simple flat plate at the local level and thus fall in the overlap between circle (2) and (3). Only one reference falls within the overlap of circles (1) and (3): the study that replaces the local optimization with a RSE of optimum local mass [80].

The overlap of all three circles shown in Figure 35 is ideal and would allow the bi-level optimization to be performed quickly while still preserving a high level of design detail. However, such an overlap was not found in literature.

This existing gap in literature will be addressed in the current research. The local-level optimization introduced in this research allows for the influence of complex panel design to be included without penalizing the run time of the entire bi-level optimization environment. In doing so, it draws upon the most advantageous aspects of the references described in Table 4. The present methodology shares the use of panel stiffness terms and RSEs with Reference [80] to improve coupling with the global level and reduce run-time. However, the manner in which the RSEs are used does not require significant offline processing time.

The only offline processing needed is to run the small number of DoE points for the failure criteria RSEs. Additionally, the methodology also incorporates the complexity of a detailed stiffened panel design, as in [86] and [90]. Together, these features fill the needs of having a fast local-level optimization which also incorporates the influence of complex stiffener design. This is demonstrated in the remaining chapters of the thesis.

2.9 Simplifications for Composite Design

This section contains simplifications for composite materials to make them applicable to the optimization techniques found in the literature presented previously. Composite materials are notoriously difficult to optimize because of the vast amount of design freedom they allow. The simplifications discussed in this research are used to make the design space tractable while still taking advantage of the tailorability of composites.

Even considering the power of modern computers, the design of composite stiffened panels is still challenging considering the enormity of the design space. In a metallic panel, the only material-related parameter is the thickness of the parts of the panel. For a composite panel, thickness becomes a discrete variable dependent on the number of plies. Each ply has an associated material angle, drastically increasing the number of variables. A 50 ply laminate could potentially have 50 variables defining its layup. This is just for a single laminate; design of a stiffened panel with multiple laminates poses an even more complex design problem. The laminate selection of the skin and stiffener are coupled because the relative stiffness of the two defines the load distribution in the panel.

This level of design complexity is challenging for detail design, but is even more burdensome for conceptual design where many design iterations are performed. Thus, significant simplifications are needed for the design of composite stiffened panels to have a tractable design space that can be quickly iterated upon. Below is a review of simplifications made in literature to improve the efficiency of composite design. Lessons learned from this literature review provides a foundation for application of the presented methodology to composite stiffened panels.

The most common simplification made to composite laminate design is to limit the

ply orientations to 0° , +/-45° , and 90° , as opposed to allowing any continuous value of orientation. Unfortunately, this simplification introduces many discrete variables to the stiffened panel optimization. The final design space is a function of both continuous and discrete variables, which makes it more difficult to handle with traditional optimization techniques.

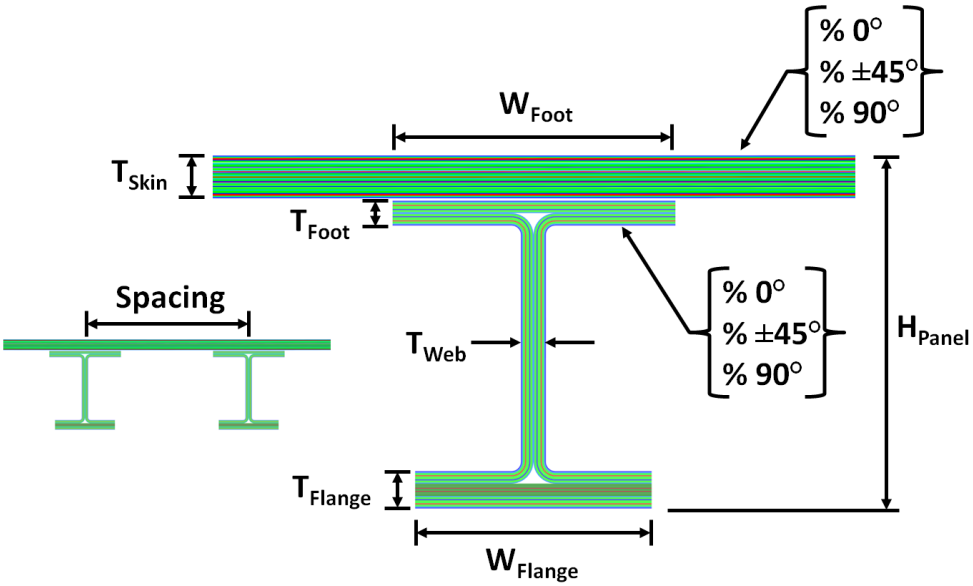

Figure 36: Physical Design Variables for a Composite I-Stiffened Panel with Ply Percentages.

A further simplification is to reduce the composite material variables to thickness and percentage of 0° , +/-45° , and 90° plies. This results in four design variables for the laminate: total thickness and the percentages of the three ply orientations. Figure 36 shows the resulting 14 design variables after simplification of a composite I-stiffened panel. This simplification is implemented as a central part of the composite optimization tools found in Altair's Optistruct [40] and Collier Research's HyperSizer [1] software. Doing so returns the composite panel design space to being a function of purely continuous variables.

The material definition that results from this simplification is similar to that of an orthotropic material, and is usually referred to as an effective laminate or smeared laminate. The material properties of an effective laminate usually are derived assuming symmetry and balance in the laminate, such that the bending-extensional coupling stiffness terms ([B]) are

zero. Stiffnesses are calculated by building a pseudo-laminate from the specified percentage of 0° , +/-45° , and 90° plies, and then calculating the ABD matrix for the laminate. The ABD matrix is then inverted and used to determine equivalent smeared properties, as shown in Equation 11 below [91]. The inverted A matrix terms (a_{11}, a_{22}, a_{12}, a_{33}) are used for these calculations, as well as thickness of the laminate (t). Calculations for bending stiffness are similar, using the bending terms from the ABD matrix.

$$E_1 = \frac{1}{a_{11}t} \tag{11a}$$

$$E_2 = \frac{1}{a_{22}t} \tag{11b}$$

$$\nu_{12} = -\frac{a_{12}}{a_{11}} \tag{11c}$$

$$G_{12} = \frac{1}{a_{33}t} \tag{11d}$$

Although helpful, the effective laminate simplification is not perfect and comes with an additional set of limitations. This four-variable representation of the composite laminate does not contain any information about where the various plies are located in the laminate (also known as "stacking sequence"). Ply location can have a drastic impact on laminate stiffness, as shown by the example in Figure 37. Moving the stiff 0° plies to the outside of the laminate can significantly increase the bending stiffness; Figure 37 shows that the bending stiffness can more than double just by rearranging the plies.

Fortunately, the stacking sequence does not have as great of an impact on the bending stiffness of stiffened panels about the primary bending axis (Y-axis). This is because the change in distance from the reference plane for the stiff plies (0°) is much smaller than in an unstiffened laminate. Thus, moving 0° plies from the center of the skin laminate to the outside of the skin laminate only has a small effect on the primary bending stiffness. This is shown in Figure 38, where the stiffener laminate and dimensions remain the same, but the laminate of the top skin is rearranged in the same way as the previous example.

Note that at the local level, the bending stiffness of an object in the stiffener is still potentially inaccurate. This can cause inaccuracy with failure criteria that depend on the stiffness of stiffener objects, such as local buckling of the web. However, overall panel

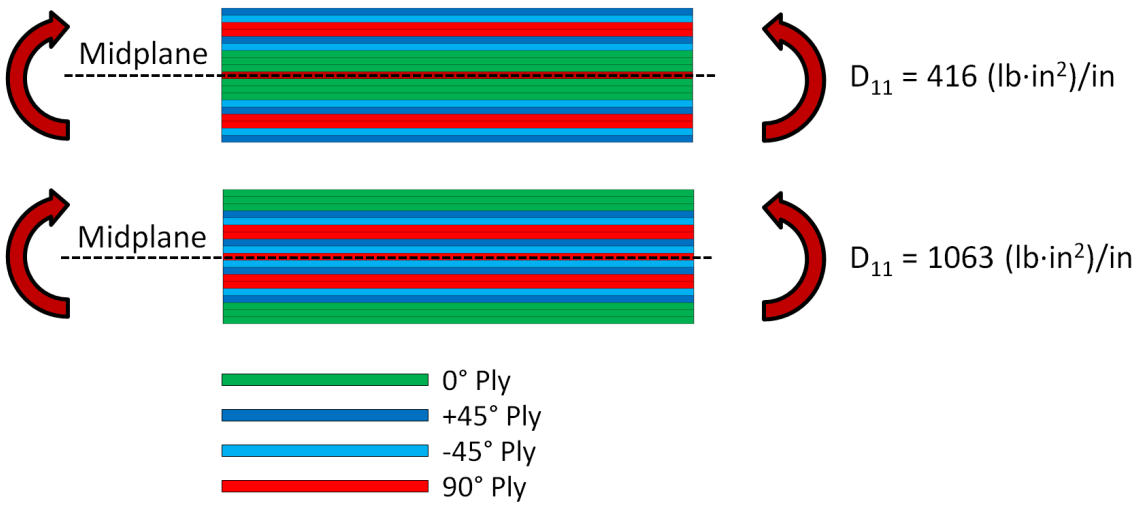

Figure 37: Example of D_{11} Stiffness Dependence on Stacking Sequence for a Solid Laminate

buckling is typically a more critical failure mode except for stiffeners with high aspect ratios, or stiffeners with significant bending moments. Thus, the overall impact on stiffened panel sizing accuracy is small.

Several other approaches have also been considered in previous research. One of the most popular methods for simplifying composite laminate design is the use of Lamination Parameters (LPa)s. These terms appear in the derivation of the smeared stiffness ABD matrix for a composite laminate as a part of CLT [92]. However, it was not until 1985 that these terms were actually utilized in the design of composite laminates, with one of the first applications by M. Miki [77]. LPas provide a similar simplification to using ply percentages, but are more advanced because they also retain information about the stacking sequence. There are a total of 16 possible lamination parameters, although this number can be reduced if assumptions are made about symmetry and balance of the laminate. This number of variables is much more suitable for design than considering the individual orientation of every single ply in a laminate.

In the time since the pioneering paper on applying LPas , the LPa approach as been used in many composite laminate optimization studies. One application is to use LPas for a low-fidelity solution in a two-stage optimization as done by A. Todoroki [93], [94]. In the first stage, the LPas are used as design variables to determine a range of values which

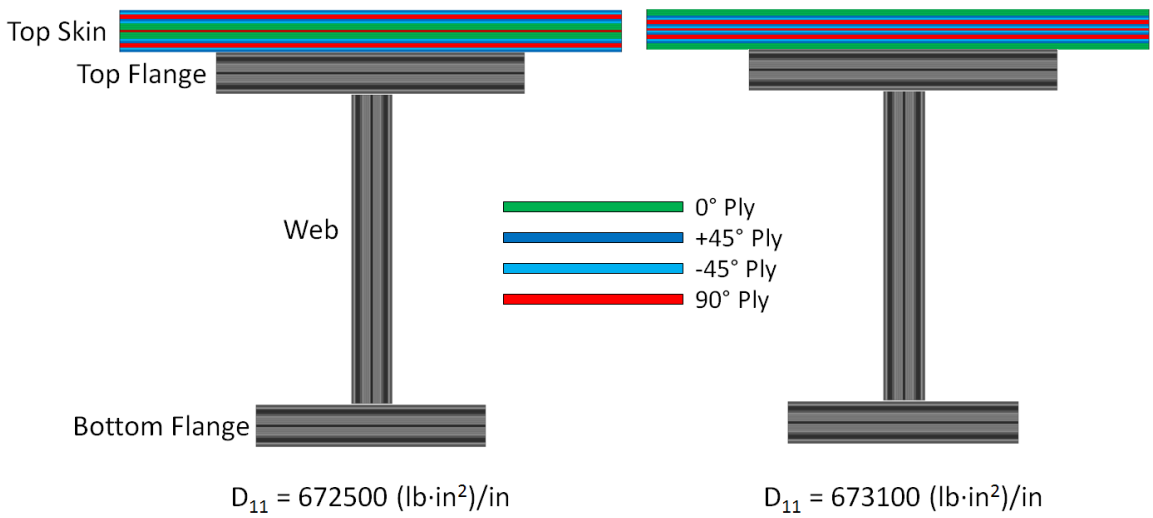

Figure 38: Example of D_{11} Stiffness Dependence on Stacking Sequence for a Stiffened Panel

contain the optimum solution for a buckling load. In the second stage, the LPa ranges are used to bound a high-fidelity optimization to determine actual discrete laminate definitions. Since the LPas in the first stage have far fewer design variables, they are useful to quickly reduce zero in on the optimum portion of the design space.

The LPa approach has also been extended for use in composite stiffened panels. This application incorporates similar approaches described above for unstiffened panels into the various parts of a stiffened panel [67],[95],[96]. For stiffened panel optimization, the lamination parameters are used in the stage of design where the overall dimensions of the stiffener are being determined. The use of LPas permits the optimization to be performed in terms of continuous variables. Once the panel dimensions and local LPas are determined, a high-fidelity approach is used to back-out the final laminate design (location and angle of plies).

Aside from the references listed above, there is little existing literature that demonstrates the use of LPas in stiffened panels. This is due to the low contribution of local bending stiffness to the overall bending stiffness of the panel, as described above. Thus, use of LPas provides an unnecessary level of fidelity. Ply percentages are usually the preferred approach when it comes to optimization of composite stiffened panels.

Additionally, a limitation of LPas arises from the fact that they are a stiffness-based

representation of the material. While this is advantageous for buckling analyses, strength analyses require special consideration to be evaluated. Typically, failure of a composite laminate is evaluated by using the overall laminate strain and curvature to calculate stresses in each ply to determine if any of the plies exceed the material allowable [92]. Because LPas do not contain any ply-level information, it is necessary to find alternative methods for evaluating strength criteria, such as mapping Tsai-Wu failure criteria for the plies into laminate strain envelopes [97].

Thus, some lessons can be drawn from these applications of LPas , summarized below.

1. Using equivalent stiffness terms as design variables greatly reduces complexity of the design space.

2. Local bending stiffness of stiffener flanges is not greatly important for panel optimization.

3. An approach is needed to map panel failure criteria to the equivalent stiffness terms if they are used as optimization variables.

The research presented in this thesis does not use an approach as complex as LPas because they contain too much information about the the stacking sequence of the laminates, decreasing the efficiency of the optimization. The composite laminate variables are instead treated with the first approach described in this section, using thickness and percentage of 0° , +/-45° , and 90° plies to represent the laminate (referred to as effective laminates).

CHAPTER III

METHODOLOGY

This chapter develops the methodology needed to accomplish the goals set forth in Chapter 1 by improving panel optimization efficiency to a level suitable for rapid conceptual design. In developing the panel optimization methodology, this chapter will examine varying levels of fidelity for the structural analyses (failure criteria) as well as different optimization approaches. This chapter, as well as Chapter 4, use a single metallic I-stiffened panel as the marquee example for developing the panel optimization methodology and performing validation.

Figure 39 shows the panel geometry considered in this chapter. The left side of the figure depicts a "super-stiffener," which is the smallest repeatable unit of geometry found in a stiffened panel. The super-stiffener consists of the stiffener with an attached segment of skin with width equal to the stiffener spacing. An actual stiffened panel usually has multiple stiffeners and would be constructed of repeated super-stiffeners equaling the width of the panel (b). This is shown on the right side of Figure 39. In this chapter and the next, only the super-element is depicted for simplicity.

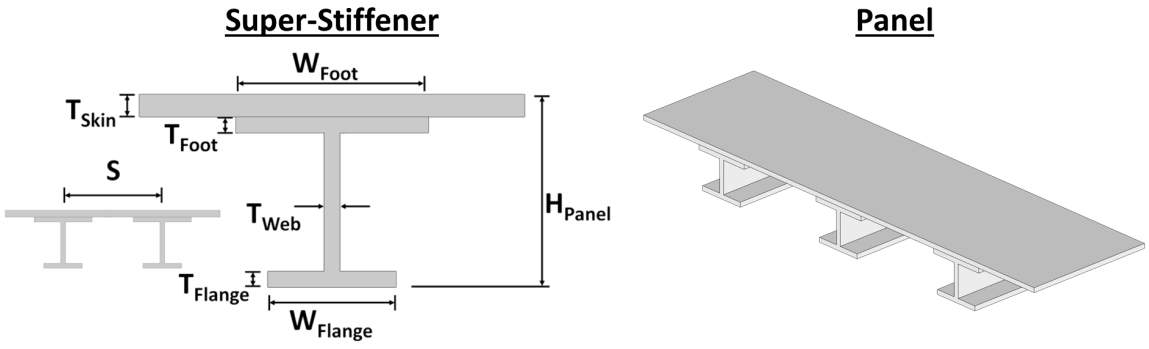

Figure 39: Dimensions of Metallic I-Stiffened Panel

Within development of the panel methodology, three levels of fidelity will be explored for the panel failure criteria: traditional analysis form (Section 2.6.1.5), 3rd order RSE in

the physical domain (Section 2.7), and 1st order RSE in the stiffness domain. These levels are summarized in Table 5. The physical domain refers to the panel dimensions as shown in Figure 39, and the stiffness domain refers to the smeared stiffness presented in Section 2.6.2. Note that the 3rd level has yet to be discussed in detail because it is a central part of the methodology developed in this chapter.

For the present RSE approach, regression is used to generate simple polynomial functions that represent the failure criteria as a function of panel stiffness or panel dimensions and applied loads. As discussed in Section 2.7.1, these RSEs have the benefit of being more computationally efficient to evaluate than the original complex analyses that they represent. Additionally, these closed form analyses allow for more efficient optimization algorithms to be used, such as gradient-based optimization (with 3rd order equations), and linear programming (with 1st order equations).

Table 5: Local Optimization Approaches Considered

	Failure Criteria	Domain	Existing Usage
Level 1	Original Analyses	Physical	Extensive
Level 2	3rd Order RSEs	Physical	Extensive
Level 3	1st Order RSEs	Stiffness	None

The first two levels of analysis fidelity presented in Table 5 are discussed in the first section of this chapter. These two are presented together in Section 3.1 because they contain approaches that have been examined in existing literature documented in Chapter 2. The first section of the current chapter applies existing approaches to the stiffened panel optimization problem to determine the best possible performance made available by existing methodology. Upon establishing this point of reference, the remainder of the chapter is dedicated to developing an approach to improve on the efficiency of the existing methods.

Level 3 from Table 5 is the stiffened panel optimization methodology developed in Sections 3.2 through 3.6 of this chapter and is the primary contribution of the current research. Development of this methodology first considers a change of variables, from panel geometry to panel stiffness terms. The change of variables is performed using RSEs (polynomial functions) to represent the panel structural analyses (failure criteria) as a function of applied

loads and the panel stiffness terms. This new stiffness-based design space is referred to as the stiffness domain. The stiffness domain uses 1st order functions to represent the failure criteria, as indicated in Table 5, because the stiffness domain approaches linearity as shown later in this chapter.

After presenting the reformulation of the design space, the optimization approach is discussed. Because 1st order approximations of the failure criteria were used, the panel can be optimized with linear programming optimization methods. The Simplex Algorithm was selected for optimization, being a well-known and well-documented method.

The final section in this chapter discusses the reverse mapping from the stiffness domain to the physical domain. This is needed at the end of a conceptual design process to generate physical designs to serve as the starting point for preliminary and detailed design.

3.1 Existing Methods to Improve Optimization Efficiency

This section considers the first two fidelity levels of failure criteria representation from Table 5. The first is the "traditional" approach, which uses the original form of the failure criteria, regardless of how complex. HyperSizer is an example of a tool which falls into this category. The second level of simplification is to use regression to develop 3rd order RSEs that represent the failure criteria as a function of panel dimensions and loads. The pros and cons of these approaches are discussed by considering an example optimization of a metallic I-stiffened panel.

Within the first two levels of analysis fidelity, two approaches are considered to perform local optimization, listed below.

1. Optimize with a full factorial exploration of the design space.

2. Optimize with a standard optimization algorithm.

The single-panel example optimization problem uses broad variable bounds, as might be found in a conceptual design environment where a wide range of designs must be considered. The bounds of the metallic I-stiffened panel dimensions are given in Table 6. The loads applied to this example panel are membrane loads only: N_x =-10666 lb/in, N_y =-2240 lb/in,

N_{xy} =2500 lb/in. Additionally, the bending stiffness term D_{11} is constrained to a value of 2.666e6 lb-in^2/in.

To establish a point of comparison for the example problem, a high resolution full-factorial design space exploration was performed with approximately 10 million design points. This optimum design is presented in Table 6, along with the resulting unit mass, and represents the "global optimum" of the design space.

Table 6: Physical Variable Values and Mass for the I-Stiffened Panel

Unit	T_{skin} (in)	T_{web} (in)	T_{foot} (in)	T_{flange} (in)	H_{panel} (in)	S (in)	W_{foot} (in)	W_{flange} (in)	Unit Mass (lbm/ft^2)
Min	0.06	0.06	0.06	0.06	1.5	5	1	1	1.466
Max	0.35	0.25	0.25	0.25	3.5	9	2.25	2	10.21
Optimum	0.1830	0.07824	0.06	0.1664	2.876	5	1.069	1	3.932

3.1.1 Optimization with Original Failure Criteria Analyses (Level 1)

The first stiffened panel optimization considered is to use existing failure criteria analyses and attempt to improve upon the full-factorial approach used by HyperSizer. To develop a quantitative comparison between the approaches considered in this research, it is necessary to establish a baseline analysis time for a single design point using the failure criteria listed in Table 1. As analyzed by HyperSizer, it takes 5.7088e-4 seconds for a single design point. This baseline analysis time can be used to determine how fast an optimization will run if it uses the original form of the failure criteria analyses.

3.1.1.1 Approach 1

With a full factorial approach, 518,00 design points are needed to achieve a unit mass within 5% of the global optimum. The full-factorial was generated from six increments for the thickness dimensions, five for the panel height and spacing, and four for the flange widths. This full-factorial corresponds to a total analysis time of 295.9 seconds, the slowest approach considered in this section. Another drawback of the full factorial search is that the design variable resolution required to get a "good" solution can not be known ahead of time.

3.1.1.2 Approach 2

The most efficient and rigorous approach considered with the traditional failure criteria is the use of an optimization algorithm. Implementing a non-native optimization algorithm with the native HyperSizer failure criteria is challenging because it would require interfacing with the HyperSizer software in every single step of the optimization. Instead, the total number of design points required for the optimization was estimated to provide a run time for comparison. The estimated number of design points was based on the optimization with RSEs described in the next section. This estimation assumes that optimization with RSEs would converge in the same number of steps as optimization with the original failure criteria (using the same optimization algorithm). The main difference is that the optimization gradients would have to be calculated numerically due to the complexity of the native HyperSizer failure criteria. For each step taken by the optimizer, 10 points would need to be evaluated for each constraint (two points per each of the five independent variables) to determine the local gradient of the constraint.

Considering the discussion above, the gradient-based optimization would take approximately 10 times longer to run than its counterpart in the next section, giving a run time of approximately 30 seconds. This represents the upper limit of optimization efficiency using the original failure criteria analyses.

Next, application of RSEs will be considered to improve the efficiency of the panel optimization.

3.1.2 Optimization with 3rd Order Response Surface Equations for Failure Criteria (Level 2)

The second stiffened panel optimization considered is to use 3rd order RSEs to represent the panel failure criteria. Third order polynomial RSEs were chosen because they provide an accurate representation of the failure criteria with a low amount of regression time. In the literature discussed in Section 2.7, 3rd order RSEs were the highest order needed for accurate representation of failure criteria in the physical domain. Generation of RSEs is described in detail in the next section.

The same three categories of optimization were be considered with the RSEs as were with the original failure criteria analyses. First, it is necessary to establish the analysis time for a single design point using RSEs. This analysis time is 3.9375e-4 seconds, which is 1.45 times faster than the original failure criteria analyses due to the more simple form of the RSEs. The original failure criteria in HyperSizer contain complex equations, table-lookups, and some semi-numerical approaches [98] as discussed in Section 2.6.1.5. These are more computationally expensive than the 3rd order polynomial RSEs.

3.1.2.1 Approach 1

For the first two optimization approaches, a full factorial search of the design space, the improvement due to use of RSEs is directly proportional to the improvement in analysis time of a single design point. This is because the total number of design points is not dependent on the form of the failure criteria analysis. Thus, the full-factorial approach using RSEs is 1.45 times faster the full-factorial approach using the original failure criteria analyses. This speed increase is directly related to the difference in analysis time for RSEs versus the original failure criteria, as mentioned above.

3.1.2.2 Approach 2

The best gain in efficiency with RSEs is achieved by the third approach: application of a gradient-based optimization algorithm. The simple polynomial form of the RSEs allows for the gradient of the failure criteria to be evaluated analytically as opposed to numerically. This significantly reduces the number of function calls for each step of the optimization, requiring only one for each RSE. A panel optimization environment was set up in Matlab to find panel dimensions which minimize panel mass for the loads given above, using the panel optimization procedures outlined in Chapter 2. This optimization converges in 3 seconds, an order of magnitude faster than the previous gradient-based optimization.

3.1.3 Summary of Existing Methods

Table 7 summarizes the run times presented in the sections above. Note that Level 3 of the table has been left off and will be discussed at the end of the chapter after the methodology

has been developed for that level.

Table 7: Run Times of Local Optimization Approaches (seconds)

	Failure Criteria	Domain	Approach 1	Approach 2
Level 1	Original Analyses	Physical	295.9	33
Level 2	3rd Order RSEs	Physical	170.1	3

The results in Table 7 show that the efficiency of the panel optimization can be improved by the application of a design of experiments and response surface equations. However, in the context of rapid optimization for conceptual design and MDO, these improvements still do not produce the desired level of efficiency. Although a panel optimization time of 3 seconds is a substantial improvement over traditional methods, it would still result in a total optimization time of 10 minutes for a structure consisting of 200 panels (for a metallic design; composite would be substantially slower). If the ultimate goal is to incorporate the structural design tool in an MDO environment, this can still be a prohibitively long run time. In an MDO environment the 10-minute optimization would have to be run multiple times to achieve convergence within the structures discipline. This would then be compounded by multiple runs at the system level.

The points discussed above suggest that further simplification is needed for the panel design space to improve efficiency. In the following sections, the endeavor of further improving panel optimization efficiency will be undertaken with a change of design variables and linearization of the design space. By changing variables to stiffness terms, the design space is better suited to handle stiffness constraints as well as composite materials. The linearization (enabled by the change of variables) provides an improvement in optimization efficiency over the approaches discussed above.

3.2 Change of Variables

A change of variables is applied in this research to enable a reduction in variables and a linearization of the design space, ultimately improving the efficiency of the panel optimization. This section contains a discussion justifying the change of variables as well as the logic used to select the new variables.

The change of variables studied in this research pertains to switching from panel dimensions to equivalent panel smeared stiffness within the panel-level design environment. This is shown qualitatively in Figure 40. The use of RSEs is what facilitates the change of variables, by allowing the smeared stiffness terms from the [ABD] matrix to be mapped to failure criteria for the stiffened panel. In the regression used to generate the RSEs, the ABD terms become the independent variables. This concept will be developed over the following subsections.

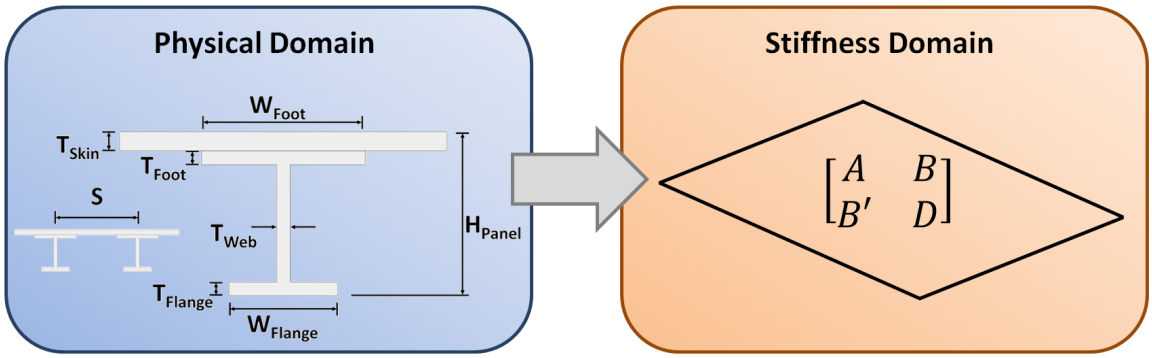

Figure 40: Change of Variables

3.2.1 Justification for Change of Variables with Isotropic Plate Example

The change of variables performed here is done to enable two key improvements to the stiffened panel design space, both of which increase the efficiency of the panel optimization. The first is a reduction in the total number of variables, from 8 to 5 for a metallic I-stiffened panel and 14 to 6 for a composite I-stiffened panel. An even more significant result is that the change of variables also promotes linearization of the design space. A linearized design space can be solved more rapidly than a nonlinear design space.

As mentioned above, the stiffened panel design space is primarily composed of the panel failure criteria that constrain the design space. Thus, the linearization depends upon being able to select design variables which cause linear behavior in the failure criteria. It is the nature of many stiffened panel failure criteria to behave linearly (or mostly linear) with respect to the equivalent stiffness terms (ABD matrix discussed in Section 2.6.2). A simple isotropic plate (Figure 41), of thickness t, can be used to explain this behavior.

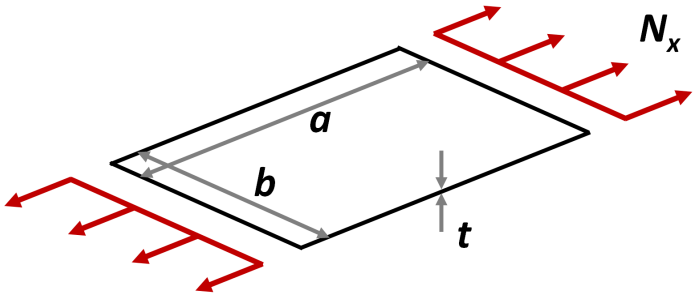

Figure 41: Flat Plate Example for Linearization

In the physical domain of the isotropic plate, t is the design variable. The failure criteria for the material strength of the plate is a linear function of t, as shown in Equation 12 for the Margin of Safety (MS) calculation. Additionally, the margin depends on the allowable stress for the material (σ_{allow}) and the running load (N_x) in the plate.

$$MS = \frac{\sigma_{allow}}{\sigma_{actual}} - 1 = (\sigma_{allow})/(N_x/t) - 1 \tag{12}$$

The failure criteria for buckling, however, is not a linear function of t, as shown in Equation 13. The buckling margin also depends on the fixity factor (k), Young's Modulus of the material (E), width of the plate (b), and length of the plate (a). Equation 13 shows that the MS is related to the third power of t and second power of a.

$$MS = \frac{P_{crit}}{P_{actual}} - 1 = \left(\frac{k\pi^2 E t^3}{12a^2}\right)/(N_x) - 1 \tag{13}$$

In the stiffness domain, the stress margin can also be written as a linear function of the design variable A_{11}, as shown in Equation 15. A_{11} is simple to calculate for an isotropic flat plate, as shown in Equation 14.

$$A_{11} = \frac{Et}{1-\nu_{12}^2} \tag{14}$$

$$MS = (\sigma_{allow})/\left(\frac{N_x E}{A_{11}(1-\nu_{12}^2)}\right) - 1 \tag{15}$$

Additionally, the buckling margin can be written as a linear function of the design variable D_{11}, as shown in Equation 17. Calculation of D_{11} for an isotropic flat plate is straight-forward, as shown in Equation 16.

$$D_{11} = \frac{Et^3}{12(1-\nu_{12}^2)} \tag{16}$$

$$MS = \left(\frac{k\pi^2 D_{11}(1-\nu_{12}^2)}{a^2} \right) /(N_x) - 1 \tag{17}$$

Thus, changing variables to stiffness terms A_{11} and D_{11} linearizes the strength and buckling failure criteria for the plate. Although the flat plate example is a perfectly linear function of stiffness terms, the behavior of more complex panels is not completely linear. Adding a stiffener to the panel causes the load to redistribute within the panel. Additionally, grouping multiple (similar) failure criteria together induces some non-linearity to the design space (discussed in the next section). However, the overall design space approaches linearity when mapped to the stiffness domain. As discussed later in Chapter 4, this linearization still provides an accuracy of 90%-95% or greater relative to the physical domain.

The above discussion raises the question: what would happen if linearization was performed without the change of variables? It is evident from the flat plate example given above that the failure criteria are nonlinear with respect to the physical dimensions. However, for the sake of completeness, the same RSE -based linearization performed in Section 3.3.4 was applied to the physical variables to document the resulting error.

The reason why linearization in the physical domain is not viable is due to the poor mapping from the physical domain to the stiffness domain if the physical domain is linear. Mapping between the two domains is imperative for creating an interface between stiffened panel design and global stiffness design with a FEM . This interface is explained in significant detail in Chapter 6.

Thus, if the panel stiffness can not be accurately calculated from a linear function of terms in the physical domain, then there is no viable way to map stiffness constraints to the panel level. Figure 42 shows the error that arises when attempting to linearize the diagonal terms from the ABD matrix as a function of the physical dimensions of an I-stiffened panel. The distributions in this figure show a broad spread of error, with some very severe outliers for the bending stiffness terms (D_{11}, D_{22}, D_{33}).

As another case against linearizing in the physical domain instead of the stiffness domain, consider the actual value versus predicted value for D_{11} when attempting to linearize in the physical domain, shown in Figure 43. Each point on the scatter plot represents an I-stiffened

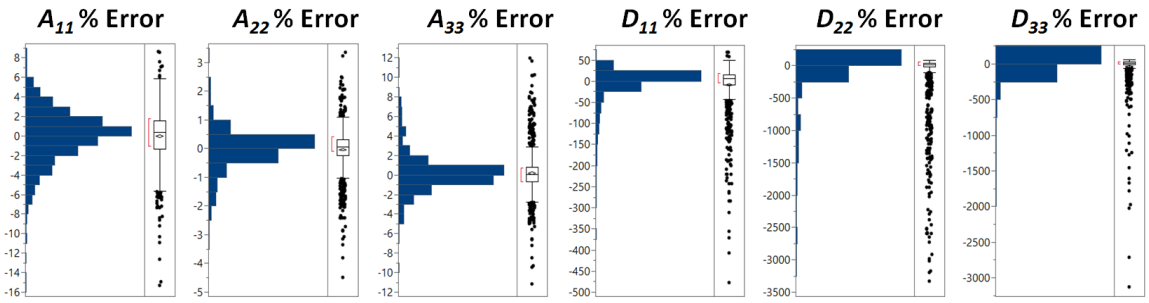

Figure 42: Prediction Error of ABD Terms from the Linearized Physical Domain

panel design. A linear function was used to predict D_{11}, which is plotted against the actual value of D_{11} evaluated from traditional nonlinear equations. The resulting error shows significant non-linearity that is not being captured. Together, these results solidify the argument that linearization can not be performed in the physical domain, necessitating a change of variables to the stiffness domain.

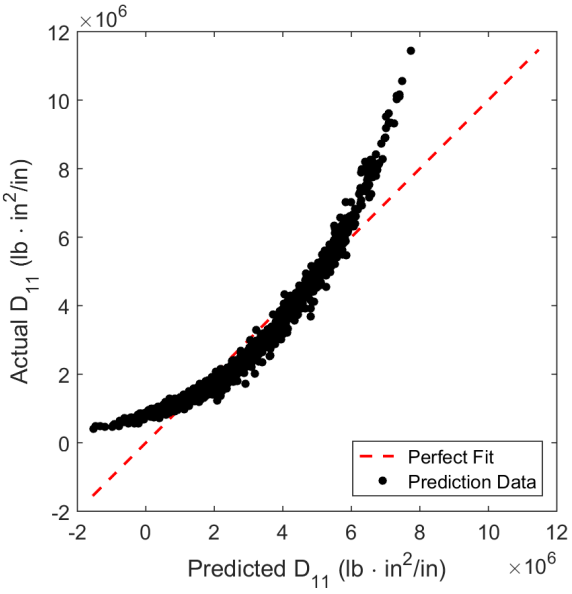

Figure 43: Actual vs Predicted Value for D_{11} with Linearized Form in Physical Domain

3.2.2 Selection of New Variables

As summarized previously, the smeared stiffness terms of the ABD matrix provide a good representation for a linear design space. The linearization was shown on a simple flat plate in the previous section. The concept of linearization in the stiffness domain will now be

developed for the metallic I-stiffened panel. This section describes the process used to select terms from the ABD stiffness matrix to form the stiffness domain of the I-stiffened panel.

Of the 18 unique terms in the ABD matrix, only 5 are used as design variables for the I-stiffened panel. This is because typically only a subset of the terms dominate the performance of the panel. For the methodology developed here, A_{11}, A_{22}, A_{33}, D_{11}, and D_{22} are the stiffness terms used as design variables. Note that these terms all come from the diagonal of the ABD matrix, making the assumption that the coupling terms are negligible. This is an acceptable assumption for closed-cell structures with substantial volume, such as a commercial aircraft wing box or launch vehicle body [58]. For thin structures, the coupling terms of the panel become much more relevant [44]. The description below provides details of how the subset of ABD terms was selected.

The first reduction in ABD terms is simply due to terms which are zero for the selected stiffened panel construction. For both a metallic stiffened panel and a composite stiffened panel with balanced laminates, the A_{13}, A_{23}, B_{13}, B_{23}, D_{13}, and D_{23} terms will be zero. This is shown in Figure 44 for the I-stiffened metallic panel. The ABD matrix shown in this figure was calculated with HyperSizer [1], which uses the extension of CLT described in Reference [55].

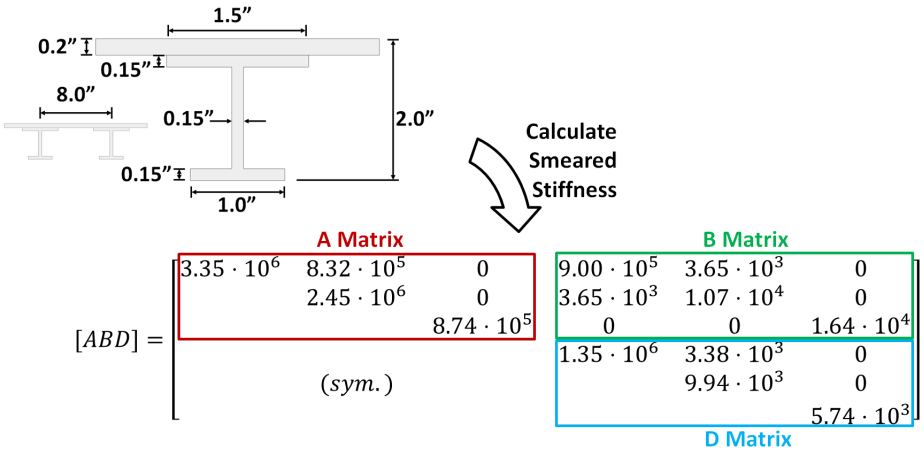

Figure 44: Example ABD Matrix for Metallic I-Stiffened Panel

Of the remaining non-zero ABD terms, further reductions can be made by examining the sensitivity of panel failure criteria to the various terms as well as coupling between the

ABD terms. Figure 45 displays a scatter plot of Margin of Safety (MS) versus the non-zero ABD terms for the metallic I-stiffened panel. Plots like these were used to examine the sensitivity of the failure criteria to the ABD terms. The plots were generated by applying a fixed load to the stiffened panel (N_x =-8000 lb/in, N_y = -2800 lb/in, N_{xy} =2475 lb/in) and varying the geometry of the panel. For each variation, the ABD terms and MS of failure criteria were evaluated in HyperSizer.

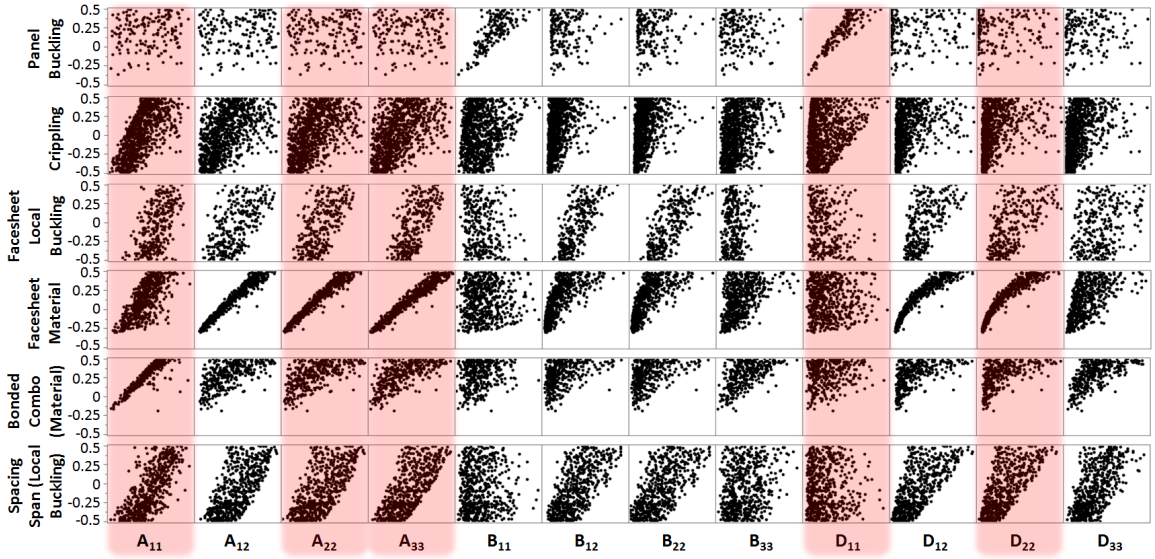

Figure 45: Margin of Safety for Various Failure Criteria versus ABD Terms, Fixed Load Condition

Scatter plots in Figure 45 that show a distinct linear trend help determine if a particular ABD term has a useable linear relationship with the failure criteria. Any ABD terms showing a distinct trend for any of the failure criteria were selected as the final set of design variables for the stiffness domain. Note that it is not necessary for the selected ABD terms to show a linear trend for *all* of the failure criteria. As long as each of the failure criteria are linear to at least one of the stiffness terms, it can be represented in the stiffness domain.

Additionally, note that for some of the failure criteria, multiple stiffness terms work together in a linear fashion to represent the MS. In these scenarios, the linear trend is not evident unless the stiffness terms are plotted in three dimensions or higher. This is because some of the failure criteria are related to multiple stiffness terms as an n-dimensional plane. An example of this behavior can be seen with the spacing span failure criteria in Figure 45.

The stiffness terms which appear as wide bands with distinctly linear borders (A_{22}, A_{33}, and D_{22}) exhibit this behavior. Thus, the spacing span failure criteria can not be represented by any of the three terms by themselves, but a linear combination of these three terms provides a correlation with the failure criteria.

Some of the ABD terms with distinct linear trends were *not* chosen due to overlap with other terms. For example, consider ABD term A_{12}, which couples in-plane extension in the x and y direction. This term is primarily controlled by the panel skin thickness. Similarly, the lateral stiffness term A_{22} is also primarily controlled by panel skin thickness. Thus, there is essentially a one-to-one relationship between these two terms, as shown in Figure 46 (along with other linked terms). For this reason, it is not necessary to include both terms in the design space.

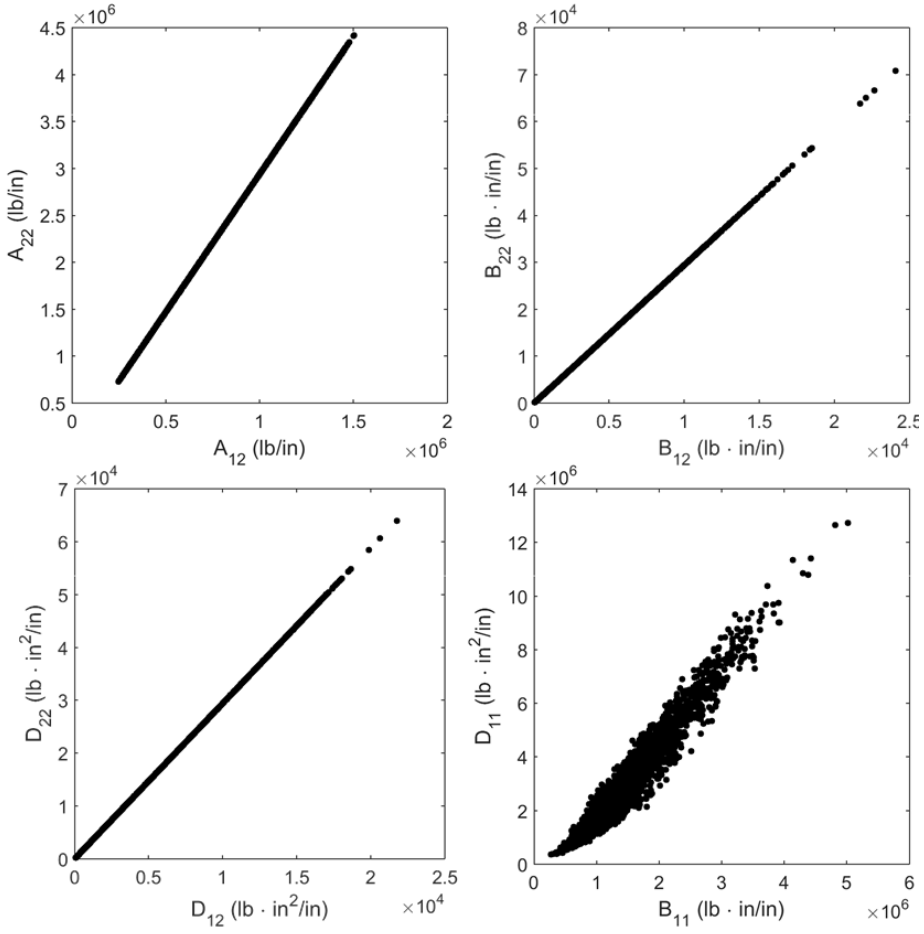

Figure 46: Relationships between Linked ABD Terms for Metallic I-Stiffened Panel

Although the stiffness term selection process described above is similar to a traditional sensitivity analysis, such an analysis can not be used in the stiffness domain presented here. This is because there is significant coupling between the independent variables (stiffness terms) as shown in the scatter plots of Appendix A. These scatter plots show that many of the stiffness terms cannot physically vary completely independently of each other. Thus, any sensitivity analysis of failure criteria with respect to stiffness terms will be heavily biased by the stiffness term interactions. However, the visual-based sensitivity analysis shown above has been shown in this research to produce a useable subset of ABD terms for optimization.

The final consideration to be made in selecting stiffness terms is how to choose those which have a significant relation to the mass of the panel. For example, a stiffness term such as D_{22} is governed primarily by the skin and foot of the stiffener. For this reason, D_{22} would not capture the mass influence of other parts of the panel, such as the web and cap. Thus, it is preferable to chose ABD terms which capture the stiffness of all parts of the panel, allowing the terms to be mapped to the overall mass of the panel. This is easily visualized by generating a scatter plot for unit mass versus the remaining down-selected panel stiffness terms, as shown in Figure 47.

From Figure 47, it is evident that the axial stiffness term A_{11} has the most direct relationship to panel mass. As with the failure criteria MS, it is only necessary to have one stiffness term with a strong linear relationship to unit mass. The terms that have a non-linear relationship with panel unit mass are simply left out of the linear mass expression (given in Section 3.5.2).

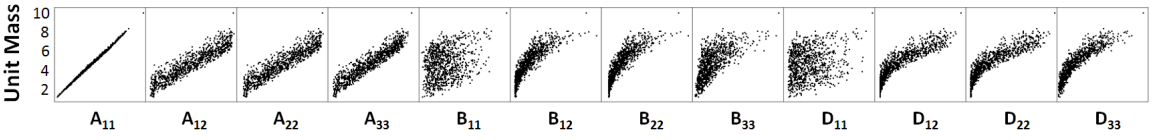

Figure 47: Unit Mass versus ABD Terms for Metallic I-Stiffened Panel

The next section will describe how the selected subset of stiffness terms A_{11}, A_{22}, A_{33}, D_{11}, and D_{22} are used in mapping from the physical domain to the stiffness domain.

3.2.3 Relationship Between Physical and Stiffness Domain

This section describes development of the equations that relate the physical and stiffness domain for the I-stiffened panel. The ABD stiffness terms for a stiffened panel are calculated with an extension of CLT [92]. CLT was originally developed to derive an equivalent plate stiffness for a laminated plate consisting of plies with various stiffnesses, orientations, and thicknesses. Stiffened panels are handled by treating each part of the panel as an equivalent to a ply. The stiffness contributions from each "ply" are summed up to give a stiffness representation of the plate as a whole.

To describe the derivation of the panel stiffness terms, the steps of the traditional CLT process will be outlined first. The initial step is calculating the reduced stiffness matrix based on material properties. This step is shown in Equation 18 and 19.

$$[Q] = \begin{bmatrix} Q_{11} & Q_{12} & 0 \\ Q_{21} & Q_{22} & 0 \\ 0 & 0 & Q_{33} \end{bmatrix} \tag{18}$$

$$Q_{11} = \frac{E_1^2}{E_1 - \nu_{12}^2 E_2} \tag{19a}$$

$$Q_{12} = Q_{21} = \frac{\nu_{12} E_1 E_2}{E_1 - \nu_{12}^2 E_2} \tag{19b}$$

$$Q_{22} = \frac{E_1 E_2}{E_1 - \nu_{12}^2 E_2} \tag{19c}$$

Next, the transformed reduced stiffness matrix is calculated for rotated plies as shown in Equation 20 and 21. This matrix must be calculated for every unique combination of stiffness and ply angle (θ) considered in the laminate.

$$[\overline{Q}] = \begin{bmatrix} \overline{Q}_{11} & \overline{Q}_{12} & \overline{Q}_{13} \\ \overline{Q}_{21} & \overline{Q}_{22} & \overline{Q}_{23} \\ \overline{Q}_{31} & \overline{Q}_{32} & \overline{Q}_{33} \end{bmatrix} \tag{20}$$

$$\overline{Q}_{11} = Q_{11}cos(\theta)^4 + 2(Q_{12} + 2Q_{33})cos(\theta)^2 sin(\theta)^2 + Q_{22}sin(\theta)^4 \tag{21a}$$

$$\overline{Q}_{12} = \overline{Q}_{21} = Q_{12}(cos(\theta)^4 + sin(\theta)^4) + (Q_{11} + Q_{22} - 4Q_{33})cos(\theta)^2 sin(\theta)^2 \tag{21b}$$

$$\overline{Q}_{13} = \overline{Q}_{31} = (Q_{11} - Q_{12} - 2Q_{33})cos(\theta)^3 sin(\theta) - (Q_{22} - Q_{12} - 2Q_{33})cos(\theta)sin(\theta)^3 \quad (21c)$$

$$\overline{Q}_{22} = Q_{11}sin(\theta)^4 + 2(Q_{12} + 2Q_{33})cos(\theta)^2 sin(\theta)^2 + Q_{22}cos(\theta)^4 \quad (21d)$$

$$\overline{Q}_{23} = \overline{Q}_{32} = (Q_{11} - Q_{12} - 2Q_{33})cos(\theta)sin(\theta)^3 - (Q_{22} - Q_{12} - 2Q_{33})cos(\theta)^3 sin(\theta) \quad (21e)$$

$$\overline{Q}_{33} = (Q_{11} + Q_{22} - 2Q_{66})cos(\theta)^2 sin(\theta)^2 + Q_{33}(cos(\theta)^4 + sin(\theta)^4) \quad (21f)$$

The final step is to sum up the terms from the transformed reduced stiffness matrix to form the extensional, coupling, and bending terms of the ABD matrix. This is shown below in Equations 22, 23, and 24, respectively. These terms are calculated based on the through-thickness location (z) of the kth ply of n total plies.

$$A_{ij} = \sum_{k=1}^{n} \{Q_{ij}\}_k (z_k - z_{k-1}) \quad (22)$$

$$B_{ij} = \frac{1}{2} \sum_{k=1}^{n} \{Q_{ij}\}_k (z_k^2 - z_{k-1}^2) \quad (23)$$

$$D_{ij} = \frac{1}{3} \sum_{k=1}^{n} \{Q_{ij}\}_k (z_k^3 - z_{k-1}^3) \quad (24)$$

Now that the traditional CLT process has been introduced, the next step is to adapt it to stiffened panels. This is based on the fundamentals presented in Reference [99] and [100]. The adaptation will be demonstrated only for the diagonal terms in the ABD matrix because these are the terms of interest for this research, as described previously in Section 3.2.2. The first step of the adaptation is to decompose the I-stiffened panel into objects that are equivalent to plies in a laminated plate. The decomposition is shown in Figure 48.

The summation form in Equations 22 through 24 indicates that the ABD contributions of each object can be linearly summed to achieve the overall ABD matrix; this is shown in Equation 25.

$$[ABD]_{panel} = [ABD]_{skin} + [ABD]_{foot} + [ABD]_{web} + [ABD]_{cap} \quad (25)$$

Next, calculation of the individual terms for each object of the panel will be considered. This calculation will be done for a panel consisting of a skin with an I-stiffener fastened to it. One of the primary assumptions for this construction method is that only the skin contributes to the lateral membrane stiffness term (A_{22}). This assumption implies that

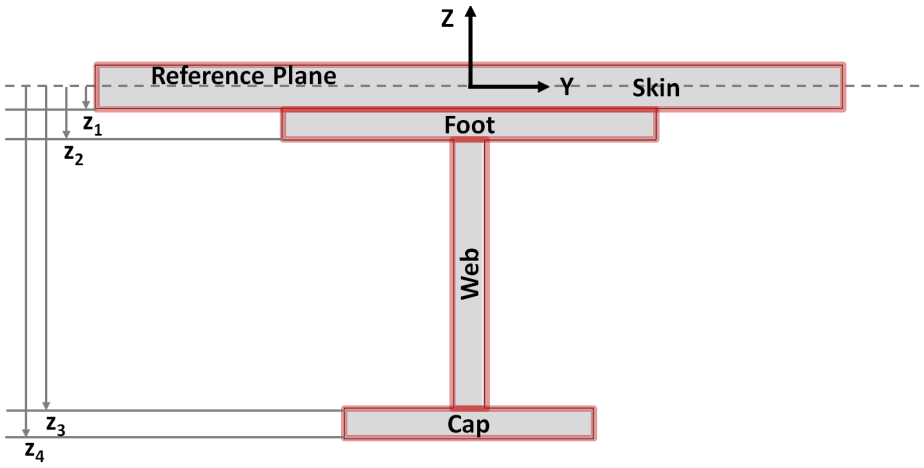

Figure 48: Objects of Decomposed I-Stiffened Panel

substantial lateral load cannot be transferred through the fasteners into the foot of the stiffener. It also implies that the Poisson contribution to axial stiffness will be ignored for all objects except the skin. The impact of these assumptions will be observed in deriving the diagonal ABD terms below.

An additional assumption is made by setting $\theta = 0$ for all of the terms in the transformed reduced stiffness matrix (Equation 20). This greatly reduces the complexity of the ABD calculation for the stiffened panel, causing $[\overline{Q}] = [Q]$. The implication of this assumption is that the objects of the stiffener are composed of a homogeneous orthotropic material represented only by the properties E_1, E_2, and ν_{12}. This assumption is not necessary for the ABD derivation; a unique ABD matrix could be derived for each object if that level of fidelity was necessary. However, the simplified representation provides enough detail for the purposes of this research. Derivation of the E_1, E_2, ν_{12} representation for a laminate will be discussed below.

In the derivation of the ABD terms for the I-stiffened panel, a distinction is made between the material properties of the skin and stiffener. Skin properties are given the subscript $()_{sk}$ and stiffener properties are given the subscript $()_{st}$. This allows for different laminates to be used in the skin and stiffener, improving the tailor-ability of the panel stiffness.

With the above assumptions in place, derivations of the diagonal ABD terms for the

panel can be performed. First, the A_{11} contributions of the objects are given in Equation 26 below. The skin contribution is straight-forward because it is identical to the contribution of a ply in traditional CLT. The stiffener terms require an equivalent thickness (t_{cp}, t_{ft}) to be calculated, which is equal to the area of the object divided by the stiffener spacing.

$$A_{11,skin} = \frac{E_{1,sk}^2 t_{sk}}{E_{1,sk} - \nu_{12,sk}^2 E_{2,sk}} \tag{26a}$$

$$A_{11,foot} = \frac{E_{1,st} t_{ft} W_{ft}}{S} \tag{26b}$$

$$A_{11,web} = \frac{E_{1,st} t_{wb} (H - t_{sk} - t_{wb} - t_{cp})}{S} \tag{26c}$$

$$A_{11,cap} = \frac{E_{1,st} t_{cp} W_{cp}}{S} \tag{26d}$$

Next are the A_{22} terms, shown in Equation 27. These are very simple due to the decoupling assumption made above.

$$A_{22,skin} = \frac{E_{1,sk} E_{2,sk} t_{sk}}{E_{1,sk} - \nu_{12}^2 E_{2,sk}} \tag{27a}$$

$$A_{22,foot} = 0 \tag{27b}$$

$$A_{22,web} = 0 \tag{27c}$$

$$A_{22,cap} = 0 \tag{27d}$$

The A_{33} terms are very similar, as shown in Equation 28.

$$A_{33,skin} = G_{sk} t_{sk} \tag{28a}$$

$$A_{33,foot} = 0 \tag{28b}$$

$$A_{33,web} = 0 \tag{28c}$$

$$A_{33,cap} = 0 \tag{28d}$$

For calculation of terms in the [D] matrix, the location of panel objects becomes relevant due to the cubic exponent on z in Equation 24. Figure 48 displays the object locations used in the equations below. Equation 29 gives the calculation of the D_{11} terms. Similar to A_{11}, the Poisson effect only contributes to the skin terms. Another note to make about this equation is that a ratio of object width to stiffener spacing is applied to each term to

account for the stiffener object's finite width within the panel. This ratio can be seen on the end of the equation for the stiffener foot, web, and flange.

$$D_{11,skin} = \frac{E_{1,sk}^2 t_{sk}^3}{12(E_{1,sk} - \nu_{12,sk}^2 E_{2,sk})} \tag{29a}$$

$$D_{11,foot} = \frac{1}{3} E_{1,st}(z_1^3 - z_2^3)\frac{W_{ft}}{S} \tag{29b}$$

$$D_{11,web} = \frac{1}{3} E_{1,st}(z_2^3 - z_3^3)\frac{t_{wb}}{S} \tag{29c}$$

$$D_{11,cap} = \frac{1}{3} E_{1,st}(z_3^3 - z_4^3)\frac{W_{cp}}{S} \tag{29d}$$

The D_{22} terms are more simple because only the skin comes into play. These are shown in Equation 30.

$$D_{22,skin} = \frac{E_{1,sk} E_{2,sk} t_{sk}^3}{12(E_{1,sk} - \nu_{12}^2 E_{2,sk})} \tag{30a}$$

$$D_{22,foot} = 0 \tag{30b}$$

$$D_{22,web} = 0 \tag{30c}$$

$$D_{22,cap} = 0 \tag{30d}$$

Finally D_{33} is calculated in a similar manner to A_{33}, shown in Equation 31.

$$D_{33,skin} = \frac{G_{sk} t_{sk}^3}{12} \tag{31a}$$

$$D_{33,foot} = 0 \tag{31b}$$

$$D_{33,web} = 0 \tag{31c}$$

$$D_{33,cap} = 0 \tag{31d}$$

This completes the calculation of the diagonal terms from the equivalent smeared stiffness matrix for the fastened I-stiffened panel. Note that the panel construction used in the remainder of this research is a *bonded* I-stiffened panel, where the stiffener is bonded to the skin. This technique is primarily used for composite structures, but is considered for metallic panels in this research to provide a stepping-stone to composites. Derivation of the stiffness terms for the bonded panel is fundamentally similar, but has complex non-zero terms for the contribution of the stiffener foot (which is bonded to the skin). Additionally, the derivations are proprietary to Collier Research Corporation, owners of HyperSizer. For

these reasons, the exact equations used to calculate the smeared ABD terms for the bonded panel are not reproduced here.

3.3 Reformulation of Design Space

Having introduced the change of variables in the previous section, this section describes the reformulation of the design space to be a function of the stiffness terms. The design space reformulation primarily consists of recasting the panel constraints (failure criteria) and objective function (mass) in terms of smeared panel stiffness. Additionally, the constraints and objective function are linearized to allow for rapid optimization. The reformulation is centered around using logistic regression to generate linear RSEs that predict whether a panel passes or fails a group of criteria for a given set of loads. These concepts are discussed below.

3.3.1 Significance of Failure Criteria

Reformulation of the design space primarily concerns mapping the panel failure criteria from the physical domain to the stiffness domain. The panel failure criteria are what drive detailed panel design. If panels were designed only to achieve a target global stiffness, their designs could end up unrealistically tall and unwieldy. Panel failure criteria ensure that the panel has enough material to withstand material failure, enough object (skin, flange, etc) thickness to withstand local buckling, enough overall bending inertia to withstand panel buckling, and so on. The accumulative effect of these failure criteria ensure a panel design will be produced that will survive the intended flight loads.

From a mass standpoint, it is desirable to include as many failure criteria as possible in the early phases of the structural design. This helps avoid "hidden surprises" when the structure reaches the detailed stage of design. Many conceptual design approaches use a reduced set of failure criteria [64], usually to simplify the local optimization. The drawback of this simplification is that often the neglected advanced failure criteria are the most conservative, requiring a higher panel mass.

The above phenomena can be demonstrated with the optimization of a metallic I-stiffened panel in HyperSizer. A panel with a load condition of N_x =-10,000 lb/in, N_y =-3000 lb/in, N_{xy} =1500 lb/in was optimized multiple times with increasingly more conservative failure criteria, using those listed in Table 1 of Section 2.6.1. This was done to show which failure criteria dominate in terms of mass impact. The results are shown in Figure 49 below.

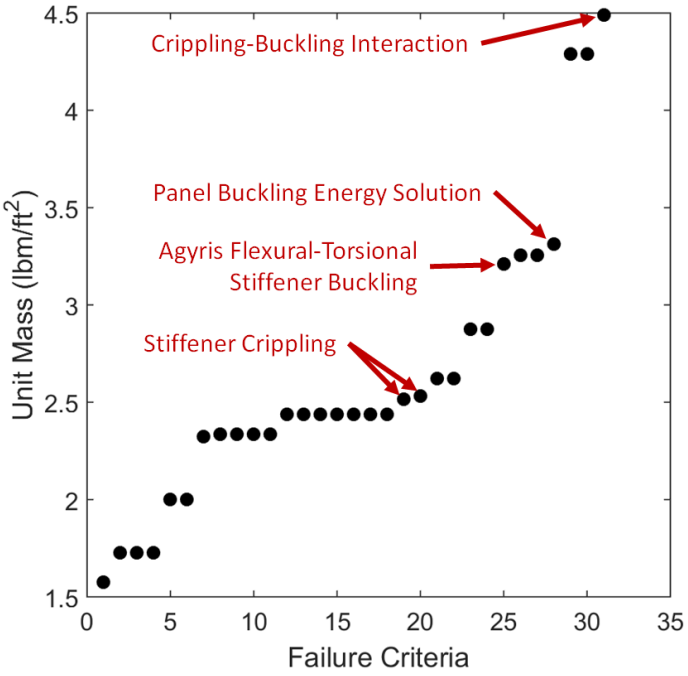

Figure 49: Mass Impact of Increasingly Conservative Failure Criteria

Note that the order of the failure criteria in Figure 49 is not the same as presented in Table 1. The failure criteria on the x-axis of Figure 49 are sorted from least to most conservative. Figure 49 shows that the more complex criteria (identified in the plot) are at the upper end of the unit mass curve and are thus more conservative. Crippling analyses, for example, are complex because they require a table-lookup for every object in the stiffened panel [101]. It can be seen that crippling analyses appear several times in the upper end of the mass curve. The energy solution for panel buckling is another complex failure criteria, using a Rayleigh-Ritz energy solution [102]. This analysis is performed numerically and excels at handling complex load conditions. Flexural-torsional buckling is at a similar level

of complexity and requires a numerical solution. The flexural-torsional analysis considers the interaction between stiffeners "tipping" over and general panel buckling [103].

This section has demonstrated a motivation to include complex panel failure criteria in the conceptual phase of design. Fortunately, the methodology presented in this research is able to include failure criteria of any complexity. This is because the failure criteria can be approximated as RSEs (a function of stiffness and loads), allowing their effects on panel mass to be included without being detrimental to the efficiency of the optimization.

3.3.2 Grouping of Failure Criteria

Grouping failure criteria is advantageous when generating RSEs because it reduces the total number of regressions that must be performed and also reduces the complexity of the final design space. If two failure criteria for the panel are similar, it is not necessary to include both in the optimization. Thus, the groups of failure criteria discussed in this section were determined by comparing the passed and failed regression points and grouping failure criteria that overlapped by 80% or greater. Additionally, failure criteria were grouped if their combined failure envelopes had a linear boundary as shown in Figure 50.

Of the 33 failure criteria original failure criteria for the metallic I-stiffened panel presented in Table 1 of Section 2.6.1, only 11 groupings are needed to accurately represent panel failure. These groupings are listed below, and come from combinations of "Object" and failure criteria "Type" in Table 1.

Often only a subset of these 11 are needed for optimization, depending on which failure criteria are prevalent for the given load condition. For example, the buckling failure criteria are not relevant for panels loaded in tension with no shear.

1. Panel Buckling
2. Stiffener Buckling
3. Panel and Stiffener Crippling
4. Facesheet Local Buckling
5. Facesheet Material Failure

6. Bonded Combo Material Failure
7. Spacing Span Local Buckling
8. Web Material Failure
9. Web Local Buckling
10. Bottom Flange Material Failure
11. Bottom Flange Local Buckling

The process of grouping failure criteria into a single RSE is done with the regression data before the RSEs are generated. Because the RSEs represent failure of the stiffened panel, a Boolean union of the failed regression points is performed for each group of failure criteria. Thus, for a given DoE point, failing any of the criteria in the group means the point is represented as a failure in the regression.

Figure 50 shows how two failure criteria with different failed points would be combined and represented by a single RSE. The points in this figure represent the regression data used to generate RSEs for the failure criteria. Green points correspond to regression points that passed the failure criteria, and red points indicate failure. In joining two failure criteria, if either criteria fails then the final point used in the regression is considered to be a failure.

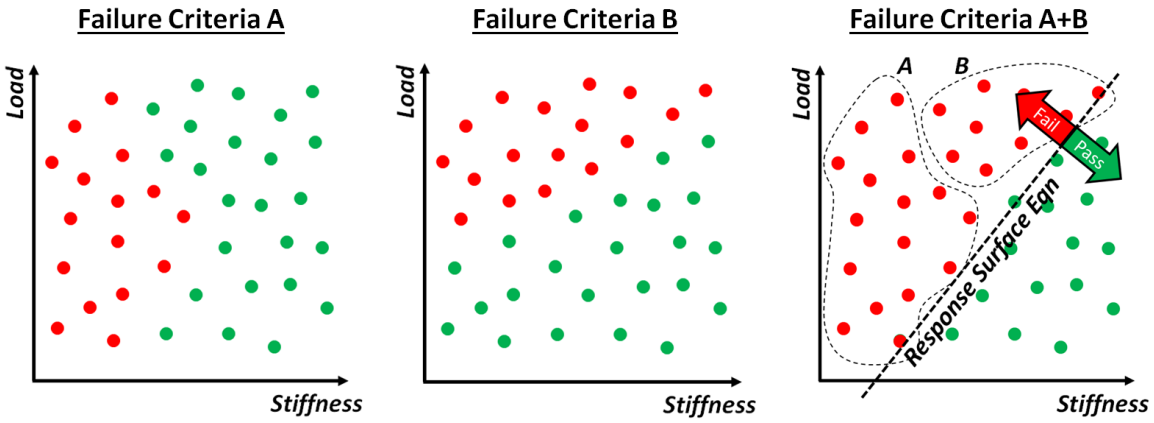

Figure 50: Combining Multiple Failure Criteria into a Single RSE

Typically, only similar failure criteria are grouped to ensure smooth boundary between the "pass" and "fail" regions of the design space. This is necessary to achieve a RSE that is

accurate. For example, it would be appropriate to combine web and flange buckling failure criteria because both of these criteria become prevalent when the panel is highly loaded in compression or does not have sufficient bending stiffness. However, it would not be appropriate to combine panel buckling and material failure because the underlying physics of these two is quite different; a panel can satisfy material failure criteria by a high margin but still fail in buckling.

3.3.3 Loads and Buckling Spans

In addition to the panel stiffness terms presented in Section 3.2.2, there is another category of terms that appear in the reformulated design space. These terms can be thought of as "panel constants" because they remain constant during the stiffened panel optimization. The panel constants considered in the current research are panel loads and buckling spans. Preserving these terms in the reformulated design space is imperative for maintaining generality of the stiffened panel optimization. In a FEA-based environment, each panel has unique loads and buckling spans that must be included in the panel optimization. Thus, when the design space reformulation is performed, these values must be available as inputs. The details of this approach are covered in the next section.

Section 2.6.1 previously discussed the buckling loads and spans considered in the current research. Note that of the six possible load components presented in Equation 10 in Section 2.6.2, only the membrane components are used. This is a common assumption for conceptual design [72], [80]. This assumption usually works well for aerospace shell structures where bending loads are low. Stiffened shell structures with a significant cross section, such as a wing box or launch vehicle barrel, primarily carry overall vehicle bending moments as tension, compression, and shear. Thus, leaving out the bending load components still provides accurate loads for optimization. Figure 51 below shows membrane loads and bending loads for the +2.5g pull-up load case on a commercial aircraft wing box FEM , demonstrating the significant difference in magnitude.

Due to the nature of the reformulation used in this research, it is necessary to pre-define the possible range of loads that can be handled by the stiffened panel design. This

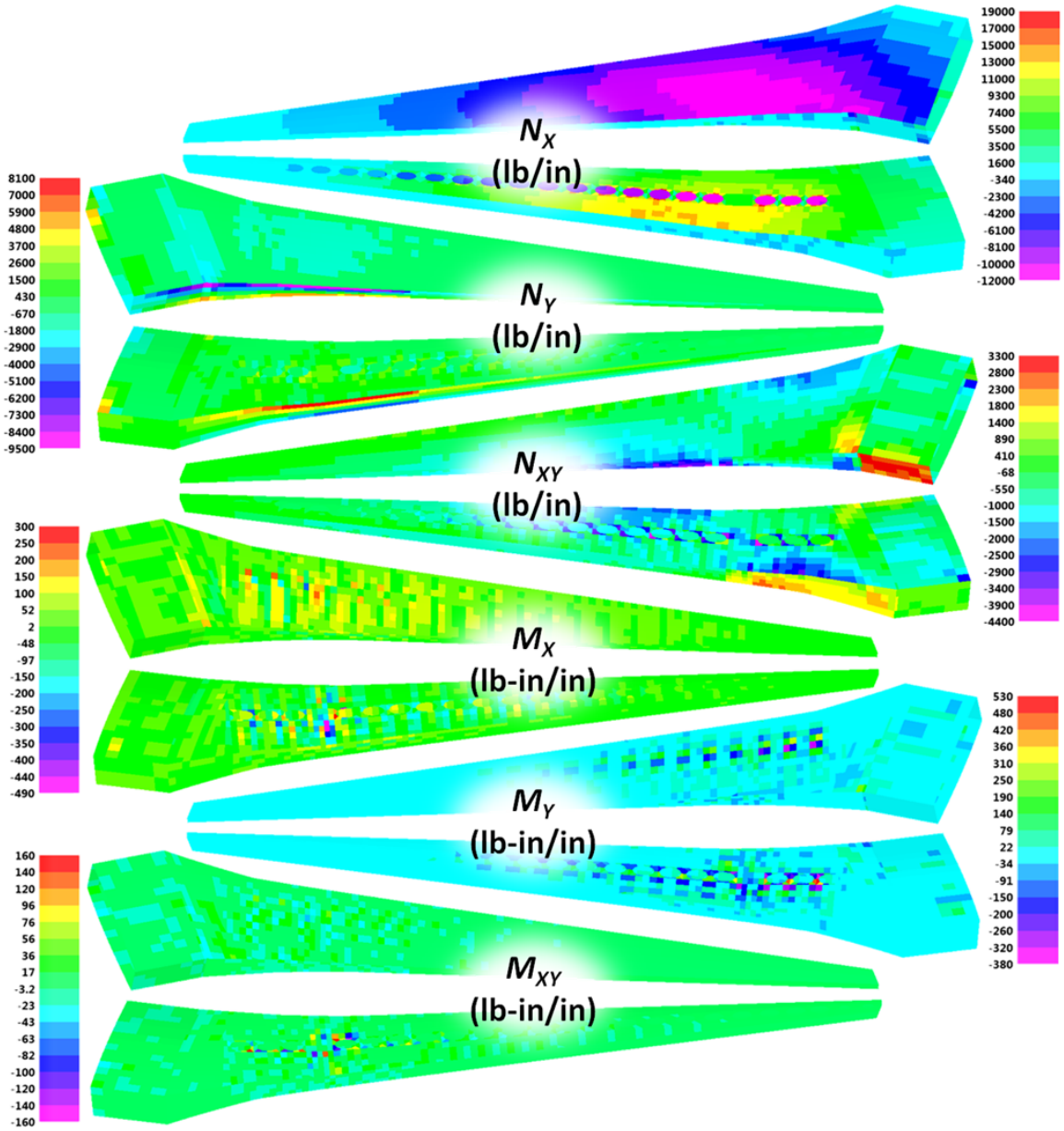

Figure 51: Magnitude of Membrane Load Components on a Commercial Aircraft Wing Box

defines the ranges of load used in the RSEs discussed in the next section. The range of load considered is ultimately up to the end-user, and depends on the magnitude of loads expected to be encountered on the structure of interest. The load range selected for the current research is broad, to demonstrate that the methodology is suitable for environments where the load magnitude may vary greatly as the design is iterated.

While it is useful to set up the stiffness-based methodology to use a wide range of loads,

a trade-off exists between the breadth of the load range and the accuracy of the stiffness-based optimization. Using wide load ranges in the stiffness-based representation of the failure criteria degrades the accuracy of the criteria because it forces the RSEs to represent a larger portion of the design space. Thus, sometimes it is necessary to break up the load ranges and do the linearization on multiple, smaller ranges of load. This sub-division must also be done when the load range include tension and compression load, because the primary failure modes change (buckling versus material failure). Figure 52 shows the load range used in the present research, and how it is broken up to account for tension and compression independently. Note that shear load is analyzed the same regardless of sign, so only the absolute value of shear load is included in the load range.

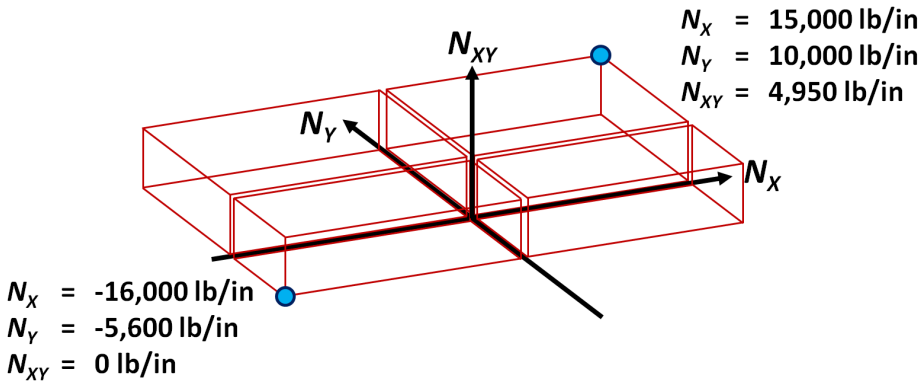

Figure 52: Load Quadrants Considered for the I-Stiffened Panel

3.3.4 Linearization Process for Failure Criteria

Having introduced the failure criteria groupings, loads, and buckling spans that form the design space, the next step is to describe reformulation of the failure criteria. As discussed previously, the reformulation consists of a change of variables and linearization enabled by the use of RSEs .

The description of failure criteria linearization below starts with justification for using RSEs . Next, the specific steps required to generate the RSEs are outlined. This is followed by a description of the regression type chosen, logistic regression, which provides a binary prediction of pass/fail for the failure criteria. Lastly, the specific form of the RSE used for this research is developed.

Note that the generation of RSEs described below, as well as the associated processing, was a manual process in this research and thus required several days of effort to generate and validate all of the RSEs . However, the regression process can be automated given enough time to code the methodology. Additionally, the RSEs only need to be generated once for a given load range and do not contribute to the total optimization run time.

3.3.4.1 Selection of Linearization Approach

Linearization of the failure criteria is done through a statistical approach (RSEs), as opposed to linearizing the original equations governing the failure criteria. This approach is used for three reasons, listed below.

1. The statistical approach allows for failure criteria to be grouped, which helps reduce the complexity of the design space. The original failure criteria are complex calculations, making it difficult and/or impossible to isolate terms and substitute the failure criteria into one another to group the analyses.

2. The form of some failure criteria makes it challenging to linearize through traditional approaches such as a Taylor Series expansion. Additionally, some failure criteria rely partially on table look-ups or use a numerical solution technique. Linearization is possible, but there can potentially be significant error associated with the numerical derivatives.

3. Most importantly, the intent is to linearize the failure criteria in terms of smeared stiffness, instead of physical dimensions. Because many of the failure criteria are a function of physical terms, it is impossible to substitute the equations for the stiffness terms into the equations for these failure criteria.

To reiterate some of the points mentioned above, consider the form of the failure criteria for web local buckling in Equation 32. This equation shows how critical buckling load $N_{x,crit}$ is calculated from web thickness t_w, material elastic and shear modulus E and G, material Poisson ratio ν, web length a, web width b, and buckling modes m, and n.

$$N_{x,crit} = \frac{-\pi^2 t_w^3}{12(1-\nu^2)} \left[E \left(\frac{m}{a}\right)^2 + 2(\nu E + 2G(1-\nu^2)) \left(\frac{n}{b}\right)^2 + E \left(\frac{n}{b}\right)^4 \left(\frac{a}{m}\right)^4 \right] \tag{32}$$

While it would be relatively straight-forward to linearize Equation 32 with respect to t_w, there is not any way to substitute the panel stiffness terms given in Section 3.2.3 into the failure criteria and then linearize. Thus, it is necessary to resort to statistical approaches for developing the linear relationship between panel stiffness terms and panel failure criteria. The approach is to use RSEs, which provide a "best fit" through the failure criteria. Development of the RSEs is discussed next.

3.3.4.2 Steps to Perform Linearization via Regression

The use of RSEs and change of variables are what enable linearization of the design space. Specifically, they provide a representation of the panel failure criteria (listed previously in Table 1) that is linear as a function of the panel stiffness terms. These failure criteria form constraints on the panel design space; thus, linearizing them provides a linear design space. The use of these RSEs was introduced as the lower-right quadrant of Table 3 in Section 2.7.2. Using RSEs with this combination of independent and dependent variables is a gap in literature addressed by this research.

Generation of the stiffness-based failure criteria RSEs requires three steps, which only need to be performed once for a given panel concept and set of load ranges. These steps are listed below and depicted in Figure 53. The general form resulting from the regression is given in Equation 33.

1. Use a DoE to generate a data set for regression.
2. Evaluate the data set with failure criteria in HyperSizer.
3. Perform regression with failure criteria performance as the dependent variable and stiffness terms as the independent variables.

$$Failure = f(A_{11}, A_{22}, A_{33}, D_{11}, D_{22}, N_x, N_y, N_{xy}, a, b) \tag{33}$$

In step 1, the process starts with a broad mixture of combinations of the independent variables and panel constants. The variable combinations are usually determined by a

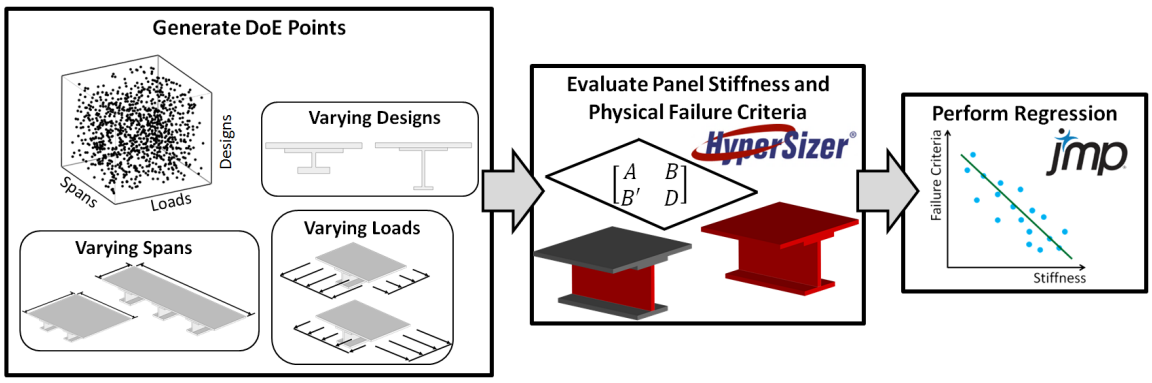

Figure 53: Process for Generating RSEs as a Function of Stiffness

space-filling DoE (discussed previously in Section 2.7.1). A DoE is necessary because a full-factorial combination of variable values usually results in an intractable number of data points to be analyzed for regression. The DoE intelligently selects a smaller number of data points that still span the entirety of the design space. A Latin-Hypercube design was used to generate the regression data for this research [76]. Each point in the DoE consists of a panel loading condition, panel buckling spans, and a combination of physical dimensions for the skin and stiffener.

The next step is to evaluate each point in the DoE to determine if the design passes the failure criteria. Additionally, the smeared panel stiffness terms are determined in this step (ABD terms). Both parts of this step were performed in HyperSizer.

The final step is to perform regression of the failure criteria against the stiffness terms calculated in the previous step. The regression uses the output results of failure criteria and stiffnesses evaluated in the previous step. Regression was performed in JMP, a statistical analysis software package [104]. The form of the resulting RSE is described in detail below.

3.3.4.3 Type of Regression Selected

All previous RSE -based approaches found in literature (outlined in Section 2.7) perform ordinary least-squares regression on either the Margin of Safety MS or Factor of Safety FS for the failure criteria ($MS = FS - 1$). The primary problem with using either of these metrics as the dependent variable is the fact that their numerical value is unbalanced in expressing whether the panel passes or fails. For example, MS ranges from -1 to 0 for

failed panels and from 0 to ∞ for panels that pass the failure criteria. An example of the imbalance is shown in Figure 54. This imbalance can be challenging to handle with simple low-order polynomials.

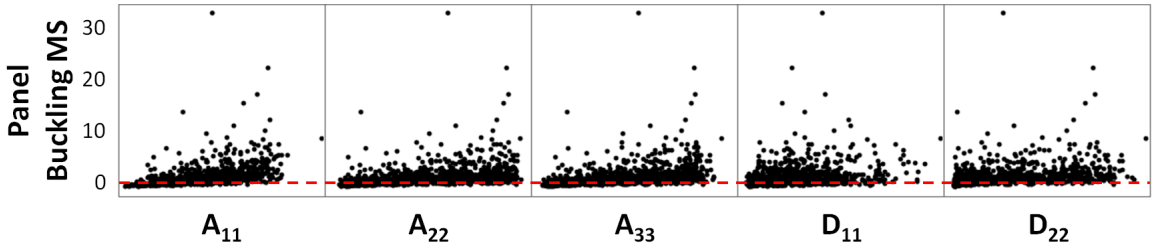

Figure 54: Variation of Panel Buckling MS versus ABD Stiffness Terms

The approach used in this research is to employ logistic regression for the RSEs [76]. Logistic regression is often used when the dependent variable is binary (only two possible responses). In the present research, the binary dependent variable of the RSEs is "pass" or "fail" for a particular failure criteria grouping. This binary response is designated with a value of 1 for panels that pass the failure criteria and a 0 for panels that do not pass. This is acceptable because the actual value of the MS or FS is not relevant for the optimization, only whether the panel is predicted to pass or fail. The challenge with fitting a RSE to a binary response is that many functions used for regression are continuous by nature, and will not necessarily return a value between 0 and 1. This is addressed in the next section with the development of the logistic regression equations.

To show the advantage of logistic pass/fail RSEs over MS RSEs, a small test was performed by generating MS RSEs to represent failure criteria for a panel loaded in compression in the x and y direction. The regression process was very similar to the one described previously in Section 3.3.4.2. The accuracy of the resulting MS RSEs was compared to the logistic pass/fail RSEs, using results from the validation described later in Section 4.1. The comparison is given in Table 8. From these results, the logistic pass/fail RSE has an advantage in accuracy ranging from 5-12%. Although this is a somewhat small improvement in accuracy, the same amount of effort is needed regardless of the dependent variable in the regression (MS or pass/fail). Thus, the logistic regression was selected for this research.

Table 8: Comparison of RSE Accuracy for MS Regression and Logistic Pass/Fail Regression

Failure Criteria	MS Accuracy	Logistic Accuracy
Panel Buckling	85.2%	91.2%
Crippling	86.4%	92.9%
Facesheet Local Buckling	82.3%	94.1%
Facesheet Material Failure	91.6%	96.5%
Spacing Span Local Buckling	87.2%	92.9%

3.3.4.4 Form of Regression Equations

The majority of references that use RSEs for panel optimization use a 2nd order polynomial form (see Table 2). However, these references provide little to no justification for the RSE function selected. Presumably, several were attempted, and the 2nd order polynomial was found to be the best compromise between accuracy and complexity. Increasing the order of an RSE polynomial usually increases accuracy up to a certain point, but requires more data points to perform the regression. As an example, an RSE of one variable requires two points for a linear fit, three points for a 2nd order fit, and so on. However, there are also dangers in using too high of an order RSE, referred to as "over-fitting." This occurs when the RSE begins to capture noise in the fitting data, rather than representing just the general trend of the response. These challenges were considered in the selection of the RSE form discussed below.

As discussed in the previous section, logistic regression was selected for this research to provide a prediction of a binary response. Equation 34 below provides the final prediction of whether the panel passes or fails.

$$P(1) = \frac{1}{1 + e^{\phi}} \tag{34}$$

Equation 34 provides a conversion between the continuous prediction metric, ϕ, and the binary response. In Equation 34 above, the probability of obtaining a value of "1" is predicted by $P(1)$. If ϕ has a value less than zero, $P(1)$ has a continuous value between 0.5 and 1.0, predicting that the panel will pass. When used in an optimization context, it is usually more simple to use ϕ as a constraint instead of ϕ and $P(1)$ together. Thus, Equation 34 is used in regression, but not in optimization. To apply the RSE to optimization, it is

only necessary to specify $\phi \leq 0$ as a constraint to ensure the failure criteria are satisfied.

The parameter ϕ is represented with a polynomial form (Equation 35) similar to those used by many regression techniques. The integer n represents the total number of stiffness terms used as design variables in the RSE. The integer c represents the number of constants in the RSE, which is five in this study; three load terms (N_x , N_y , N_{xy}) and two panel buckling span terms (a and b). The vector $[C]$ shown in Equation 36 represents these constants. The terms β and κ are regression coefficients that are determined when the logistic regression is performed.

$$\phi = \sum_{j=0}^{c}\sum_{k=j}^{c}\sum_{l=k}^{c}\beta_{jkl}[C]_j[C]_k[C]_l + \sum_{i=1}^{n}\sum_{j=0}^{c}\sum_{k=j}^{c}\kappa_{ijk}[ABD]_i[C]_j[C]_k \tag{35}$$

$$[C] = \begin{bmatrix} N_x \\ N_y \\ N_{xy} \\ a \\ b \end{bmatrix} \tag{36}$$

3.3.4.5 Reducing Number of Terms in RSEs

The drawback of the RSE form presented in Equation 35 above is that it results in a significant number of terms. With a total of 160 possible terms, the RSE can be prone to the "over-fitting" issue discussed previously. Having too many terms can cause the RSE to fit to noise in the regression data instead of just the primary trend of the data. To alleviate this issue, a reduction in terms was performed for each RSE within the regression. The term reduction was performed with the following steps. This term reduction was found to provide a 5-10% improvement in RSE accuracy.

1. An initial regression was performed with all 160 possible terms from Equation 35.

2. For each term in this initial regression, the statistical "Student's t-test" [105] is performed to determine its significance to the failure criteria. The Student's t-test defines this significance quantitatively as the probability that the regression term is zero (also

known as p-value). A low p-value indicates that the regression term is statistically relevant to the failure criteria.

3. Any terms with a p-value greater than 0.05 are dropped from the RSE. The final RSEs have between 6 and 42 terms.

Another metric that is useful for understanding the statistical significance of terms in the RSE is the t-ratio. This metric is the ratio of the regression coefficient for a given term to the standard error calculated for that coefficient. In short, this metric gives the significance of the term normalized by the error it induces. A higher t-ratio indicates the term is more relevant to the RSE [106]. The tables given in Appendix B list both the p-values and t-ratios for the panel buckling failure criteria for the I-Stiffened panel as example results.

Additionally, it is informative to plot the t-ratio to gain an understanding of the relative contribution of each term to the response (failure criteria). Figure 55 provides a plot of t-ratio for all 160 terms of the failure criteria mentioned above. Note that only the relative magnitudes of the t-ratios are significant, which is why the magnitude of the values in the plot are not given. The green box in this Figure 55 indicates the reduced set of 41 terms for the RSE. This figure demonstrates that the final set of terms selected for the failure criteria RSE are the primary contributors to accurate prediction of the criteria. The dropped terms have a relatively small contribution to the result and therefore can be neglected to simplify the RSE.

3.3.4.6 Final Form of Failure Criteria RSEs

After the term reduction has been performed on the RSEs, they are ready to be used in an optimization. For each panel optimization, the constants from $[C]$ given in Equation 36 are substituted into the RSE as a pre-processing step before the optimization. The resulting form of ϕ used in the optimization is shown in Equation 37. The constant terms K_0 and $[K]$ represents the second term from Equation 35 after the constants $[C]$ have been substituted in and regrouped with the regression coefficients. Note that all of the nonlinear terms from Equation 35 disappear because they are all related to panel constants and thus are not

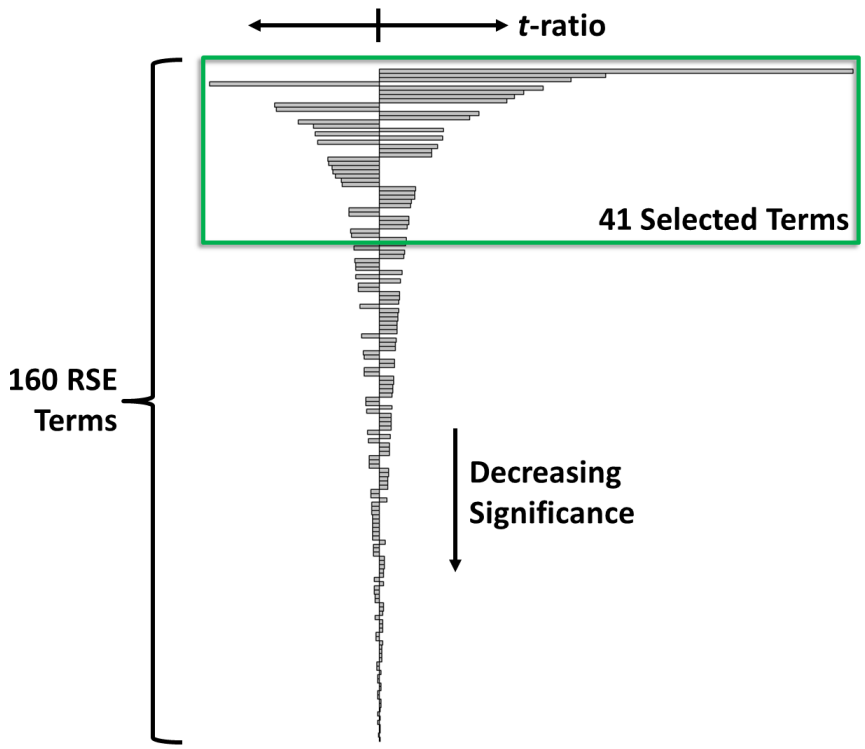

Figure 55: Relative t-Ratio Values for all Terms in Panel Buckling RSE

varied during optimization.

$$\phi = K_0 + \sum_{i=1}^{n} [K]_i [ABD]_i \tag{37}$$

Looking at the form of Equation 37, it is evident that the equation is linear as a function of the ABD stiffness terms after the constant loads and spans have been substituted. Note that the original form of the RSE in Equation 35 contains nonlinear terms. However, these terms are constants and are substituted in before the optimization is performed. Figure 56 shows an example stiffness-based design space for a stiffened panel after loads and buckling spans have been substituted. The RSEs form a linear boundary between the feasible and infeasible space.

The described approach used for these RSEs can be thought of as a local linear approximation. The nonlinear constant terms in Equation 35 give a high level of accuracy in predicting the pass/fail performance (see Chapter 4). A notional representation of the failure criteria RSEs is given in Figure 57. This figure illustrates that the failure criteria metric ϕ is linear with respect to the stiffness term A_{11} and nonlinear with respect to N_x.

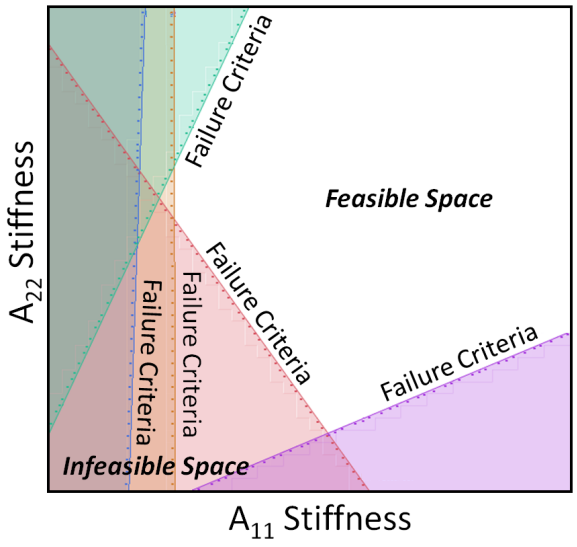

Figure 56: Notional Design Space with Linear Constraints

Similar trends exist for the remaining ABD and load terms.

Once generated, the inherent simplicity of the RSE form makes it much easier to evaluate structural integrity than many deterministic analysis tools. This is particularly true in the case of buckling, where many tools use FEA-based methods to evaluate the performance of the panel [81], [82], [70]. Replacing these analyses with a polynomial RSE simplifies the analysis and allows for more panel designs to be processed. The driver for using a linear form is that it allows Linear Programming (LPg) algorithms to be used to solve for the optimum panel-level design [107], which typically execute very quickly compared to non-linear environments. Solutions for LPg problems on the scale of those used in this study can be found 240 times faster than a comparable optimization in the non-linear physical domain, as demonstrated in the next chapter. In addition to this speed increase, it is mathematically guaranteed that the global optimum point will be found in a LPg solution because a linear design space is not capable of having local optima [107].

3.3.5 Linearization of Objective Function

In addition to the failure criteria, it is also necessary to map the objective function (panel mass) to the stiffness domain and linearize. For stiffened panel design, it is more common to use the unit mass (UM) of the panel instead of mass (m) by itself. This provides a

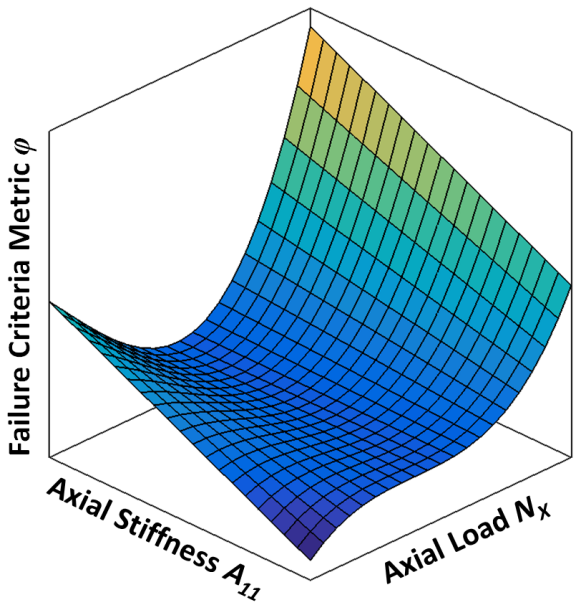

Figure 57: Mixed Linearity in Failure Criteria RSEs

better representation of the mass efficiency of the panel. Unit mass is simply the mass of the panel divided by panel area ($a \cdot b$). In the physical domain, the unit mass is described by Equation 38.

$$UM = A_{panel} \cdot \rho = (T_{sk} \cdot S + T_{ft} \cdot W_{ft} + T_{fg} \cdot W_{fg} + T_{wb} \cdot (H - T_{sk} - T_{ft} - T_{fg})) \cdot \rho \quad (38)$$

Because density and stiffness have a fixed relationship for metallics, it is straight-forward to map the equation for UM into the stiffness domain. The linear form of unit mass for metallic I-stiffened panels as a function of stiffness is given in Equation 39 of Section 3.5.2.

In a composite stiffened panel, variation in ply angles cause stiffness of the panel to vary while density of the material remains unchanged. Thus, a closed-form expression for unit mass is more difficult to obtain. This challenge is addressed in Chapter 5 when composite panels are addressed.

3.4 Boundaries for Domain Mapping

With the transformed and linearized failure criteria from the previous sections, the reformulated design space is nearly prepared for optimization. The last step needed to complete the reformulation is to enforce boundaries on the design variables. In the physical domain,

this is easily done by imposing minimum and maximum bounds on the design variables. These bounds are usually selected based on the general magnitude of load in the stiffened panel, to ensure that the bounds include a feasible design. In addition to upper and lower bounds, some other limitations exist on the range of allowed values to enforce physically realizable panel cross-sections. For example, the height of the panel can not be less than the combined thickness of the skin, stiffener foot, and stiffener flange.

Imposing bounds on the stiffness domain is challenging because the uniform bounds of the physical domain map to non-uniform bounds in the stiffness domain. This results in many combinations of stiffness terms for which there are no corresponding feasible designs in the physical domain. To address this problem, constraints were generated to ensure that the combinations of stiffness terms selected by an optimizer can be transformed back to the physical domain. Figure 58 depicts an example of the added constraints.

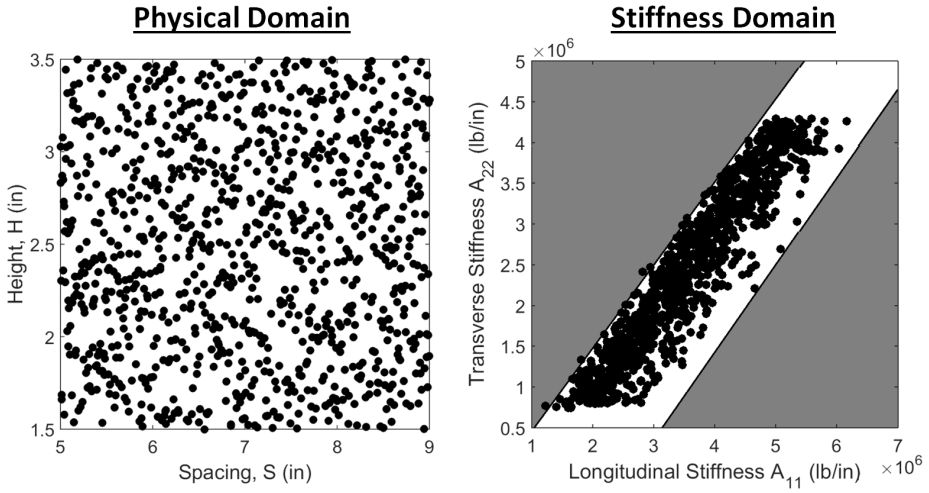

Figure 58: Added Bounds for Feasible Domain Mapping

The plot on the left side of Figure 58 displays two dimensions of the physical domain, stiffener spacing and panel height. These two variables are entirely uncoupled, so any combination of the two will result in a physically feasible panel. The points in the plot on the left are randomly-generated designs in the physical domain. The plot on the right shows the exact same designs mapped to the stiffness domain. From the points in the plot on the right, it is evident that the two stiffness terms A_{11} and A_{22} are coupled. Thus,

constraints are needed to enforce the boundaries in the stiffness domain, represented by the grayed-out portions of the plot on the right. These kinds of constraints must be generated for every possible pairing of stiffness terms used in the reformulated design space. These boundaries are created manually with the goal of minimizing outliers while also capturing the general shape of the stiffness domain border. The remainder of the domain constraints for the metallic I-stiffened panel are given in Appendix D.

Note that in addition to the constraints described above, typical minimum and maximum bounds are also applied to the stiffness domain. These are based on the minimum and maximum value of each ABD term found in the DoE used to generate the failure criteria RSEs.

3.5 Application to Metallic I-Stiffened Panel

This section presents the application of concepts discussed previously in Sections 3.3 and 3.4 to a metallic I-stiffened panel. The metallic I-stiffened panel is a central part of the demonstration for the present methodology. The previous sections set up the methodology and this section provides the details of applying the methodology to the metallic I-stiffened panel to produce a stiffness-based panel design space.

As a starting point, it is necessary to describe the metallic I-stiffened panel in the physical domain. The panel uses Aluminum 7075-T7451, a common aerospace construction material. The properties of this material are listed in Table 9.

Table 9: Properties of Aluminum 7075-T7451

Density	Stiffness					Strength			
ρ	E_t	E_c	G	ν_t	ν_c	$F_{t,u}$	$F_{t,y}$	$F_{c,y}$	$F_{s,u}$
(lb/in^3)	(Msi)	(Msi)	(Msi)			(ksi)	(ksi)	(ksi)	(ksi)
0.102	10.3	10.6	3.9	0.321	0.359	74	64	62	44

Along with material selection, the geometry variable bounds form the basis of the physical domain for the panel. The maximum values for the ranges on geometry were selected such that heaviest possible design will survive the most severe loads applied to the panel (loads from Section 3.3.3). The minimum values are based on minimum gauge (commonly 0.06" for Aluminum in aerospace structures) and on values found in structures that use a

metallic I-stiffened panel. Figure 59 displays all of the panel geometry variables considered, and Table 10 lists the ranges of these values.

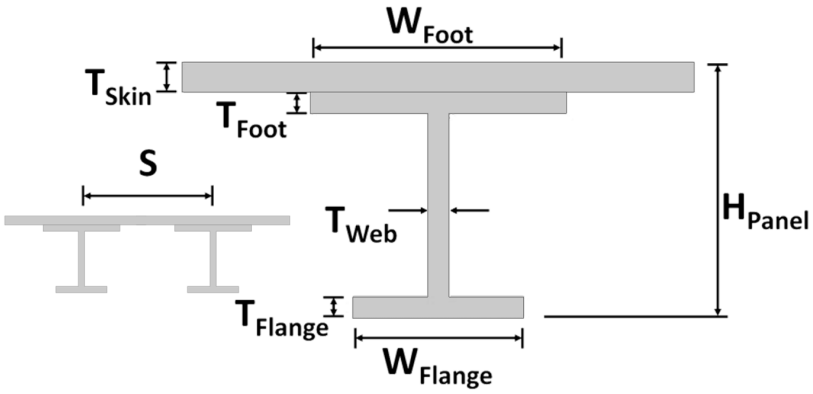

Figure 59: Physical Variables for the Stiffened Panel

Table 10: Physical Variable Bounds for the I-Stiffened Panel

	T_{skin}	T_{web}	T_{foot}	T_{flange}	H_{panel}	S	W_{foot}	W_{flange}
Min	0.06	0.06	0.06	0.06	1.5	5	1	1
Max	0.35	0.25	0.25	0.25	3.5	9	2.25	2

With the physical domain established, the linearization methodology can now be applied to create the stiffness domain. First, the stiffness-based RSEs are developed for the panel, followed by the stiffness-based objective function, and then the boundaries on the stiffness-based design space.

3.5.1 Stiffness-Based RSEs for Failure Criteria

Following the process described in Section 3.3.4, RSEs were generated for the metallic I-stiffened panel failure criteria across the four load quadrants (given previously in Section 3.3.3). Six different groups of failure criteria were considered for the panel. Not all of the eleven failure criteria groups discussed in Section 3.3.2 were needed because some were not significant within the load range considered. Groups with fewer than 10% failed designs in the regression DoE were neglected.

Of the six groups of failure criteria considered, some were not applicable in all four load quadrants. For example, the panel buckling failure criteria group is not needed for the load

quadrant with tension only loading ($+N_x, +N_y$). Additionally, note that local buckling appears in all of the load quadrants because a shear load is considered in all cases, which can cause shear buckling.

Table 11 lists the number of terms in each RSE, indicating which failure criteria are relevant for the various load quadrants. The process of achieving the reduced set of terms was described previously in Section 3.3.4.5. The final form of the failure criteria RSEs (with reduced terms) for the metallic I-stiffened panel are listed in Appendix C.

Table 11: Number of Terms in RSEs for Metallic I-Stiffened Panel Failure Criteria

Failure Criteria Group	$+N_x/+N_y$	$+N_x/\text{-}N_y$	$\text{-}N_x/\text{-}N_y$	$\text{-}N_x/+N_y$
Panel Buckling	-	41	52	53
Crippling	-	-	50	30
Facesheet: Local Buckling	52	40	11	27
Facesheet: Material Failure	51	32	49	48
Bonded Combo: Material Failure	49	12	-	39
Spacing Span: Local Buckling	62	9	34	39

3.5.2 Stiffness-Based Objective Function

As described in Section 3.3.5, the objective function (panel mass) must be transformed to stiffness terms and linearized. Similar to the linearized failure criteria, a linear representation of the panel mass as a function of the panel stiffness terms can be determined through regression. The expression for unit mass (UM) of the metallic I-stiffened panel is given in Equation 39 as a function of longitudinal membrane stiffness (A_{11}) and lateral membrane stiffness (A_{22}). The coefficients in Equation 39 were determined by regression, using the same data set generated for the failure criteria RSEs. Because A_{11} and A_{22} are directly related to the volume of the panel, Equation 39 provides a highly accurate prediction of panel mass.

$$UM = 1.4056 \cdot 10^{-6} \cdot A_{11} - 1.6329 \cdot 10^{-7} \cdot A_{22} \tag{39}$$

The simple form of the objective function in Equation 39 is conducive to generating a contour plot for visualization, shown in Figure 60. From the contour plot given in Figure 60, it is evident that A_{11} has a more significant effect on UM than A_{22}. This reflects the

sensitivities observed in Figure 47 in Section 3.2.2.

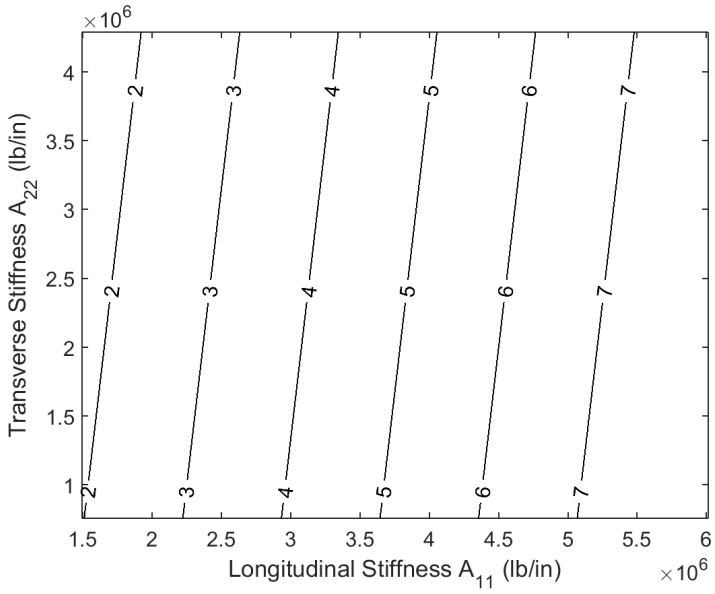

Figure 60: Contour Plot of Unit Mass (lbm/ft^2) with Respect to Membrane Stiffness

Note that as shown in Equation 39 and Figure 60, A_{22} has a negative influence on the UM of the panel. At first glance, this is counter-intuitive because an *increase* in stiffness would not be expected with a *decrease* in mass for an isotropic material. Additionally, it is counter-intuitive that the A_{22} term appears in the UM equation at all. For a more simple representation such as $E \cdot A$ (modulus time cross-section area), only the axial term would be needed to develop a linear relationship with mass.

Both phenomena described above can be attributed to the fact that the ABD representation of the panel includes the Poisson relationship between axial and lateral stiffness (described in Section 3.2.3). Thus, the A_{11} and A_{22} stiffness terms are not directly proportional to cross-sectional area. The Poisson effect causes an interaction between the two stiffness terms, requiring both of them to be used to describe UM.

3.5.3 Stiffness-Based Design Space Boundaries

The first part of establishing boundaries on the stiffness-based design space is to determine the minimum and maximum values allowed for the stiffness terms. These are determined by the minimum and maximum ABD values calculated in the regression data described in

Section 3.3.4.2. The bounds for the metallic I-stiffened panel are given in Table 12 for the five stiffness terms used for this panel.

Table 12: Stiffness Variable Bounds for the Metallic I-Stiffened Panel

	A_{11} (lb/in)	A_{22} (lb/in)	A_{33} (lb-in^2/in)	D_{11} (lb-in^2/in)	D_{22} (lb-in^2/in)
Minimum	1494722	754917	268803	508657	270
Maximum	6012890	4289118	1521905	11310030	53026

The second part of establishing boundaries on the stiffness domain is to generate the restrictions on stiffness term interaction as described previously in Section 3.4. These boundaries were generated for all ten possible pairings of the five ABD terms used for the metallic I-stiffened panel, excluding those pairings which did not exhibit any interaction between variables. An example of the boundaries generated for A_{11} and A_{22} are given in Figure 61. The remainder of the boundary plots are given in Appendix D. The gray areas indicate combinations of the two stiffness terms that are not permitted during optimization. Note that the min and max bounds from Table 12 are not shown on the plots.

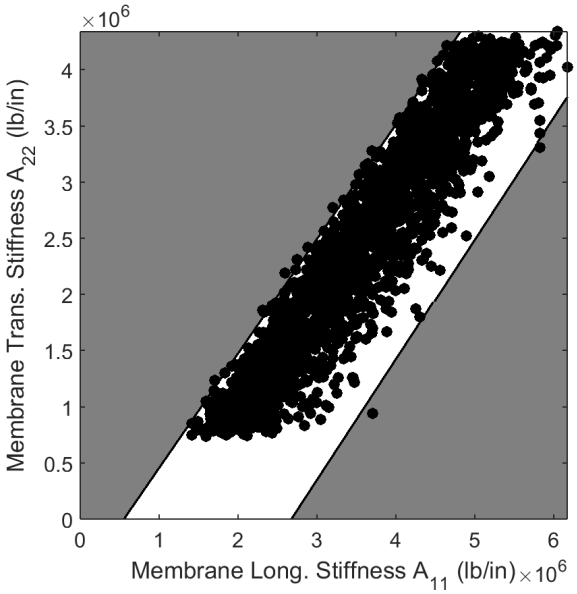

Figure 61: Bounds on Stiffness Domain for A_{22} versus A_{11}

The constraint equations that establish the variable interaction bounds are represented as linear equalities. Equations 40 and 41 correspond to left and right boundaries in Figure

61, respectively. The remainder of the constraint equations are listed in Appendix D.

$$A_{22} - 1.0196 \cdot A_{11} + 5.6440 \cdot 10^5 \leq 0 \tag{40}$$

$$A_{11} \cdot 1.0754 - A_{22} - 2.8766 \cdot 10^6 \leq 0 \tag{41}$$

3.6 Stiffness-Based Local Optimization

The previous sections in this chapter provided the details of how a panel optimization environment is reformulated to be a function of stiffness terms instead of physical dimensions. This section will discuss how optimization is performed in the new stiffness-based domain. The general statement of the optimization performed for the stiffened panel is given in Equation 42. The objective is to find a design vector $\vec{x}$ (A_{11},A_{22},A_{33},D_{11},D_{22}) which minimizes unit mass UM while meeting the constraints imposed on the panel: satisfy failure criteria RSEs ($\phi \leq 0$), satisfy required stiffness values $\vec{x}_{i,req}$, and remain within bounds $\vec{x}_{min}$ and $\vec{x}_{max}$.

$$\vec{x} \text{ for min } UM = f(A_{11}, A_{22}, A_{33}, D_{11}, D_{22}) \text{ s.t. } \begin{cases} \phi(A_{11}, A_{22}, A_{33}, D_{11}, D_{22}) \leq 0 \\ \vec{x}_i = \vec{x}_{i,req} \\ \vec{x}_{min} \leq \vec{x} \leq \vec{x}_{max} \end{cases} \tag{42}$$

The following subsections will discuss how the stiffness-based optimization described above is executed using the Simplex Algorithm. First, a comparison is made to traditional local optimization in the physical domain to identify the primary differences.

3.6.1 Comparison to Physical Domain

Local optimization of the stiffened panel was presented previously in Figure 20 of Section 2.5. Here, the traditional approach for panel optimization in the physical domain was outlined. The left side of Figure 62 shows the original local optimization outlined in this approach.

Reformulation of the stiffened panel design space fundamentally changes how the local optimization proceeds. The right side of Figure 62 shows the local optimization iteration loop after implementation of the Simplex Algorithm. Compared to the traditional local

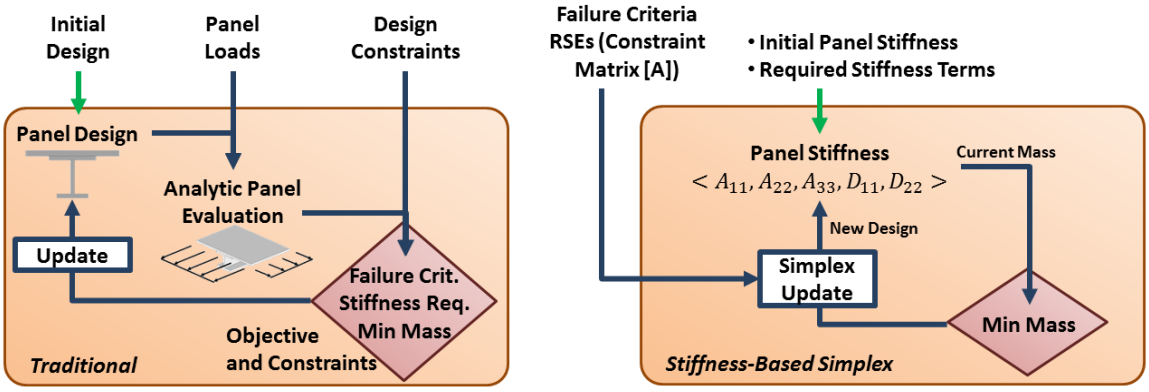

Figure 62: Comparison of Local Optimization in Physical and Stiffness Domain

optimization, the stiffness-based optimization is simpler. The subsections below summarize where and how elements of the optimization in the traditional physical domain appear in the stiffness-based optimization. The elements from the traditional optimization listed below correspond to those shown in the left side of Figure 62.

3.6.1.1 Initial Design

In the physical domain, the initial design is a set of panel dimensions describing the geometry. In the stiffness domain, the initial design is a set of stiffness terms for the panel.

3.6.1.2 Panel Loads

These are not input directly to the stiffness-based optimization as was done in the physical domain. Instead, they are built into the linear failure criteria RSEs and ultimately become a part of the linear constraints for the Simplex Algorithm. This process is described in detail in Section 3.6.2.1.

3.6.1.3 Design Constraints

Input failure criteria from the physical domain also appear in the linear RSEs in the stiffness domain, as was the case with the panel loads. Required stiffness terms, however, are simply input as a part of the initial panel stiffness and are kept fixed throughout the optimization. This is a significant difference from the physical domain, where required stiffness terms must be treated as a constraint in every iteration. As such, the stiffness-based optimization

has an advantage because application of required stiffness reduces the number of terms to optimize. This is discussed in detail in Section 3.6.2.2.

3.6.1.4 Panel Design

In the physical domain, the panel design consists of panel dimensions; in the stiffness domain, the panel design consists of stiffness terms.

3.6.1.5 Analytic Panel Evaluation

The calculation of the internal panel stress and critical buckling loads that occurs in the physical domain does not appear directly in the stiffness domain. Instead, this is contained within the linear failure criteria RSEs as described previously in Section 3.3.

3.6.1.6 Evaluation of Objective and Constraints

In the physical domain, the mass of each panel design must be evaluated along with all of the failure criteria and stiffness requirements to determine the next needed step in the optimization. In the stiffness domain, it is only necessary to evaluate panel mass because the constraints are satisfied in each step of the optimization (after initialization); this is a property of the Simplex Algorithm, as described in Section 3.6.2.4.

3.6.1.7 Design Update

A design update is necessary in both optimization environments to iterate towards the optimum solution. In the physical domain, the design update depends on the optimization algorithm used. In the stiffness domain, the update is dictated by the Simplex Algorithm. The Simplex Algorithm always steps between vertices in the design space that are formed by the linear constraints, and always in the direction of minimum mass. Iteration with the Simplex Algorithm is described in detail in Section 3.6.2.4.

3.6.1.8 Summary

Overall, optimization in the stiffness domain functions very differently than optimization in the physical domain. However, all of the core parts of the optimization exist in both domains. The following sections provide detailed descriptions of features that are unique

to the stiffness-based optimization, such as the constraint matrix needed in the Simplex Algorithm.

3.6.2 Linear Programming Solution

The primary benefit of linearizing the design space is that a new category of optimization algorithms are available, usually referred to as Linear Programming (LPg) algorithms. The Simplex Algorithm was selected because it is one of the most widely-used and widely-available LPg algorithms [107]. The MathWorks MATLAB implementation of the Simplex Algorithm was used in this research [108]. This algorithm is popular due to its standardized and deterministic solution method. The Simplex Algorithm can optimize a linear design space very quickly; run time with five variables is on the order of 1/10th of a second on a personal computer including pre-processing of the constraints.

The most important part of the Simplex Algorithm is the constraint matrix, which forms the vertices in the design space needed for iteration. Development of the constraint matrix for stiffness-based panel optimization is described below.

3.6.2.1 Generation of Simplex Constraint Matrix

The primary input to the Simplex Algorithm is a matrix of all the constraints imposed on the optimization problem. The constraints can easily be converted to matrix form because they are all linear. Equation 43 gives the basic form of the constraint matrix. The matrix $[A]$ contains the variable coefficients, $\vec{x}$ is the vector of design variables, and $\vec{b}$ is the vector of intercepts for the constraints.

$$[A]\vec{x} \leq \vec{b} \tag{43}$$

For the optimization considered in this research, the constraint matrix consists of three main parts. Construction of the constraint matrix is shown in Figure 63. The first part contains the RSEs that represent the panel failure criteria. The RSEs are converted to matrix form by first substituting the panel constants (loads and buckling spans) for the panel to be optimized. This gives the RSEs a linear form, allowing the failure criteria constraint of $\phi \leq 0$ to be represented as $[A]\vec{x} \leq \vec{b}$. The second part of the constraint matrix is the variable interaction bounds presented previously in Section 3.5.3. In Figure 63, an

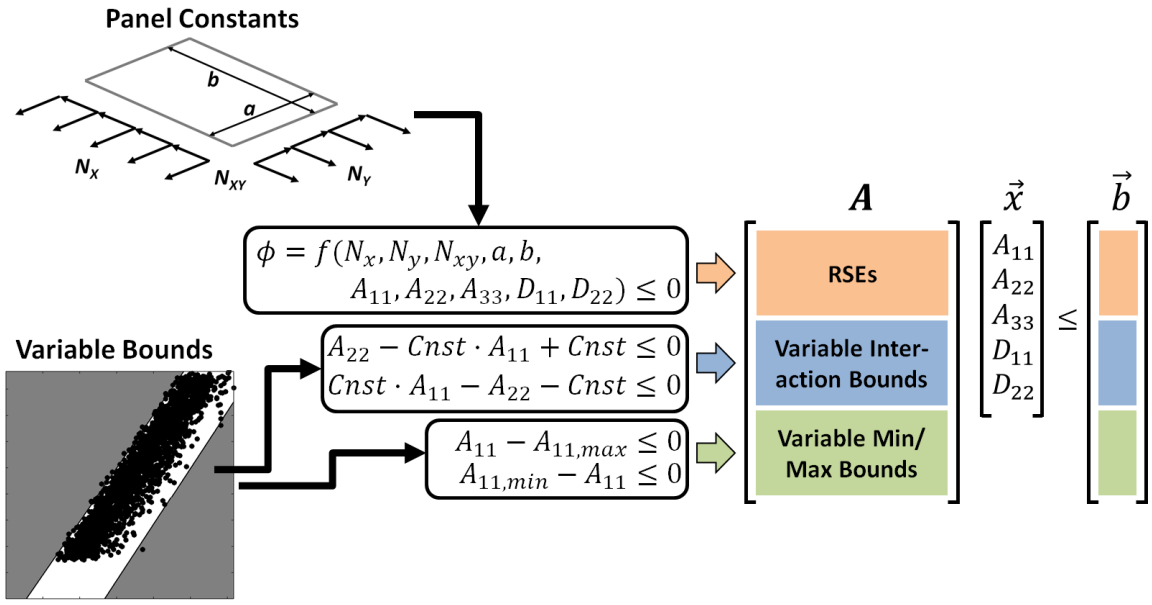

Figure 63: Generation of Constraint Matrix for Simplex Algorithm

example of these constraints is shown for the A_{11} vs A_{22} interaction. These bounds are already represented as linear inequalities, making them easy to represent in $[A]\vec{x} \leq \vec{b}$ form. The third part of the constraint matrix is generated similarly; the min and max bounds can be represented by inequalities as shown in Figure 63 for the A_{11} bounds.

Note that the first part of the constraint matrix $[A]$, failure criteria RSEs (highlighted in orange in Figure 63), is different for every panel optimization. This is because the panel loads and buckling spans are usually unique for each panel. The last two parts of the constraint matrix (highlighted in blue and green in Figure 63) remain fixed as long as the geometry bounds do not change.

3.6.2.2 Handling Stiffness Requirements in Simplex Optimization

As indicated previously in Section 3.6.1, any imposed stiffness constraints can be substituted directly into every design point because the design variables themselves are stiffness terms. This occurs in the constraint matrix generation depicted in Figure 63. The value of the required stiffness is substituted into the equations when they are put in matrix form. This has the impact of shrinking the width of the $[A]$ and length of $\vec{x}$ by the number of stiffness terms substituted. Equation 44 shows how the constraint matrix is rearranged when a

constraint on A_{11} stiffness is imposed. Terms a_{ij} represent entries in the $[A]$ matrix and terms b_i represent entries in $\vec{b}$ from the Simplex constraint. The integer m represents the total number of Simplex constraints. The rearranging shown in Equation 44 demonstrates the assertion made earlier that imposing stiffness constraints reduces the dimensionality of the stiffness-based design space.

$$\begin{bmatrix} a_{12} & a_{13} & a_{14} & a_{15} \\ a_{22} & a_{23} & a_{24} & a_{25} \\ \vdots & & & \vdots \\ a_{m2} & a_{m3} & a_{m4} & a_{m5} \end{bmatrix} \begin{bmatrix} A_{22} \\ A_{33} \\ D_{11} \\ D_{22} \end{bmatrix} \leq \begin{bmatrix} b_1 - a_{11} \cdot A_{11,req} \\ b_2 - a_{21} \cdot A_{11,req} \\ \vdots \\ b_m - a_{m1} \cdot A_{11,req} \end{bmatrix} \tag{44}$$

3.6.2.3 Form of Objective Function for Simplex Algorithm

The final part of the input to the Simplex Algorithm is a vector of coefficients of the objective function. These simply come from re-writing the objective function in the vector form $UM = f(\vec{x})$. An example using the unit mass expression for the metallic panel is given in Equation 45. Note that any constant terms in the objective function are dropped because only the gradient of the objective function is relevant in the Simplex Algorithm.

$$UM = 1.4056 \cdot 10^{-6} \cdot A_{11} - 1.6329 \cdot 10^{-7} \cdot A_{22} \tag{45a}$$

$$UM = \begin{bmatrix} 1.4056 \cdot 10^{-6} & -1.6329 \cdot 10^{-7} & 0 & 0 & 0 \end{bmatrix} \begin{bmatrix} A_{11} \\ A_{22} \\ A_{33} \\ D_{11} \\ D_{22} \end{bmatrix} \tag{45b}$$

3.6.2.4 Final Form of Optimization and Iteration Procedure

Drawing on the constraint and objective functions given above, the resulting form of the optimization statement for the Simplex Algorithm is given in Equation 46 and 47.

$$\vec{x} \text{ for min } f(\vec{x}) \text{ s.t. } \{[A]\vec{x} \geq \vec{b} \tag{46}$$

$$\vec{x} =< A_{11}, A_{22}, A_{33}, D_{11}, D_{22} > \tag{47}$$

The Simplex Algorithm optimizes by pivoting across vertices formed by the linear constraints. The location of each step the algorithm takes is defined by the intersection of constraints from the constraint matrix above. The number of constraints that form each vertex is equal to the dimensionality of the design space (number of variables). As an example, a vertex in a 2D design space is formed by the intersection of two lines. There are five variables in the metallic panel design space so five constraints are needed to form a vertex.

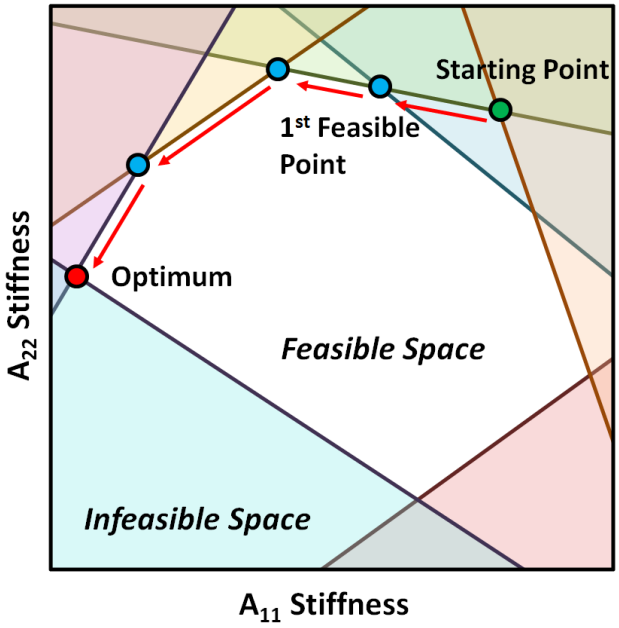

Figure 64: Iteration Process for Simplex Algorithm

Iteration in the Simplex Algorithm starts with finding a feasible design point (Figure 64). In a linear design space with many more constraints than design variables, there will be many constraint vertices which violate other constraints. The Simplex Algorithm is initialized with a random vertex; if this vertex is infeasible, the algorithm iterates until a feasible vertex is found. Once a feasible vertex is found, the Simplex algorithm begins stepping through adjacent vertices, always moving in the direction of lower mass. Note that each step between vertices corresponds to a complete loop of the flow chart on the right side of Figure 62. Once a vertex is found where no further improvement in mass is available, the

algorithm has converged. Note that in a linear design space, there is only a global optimum and no local optimum.

This completes the description of the stiffness-based optimization used in this research. As described above, the process is only able to handle one load case in the optimization. This is acceptable for the current research because the provided examples only use one load case for demonstration purposes. The next section discusses an extension of the above methodology to handle multiple load cases.

3.6.3 Optimizing with Multiple Load Cases

The current research performs panel optimization with only a single load case (combination of N_x , N_y , N_{xy}). However, as many as ten load cases are often considered in the conceptual design phase for structures. The easiest and most rudimentary approach to handling multiple load cases would be to simply optimize the panel for each load case, one at a time, and then take the result from the most conservative (heaviest) load case. However, this process has the possibility of selecting a panel design that can potentially fail with respect to other load cases.

For example, consider two load cases: one with only high axial compression (N_x) and another with only some lateral compression (N_y). The high N_x load case would result in a higher panel mass than the low N_y case. However, the panel design produced by the high N_x load case would be tall and slender to maximize D_{11} bending stiffness and resist panel buckling. The D_{22} bending stiffness for this design would be low, and even a small amount of compressive N_y would cause the skin between the stiffeners to buckle. This means the design that is optimum for the first load case is actually infeasible for the second load case.

Thus, it is necessary to be able to extend the methodology presented in this research to properly handle multiple load cases by simultaneously optimizing to all of them. This can be achieved by reusing the failure criteria RSEs for each unique load case and imposing them as additional constraints on the design space. For example, if there were 10 load cases and 6 failure criteria RSEs, a total of 60 constraints would be added to the Simplex constraint matrix (described in the previous section) to cover the failure criteria. This is

illustrated in Figure 65.

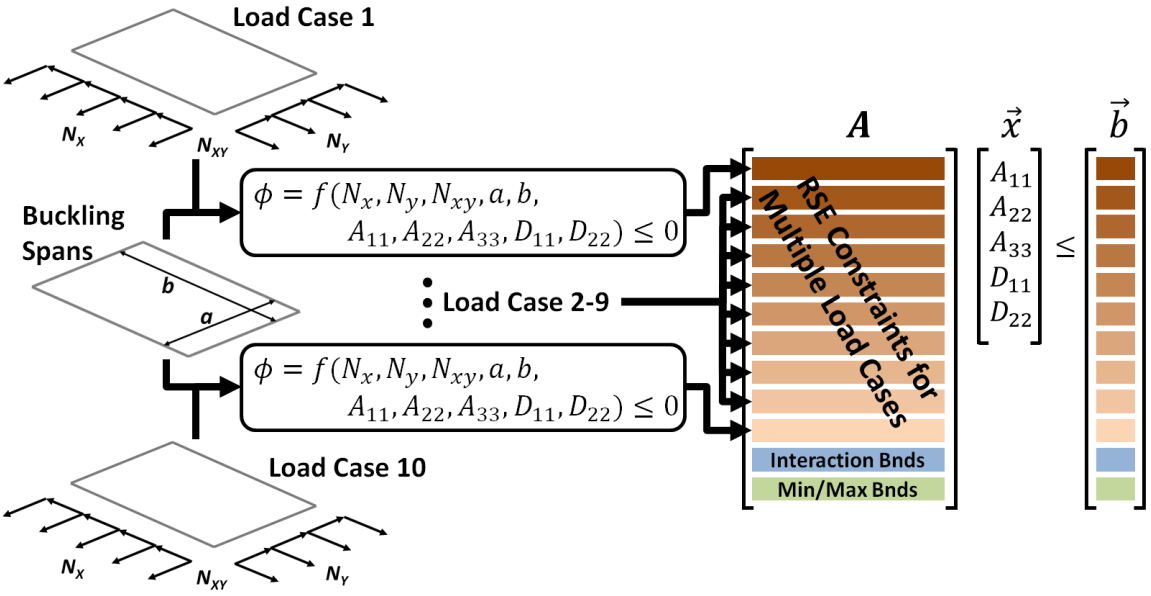

Figure 65: Representing Multiple Load Cases as Additional Constraints in Simplex Matrix Form

The challenge of including many load cases is that the complexity of the design space will grow quickly because there will be many more vertices. Even though the Simplex Algorithm is very efficient, it is not impervious to an intractably large design space. With 60 failure criteria constraints, the total number of constraints for the example given in the previous section rises to 84. The total number of vertices is determined by $\binom{84}{5}$, which is 3.087e7. Thus, the design space is 217 times larger from increasing the number of constraints by a factor of 2.8.

To avoid a severe penalty to solution time, it is necessary to develop an approach to reduce the number of constraints imposed by multiple load cases. Fortunately, redundant constraints are easy to identify and eliminate in a linear design space. The left side of Figure 66 shows an example of a redundant constraint that can be eliminated.

The elimination process performs a pairwise evaluation for redundant constraints by considering every possible pairing of the failure criteria RSEs. This determines which constraints are superseded by other constraints and can be eliminated. The process is outlined in the steps below.

1. For each load case, substitute loads and buckling spans into failure criteria RSEs to generate the linear constraint equations (as previously shown in Figure 63).

2. Select a pair of failure criteria constraints to compare.

3. Of the two criteria, select one "active" criteria to be evaluated.

4. For the selected "active" failure criteria, calculate all vertices where it intersects with min/max bounds of the design variables. Each failure criteria can intersect with N-1 bounds simultaneously, where N is the number of design variables.

5. Discard vertices that violate other min/max bounds.

6. Take all of the vertices lying on the "active" failure criteria and evaluate them with respect to the other criteria in the pair.

7. Check feasibility relative to the other criteria.

   (a) If all evaluated vertices are *feasible* with respect to the other failure criteria, the other failure criteria can be discarded.

   (b) If all evaluated vertices are *infeasible* with respect to the other failure criteria, the selected "active" failure criteria can be discarded.

   (c) If there is a mixture of feasible and infeasible vertices with respect to the other failure criteria, both criteria must be kept.

An example with the possible outcomes described above is depicted in Figure 66. The example presents two failure criteria constraints plotted as a function of A_{11} and A_{22}. The infeasible portion of the failure criteria is shown with gray shading. Failure Criteria 1 in the figure is the "active" constraint. As shown on the figure, vertex 1, 2, 3, and 4 are the intersections of the active constraint with max A_{22}, min A_{11}, min A_{22}, and max A_{11}, respectively. Vertices 1 and 4 are discarded because they violate the other boundaries of the design space. Next, the remaining vertices are evaluated with respect to the other failure criteria.

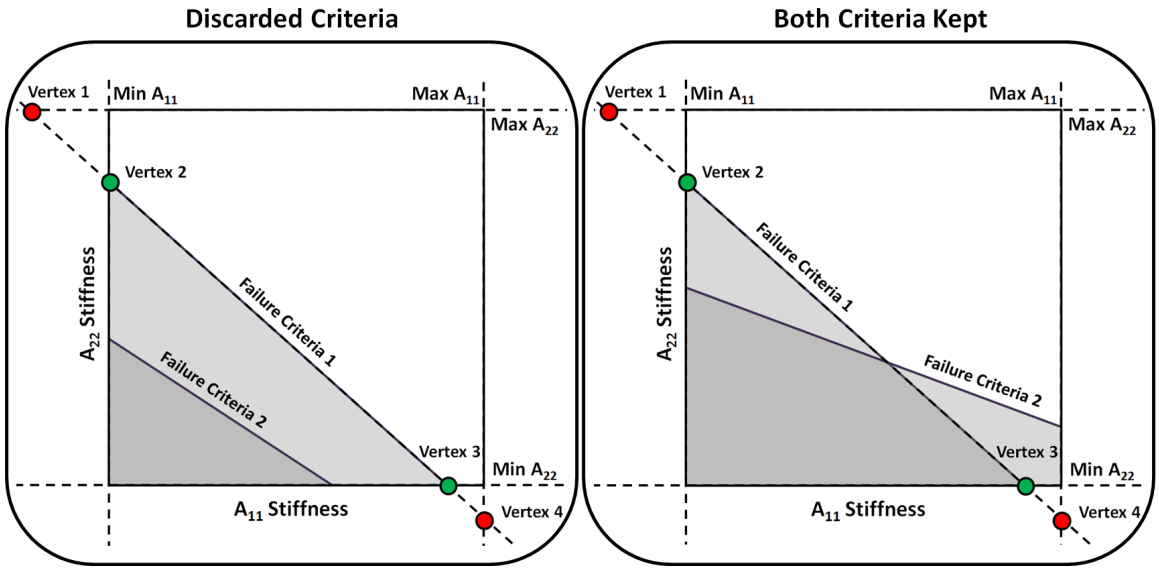

Figure 66: Example for Checking Constraint Redundancy

In the first case considered (left side of Figure 66), vertices 2 and 3 are both feasible with respect to the other failure criteria. Thus, Failure Criteria 2 is entirely eclipsed by Failure Criteria 1. Upon visual inspection of the plot, it is evident that any point in the design space that is infeasible with respect to Failure Criteria 2 is also infeasible with respect to Failure Criteria 1. Mathematically speaking, all infeasible points defined by Failure Criteria 2 (Cr_2) are a subset of infeasible points from Failure Criteria 1 (Cr_1) within the domain X created by min/max bounds on A_{11} and A_{22}, as shown in Equation 48.

$$\forall \vec{x} \in X, Cr_2 \subseteq Cr_1 \tag{48}$$

A similar outcome to the above is the case where vertices 2 and 3 were both infeasible with respect to Failure Criteria 2. In this case, Failure Criteria 1 would be redundant and thus eliminated. This case is not illustrated in Figure 66, but would look very similar to the previous case if the location of Failure Criteria 1 and 2 were switched.

The third and final possible outcome is depicted in the right side of Figure 66. In this case, vertex 2 is feasible with respect to Failure Criteria 2 but vertex 3 is not. This means there are portions of the design space which are uniquely constrained by either of the two constraints. Thus, it is necessary to keep both constraints.

Although the example described above is in two dimensions, the methodology can easily be expanded to a greater number of dimensions. The only difference for a greater number of dimensions is the number of vertices that must be calculated. In the given two-dimensional example, there were a total of four min/max bounds on the design space. Of these four, only one a time could intersect with the active failure criteria (two lines intersect to form a point). The total number of vertices is then defined by 4-choose-1 = 4. In a three-dimensional case, there would be a total of six min/max bounds. Of these six, only two at a time could intersect the active failure criteria (three planes intersect to form a point). The total number of vertices would be defined by 6-choose-2 = 15. Obviously this trend can continue on for any number of dimensions.

Thus, the filtering methodology presented above provides a general approach to eliminate redundant constraints caused by the use of multiple load cases. The actual number of constraints eliminated is highly problem-dependent. If one load case is much more severe than the others, it is likely that the majority of the remaining load case constraints would be eliminated. In cases where the relative magnitude of N_x , N_y , and N_{xy} are similar between load cases, it is likely that only a few load cases would be eliminated.

3.7 Calibration of Optimum Mass

To further improve the accuracy of mass resulting from the optimization described in the previous section, a calibration was applied depending on the values of panel load and buckling span. This calibration helps tighten the error distributions presented later in Section 4.2. The data points used to create the calibration curves were generated in a manner very similar to that described in Section 4.2. The calibration curves were developed through regression of unit mass error across a variety of panel loads and buckling spans. These curves are simple polynomials varying from 2nd order to 5th order and are a function of only loads N_x , N_y , N_{xy} and spans a and b. Equation 49 gives the general form of the calibration curves, with r representing the order of the polynomial.

$$Correction = \sum_{i=0}^{r} \sum_{j=0}^{(r-i)} \sum_{k=0}^{(r-j)} \sum_{l=0}^{(r-k)} \sum_{m=0}^{(r-l)} c_{ijklm} (N_x)^i (N_y)^j (N_{xy})^k (a)^l (b)^m \tag{49}$$

A demonstration of the calibration curve for the -N_x/+N_y load quadrant is given in

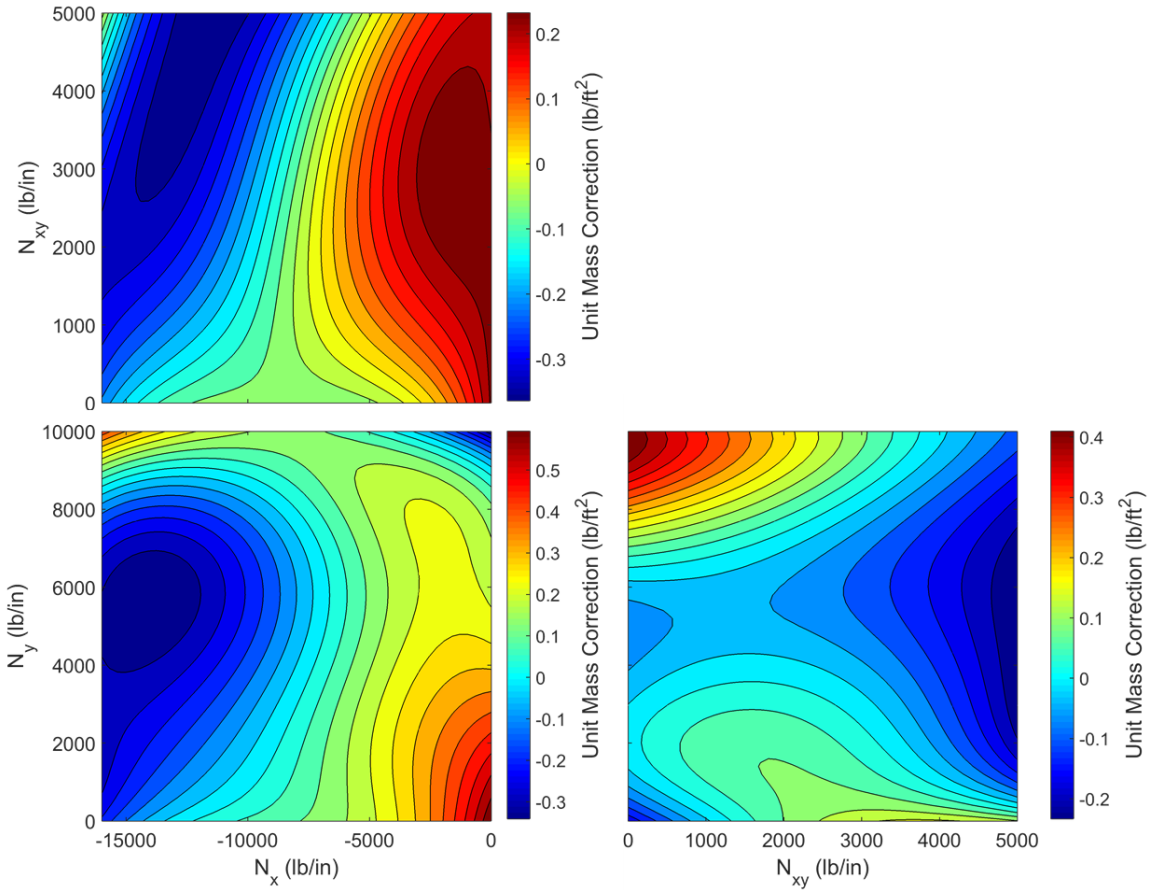

Figure 67: Example of Calibration Curves for the -N_x/+N_y Load Quadrant

Figure 67 for the metallic I-stiffened panel. This figure shows the calibration curve plotted in two dimensions for each combination of N_x , N_y , and N_{xy} . Because this is a two dimensional plot of a five-dimensional function, the un-plotted terms had to be assigned a fixed value. The un-plotted terms were fixed at the midpoints of their allowed ranges.

3.8 Summary of Response Surface Applications

RSEs appear in several locations throughout this chapter. This section provides a brief summary of each application to differentiate between the RSE applications. Table 13 lists the primary characteristics of each RSE application. Additionally, a description of each application is given below.

1. RSEs were used for gradient-based optimization in the physical domain to provide a point of comparison for panel optimization techniques existing in the literature.

Table 13: Summary of RSE Usage in this Research

	Application	Section	Dependent Variable	Independent Variables	Order
1	Failure Criteria (Physical Domain)	3.1.2	Criteria pass/fail	Panel dimensions: T_{sk}, T_{ft}, T_{wb}, T_{cp}, H, S, W_{ft}, W_{cp} Panel loads: N_x , N_y , N_{xy} Panel spans: a, b	All: 3rd
2	Failure Criteria (Stiffness Domain)	3.3.4	Criteria pass/fail	Panel stiffness terms: A_{11}, A_{22}, A_{33}, D_{11}, D_{22} Panel loads: N_x , N_y , N_{xy} Panel spans: a, b	Stffnss: 1st Loads: 3rd Spans: 3rd
3	Panel Unit Mass (Stiffness Domain)	3.5.2	Unit mass	Panel stiffness terms: A_{11}, A_{22}	All: 1st
4	Unit Mass Correction (Stiffness Domain)	3.7	Unit mass error	Panel loads: N_x , N_y , N_{xy} Panel spans: a, b	All: 3rd

2. The linear failure criteria RSEs are one of the primary developments of the current research. They are linear in terms of panel stiffness so that the panel can be quickly optimized with the Simplex Algorithm.

3. A linear expression for unit mass as a function of panel stiffness is necessary to complete the optimization environment for the RSE described above.

4. A correction RSE was used to provide a small calibration to the final mass produced by the Simplex Algorithm to improve accuracy.

3.9 Retrieving Physical Designs from Optimum Stiffness

The stiffness-based methodology described in the previous sections has a significant advantage in efficiency over traditional methods in the physical domain. This advantage is built upon the assumption that the detailed geometry of stiffened panels is not needed during the conceptual design of a structure, only masses and stiffnesses are needed. However, designers will always eventually reach a point where focus shifts from rapid iteration at the global structure level to the details of the structure. At this point, a physical design for the

panel will need to be derived from the final stiffness distribution. This section describes an approach to accomplish this task.

The primary challenge of mapping from the stiffness domain back to the physical design is that the mapping is non-unique because there are fewer variables in the stiffness domain than the physical domain. Thus, obtaining a physical design from stiffness terms is more complex than rearranging the equations given in Section 3.2.3 and solving for the panel geometry. Additionally, the non-uniqueness of the mapping provides opportunity for failure criteria to be violated if a bad combination of physical dimensions are selected.

This section discusses the approach developed to generate designs in the physical domain from points that have been optimized in the stiffness domain. Ideally, this would be done by rearranging the equations that define stiffness as a function of physical terms (given in Section 3.2.3) to provide a reverse mapping. However, there are several reason why this approach is not practical, listed below.

1. Some of the stiffness equations are substantially complex and thus very challenging to manipulate into a reverse mapping. Even with advanced computer-based equation manipulation tools such as Mathworks' Mathetmatica program [109], a closed-form reverse mapping of the stiffness equations is not possible for some stiffener concepts.

2. Each stiffened panel concept (listed in Section 2.6.1) would require a unique solution of the stiffness equations. This is contrary to the objective of achieving a general methodology that can be easily applied to any panel concept and material system.

3. Some panel concepts have stiffness equations that would cause physical dimensions to be over-defined in a reverse mapping. For example, a fastened I-stiffened panel has stiffness terms A_{22}, A_{33}, and D_{22} that are all a function of the physical variable T_{sk}. In this scenario, a closed-form reverse mapping could potentially yield conflicting physical designs.

For the reasons listed above, a numerical reverse-mapping process was selected instead of a closed-form process. To obtain physical designs from stiffness designs, the reverse

mapping is posed as an optimization problem. The optimization seeks a combination of physical variables which produces a stiffness design as close as possible to the stiffness design obtained from the panel optimization. The optimization is constrained such that the panel mass determined in the stiffness-based optimization must be met. Additionally, the physical designs can be constrained to meet geometry or material rules specified for the panel. Equation 50 gives the optimization statement for the reverse mapping. Note that this optimization is performed entirely independent of the stiffness-based optimization described previously. The reverse mapping optimization is purely a post-processing technique used to obtain physical designs when the stiffness-based optimization is complete.

$$\vec{X}_{physical} \text{ for min } d_{[ABD]} \text{ s.t. } \begin{cases} MS_i \geq 0 \\ UM = UM_{target} \\ R_{WFG} \geq 1.0 \\ 0.4 \leq R_{SA} \leq 0.6 \end{cases} \tag{50}$$

The objective and constraint functions of the optimization statement are described in detail in the sections below. In summary, the objective stated in Equation 50 is to find a set of physical dimensions ($X_{physical}$) for the panel that has a minimum difference in stiffness ($d_{[ABD]}$) from the design determined by the stiffness-based optimization. The resulting design must satisfy all failure criteria ($MS_i \geq 0$), achieve the mass determined in the stiffness-based optimization ($UM = UM_{target}$), and achieve appropriate panel geometry ratios (R_{WFG} and R_{SA}).

Because the reverse mapping optimization uses closed-form equations for the objective and constraint functions, it is able to solve for physical designs very quickly. This efficiency is beneficial because it is necessary to explore a multitude of physical designs for each panel stiffness design. Due to the non-unique mapping from the stiffness domain to the physical domain, it is possible to select a combination of physical variables ($X_{physical}$) that match the required stiffness, but do not satisfy the failure criteria for the panel. Generating a spread of physical designs that all represent the original stiffness design increases the likelihood of finding a design which also satisfies all of the failure criteria in the physical domain.

The following sections describe the details of the process for reverse mapping to physical designs from stiffness designs for a metallic I-stiffened panel. Additionally, the process is demonstrated for different combinations of load to prove viability.

3.9.1 Objective Function for Reverse Mapping

The objective function describes similarity between the stiffness terms corresponding to a physical design and the target stiffness as determined by the stiffness-based optimization. The similarity is calculated by the "distance" between the two sets of stiffness terms. This is achieved by normalizing the difference in each stiffness term by the range allowed for the stiffness term. After normalization, the difference for each stiffness term varies between zero and one, allowing for a total Euclidean distance to be calculated. The normalization and Euclidean distance are shown in Equation 51.

$$d_{A_{11}} = \frac{A_{11,target} - A_{11,current}}{A_{11,max} - A_{11,min}} \tag{51a}$$

$$d_{A_{22}} = \frac{A_{22,target} - A_{22,current}}{A_{22,max} - A_{22,min}} \tag{51b}$$

$$d_{A_{33}} = \frac{A_{33,target} - A_{33,current}}{A_{33,max} - A_{33,min}} \tag{51c}$$

$$d_{D_{11}} = \frac{D_{11,target} - D_{11,current}}{D_{11,max} - D_{11,min}} \tag{51d}$$

$$d_{D_{22}} = \frac{D_{22,target} - D_{22,current}}{D_{22,max} - D_{22,min}} \tag{51e}$$

$$d_{[ABD]} = \sqrt{d_{A_{11}}^2 + d_{A_{22}}^2 + d_{A_{33}}^2 + d_{D_{11}}^2 + d_{D_{22}}^2} \tag{51f}$$

In the equations above, d describes the normalized difference between the target and current stiffness in the optimization. All of these terms are used to calculate the Euclidean distance ($d_{[ABD]}$) between the two sets of stiffness terms. This formulation provides a single scalar value for the objective function, which is necessary for optimization.

3.9.2 Constraint Functions for Reverse Mapping

There are two main groups of constraint functions to consider. The first pertains to matching the panel mass determined by the stiffness-based optimization for the panel (UM_{target}). This forms an equality constraint which specifies the exact amount of material that can be

used in mapping to a physical design. Calculation of the equality constraint C_{eq} is shown in Equation 52. This constraint is satisfied when $C_{eq} = 0$, meaning $UM_{current}$ for the current set of physical dimensions matches the target value.

$$UM_{current} = \frac{1}{S}(T_{sk} \cdot S + T_{ft} \cdot W_{ft} + T_{wb} \cdot (H - T_{sk} - T_{ft} - T_{cp}) + T_{cp} \cdot W_{cp}) \tag{52a}$$

$$C_{eq} = UM_{target} - UM_{current} \tag{52b}$$

The second group of constraint functions pertain to enforcing geometry and material rules in the panel cross-section [62]. One example for metallic I-stiffened panels is to enforce that the bottom flange of the stiffener be wider than the top flange, shown in Equation 53. This rule has roots in both design and manufacturing to prevent the stiffener from overloading the rivets used to attach it to the skin, as well as to ensure that the top flange the stiffener is easy to inspect (not obscured by the bottom flange). Another example is the ratio of stiffener cross-section area to total cross-section area (R_{SA}), shown in Equation 54. This rule is used to improve survivability of the structure in the event that either the skin or stiffener are severely damaged. The area ratio ensures that the skin and stiffener carry a similar amount of total load, thus improving the likelihood that one will survive if the load-carrying capacity of the other is reduced due to damage. Examples of good and bad geometry considering both rules are shown in Figure 68.

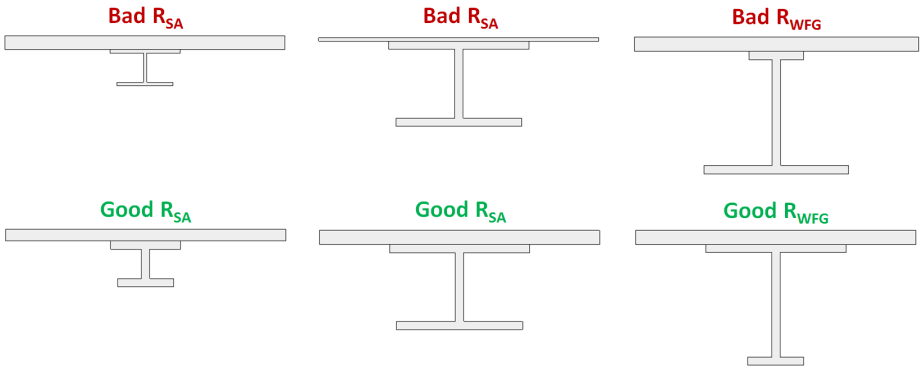

Figure 68: Acceptable and Unacceptable Geometry for the I-Stiffened Panel

$$R_{WFG} = \frac{W_{ft}}{W_{cp}} \tag{53a}$$

$$R_{WFG} \geq 1.0 \tag{53b}$$

$$C_{ineq}(1) = 1.0 - R_{WFG} \tag{53c}$$

$$R_{SA} = \frac{A_{stiffener}}{A_{panel}} \tag{54a}$$

$$0.4 \leq R_{SA} \leq 0.6 \tag{54b}$$

$$C_{ineq}(2) = 0.4 - R_{SA} \tag{54c}$$

$$C_{ineq}(3) = R_{SA} - 0.6 \tag{54d}$$

Equation 53 and 54 are both inequality constraints and are satisfied when C_{ineq} is negative. For the demonstration performed in this research, only the R_{WFG} rule is considered for the sake of simplicity. Implementing the R_{SA} rule has a significant impact on the panel mass optimization because it reduces the design space. For example, having tension in the x and y direction and low shear corresponds a very small stiffener. Implementing a minimum R_{SA} value would drive the design far away from the optimum solution, which is why the rule is not considered in this demonstration.

3.9.3 Generating Many Physical Designs from a Single Stiffness Design

To ultimately ensure that the physical design produced by the reverse mapping is feasible, it is necessary to run the final result through the failure criteria calculations. The nature of the non-unique mapping from the stiffness domain to the physical domain means that it is possible to choose design points outside of the feasible space in the reverse mapping process. This challenge is overcome by simply generating a spread of design points in the reverse mapping, instead of a single point. The panel failure criteria are checked for each design generated, and the one with the highest margins is selected as the final point for the reverse mapping.

The spread of reverse-mapped points is generated by enforcing a variety of different variable values in the reverse mapping optimization. For example, the thickness of the skin could be forced to have a value specified at a variety of different increments. This requires

the reverse mapping optimizer to find values for the other seven dimensions that satisfy the objective and constraints described in the previous sections. Multiple variables can be dictated to further increase the number of output physical designs. The process is outlined in Figure 69.

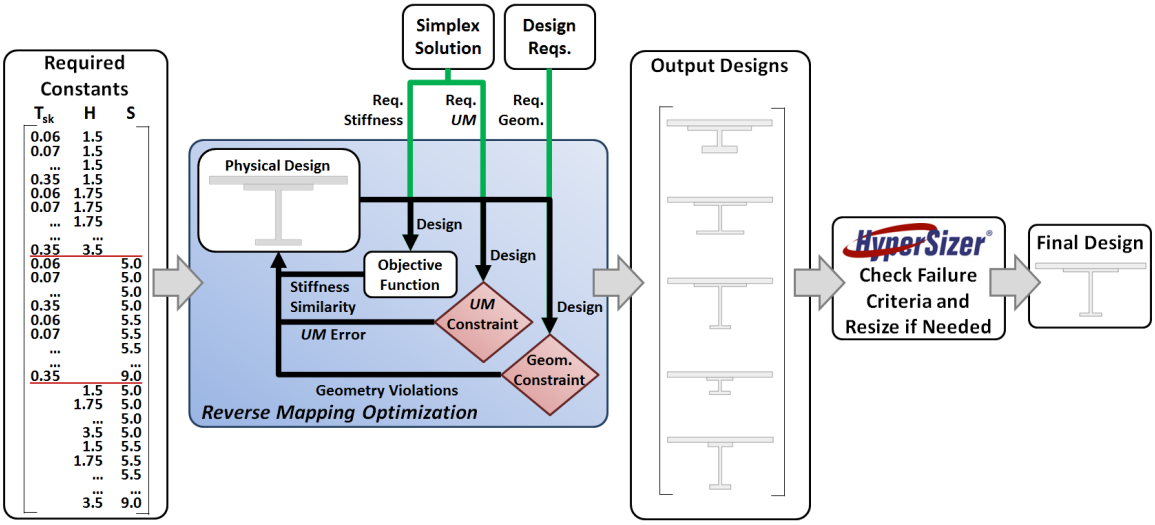

Figure 69: Process for Generating Physical Design From Final Panel Stiffness

In Figure 69, the process starts out with a set of specified constants. For this study, skin thickness (T_{sk}), stiffener height (H), and stiffener spacing (S) were selected to be specified in the reverse mapping. Of these three, variables, only two were specified at a time as shown in the figure. Each set of specified variables is passed to the reverse mapping optimization (blue box) where they are held constant during the optimization. The optimizer must find combinations of the other six variables which satisfy the reverse-mapping conditions. For each iteration of the reverse mapping optimization, the current physical design is compared to the stiffness design and unit mass of the stiffness-based solution as discussed in the previous two sections. Additionally, any applied geometry rules are also checked. Based on similarity to the target stiffness from the stiffness-based solution, as well as the constraint values, the current physical design is updated until it converges on a viable solution. This is repeated for for each set of required T_{sk}, H, and S to build a variety of output designs, all of which satisfy the requirements for the reverse mapping. Each of these output designs are then run through HyperSizer to check the failure criteria for the loads applied to the panel.

Whichever output design has the highest margins is the one selected as the final design.

Due to the small amount of error that can exist in the stiffness-based solution, it is possible for a small adjustment to be needed for the final solution. This is necessary when all of the designs output from the reverse mapping optimization yield negative margins when run through the HyperSizer failure criteria. There are two possible root causes for this problem. The first is that the mass predicted by the stiffness-based solution can be slightly too low, which means that there is not enough material available for the reverse mapping optimization to produce a viable panel. The second possible cause is that there is some error in the stiffness design of the stiffness-based solution. In both cases, the problem can be solved by using HyperSizer to perform a small re-sizing of the design output from the reverse mapping optimization. This is done by checking small permutations ($\pm 15\%$) of the best design output by the reverse mapping to find a viable solution that passes all of the failure criteria. Because the reverse mapping solution is already very close to being viable, the final resizing can be done very quickly.

3.9.4 Demonstration of Reverse Mapping

This section demonstrates the process above to show that it is able to correctly perform the reverse mapping from the stiffness domain to the physical domain. The verification was performed for four load combinations, one from each $x - y$ load quadrant. These load combinations are shown in Table 14. The same buckling spans were used for each load combination and are also listed in the table.

Table 14: Load Combinations Tested for Reverse Mapping

Type	Metric	Load 1	Load 2	Load 3	Load 4
Loads (lb/in)	N_x	-8000	7500	-8000	7500
	N_y	-2800	5000	5000	-2800
	N_{xy}	2500	2500	2500	2500
Spans (in)	a	24	24	24	24
	b	67.5	67.5	67.5	67.5

To establish a point of comparison for the reverse mapping of each load combination, a high-fidelity optimization was performed in HyperSizer. The result of this optimization

provides dimensions, stiffness, and unit mass to compare against the result from the reverse mapping process. HyperSizer results for each of the four load combinations are shown in Table 15.

Table 15: Results from High-Fidelity HyperSizer Optimization

Type	Metric	Load 1	Load 2	Load 3	Load 4
Dimensions (in)	T_{sk}	0.184	0.120	0.164	0.179
	T_{wb}	0.060	0.060	0.123	0.060
	T_{ft}	0.060	0.123	0.060	0.060
	T_{cp}	0.123	0.060	0.100	0.060
	H	2.300	1.500	2.071	1.786
	S	5.000	7.500	7.286	5.000
	W_{ft}	1.000	1.000	1.000	1.000
	W_{cp}	1.000	1.000	1.500	1.000
Membrane Stiffness (lb/in)	A_{11}	2,811,000	1,777,000	2,556,000	2,555,000
	A_{22}	2,234,000	1,445,000	1,975,000	2,165,000
	A_{33}	756,000	502,000	665,000	733,000
Bending Stiffness (lb-in^2/in)	D_{11}	1,574,000	244,000	1,212,000	539,000
	D_{22}	6,980	1,931	4,772	6,365
Mass (lb/ft^2)	UM	3.586	2.262	3.271	3.238

Next, the stiffness-based optimization and reverse mapping process was executed for the four points. The results from the reverse mapping are given in Table 16. To provide a clear understanding of how the designs compare, the cross-sections from HyperSizer and the reverse mapping are shown in Figure 70 for each of the four points. It is important to note that the geometry depicted in this figure is the stiffened panel "super-stiffener" introduced at the beginning of this chapter. The width of the super-stiffener reflects the spacing between stiffeners (S) *not* and is not in any way related to the total width of the panel (b). A full panel would be constructed of b/S repeated super-stiffeners, rounded to the nearest integer.

Some additional features to note about Figure 70 are listed below.

- Panels with compressive y load consistently have a small spacing span to reduce local buckling between stiffeners.
- Panels with tension y load are not sensitive to stiffener spacing, meaning equally optimum designs can have significantly different stiffener spacing.

- The panel with tension load in the x and y direction has the least amount of material because material failure criteria are usually less conservative than buckling criteria.
- The panel with tension x load and compressive y load has a small stiffener but thick skin because the stiffener does not substantially contribute to stiffness in the y direction.

Overall, the designs produced by the reverse mapping process are fairly similar to those determined by HyperSizer. One noticeable difference is that the stiffener heights for load combination #2 are substantially different. However, this is an inconsequential difference because stiffener height has very little relevance for load cases that have tension load only. Another noticeable difference is that two stiffeners for load combination #3 are shaped slightly differently. Despite the difference in shape, they both have a similar cross-sectional area and bending stiffness.

Table 16: Results from Reverse Mapping

Type	Metric	Load 1	Load 2	Load 3	Load 4
Dimensions (in)	T_{sk}	0.185	0.121	0.156	0.180
	T_{wb}	0.060	0.060	0.068	0.061
	T_{ft}	0.060	0.060	0.060	0.062
	T_{cp}	0.111	0.060	0.212	0.063
	H	2.225	2.811	1.635	1.713
	S	5.000	6.895	5.150	5.000
	W_{ft}	1.250	1.000	1.067	1.062
	W_{cp}	1.000	1.000	1.067	1.020
Membrane Stiffness (lb/in)	A_{11}	2,815,000	1,850,000	2,614,000	2,586,000
	A_{22}	2,255,000	1,457,000	1,899,000	2,186,000
	A_{33}	767,000	496,000	647,000	742,000
Bending Stiffness (lb-in^2/in)	D_{11}	1,356,000	1,266,000	1,092,000	508,000
	D_{22}	7,273	1,949	4,347	6,585
Mass (lb/ft^2)	UW	3.589	2.362	3.364	3.277

Ultimately, the small differences between the HyperSizer solution and the reverse mapping solution described above are not problematic as long as the overall panel mass and stiffness is similar, and the panels pass all of the failure criteria. The percent difference between the HyperSizer solution and reverse mapping solution for stiffness and mass is shown in Table 17. The most important result in Table 17 is that the panel mass is very

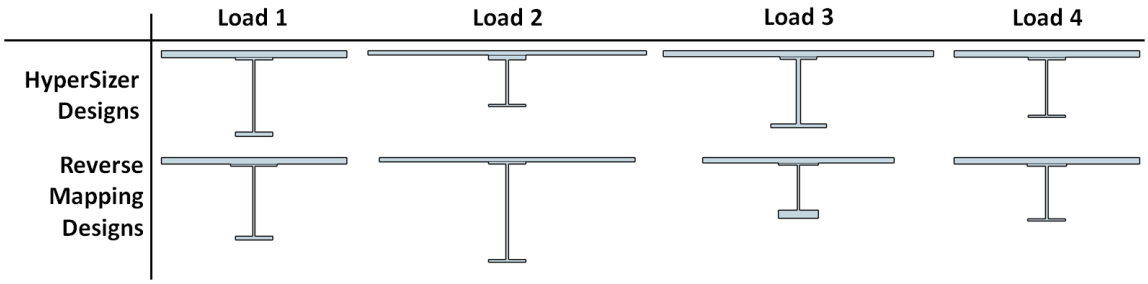

Figure 70: Comparison of Final Designs from HyperSizer and Reverse Mapping Process

similar between the two solutions. This indicates that the stiffness-based optimization is able to correctly predict optimum mass for the panel. Additionally, the stiffness terms are very similar between the two solutions. The exception is D_{11}, which is inconsequential for tension-only loading as described above. These results indicate that the reverse mapping process functions as expected.

Table 17: Difference Between HyperSizer and Reverse Mapping Results

Type	Metric	Load 1	Load 2	Load 3	Load 4
Membrane Stiffness (% Diff.)	A_{11}	0.165	4.082	2.255	1.207
	A_{22}	0.962	0.861	-3.836	0.988
	A_{33}	1.530	-1.191	-2.656	1.212
Bending Stiffness (% Diff.)	D_{11}	-13.882	419.328	-9.898	-5.687
	D_{22}	4.197	0.931	-8.907	3.453
Mass (% Diff.)	UW	0.086	4.412	2.856	1.231

CHAPTER IV

VALIDATION OF APPROACH

This chapter provides a validation of the concepts developed in the previous chapter. Three different forms of validation are performed. In each, the stiffness-based optimization from the previous chapter is compared to HyperSizer, a commercial structural analysis tool. These comparisons are done for the metallic I-stiffened panel.

The first verification is to show that the linear RSEs developed to represent the panel failure criteria are accurate. This is done by analyzing 4,000 randomly-generated panel designs with both the RSEs and with HyperSizer. The results from both analyses were compared to develop an idea of overall accuracy of the RSEs.

Second, validation of the overall linear design space was performed. This validation demonstrates that the new stiffness-based design space functions as expected and produces panel masses that are consistent with the physical-based design space. The stiffness-based optimization was checked at 800 randomly-generated combinations of panel loads and compared against a high-fidelity optimization performed in HyperSizer.

The last validation performed was focused towards interfacing the stiffness-based tool with an FEM design environment. Interfacing between the panel optimization and the global FEM optimization is achieved by specifying a stiffness that must be consistent at both levels. Thus, it is necessary to ensure that the stiffness-based panel optimization can handle the application of required stiffness values. Thus, the stiffness-based tool must be able to determine if a required stiffness value is feasible for the applied loads without the structure failing. Validation of this ability is performed by optimizing the panel for 800 randomly-generated loads with both HyperSizer and the stiffness-based tool. Results of the two tools are compared to determine accuracy of the stiffness-based tool.

The final topic discussed in this chapter is the trade between accuracy and efficiency that can be made with stiffened panel optimization. The accuracy and efficiency of the

stiffness-based tool is compared to that available from a traditional panel optimization tool (HyperSizer).

Together, the topics presented in this chapter demonstrate that the stiffness-based panel design tool presented in this research has favorable characteristics for use in conceptual structure design.

4.1 Failure Criteria Representation

This section contains a validation that the RSEs generated for the panel sizing accurately represent the failure criteria for the stiffened panel. The RSEs lose some accuracy because they are a lower-order approximation of the actual failure criteria. To retain the physics-based nature of the original failure criteria, it is desirable to have an accuracy of 90% or greater. This level of accuracy will be demonstrated in this section.

4.1.1 Description of Validation Process

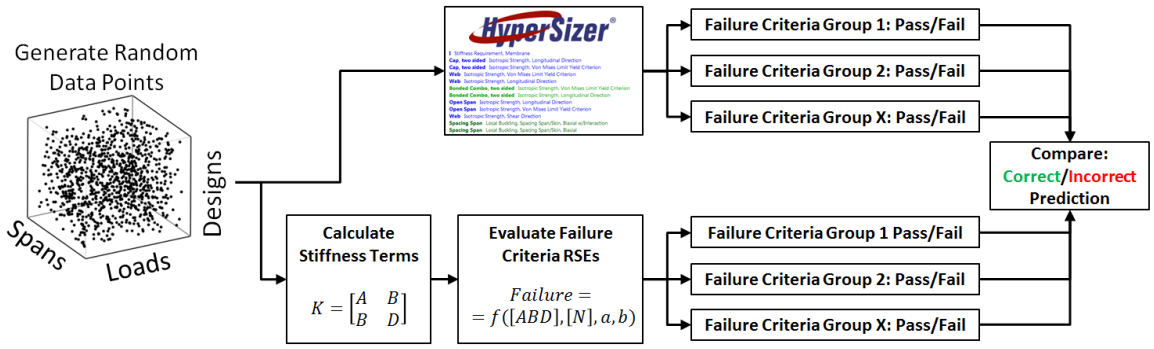

Figure 71: Process to Evaluate Prediction Accuracy of RSEs

The metric used to characterize the RSEs is Model Representation Accuracy (MRA) [76], which defines the percentage of design points whose failure criteria are correctly predicted by the RSE. Equation 55 shows how MRA is calculated.

$$MRA = \frac{\#Correct}{\#TotalPoints} \cdot 100 \tag{55}$$

This metric was used in place of the more traditional coefficient of determination (R^2) metric because R^2 by itself does not give a true indication of prediction accuracy.

Figure 71 illustrates the process of generating MRA values for each RSE. The MRA for the failure criteria RSEs was determined by first generating a set of 1,000 random data points for each RSE. Each random data point consists of a randomly generated physical design, randomly generated loads, and random buckling spans. The random data points were run through HyperSizer to establish which ones passed or failed the criteria listed in Table 1.

The final step was to run the random data points through the RSEs to determine the predicted pass/fail performance. This required calculating the stiffness terms for each of the random physical designs. Then the ABD stiffness terms, panel loads, and panel spans were input to the RSEs. The predicted performance was compared to the performance from HyperSizer to calculate the accuracy of the RSEs. In discussing the accuracy of the RSEs, the RSE is considered to be a "prediction" of panel performance and the HyperSizer result is the "actual" performance. Because the failure criteria are binary (pass or fail), there are four possible categories when predicted performance is compared to actual performance, shown below.

1. Correct pass prediction
2. Correct failure prediction
3. False pass prediction
4. False failure prediction

The first two categories contain the cases where both the predicted and actual performance are the same, either indicating pass or fail for the same panel. As the name suggests, these two categories contain points for which the RSEs correctly predicted panel performance. The sum of the number of data points in the first two categories divided by the total number of data points provides the MRA metric. Conversely, the incorrect predictions fall into the third and fourth categories. The third category represents cases where the panel was predicted to pass by the RSE, but failed when evaluated by HyperSizer. The fourth category represents cases where the panel was predicted to fail, but passed when evaluated in HyperSizer.

Note that the process was repeated four times for each of the load quadrants presented in Section 3.3.3. This was necessary because separate RSEs were developed for each load quadrant.

4.1.2 Accuracy for Metallic I-Stiffened Panel

Table 18 summarizes the MRA for each RSE in the four load regimes. Some of the failure criteria categories were not used for all load quadrants; these are represented by "-" in the table. Note that failure criteria groups related to the web and flange do not appear in the table; these failure modes were not prevalent enough in the observed load regimes to necessitate the development of RSEs.

Table 18: Model Representation Accuracy (%) of Failure Criteria RSEs

RSEs	$+N_x/+N_y$	$+N_x/\text{-}N_y$	$\text{-}N_x/\text{-}N_y$	$\text{-}N_x/+N_y$
Panel Buckling	-	96.3	91.2	91.2
Crippling	-	-	92.9	94.6
Facesheet: Local Buckling	94.5	94.8	94.1	95.2
Facesheet: Material	96.7	97.8	96.5	96.9
Bonded Combo: Material	96.4	98.2	-	96.8
Spacing Span: Local Buckling	93.7	94.8	92.9	93.9

Table 18 shows that all of the failure criteria RSEs have an accuracy greater than 90%, many with accuracy over 95%. Thus, the developed RSEs may be acceptable for use in a conceptual sizing environment. In the next section, it will be shown that this failure criteria accuracy translates to a satisfactory level of performance when used in an optimization.

In addition to overall accuracy of the RSEs, it can be useful to plot the prediction metric ϕ against panel load to ensure that there are not any systematic error trends. The prediction metric ϕ from Equation 35 is negative when the RSE predicts the panel will survive the applied loads and positive when it will fail. Figure 72 shows how the four prediction categories are distributed across a range of loads for the $\text{-}N_x/\text{-}N_y$ load regime, for the panel buckling failure criteria group. In general, the errors are randomly distributed across the range of loads, indicating a satisfactory regression. The remainder of the failure criteria show a similar trend in all load regimes, as shown in Appendix E.

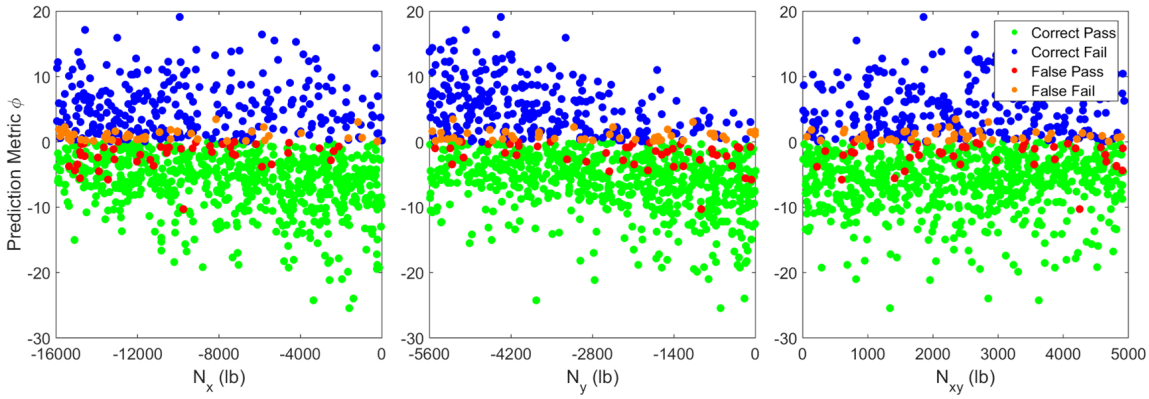

Figure 72: Panel Buckling Prediction Metric versus Applied Load

4.1.3 Sources of Error

The primary source of error in the failure criteria RSEs is due to the fact that simple polynomials were used to represent complex equations, table-lookups, and semi-numerical approaches. As discussed in Section 3.3, there is no closed-form approach for substituting panel stiffness expressions into the original failure criteria to perfectly linearize them. Thus, using regression will inherently cause error when the failure criteria are linearized.

Unfortunately, fitting error due to regression is essentially impossible to visualize in the stiffness domain. An example of the desirable, but unobtainable regression error plot is shown in Figure 73. This type of plot is unobtainable primarily due to the interactions that occur between the stiffness terms, as discussed in Section 3.4. In order to visualize linearization error in a 2D plot, it would be necessary to lock all the remaining stiffness terms at a fixed value. However, this is impossible due to the interactions described previously. Visualization of linearization error would only be possible in five dimensions (number of stiffness terms) so that effects of interactions could be included, but it challenging to produce a coherent plot with that many dimensions and data points.

However, another approach can be taken to visualize error resulting from the linearization. This can be accomplished by mapping error back to the physical domain. To generate the 2D maps shown below, every physical variable was set fixed except for the two shown in each of the figures. Additionally, load and buckling spans were set to fixed values. Next, full factorial combinations of the variables of interest were created, panel height versus stiffener

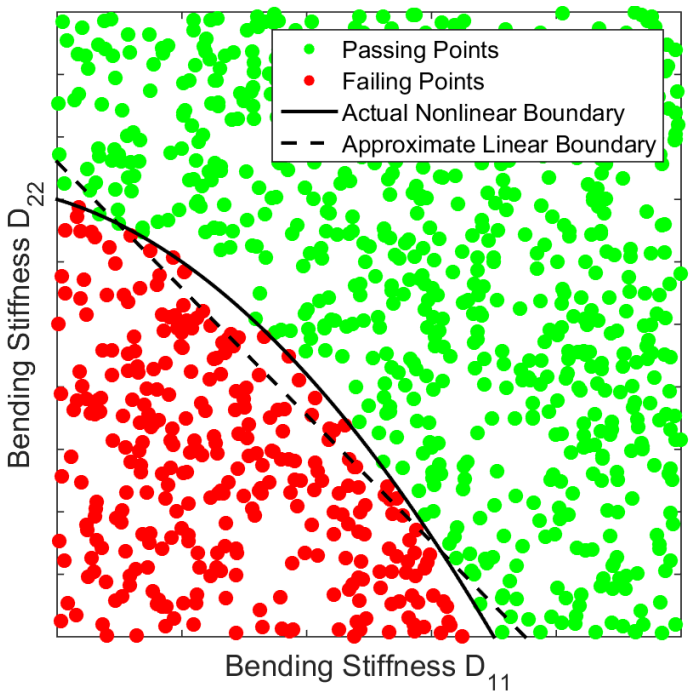

Figure 73: Notional Feasibility Border in Stiffness Domain

spacing for Figure 74 and skin thickness versus stiffener spacing for Figure 75. Finally, the generated points were run though HyperSizer to determine which combinations of the design variables failed. These results were compared to pass/fail predictions from the panel RSEs using the same four categories described in Section 4.1.1.

The resulting 2D maps in Figure 74 and Figure 75 demonstrate the primary source of error in the RSEs, which is inaccuracy in representing the boundary between feasible and infeasible. Note that because the error has been mapped to the physical domain for visualization, the feasibility boundary is not necessary linear.

Figure 74 gives an example of the feasibility boundary map for the Crippling failure criteria group. Overall, only 8% of the points were incorrectly predicted by the RSE. Figure 75 is an example of the failure criteria group for local buckling of the spacing span. The overall error for this map is only 4%. These errors are very similar to those presented in the previous section, indicating that MRA is a suitable approach for quantifying the RSE error. Similar maps can be generated for any combination of variables and failure criteria RSEs, and other load conditions could be considered as well.

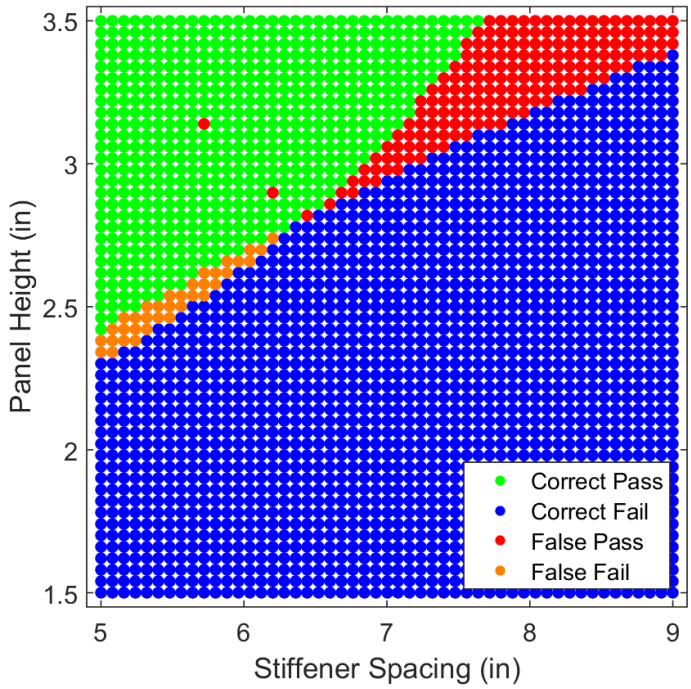

Figure 74: Feasibility Boundary Prediction Accuracy for Crippling in Physical Domain

Another source of error in the regression is the reduction of total number of design variables. Although the reduction was justified previously in Section 3.2.2, some design information is still lost in reducing the number of variables. This error would be difficult to distinguish from the error discussed above because it would require full reformulation of the design space with more design variables than the five currently considered and thus will not be discussed in this research.

4.2 Panel Mass Optimization

The next component of testing is to verify the final mass result of the stiffness-based optimization. This is done by comparing against a traditional stiffened panel optimization tool (HyperSizer) that operates in the physical domain. The results in this section will show that the accuracy of the failure criteria RSEs is high enough to facilitate accurate optimization in the stiffness domain.

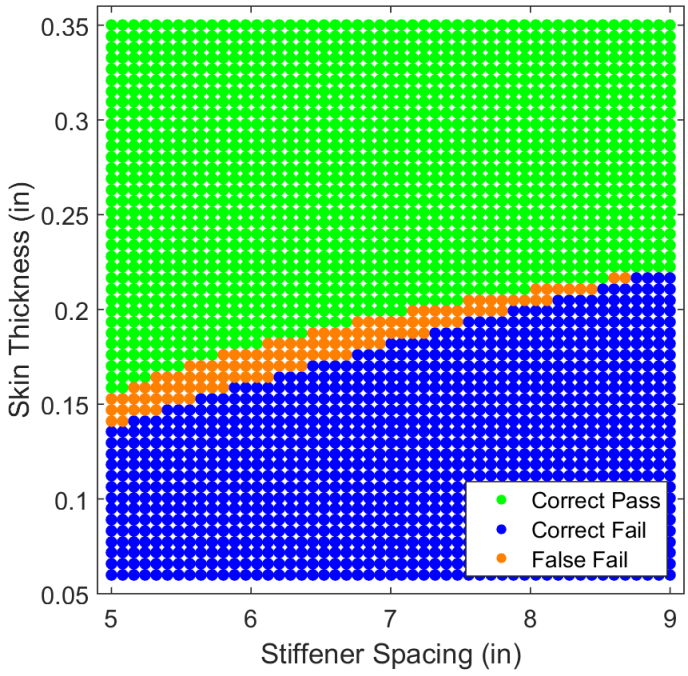

Figure 75: Feasibility Boundary Prediction Accuracy for Spacing Span Local Buckling in Physical Domain

4.2.1 Description of Validation Process

The stiffness-based optimization was verified by comparing to a traditional physical variable optimization for the same applied panel loads. The comparison was made with the optimum unit mass for the stiffened panel determined by the two approaches, as shown in Figure 76. A randomized set of loads and buckling spans were generated to create comparison points for the two solvers. This is slightly different from the randomized input for the failure criteria validation, where randomized physical geometry was also generated. For the current validation, the panel design is determined by the optimizer.

Each point was optimized in both HyperSizer and the stiffness-based optimizer to determine the unit mass for the given load and buckling spans. Finally, these two masses were compared to determine the error developed in the stiffness-based optimizer, considering the HyperSizer mass to be the "actual" mass. This process was repeated for each of the four load regimes because each uses a different set of RSEs.

The error for the optimized mass is more complicated to report than error for the failure criteria because it is a comparison of two continuous metrics over a variety of different

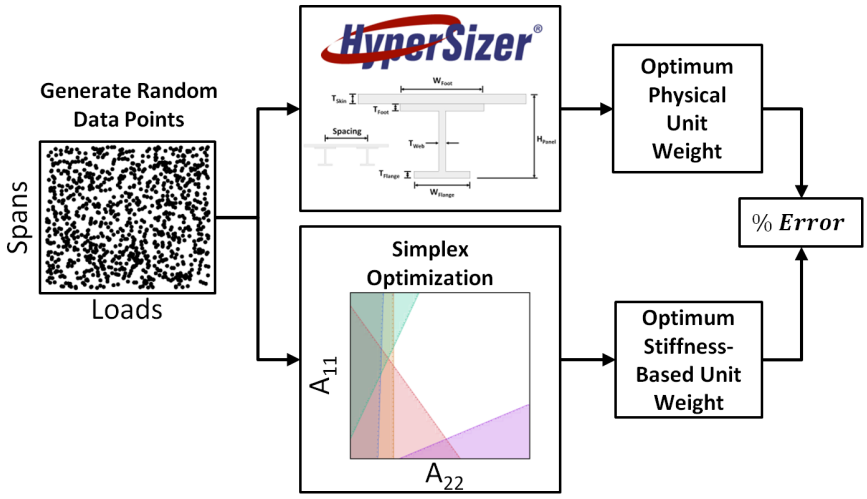

Figure 76: Process to Determine Error for Predicted Unit Mass

conditions. Several metrics were used to quantify the distribution of error for stiffness-based approach. The average value of the error ($\bar{e}$) indicates the presence of net error in the unit mass prediction made by the stiffness-based solution. The next metric, Root Mean Square (RMS) of the error (e_{rms}) indicates the average distance of the error from zero. The final metric is the standard deviation of the error (σ_e), which indicates the variability of the error about the mean. Ideal values for these three metrics are zero, if the prediction was perfect. Figure 77 demonstrates where these three metrics fall on a histogram of the prediction error.

4.2.2 Accuracy for Metallic I-Stiffened Panel

Using the concepts discussed above, the distribution of error over a variety of load conditions will be considered. Distributions of error must be considered because the methodology will perform better for some load cases than others. Additionally, error distributions from before and after application of the calibration curves from Section 3.7 will be presented. Note that each of the four load quadrants presented in Section 3.3.3 was considered separately because a different set of RSEs was used in each load quadrant.

As an example of the error distributions, Figure 78 shows the uncalibrated and calibrated mass errors for the -N_x/+N_y load quadrant resulting from the processes described above. The distributions for the remainder of the load quadrants are presented in Appendix F.

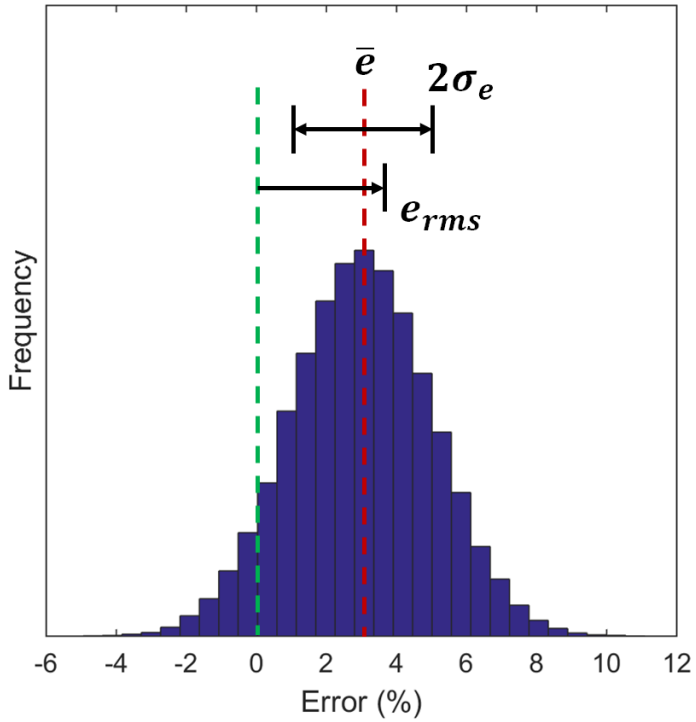

Figure 77: Values Used to Represent Mass Prediction Error

Table 19 lists the uncalibrated error metrics corresponding to the presented distributions. Table 20 lists the same metrics for the calibrated masses.

Table 19: Uncalibrated Error (%) for Predicting Optimum Panel Mass

Metric	$+N_x/+N_y$	$-N_x/+N_y$	$-N_x/-N_y$	$+N_x/-N_y$
$\bar{e}$	6.32	1.39	6.33	-3.00
e_{rms}	20.51	12.58	15.48	8.83
σ_e	14.64	9.69	10.29	6.18

Table 20 shows that the stiffness-based sizing environment is capable of producing reliable optimum unit masses for the stiffened panel across a wide range of applied loads. The error has a tight distribution and is close to being centered on zero error. The result is that the vast majority of the error is within ±10%. Although some accuracy is lost relative to traditional sizing methods, the stiffness-based optimizer enables panel optimization to be performed much faster than traditional approaches, as shown in the last section of this chapter.

The final way in which the error in the stiffness-based mass is presented is with a scatter

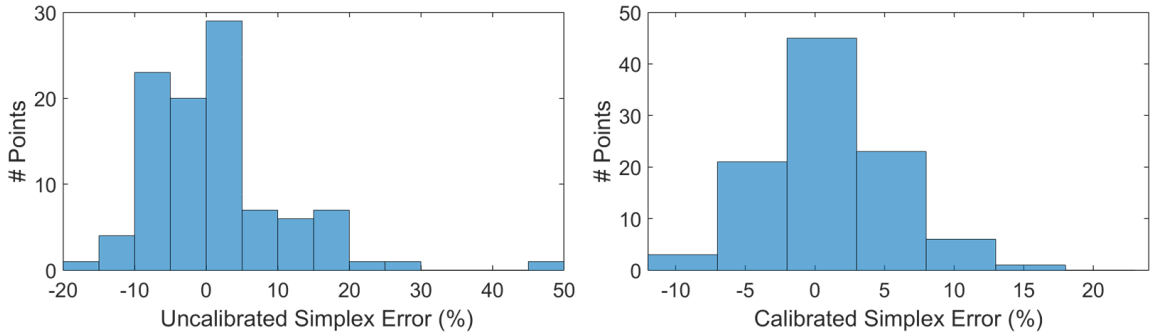

Figure 78: Mass Error Distributions: $-N_x/+N_y$ Quadrant

Table 20: Calibrated Error (%) for Predicting Optimum Panel Mass

Metric	$+N_x/+N_y$	$-N_x/+N_y$	$-N_x/-N_y$	$+N_x/-N_y$
$\bar{e}$	3.11	1.27	-4.24	0.78
e_{rms}	9.33	6.46	8.36	5.37
σ_e	6.55	4.86	4.95	4.10

plot of the validation points over the range of loads that were tested. These plots can be used to identify which combinations of load cause the stiffness-based optimizer to perform well or poorly. An example of these scatter plots is given below for the $-N_x/+N_y$ load quadrant and the remainder of the plots are in Appendix F. Figure 79 shows the error scatter plot before calibration is applied. This plot indicates that the stiffness-based optimization is over-conservative at low load values of N_x for reasons discussed below. Figure 80 shows that after calibration, the over-conservativeness has been rectified.

4.2.3 Sources of Error

This section presents a discussion on potential and identified sources of error in the stiffness-based panel optimization. The first component of error considered is the error induced from linearization of the failure criteria, which has been presented in the previous validation section. Additional sources of error are the bounds on stiffness term interactions as well as implementation of minimum gauge for the panel dimensions.

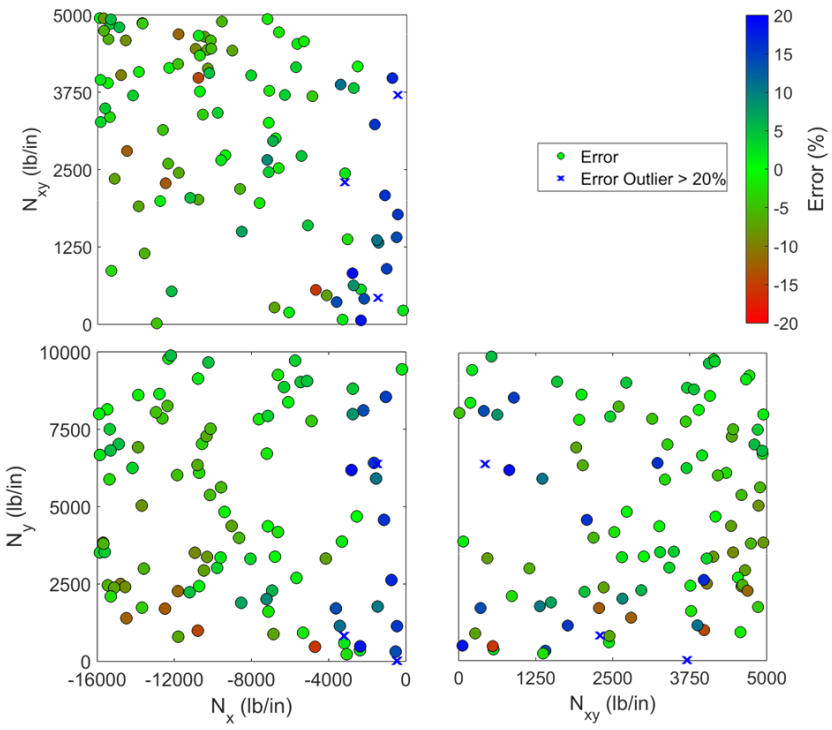

Figure 79: Uncalibrated Mass Error for Random Load and Span: $-N_x/+N_y$ Quadrant

4.2.3.1 Linearization of Failure Criteria

Error in the mass determined by the stiffness-based optimization is primarily caused by linearization of the design space. As was shown in Section 4.1, linearization of the failure criteria causes some inaccuracy in determining if a combination of panel stiffness is feasible for a given set of applied loads. The result is that the stiffness-based optimization may ultimately select a final design point that is not feasible if the design were mapped back to the physical domain. This would cause the stiffness-based optimizer to be *under-conservative*, producing a lighter design than what is determined in the physical domain. The opposite is also possible, where error in linearized failure criteria predicts that a particular design point is not feasible, when it is in reality. This would cause the stiffness-based optimizer to be *over-conservative*, meaning the design is heavier than necessary.

Table 20 shows that the latter case described above is more prevalent. The metrics in Table 20 represent 800 checked data points across all four load quadrants. Positive average error ($\bar{e}$) indicates the prediction is over-conservative and negative error indicates

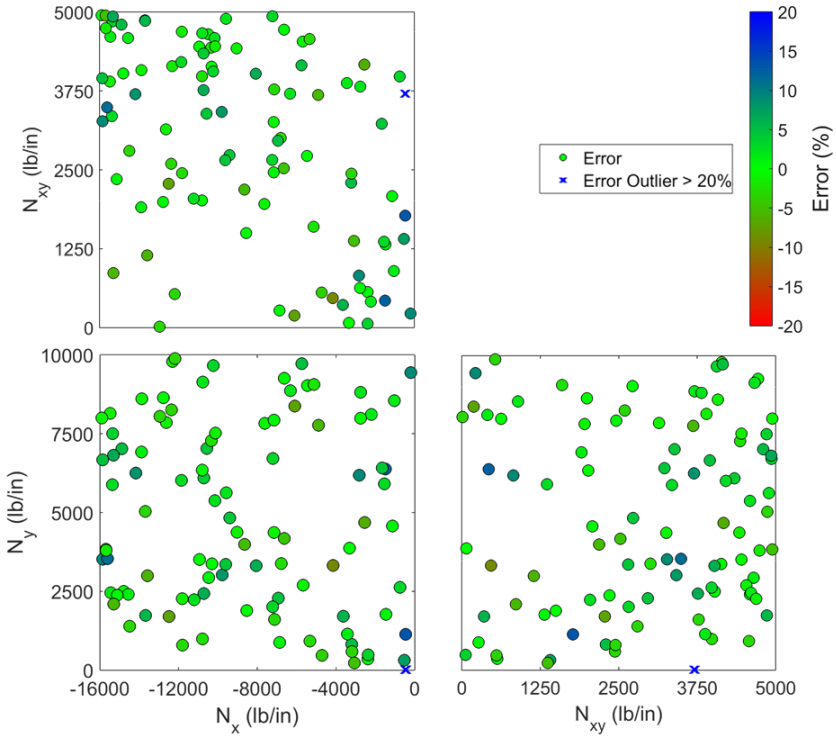

Figure 80: Calibrated Mass Error for Random Load and Span: $-N_x/+N_y$ Quadrant

the prediction is under-conservative.

4.2.3.2 Bounds on Stiffness Term Interaction

In addition to linearization of the failure criteria, another potential source of error are the linear stiffness interaction bounds imposed on the design space, as described generally in Section 3.4 and implemented in Section 3.5.3. These bounds were imposed to ensure that combinations of stiffness terms selected by the optimizer would correspond to designs that actually exist in the physical domain. As was shown in Section 3.5.3, some of the stiffness terms have nonlinear interactions that are approximated with linear functions. These approximated boundaries have associated error, meaning that the stiffness-based optimizer can potentially select combinations of stiffness terms that are not physically realizable. Similar to the error discussed above, the stiffness-based optimizer could potentially be over-conservative or under-conservative. This depends on whether the approximated boundaries are accidentally eliminating feasible designs, or accidentally allowing infeasible designs. An

example of both cases is shown in Figure 81 below.

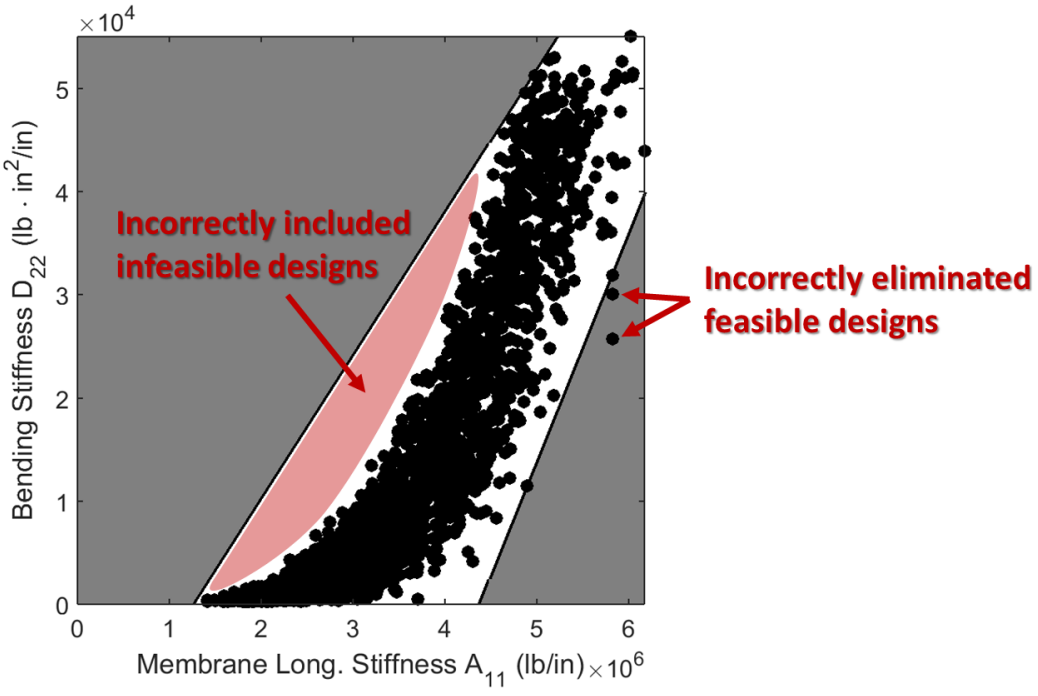

Figure 81: Types of Error Caused by Interaction Bounds on Stiffness Terms

4.2.3.3 Representation of Minimum Gauge

Minimum gauge for a stiffened panel refers to the minimum physical dimensions allowed for the panel design. The challenge of handling min gauge is that there are fewer regression points in the vicinity of the min gauge boundary than the rest of the design space, causing the failure criteria to be less accurate at the lower end of the design space. The result is that optimized designs produced by the stiffness-based optimizer close to minimum gauge have worse mass error than designs in other parts of the design space.

Figure 82 shows a plots of optimized unit mass error versus the HyperSizer unit mass for the four load quadrants. As seen in the figure, the $+N_x/+N_y$ quadrant has the most validation points near min gauge and these points have more error than the rest. Similarly, the $-N_x/-N_y$ quadrant encounters min gauge issues for panels with lower load. In this quadrant, the error occurs at a slightly higher unit mass because the panel has a taller and wider stiffener to resist buckling, but is still encountering min gauge on the thickness of the

panel objects.

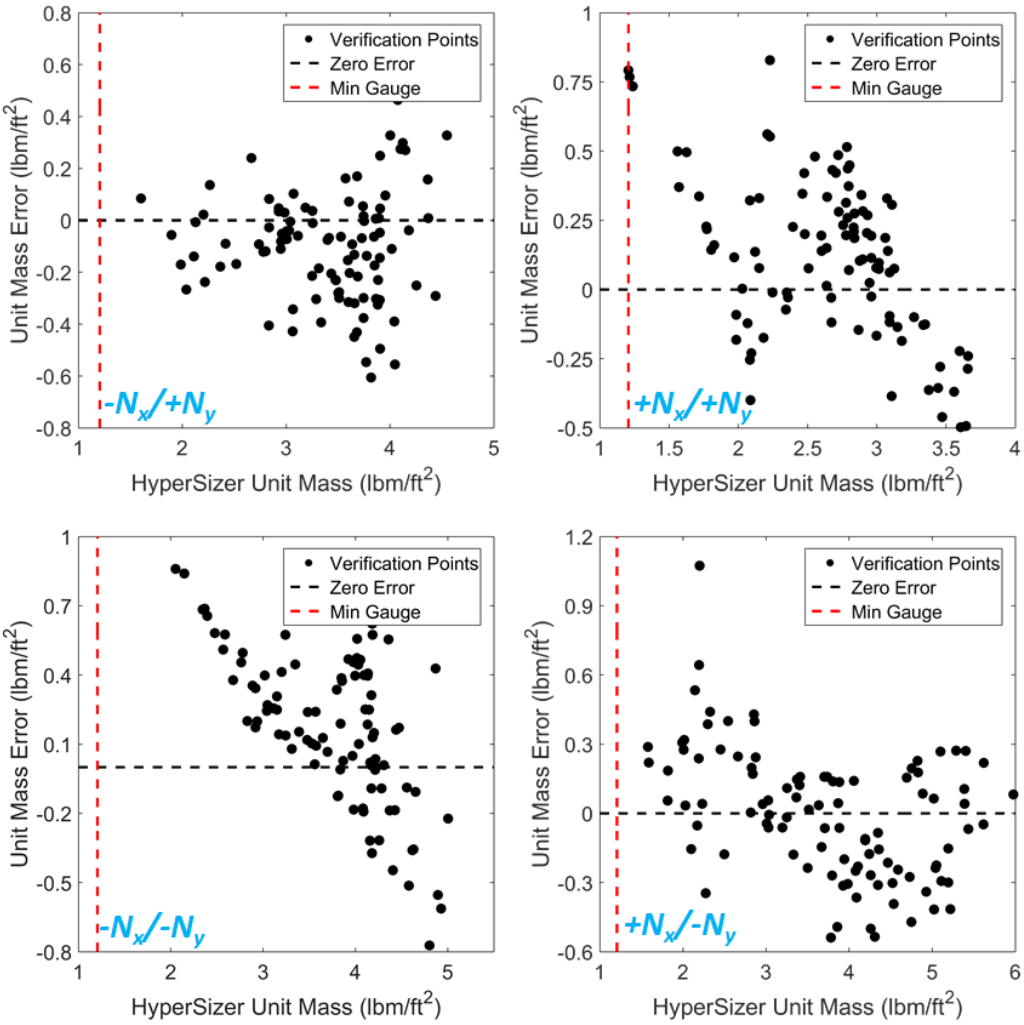

Figure 82: Unit Mass Error from Stiffness-Based Optimizer for All Four Load Quadrants

The error caused by minimum gauge could potentially be handled by applying min gauge only in the stiffness domain and not in the physical domain. For example, the thickness of the material could be allowed to go down to essentially zero in the regression data. This would ensure that the RSEs capture only the physics-based traits of the failure criteria and are not distorted by the minimum gauge bounds. In this case, min gauge would be applied in the stiffness domain simply by scaling up optimum stiffness designs that have a unit mass less than the min gauge panel.

4.3 Feasibility of Required Stiffness

The final component of validation is to demonstrate that stiffness constraints can be properly handled. This is necessary for the optimizer to be able to interface with a FEM-based conceptual design environment. Any process which requires stiffness to be controlled at the global level (e.g. global buckling or displacement constraints) must be able to enforce stiffness constraints when the local panel optimization is performed. This provides consistency between the global and local design environment.

To properly handle stiffness constraints, the tool must be able to determine if the required stiffness allows for a strong enough panel to survive the loads applied to the panel. For example, if a panel is highly loaded in axial compression ($-N_x$) but is required to have a low axial stiffness (A_{11}), there will not be enough available material to generate a panel cross section with enough bending stiffness to survive buckling. The stiffness-based failure criteria RSEs must be able to correctly identify these scenarios.

4.3.1 Description of Validation Process

The accuracy of the stiffness-based feasibility prediction was determined in a similar manner to the validation performed in Section 4.2. The process used for this validation is depicted in Figure 83. To calculate the accuracy, a set of random loads and buckling spans were first generated to provide data points to check. Next, the data points were submitted to both HyperSizer and the stiffness-based sizing tools, with a randomly-generated required A_{11} stiffness applied. For each data point, both tools determined if any panel cross sections exist which satisfy the required A_{11} as well as all of the failure criteria for the applied loads.

For each data point, the results were lumped into either a "pass" or "fail" category depending on whether they meet the criteria above. In the final step, the results from the two tools were compared to determine the accuracy of the stiffness-based feasibility prediction, with HyperSizer considered to be the "exact" solution. Each of the comparisons fit into the same four categories presented in Section 4.1.

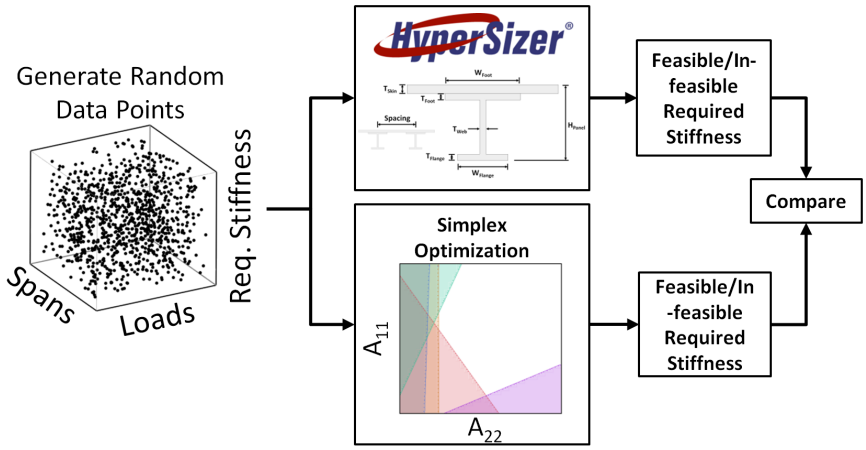

Figure 83: Process to Calculate Stiffness-Based Optimization Error for Feasibility of Required Stiffness Terms

4.3.2 Accuracy for Metallic Panels

Table 21 displays the percentage of random validation data points that fell into each prediction accuracy category. The bottom row of Table 21 shows that the MRA of the stiffness-based solution is at 96% or better for all four load regimes, validating the application of stiffness requirements in the stiffness-based optimization. These results indicate that the stiffness-based design space can predict with ≥96% accuracy if a required panel stiffness is feasible for the loads applied to the panel.

Table 21: Accuracy (%) of Predicting A_{11} Feasibility for Applied Loads

% of Total	$+N_x/+N_y$	$+N_x/-N_y$	$-N_x/-N_y$	$-N_x/+N_y$
Correct Pass	85	73	64	72
Correct Fail	12	23	34	24
False Pass	0	2	2	0
False Fail	3	3	1	4
Total Accuracy	97	96	98	96

To better visualize the accuracy presented in Table 21, the feasibility prediction for $-N_x/-N_y$ loading is shown in Figure 84. To generate this plot, the buckling spans, N_y, and N_{xy} load were held constant while the N_x load and required A_{11} were randomly varied. In Figure 84, there is a distinct border between feasible and infeasible combinations of N_x and required A_{11}. At more severe N_x loads, a heavier panel is needed, so only designs with a

high A_{11} are feasible. Conversely, lightly loaded panels are able to have a lower A_{11} and still survive the applied loads.

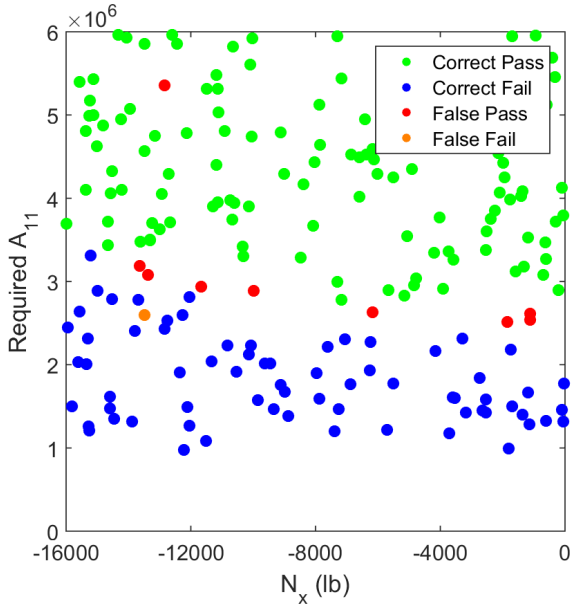

Figure 84: Map of Feasibility Prediction Accuracy Across Required Stiffness and Load

It is important to note that the majority of the errors fall along the border between feasible and infeasible. This means the stiffness-based solution will not cause severe errors if implemented in a global optimization with a FEM. For example, a panel with an excessively low A_{11} will not be deemed feasible when in reality no such cross section can exist. This ensures that a FEM-based optimization will still achieve an accurate mass estimation for a particular global stiffness distribution.

4.3.3 Sources of Error

Error in predicting feasibility of required stiffness has very similar roots to the error produced in the optimization of panel mass. Both utilize the same process with the Simplex Algorithm. The only difference is that the validation in this section has a required stiffness substituted into the stiffness-based equations representing the design space. See section 4.2.3 for discussion on sources of error.

4.4 Accuracy vs Efficiency

The stiffness-based optimization tool developed in this research is characterized by a sacrifice in accuracy of up to 10% to provide a significant improvement in optimization efficiency. To complete the discussion on accuracy, it is necessary to also consider the balance between accuracy and efficiency for traditional tools. In the discussion here, "accuracy" refers to the ability of the optimizer to get close global optimum solution for the given load condition. The global optimum was established with a very high resolution full-factorial design space exploration.

Before describing the balance accuracy and efficiency, it is necessary to describe how these characteristics are varied in the optimization performed by HyperSizer. Because HyperSizer uses a full-factorial design exploration approach, it is necessary to define a number of increments to be explored between the min and max bounds for a variable. Increasing the number of increments will provide a more optimum panel design, but will also take longer to run. Thus, the balance between accuracy and efficiency can be controlled through the number of increments for each variable. This is depicted in Figure 85.

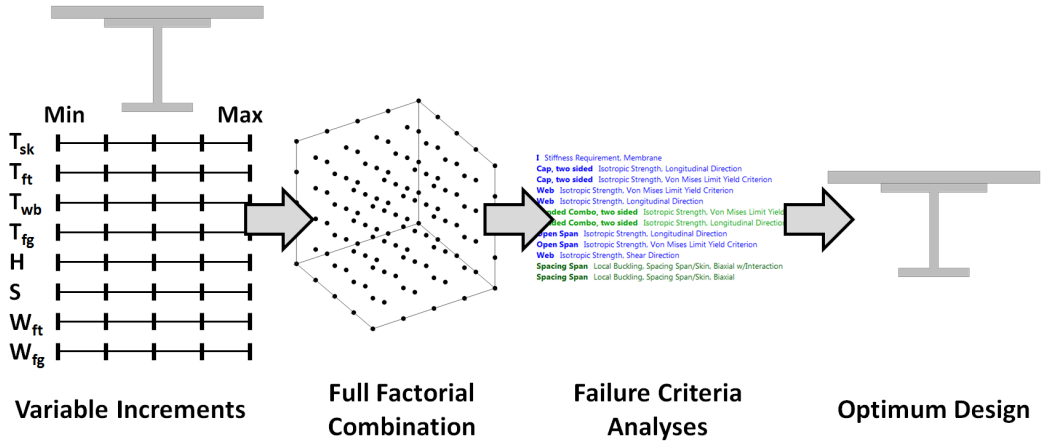

Figure 85: HyperSizer Optimization with Variable Increments

The most general approach for handling the number of variable increments in HyperSizer would be to assign the same number of increments to all of the variables. This assumes that the user knows nothing about the sensitivity of optimum panel mass to each of the variables. This is usually the case for conceptual design with a large number of panels. In

conceptual design, the loads in each panel are unfamiliar to the designer which makes it challenging to know the sensitivity of the optimum mass to each variable. Having a large number of panels increases the challenge of understanding mass sensitivity. As the panel designs become better understood, it is possible to customize the number of increments for each variable, providing more increments for variables that have a greater impact on mass and fewer increments for variables that have less impact.

To illustrate the trade between accuracy and efficiency, a simple Monte Carlo simulation was run with randomized numbers of increments for each variable (between three and six increments). The product of the number of increments for all of the variables defines the number of designs that HyperSizer considers, thus defining the run time. The Monte Carlo simulation represents a large number of approaches a designer might take, including good and bad. This was done for a single load condition: N_x =-10,000 lb/in, N_y =-3000 lb/in, N_{xy} =2500 lb/in. The result of the Monte Carlo simulation is shown in Figure 86.

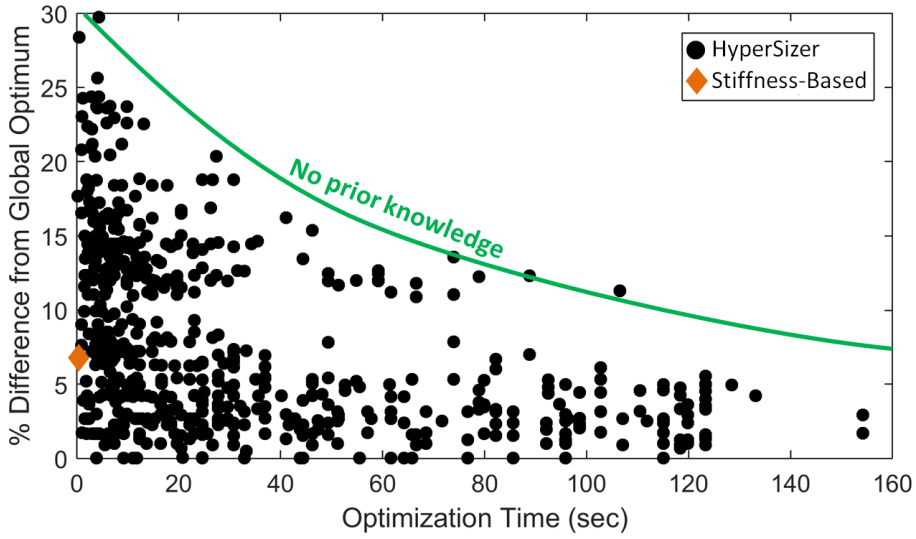

Figure 86: Trade Between Accuracy and Efficiency for Panel Optimization

In Figure 86, every single point represents an optimized panel for the given load condition. For the HyperSizer designs, there is a distinct upper limit on unit mass for a given analysis time. This limit represents optimization with no prior knowledge of the panel, where a uniform number of increments is applied to all of the variables. A low number of

increments corresponds to low run times, but at a severe sacrifice of accuracy.

As an example, consider a desired run time of 15 seconds and optimization accuracy within 10% of the global optimum. Starting on the "no prior knowledge" curve, as would be necessary in conceptual design, HyperSizer would only be able to get within about 25% of the global optimum with 15 seconds of run time. At the other end of the spectrum, a run time of over two minutes per panel is required to ensure that the optimum design is within 10% of the global optimum (with no prior knowledge). Obviously run times this high are not useful for rapid trade studies.

The points that lie under the "no prior knowledge" curve are designs which were produced with some knowledge about variable sensitivities. These designs represent cases were the number of increments were tuned for each variable to achieve lower mass without significant run time. The challenge is that the variable sensitives are different for every load condition and also depend on the min/max bounds specified for the dimensions. The problem is further compounded when multiple load cases are considered for the panel. Thus, it can be difficult to get below the "no prior knowledge" curve in a fast-paced conceptual design environment.

The final feature to consider in Figure 86 is the optimum design produced by the stiffness-based optimization using the methodology presented in this research. The stiffness-based result is represented by a single point because it is not possible to adjust accuracy versus efficiency within the algorithm. The stiffness-based optimizer finds the same global optimum every time with approximately the same run time, regardless of starting point. Note that the stiffness-based optimum mass is not the same as the HyperSizer global optimum mass due to errors described in the previous sections in this chapter. However, the stiffness-based optimizer is able to get within 7% of the true global optimum with a run time of 0.13 seconds. Compared to existing panel optimization methods presented in Section 3.1, this run time is an order of magnitude improvement as compared to the previous run time of 3 seconds (Section 3.1). Compared to the original HyperSizer optimization on the "no prior knowledge" curve, this is a run time improvement of three orders of magnitude.

CHAPTER V

APPLICABILITY TO COMPOSITES

In Chapter 3, a methodology was developed to perform a change of variables for panel optimization and also linearize the design space to improve optimization efficiency. The methodology was described and demonstrated for a metallic I-stiffened panel. This chapter focuses on applying the same methodology to a composite unstiffened laminate and a composite I-stiffened panel, pictured in Figure 87. In general, composites are traditionally more difficult to optimize due to higher complexity compared to metallic panel.

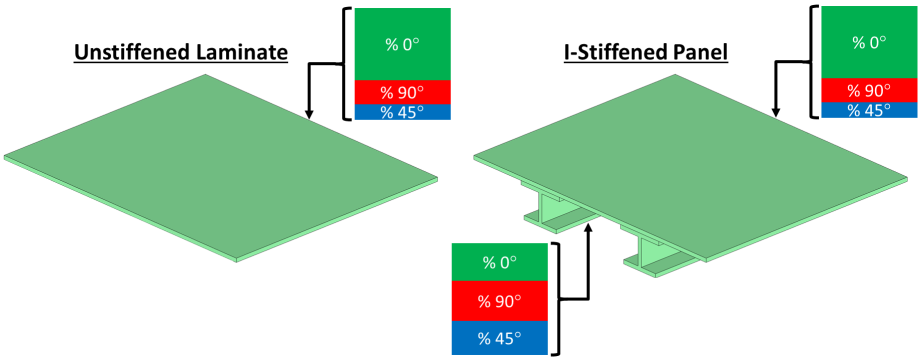

Figure 87: Composite Panels Considered with Stiffness-Based Methodology

The additional complexity introduced by composites is the variability of material stiffness caused by changes in ply angles within the laminates. This essentially introduces a new set of variables to the optimization. As discussed previously in Section 2.9, there are a number of approaches taken in literature to handle the material definition in the conceptual design of composite structures. The approach used in this research is to define the percentages of each ply orientation in the laminate. This is also sometimes referred to as an Effective Laminates (EL) approach. Also, only orientations of 0° , +/-45° , and 90° are considered in this research.

For the unstiffened laminate, this introduces three new variables compared to a metallic plate of similar geometry. Additionally, new variables are needed to handle the bending

stiffness of the laminate (discussed later). For the composite I-stiffened panel, the percentage of the three ply orientations are considered to vary independently in the skin of the panel and in the stiffener. Thus, a total of six new variables are introduced to the panel optimization compared to an identical metal panel. The topics presented in this chapter show that the panel methodology developed in Chapter 3 is capable of handling this increased complexity without significant modification, thus preserving the efficient run times demonstrated in the previous chapter.

Compared to traditional optimization methods used for composite panels, the run time of the linear optimization used in this research scales much more favorably for an increased number of variables. Additionally, the stiffness-based approach requires fewer extra variables to handle composites than are needed in the physical domain. Combining these two attributes, the improvement in optimization efficiency provided by the stiffness-based methodology is even more substantial for composite materials than metallics. This performance will be demonstrated in this chapter.

This chapter presents a parallel development of the two panel concepts pictured in Figure 87. These were selected to demonstrate two different approaches of applying the stiffness-based methodology to composite structures. The unstiffened laminate uses a higher fidelity approach in the stiffness domain. In addition to accounting for the percentage of 0° , +/- 45° , and 90° plies, the stiffness domain also includes laminate bending terms to capture the effect of ply locations in the laminate. Manufacturing rules are also included for the unstiffened laminate to further increase the fidelity of the approach. On the other hand, development of the composite I-stiffened panel closely follows that of the metallic I-stiffened panel. Thus, the fidelity of the composite material representation is less than the unstiffened panel. This allows for the geometry of the I-stiffened panel to still be optimized efficiently.

In the sections below, the stiffness-based optimization methodology is developed for the composite panels. The first step is to adapt the failure criteria RSEs for the composite panels. This requires selecting new failure criteria, new variables for optimization, and then constructing the new RSEs. Next, the objective function (mass) is developed for the optimization. The last components needed for the stiffness based optimization are the stiffness

domain boundaries, which are developed in a similar manner to the metallic panel. Having set up the optimization environment, the performance of the composite optimization is assessed, considering accuracy of the optimization as well as efficiency compared to traditional optimization approaches.

For the composite panels, a graphite epoxy tape material was selected. Tape was selected over fabric because Automated Fiber Placement (AFP) is becoming a popular manufacturing method. The properties of the AS4/3502 graphite/epoxy tape used for the composite panels are listed in Table 22, as found for this material in HyperSizer [1].

Table 22: Properties of AS4/3502 Graphite/Epoxy Tape [1]

Density	Stiffness					Strength			
ρ	E_1	E_2	ν	G_{12}	F_{tu1}	F_{tu2}	F_{cu1}	F_{cu2}	F_{su12}
(lb/in^3)	(Msi)	(Msi)		(Msi)		(ksi)	(ksi)	(ksi)	(ksi)
0.057	18.65	1.38	0.34	0.543	107.4	11.91	75.31	11.55	5.864

5.1 Adaptation of Failure Criteria RSEs

Previous development of the linear RSEs for panel optimization was demonstrated on a metallic I-stiffened panel. The intent of this section is to show that the same RSE approach is applicable to failure criteria for composite panels. The most obvious difference for the composite panel is that different failure criteria are used. Additionally, the effect of ply angle variation in the skin and stiffener must be included in the failure criteria regressions. These topics are discussed below, followed by discussion on the final accuracy of the failure criteria RSEs.

5.1.1 Composite Failure Criteria

The tables in Appendix G list all of the failure criteria considered for the composite panel. Each section of the tables represent the groupings used for the RSEs ; each group corresponds to a single failure criteria RSE. Both the unstiffened panel and the I-stiffened panel use failure criteria from this table.

The main difference between metallic and composite failure criteria is that the material-based failure modes are significantly different. Composite materials have a significantly

higher number of failure modes that result from its non-homogeneous characteristics. For example, a laminate can fail either in the matrix or in the fibers and the governing failure mode depends on the number of plies in each orientation as well as their location in the laminate.

One analysis that is unique to composites is the ply-by-ply stress and strain analysis. This analysis is important because the load condition on the laminate can be such that only a few of the plies fail while the remainder do not. The variability is due to the fact that strain in the plies depends on distance from the neutral axis of the laminate. This is compounded by the variability in ply orientation through the laminate. The derivation of these ply-by-ply stresses and strains can be found many textbooks on composite analysis, such as by Hahn and Tsai [92], and therefore will not be discussed here. An example plot of stress in the x direction through the thickness of a laminate is shown in Figure 88. With the stresses and strains derived for each ply, a number of criteria can be checked including basic stress and strain limits in the x, y, and xy directions and also more advanced criteria such as the Tsai-Hill [110], Tsai-Wu [111], Tsai-Hahn [92], and Hoffman [112] interaction criteria.

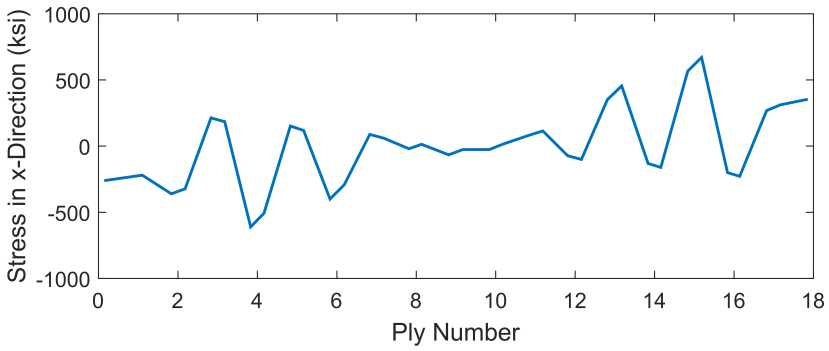

Figure 88: Example of Ply-by-Ply Stress Through the Thickness of a Laminate

Unlike the material failure criteria described above, stability criteria remain very similar to the metallic panel because the bending stiffness of a composite panel can be resolved into the same stiffness representation as a metallic panel. The only difference between the two material systems for this category of failure criteria is in crippling. A composite-specific

crippling criteria is used to account for the variation in stiffness between different parts of the panel due to ply angle variation.

5.1.2 Variables for Optimization

Depending on the desired level of fidelity, different variable representations can be used for the stacking sequence of a composite laminate (discussed in Section 2.9). Two different approaches are taken for representation of the unstiffened laminate and I-stiffened panel presented in this research. The goal with the unstiffened laminate is to demonstrate a slightly higher level of fidelity in the variable representation, making it easier to map from the stiffness domain back to an actual discrete laminate representation in the physical domain. With the I-stiffened panel, the goal is to use a higher level of abstraction in the panel variables to maintain efficiency while still accurately capturing the variability of the composite material.

5.1.2.1 Variables for the Unstiffened Laminate

Selection of variables for the unstiffened laminate differs from the metallic I-stiffened panel because of the additional complexity of the composite material, as well as the desire to demonstrate a higher fidelity optimization with the composite laminate. The selection process starts with a discussion of the design variables in the physical domain to prompt the selection of variables in the stiffness domain. The final set of variables chosen for optimization in the stiffness domain actually includes a small number of physical variables, for reasons described in the sections below. Note that this is entirely permissible within the methodology presented in Chapter 3 as long as an accurate linear relationship can be drawn between the selected variables and the failure criteria.

Physical Domain

For an unstiffened laminate, the highest fidelity representation that can be used in the physical domain is a discrete representation of the stacking sequence where the total number of plies can be varied and the orientation of each ply can be continuously varied. In most aerospace applications, the ply angles are typically limited to 0° , 45° , and 90° orientations for the purpose of reducing design complexity as well as testing effort in deriving stress

and strain allowables for the material. However, even with the simplification, the design space is still substantially complex. A 25-ply laminate constructed with tape material would have $3^{(25)} = 8.47 \cdot 10^{11}$ possible combinations of ply orientation. For stiffened panels, it is sufficient for conceptual design to further simplify the design space by only dealing with the number of plies in each orientation in the laminate (discussed in Section 2.9 and also in the next subsection) and neglecting the stacking sequence. However, for unstiffened panels it is necessary to retain some information about the discrete stacking sequence because this information is critical to failure in bending and buckling. Some examples of discrete laminate representations are shown in Figure 89. The present research uses a range of laminate thickness from 8 plies (0.044in) to 174 plies (0.957in) in the physical domain.

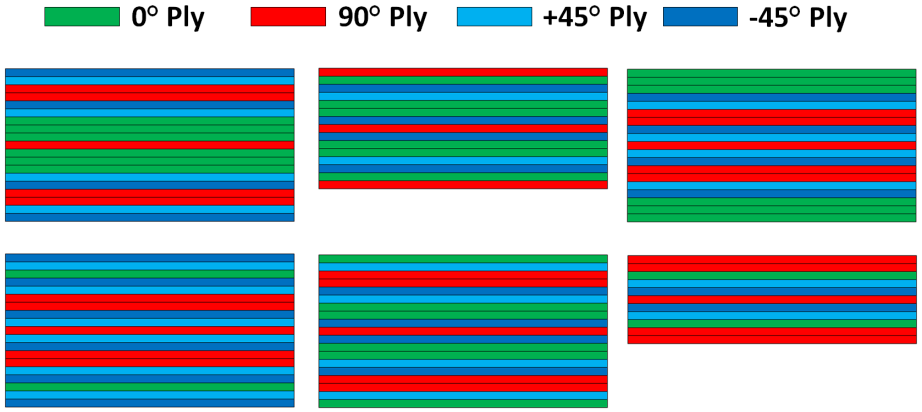

Figure 89: Examples of Discrete Laminate Stacks

Stiffness Domain

When selecting variables in the stiffness domain for the unstiffened laminate, it is necessary to consider the balance between fidelity and efficiency. For example, the lamination parameters (LPas) presented in Section 2.9 provide a very accurate representation of laminate stiffness but are still considerably complex, requiring 16 variables to represent the laminate. However, applying the stiffness-based approach presented in this research allows for significant reduction in the number of variables while still accurately capturing the stiffness of the laminate.

Within the consideration described above, it is also important to select variables that

interface well at the global level. For the unstiffened laminate, it is desirable to have variables allow for global stiffness designs to be generated that easily map back to a realistic global physical design. For example, it would not be useful to generate a global stiffness design that maps back to a physical design that requires a large change in laminate thickness over a small portion of the structure.

Considering this requirement, a mixture of physical and stiffness variables were used for the "stiffness" domain of the unstiffened laminate. The variables represent the thickness of the laminate (t), the percentage of 0° , 90° , and 45° plies (P_0, P_{90}, and P_{45}), as well as the bending stiffness of the laminate about the x and y axis.

A unique parametrization was selected for the ply percentages to promote useability at the global level. The challenge with using the P_0, P_{90}, and P_{45} values directly is that the distribution of these terms can be challenging to control at the global level. This is because the present research uses algebraic functions to control the spacial distribution of global variables. The distribution is controlled by driving the global variable value at a small number of control points (see Section 6.2.2 for a detailed description of how this is performed). This approach works well for a single global variable, but when multiple variables are considered, any interaction constraints between the variables are difficult to enforce. For the P_0, P_{90}, and P_{45} variables, the interaction constraint is that the sum of the percentages must equal 100%. If the distribution of P_0, P_{90}, and P_{45} over a structure is driven by an algebraic function, it is difficult to ensure that the three terms sum up to 100% everywhere on the structure.

To avoid the problems discussed above, a parametrization for the ply percentages was selected that eliminates the interaction constraints between laminate variables. To describe this parametrization, it is necessary to introduce the design space for the P_0, P_{90}, and P_{45}. In a 3D plot of these three variables, the design space appears as a triangular segment of a plane with its corners located at the extreme possible combinations of the ply percentages, as depicted in Figure 90. Each corner is at the maximum percentage allowed (60%) for one of the three the ply angles, requiring the other two ply angles to be at the minimum allowed value (20%). Any combination of ply percentages that sums to 100% and obeys the

min/max rules for the percentages falls on the surface of the triangular segment.

The new ply percentage parametrization is represented by two vectors that always lie on the face of the the segment to ensure that all design points are also on the triangular segment. This is referred to as the r-s parametrization and is shown in Figure 90. The vector $\vec{R}$ is defined along the line from point M_1 (max number of 0° plies) to point M_2 (max number of 90° plies). The length of $\vec{R}$ is defined by the normalized parameter r; a value of zero means $\vec{R}$ has zero length, and a value of one means $\vec{R}$ has a length of $||M_2 - M_1||$. Point A then lies at the end of $\vec{R}$, and is the base for vector $\vec{S}$. The direction of vector $\vec{S}$ is defined by the line from point A to M_3. Another normalized parameter s is used to define the length of $\vec{S}$; $s = 0$ gives $\vec{S}$ zero length and $s = 1$ gives $\vec{S}$ a length of $||M_2 - A||$.

Equation 56 through 59 shows how the ply percentages are represented with the r-s parametrization.

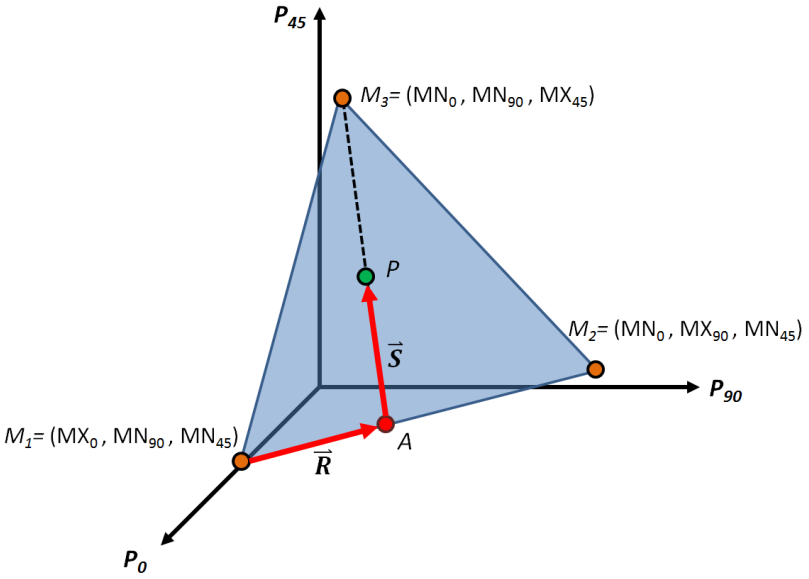

Figure 90: Parametrization of Ply Percentages for Unstiffened Laminate

$$\vec{R} = r \cdot (M_2 - M_1) \tag{56}$$

$$A = M_1 + \vec{R} \tag{57}$$

$$\vec{S} = s \cdot (M_3 - A) \tag{58}$$

$$P = \vec{S} + A = (P_0, P_{90}, P_{45}) \tag{59}$$

It is evident from Figure 90 that the r-s parametrization allows for any point on the triangular segment to be selected without worry of straying from the design space. The result is that r and s can be selected completely independently (within the bounds of 0 and 1) to drive the ply percentages in the laminate. The value of r controls the balance between 0° and 90° plies, and the value of s controls the addition of 45° plies to the laminate. The lack of coupling between r and s is highly beneficial for the global optimization scheme discussed in Chapter 6.

Thus, the final set of variables for the stiffness domain of the unstiffened laminate are: ply thickness t, parameters r and s, and bending stiffnesses D_{11} and D_{22}. Although this set of variables is a mix of physical and stiffness terms, it is fully compatible with the methodology introduced in this research because the physical terms are used in a linear manner. This will be discussed in Section 5.1.3 where the development of failure criteria RSEs for composite panels is discussed. The range of these variables used for optimization is shown Table 23.

Table 23: Variable Ranges for Stiffness Domain of the Unstiffened Laminate

	t (in)	r	s	D_{11} (lb-in^2/in)	D_{22} (lb-in^2/in)
Min	0.044	0	0	24.612	24.612
Max	0.957	1	1	834,690	834,690

5.1.2.2 Variables for the I-Stiffened Panel

The process of selecting variables for the composite I-stiffened panel is similar to the metallic panel. The main difference is the introduction of six new variables in the physical domain to represent the ply percentages in the skin and stiffener. However, when mapped to the stiffness domain, the ply angle variations become wrapped up in the overall stiffness representation of the laminate. These concepts are discussed in detail below.

Physical Domain

The variables for the physical domain of the composite I-stiffened laminate are quite similar to that of the metallic panel. All of the geometry variables are identical to those of the

metallic panel. The difference for the composite panel is that additional variables are needed to describe the percentage of each ply orientation in both the skin and stiffener of the panel, as shown in Figure 91. These percentages are allowed to vary between 20% and 60% for each of the three ply orientations. With these ply percentages, the composite I-stiffened panel uses the effective laminate approach presented in Section 2.9. In this approach, the laminate has an equivalent stiffness in the x, y, and xy directions that is constant through the thickness of the laminate. The equivalent laminate representation can result in inaccurate local bending stiffnesses, but this is less of an issue for stiffened panels compared to unstiffened laminates.

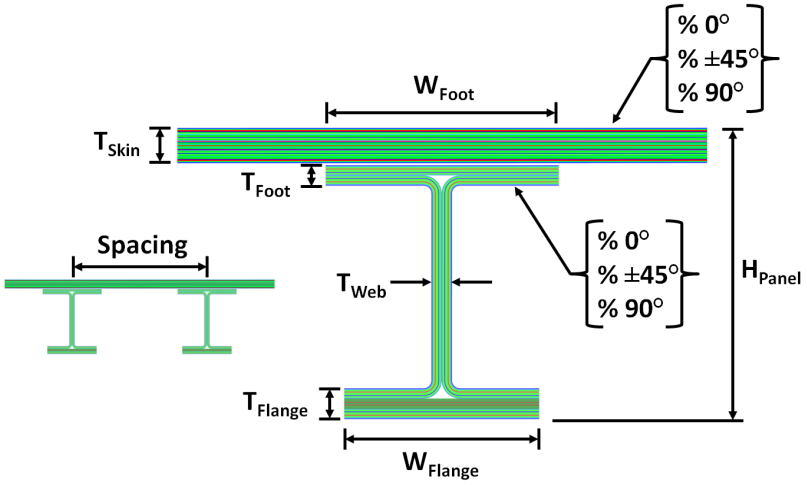

Figure 91: Variables for the Composite I-Stiffened Panel

Stiffness Domain

The stiffness domain for the composite I-stiffened panel is similar to that of the metallic panel, and therefore will not be discussed in significant detail here. Because the inclusion of ply angle variability in the panel ultimately results in variability in the overall panel stiffness, the stiffness variables selected for the metallic panel are fully applicable to the composite panel. The only difference in variables used for the stiffness domain of the composite I-stiffened panel is the addition of the term A/S (stiffener cross-section area A divided by stiffener spacing S, which is necessary to accurately calculate the mass of the panel from the stiffness domain. This is covered in Section 5.2.2. The variables for the composite

I-stiffened panel in the stiffness domain are: A_{11}, A_{22}, A_{33}, D_{11}, D_{22}, and A/S. The ranges of these variables are given in Table 24.

Table 24: Variable Ranges for Stiffness Domain of the Unstiffened Laminate

	A_{11}	A_{22}	A_{33}	D_{11}	D_{22}	A/S
Min	1,005,000	379,000	90,090	303,000	119	0.1226
Max	7,478,000	6,350,000	1,618,000	11,981,000	141,000	0.7873

5.1.3 Constructing Failure Criteria RSEs for Composite Panels

The process for generating RSEs to represent failure criteria for composite panels is quite similar to that of metallic panels. The updated process is depicted in Figure 92. The only difference from metallic panels is that ply angle variability is included in the DoE of regression points. Thus, the tailorability of the composite material becomes built into the failure criteria RSEs in the form of stiffness variability. This allows the panel optimizer to take advantage of the composite material without having to deal with the additional variables related to ply orientations in the skin and stiffener, thereby providing a significant benefit in optimization efficiency compared to the physical domain.

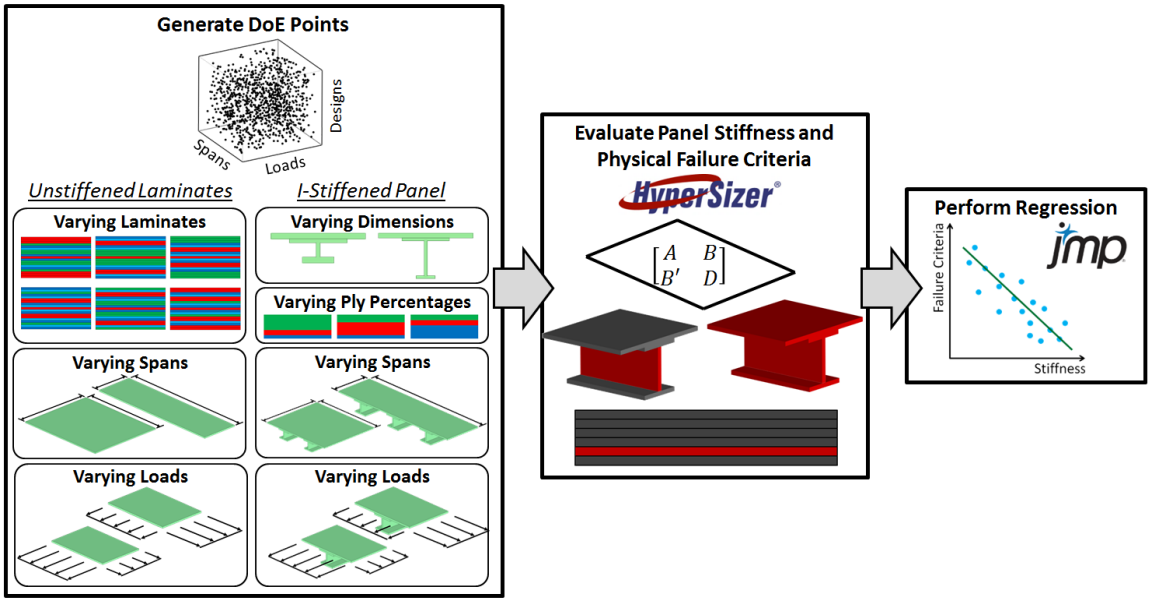

Figure 92: Failure Criteria RSE Generation with Composites

Figure 92 highlights the information that is input to the regression DoE for both the

unstiffened laminate and the I-stiffened panel. The main difference between the composite and metallic DoE is that the ply variability information must be included in the physical designs that are generated. The rest of the DoE inputs remain the same as metallic panels, with varying buckling spans and applied loads. The two subsections below describe the specific detail of how ply angle variability is included in the regression for the two different types of composite panel considered in this research.

5.1.3.1 RSE Development for Unstiffened Laminates

As described previously, the unstiffened laminate application in this research is used to demonstrate a higher fidelity approach for representation of composite materials. As such, generation of the regression DoE is more complicated. As shown in Figure 92, the DoE must vary how the ply angles are distributed throughout the thickness of the laminate. This has a significant impact on the bending stiffness of the laminate. Additionally, it is desirable to include layup rules for the laminate so that the DoE is representative of actual laminates that could be used in the final design of a structure.

Layup rules are are typically used to mitigate failure modes that are difficult to predict with traditional composite analysis, such as delamination and damage tolerance. Two layup rules were used for the unstiffened laminate: max adjacent plies and 45° ply dispersion.

The first, max adjacent plies, limits the number of plies of the same angle that can be placed next to each other. The rule used here is that no more than four adjacent plies can appear in the laminate. This rule prevents large fluctuations in stiffness through the thickness of the laminate, thus reducing strain discrepancy through the laminate to mitigate delamination.

The second layup rule enforces dispersion of 45° plies through the laminate. The rule used here is that a 45° ply must appear after every six plies, or more frequently. Plies at 45° orientation are generally considered to more capable of arresting cracks than plies oriented with the primary load path. Dispersing 45° plies throughout a laminate helps reduce the likelihood of catastrophic failure in the event that a crack is initiated in the laminate.

Bringing all of this information together dictates the process used to generate a DoE of laminates for failure criteria regression, as depicted in Figure 93. The steps shown in this figure are described below.

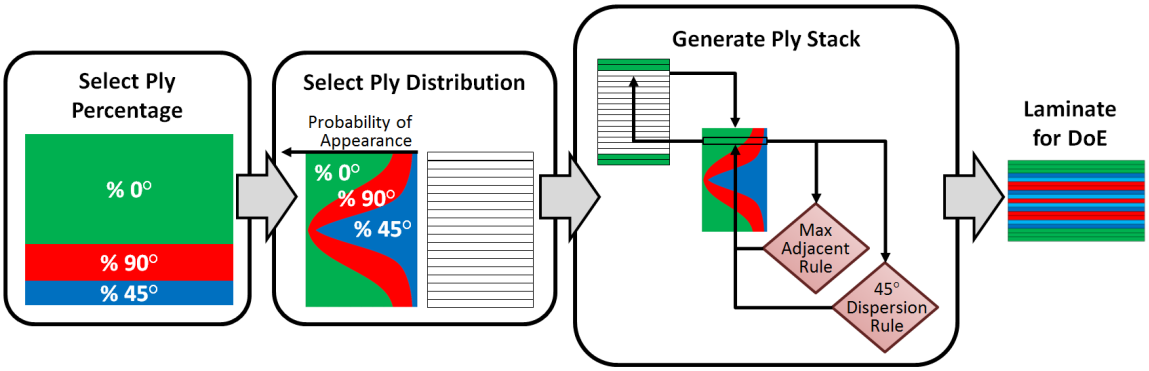

Figure 93: Steps to Generate Laminates for the RSE DoE of Unstiffened Laminates

1. For each DoE point, a set of ply percentages and total laminate thickness is established first. The percentage of each ply angle is allowed to vary between 20% and 60%. With this information, discrete ply counts for each orientation are generated based on the thickness of the ply material.

2. Next, a ply distribution pattern is selected. This establishes the probability of whether a particular ply angle is more likely to appear towards the outside or inside of the laminate, thereby controlling bending stiffness for a given laminate thickness.

3. The final step is to build the laminate stack based on information from the first two steps, and also including the layup rules discussed previously. The ply stack is built one ply at a time, from the outside in. The angle for each ply is selected according to the distribution established in the previous step. Each time a ply is added to the laminate, the layup rules are checked and enforced if necessary. This process results in a laminate that is ready to be used in the DoE for RSE generation.

Repeating the process above for a variety of ply percentages and distributions provides a DoE that is representative of all possible laminates that can be achieved within the specified layup rules. Including all of this information in the DoE means that it will be built into

the failure criteria RSEs, and thus accounted for during the stiffness-based optimization for the laminate. Having a realistic laminate representation means that optimized mass will be more representative of the final as-built laminate. Additionally, maintaining an accurate representation makes it easier to map from the stiffness domain back to an actual laminate.

After combining the generated laminates with loads and spans, all of the DoE points are run through HyperSizer to evaluate the failure criteria, and then used to generate the failure criteria RSEs as was done with the metallic panel. As before, these failure criteria RSEs predict failure of the panel as a function of stiffness terms, panel loads, and panel buckling spans. To maintain a linear relationship between the variables and the failure criteria, the terms t, r, and s were used strictly for material failure modes and terms D_{11} and D_{22} were used strictly for buckling failure modes.

5.1.3.2 RSE Development for I-Stiffened Panels

Generation of the RSEs for the composite I-stiffened panel is much more similar to the process for the metallic I-stiffened panel than the composite unstiffened laminate. This is because a more simplistic representation of the composite material was chosen for the I-stiffened panel, as described previously in Section 5.1.2.2. The DoE used for regression of the RSEs does not require laminates to be generated. Only the ply percentages need to be selected, which is sufficient to create the effective laminate representation for the skin and stiffener. Variation in ply percentages was allowed between 20% and 60% in 10% increments for each of the three ply angles, enforcing that the total adds up to 100%. This results in 15 laminate definitions for the regression DoE to select from as shown in Table 25.

These laminate definitions are integrated into the DoE points for the laminate regression (shown previously in Figure 92), and the rest of the regression proceeds as was described previously for the metallic panel. By including these variations in ply percentages in the DoE , the stiffness variation allowed by the composite material becomes built into the stiffness domain. This can be seen by referring back to the panel stiffness equations presented in Section 3.2.3. Variation in ply percentages in the skin and stiffener changes the effective modulus (E_{sk} and E_{st}), which feeds into panel stiffness.

Table 25: Ply Angle Variations Allowed in Regression DoE

	% 0° Plies	% 45° Plies	% 90° Plies
1	20	60	20
2	20	50	30
3	20	40	40
4	20	30	50
5	20	20	60
6	30	50	20
7	30	40	30
8	30	30	40
9	30	20	50
10	40	40	20
11	40	30	30
12	40	20	40
13	50	30	20
14	50	20	30
15	60	20	20

5.1.4 Accuracy of Composite Failure Criteria RSEs

The process for checking the accuracy of the composite panel failure criteria is nearly identical to that described in Section 4.1 for metallic panels. The metric used to quantify the RSE accuracy is Model Representation Accuracy (MRA), which indicates how accurately the RSE (model) is able to predict failure for randomly-generated panels. To calculate this metric, 1,000 panels are created with random applied loads, buckling spans, and laminate definitions. Each of these panels is first run through HyperSizer to establish a "truth" model of panel failure. Next, each panel was also evaluated with the failure criteria RSEs to predict failure. Comparing the two sets of results for the 1,000 panels establishes how accurately the RSEs were able to predict failure.

As with the metallic panels, this validation was performed for each of the four load quadrants separately, producing a MRA value for each quadrant. The results for the composite unstiffened laminate and I-stiffened panel are presented in the sections below.

5.1.4.1 RSE Accuracy Unstiffened Laminate

Due to the simple geometry of the unstiffened laminate, the failure criteria RSEs were able provide a highly accurate prediction of both material and stability failure modes. To improve

accuracy of buckling failure predictions, the buckling criteria was split up into two RSEs, one which captures general buckling due to compressive load and another which captures buckling due to shear loads. This was primarily done to improve buckling prediction in cases where compressive loads are small or non-existent but shear loads are high. The material failure modes were also split up for one of the load quadrants to improve accuracy, but were left grouped together for the other three quadrants. The accuracy of each of the RSEs are given in Table 26. Failure criteria that are not applicable in a particular load quadrant were left blank.

Table 26: Model Representation Accuracy (%) of Laminate Failure Criteria RSEs

RSEs	$+N_x/+N_y$	$-N_x/+N_y$	$-N_x/-N_y$	$+N_x/-N_y$
Panel Buckling	97.4	97.4	97.2	97.2
Shear Buckling	97.4	98.6	98.9	98.2
All Material Modes (Grouped)	98.7	97.2	98.3	-
Material Failure: x-Dir.	-	-	-	95.9
Material Failure: y-Dir.	-	-	-	97.1
Material Failure: xy-Dir.	-	-	-	96.0
Material Failure: Quadratic Interactions	-	-	-	96.4

5.1.4.2 I-Stiffened Panel

Table 27 gives the MRA of the failure criteria RSEs for the composite I-stiffened panel. There are more criteria to consider than for the unstiffened plate due to the higher geometric complexity of the I-stiffened panel. In Table 27, the stability criteria are listed first, followed by the material failure criteria. Similar to the previous results, the RSEs were split into four load quadrants to improve accuracy. Failure criteria that are not applicable in a particular quadrant were left blank.

Overall, the RSEs are slightly less accurate than those for the unstiffened laminate discussed previously because of increased complexity. However, the accuracy of all the RSEs still exceeds the targeted 90% minimum.

5.2 Stiffness-Based Objective Function

To be able to perform optimization of the composite panels in the stiffness domain, it is necessary to have a function capable of accurately calculating panel mass from terms in the

Table 27: Model Representation Accuracy (%) of Composite I-Stiffened Panel Failure Criteria RSEs

RSEs	$+N_x/+N_y$	$-N_x/+N_y$	$-N_x/-N_y$	$+N_x/-N_y$
Panel Buckling	-	97.3	93.7	96.2
Stiffener Buckling	-	91.3	94.3	-
Crippling	-	93.2	91.8	-
Local Buckling: Facesheet	97.2	92.1	94.7	95.5
Local Buckling: Spacing Span	95.1	93.4	94.6	96.5
Material Failure: All Facesheet Modes	95.1	95.3	95.0	93.0
Material Failure: Facesheet x-Dir.	95.8	94.4	-	94.1
Material Failure: Facesheet y-Dir.	96.1	95.7	-	96.2
Material Failure: Facesheet xy-Dir.	97.4	95.5	-	95.4
Material Failure: Bonded Combo	94.3	93.1	93.6	92.4
Material Failure: Web	98.7	97.9	98.5	98.1
Material Failure: Bottom Flange	98.7	98.0	97.9	97.6

stiffness domain. This is more challenging for composite panels because ply angle variation within the panel can cause a panel of a fixed mass to have a wide range of possible stiffness values. Thus, calculating mass from the stiffness domain can potentially be inaccurate depending on the stiffness terms used. The steps taken to mitigate this inaccuracy are presented in the sections below for the unstiffened laminate and the I-stiffened panel.

As with the metallic panel presented in Chapter 3, unit mass (UM) is used for the panel so that the mass efficiency of the panel can be described independently from the overall size of the panel. Unit mass has dimensions of lbm/ft^2.

5.2.1 Objective Function for the Unstiffened Laminate

Calculation of mass is straight-forward for the unstiffened laminate because thickness of the panel (t) was included in the variables selected for optimization, in addition to panel stiffness terms (as described in Section 5.1.2.1). The unit mass of the unstiffened laminate is directly proportional to the thickness of the laminate. Equation 60 shows how the unit mass for the unstiffened laminate is calculated from thickness. The coefficient in this equation represents the density of the material times a conversion factor of 144 in^2/ft^2.

$$UM = 8.208 \cdot t \tag{60}$$

5.2.2 Objective Function for the I-Stiffened Panel

For the metallic I-stiffened panel, the mass of the panel could be directly related to the smeared stiffness terms of the panel because the material stiffness and density were fixed. The same can not be said for composites because ply angle variation changes the stiffness of the material while maintaining the same density. Thus, it is not possible to develop a perfect linear relationship between panel mass and the smeared stiffness terms. To demonstrate this, regression was used to create a linear function of A_{11}, A_{22}, A_{33}, D_{11}, and D_{22} that predicts the Unit Mass (UM) of the I-stiffened panel. The resulting function is given in Equation 61.

$$UM = 0.5584 + 3.842 \cdot 10^{-7} \cdot A_{11} 3.454 \cdot 10^{-7} \cdot A_{22} 7.645 \cdot 10^{-7} \cdot A_{33} 5.446 \cdot 10^{-8} \cdot D_{11} 9.275 \cdot 10^{-7} \cdot D_{22} \tag{61}$$

The equation given above provides only an *approximation* of UM, so there will be some associated error. Figure 94 shows a distribution of prediction error resulting from a test of prediction ability for randomly-generated panel designs. This amount of error found in Figure 94 indicates that a function of panel stiffness terms alone is not accurate enough to be used for mass calculation in a panel optimization environment. To resolve the error in the mass calculation, it is necessary to introduce a physical dimension to the set of variables used in the optimization.

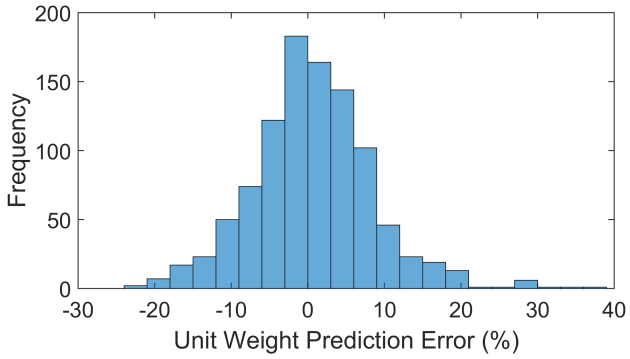

Figure 94: Error Distribution for Linear ABD Prediction of Unit Mass

In adding a new term, it is desired is to achieve an exact linear relationship with the UM of the panel. The term which provides this relationship is the cross-sectional area of the

panel divided by the stiffener spacing (A/S). Equation 62 describes the relationship between the two terms. The coefficient in this equation represents the density of the material times a conversion factor of 144 in^2/ft^2. Note that the coefficient is that same as for the unstiffened laminate, indicating that the A/S term is essentially an equivalent smeared thickness.

$$UM = 8.208 \cdot (A/S) \tag{62}$$

The addition of the A/S term brings the total number of terms to six, compared to the 14 needed in the physical domain. Introduction of the A/S term causes a few small differences from the metallic panel optimization, but the process remains mostly the same. Mainly, the A/S term must be included in the RSEs discussed in the previous section. Additionally, the interaction limits between A/S and the other stiffness terms must be defined, as shown in the next section.

5.3 Stiffness-Based Design Space Boundaries

As was described in Section 3.5.3 for the metallic panel, boundaries are needed in the stiffness-based design space to ensure that only physically realizable combinations of stiffness terms are selected. The process for composite panels is very similar. The primary difference is that the interactions between the stiffness terms are broader than the metallic panel due to the stiffness variability introduced by ply angle variation. This can be observed in Figure 95 below. The figure contains a plot of points randomly generated in the physical domain and mapped to the stiffness domain, for both a metallic and composite I-stiffened panel.

For a simple metallic flat plate, the relationship between A_{22} and A_{11} would be perfectly linear. The dispersion of A_{22} versus A_{11} for the metallic I-stiffened panel show above is due to the influence of the stiffener attached to the skin. The fan-shaped dispersion shown for the composite panel is due to the range of stiffness allowed by ply angle variation. Similar plots for other stiffness terms can be found in Figure 166 in Appendix A.

Once domain boundaries are developed to handle this dispersion, these are applied as constraints in the Simplex Algorithm, just like the domain boundaries for the metallic panel. The process of applying linear constraints to the Simplex optimization is described in Section 3.6.2.

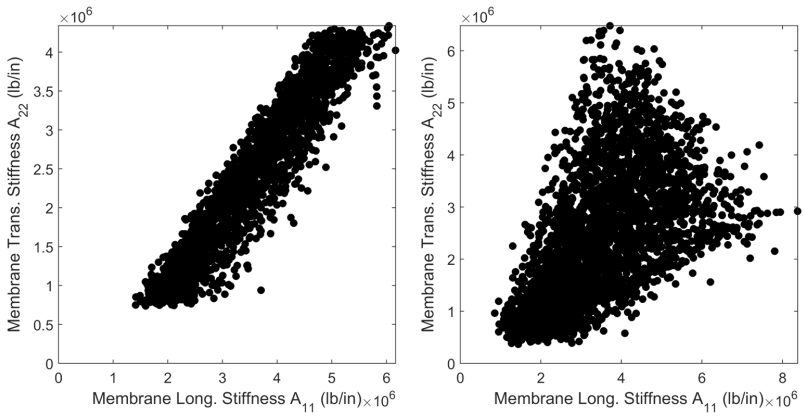

Figure 95: Comparison of A_{22} versus A_{11} Distribution for Metallic and Composite Panels

5.3.1 Stiffness Boundaries for the Unstiffened Laminate

The stiffness domain boundaries for the unstiffened laminate are more simple than the I-stiffened panel because of the selected parametrization. The variables t, r, and s in the stiffness domain for the unstiffened laminate do not exhibit any interactions that must be constrained, as shown in Figure 165 of Appendix A. This means any combination of t, r, and s can be mapped back into the physical domain. However, there are interactions with the bending terms that must be constrained against, as shown in Figure 96. The remainder of the stiffness domain boundaries are given in Appendix D.2.

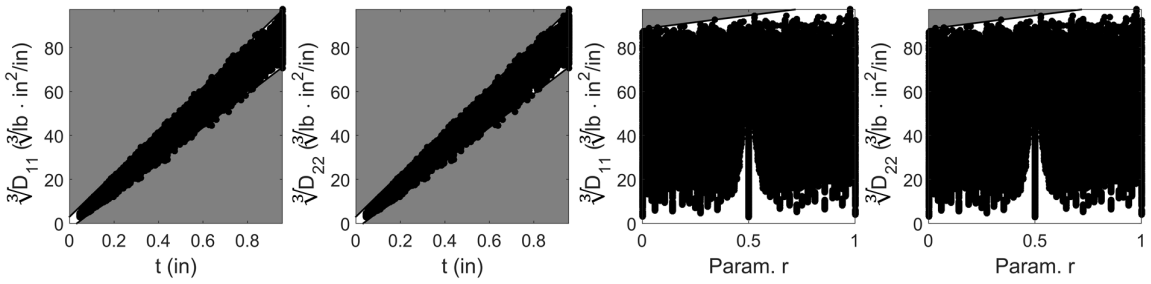

Figure 96: Variable Interaction Constraints for Composite Unstiffened Laminate

One aspect of the stiffness domain constraints for the composite laminate that differs from the metallic panel is the use of a cube root to improve the fit of the bending constraints. For example, the point cloud in the leftmost plot of Figure 96 has a significantly nonlinear trend when plotted as D_{11} versus t. Because the stiffness constraints must be linear to be

used in the Simplex Algorithm, error would arise in attempting to bound a nonlinear point cloud. Thus, taking the cube root of the D_{11} and D_{22} regression points makes the point cloud of regression points more suitable to be bounded by linear constraints.

Note that this approach requires $\sqrt[3]{D_{11}}$ and $\sqrt[3]{D_{22}}$ to be used as independent variables for the failure criteria RSEs, instead of D_{11} and D_{22} directly. This has a slight adverse effect on the failure criteria RSE accuracy, but the accuracies are all still high as presented previously in Section 5.1.4.1.

5.3.2 Stiffness Boundaries for I-Stiffened Panel

The stiffness interactions for the composite I-stiffened panel are handled in a manner very similar to the metallic I-stiffened panel, by adding linear constraints that enforce the boundaries of the physical domain when mapped to the stiffness domain. Figure 97 shows an example of some of the enforced boundaries for the composite I-stiffened panel. The rest are given in Section D.3 of Appendix D.

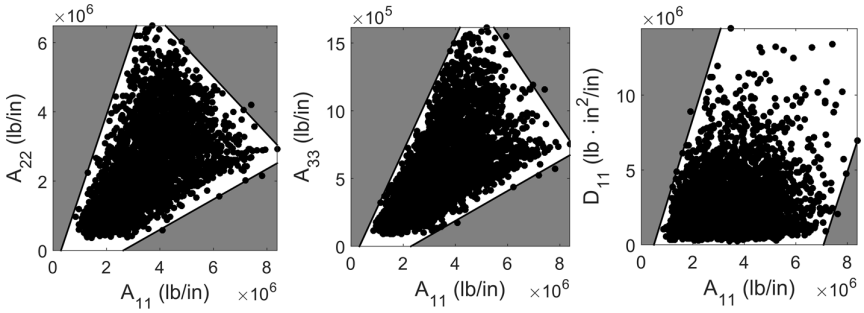

Figure 97: Application of Linear Constraints to Map Boundaries of Physical Domain to Stiffness Domain for Composite I-Stiffened Panel

5.4 Validation of Mass Optimization

As with the metallic panel, it is necessary to perform validation of the optimized mass to ensure that all contributing parts (failure criteria RSEs, stiffness interaction boundaries, and stiffness-based objective function) work together correctly. It is not sufficient to perform validation on each part independently, so the final optimization results are compared against a high-fidelity optimization to ensure the process as a whole is accurate.

The process for mass validation is essentially identical to that of the metallic I-stiffened panel presented in Section 4.2, aside from the difference in material parameters. A set of 200 data points was created consisting of randomly-generated panel loads and buckling spans to be optimized. The data points were first optimized in HyperSizer with a high-resolution design space exploration to establish the "true" optimum mass. Next, the same design points were optimized with the stiffness-based methodology developed in this research. The resulting mass from the two optimizations of each data point were compared to establish a percent accuracy for the methodology.

The same three error metrics are used for the composite panel validation as were presented for the metallic panel in Section 4.2. These were average error ($\bar{e}$), root mean square of the error (e_{rms}), and standard deviation of the error (σ_e). These three statistics were needed to represent the error of all 200 test points as digestible metrics. Refer to Figure 77 in Section 4.2 for a visual representation of these metrics. In general, lower values of these metrics indicate that the stiffness-based optimization is more accurate.

A calibration was also applied to the optimized mass of the composite panels to further improve accuracy. The error before and after calibration is presented below for the unstiffened laminate and the I-stiffened panel.

5.4.1 Optimization Validation for the Unstiffened Laminate

Table 28 and 29 display the uncalibrated and calibrated error, respectively, for optimized unit mass. For the uncalibrated error, the mean value for some of the load quadrants are unsatisfactory. However, this is easily corrected in the calibration by shifting all of the values up or down. Table 29 shows that the corrected mean error is near zero for each load quadrant. Although the mean value of the uncalibrated distribution shows some error, the standard deviation indicates an accurate representation of the mass trends. This metric provides the best indication of how well the stiffness-based optimization captures the mass trend as a function of applied load. In the calibrated data set, standard deviation of the error is improved further.

The primary source of error in the results shown above is due to prediction problems

Table 28: Uncalibrated Error (%) for Predicting Optimum Panel Mass - Unstiffened Laminate

Metric	$+N_x/+N_y$	$-N_x/+N_y$	$-N_x/-N_y$	$+N_x/-N_y$
$\bar{e}$	-19.03	-13.70	-13.97	-11.33
e_{rms}	22.21	14.65	15.55	14.96
σ_e	11.49	5.18	6.86	9.80

Table 29: Calibrated Error (%) for Predicting Optimum Panel Mass - Unstiffened Laminate

Metric	$+N_x/+N_y$	$-N_x/+N_y$	$-N_x/-N_y$	$+N_x/-N_y$
$\bar{e}$	-0.64	-1.13	-1.75	-0.26
e_{rms}	6.21	5.26	5.19	5.41
σ_e	6.20	5.15	4.90	5.42

at minimum gauge of the structure. This is made evident by the fact that the x-tension/y-tension load quadrant has the greatest error. This load state is less severe than compression, resulting in more panels that are at the minimum gauge allowed for the panel.

5.4.2 Optimization Validation for the I-Stiffened Panel

Table 30 and 31 display the uncalibrated and calibrated error, respectively, for optimized unit mass of the composite I-stiffened panel. The discussion given above for the unstiffened laminate is applicable to this panel concept.

Table 30: Uncalibrated Error (%) for Predicting Optimum Panel Mass - I-Stiffened Panel

Metric	$+N_x/+N_y$	$-N_x/+N_y$	$-N_x/-N_y$	$+N_x/-N_y$
$\bar{e}$	-5.68	-29.08	-15.93	-21.19
e_{rms}	15.83	31.45	18.3	23.06
σ_e	14.81	12.02	9.04	9.11

The primary source of error for this panel concept is accurately mapping the boundaries of the physical domain to the stiffness domain. This concept is discussed in Section 5.3. The composite I-stiffned panel is more challenging to handle because the boundaries in the stiffness domain are more irregular and thus more difficult to represent with linear constraints. Steps can be taken to reduce this problem as described in Section 9.2.1.

Table 31: Calibrated Error (%) for Predicting Optimum Panel Mass - I-Stiffened Panel

Metric	$+N_x/+N_y$	$-N_x/+N_y$	$-N_x/-N_y$	$+N_x/-N_y$
$\bar{e}$	-6.36	-4.04	-0.77	0.75
e_{rms}	11.45	8.69	6.29	6.86
σ_e	9.55	7.72	6.26	6.83

5.5 Accuracy versus Efficiency

As was done for the metallic I-stiffened panel, it is important to characterize the efficiency of the new panel methodology compared to HyperSizer. This section uses an approach identical to the one presented in Section 4.4. As before, "accuracy" in this context refers to similarity to the global optimum solution. For both the unstiffened laminate and the composite I-stiffened panel, a large number of HyperSizer optimizations were performed to establish the lower bound of performance available from the full-factorial solution. This lower bound represents the optimization accuracy and efficiency that would be expected from starting the optimization with no prior knowledge about the solution.

5.5.1 Unstiffened Laminate

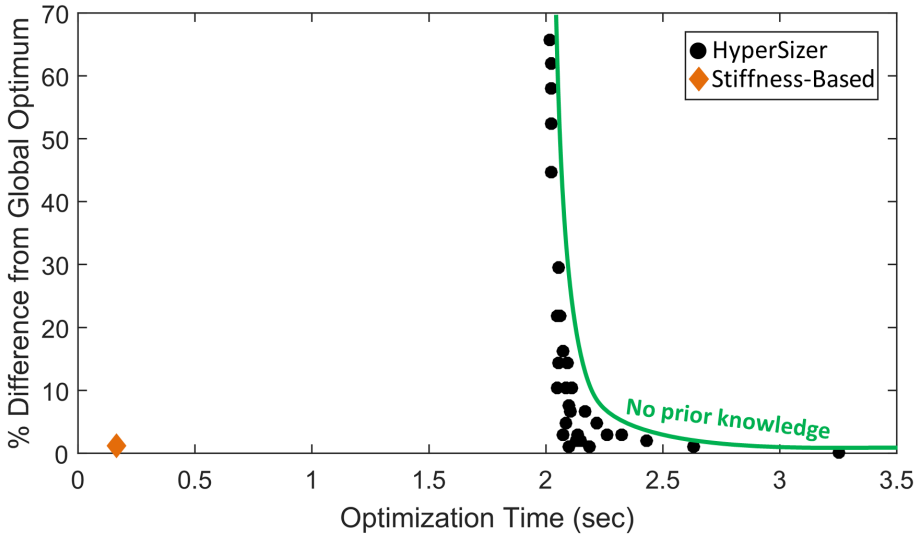

Figure 98: Accuracy versus Efficiency for the Composite Laminate

The accuracy versus efficiency data for the composite unstiffened laminate is given in Figure 98. The improvement in efficiency over HyperSizer is substantially less for the

composite laminate than was found previously in Section 4.4 for the metallic I-stiffened panel. This is to be expected because HyperSizer has fewer variables to optimize for the unstiffened composite laminate: thickness, percent 0° , percent 45° , and percent 90° plies.

The net shift of the HyperSizer points on the time axis of Figure 98 represents the time it takes for HyperSizer to generate discrete laminate representations for the panel, which is approximately two seconds.

In comparison to the HyperSizer design points, the stiffness-based point (Simplex) has a significant advantage in efficiency and accuracy. The Simplex Algorithm executes in 0.16 seconds per panel on average. This result is also shown on Figure 98.

5.5.2 I-stiffened Panel

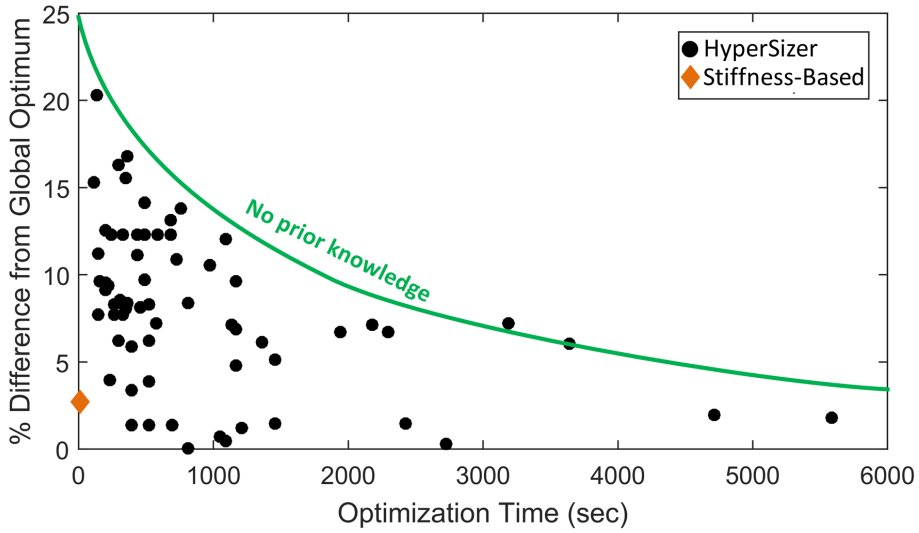

Figure 99: Accuracy versus Efficiency for the Composite I-Stiffened Panel

The composite I-stiffened panel has a significantly higher penalty to efficiency for improved accuracy compared to the unstiffened laminate shown above (for HyperSizer). Figure 99 shows the approximate curve that trades optimization accuracy for efficiency, assuming no prior knowledge of the design space. The poor efficiency is due to the high number of design variables for this panel. The composite I-stiffened panel has six more variables than the metallic I-stiffened panel (in the physical domain) for a total of 14, making optimization more time-consuming.

In the stiffness domain, there is only one more variable for the composite panel than for the metallic panel (the term A/S). Thus, the stiffness-based optimization is only slightly slower for the composite panel compared to metallic. Run time with the stiffness-based optimization is 0.18 seconds for this example. Compared to the HyperSizer curve in Figure 99, this optimization is vastly more efficient, by a factor of approximately 36,000. This result shows that the stiffness-based optimization methodology developed in this research has the biggest advantage for composite I-stiffened panels.

CHAPTER VI

METHODOLOGY FOR COUPLING WITH A FINITE ELEMENT MODEL

To transition from the panel-level methodology presented in the previous three chapters to the global FEM -based optimization in the next two chapters, it is necessary to discuss the approaches used to couple the panel level and global (FEM) level. This chapter provides the details on the interface between the panel-level optimization and the global optimization. The FEM -based examples presented in Chapters 7 and 8 cover optimization of a metallic wing box and a composite wing, respectively. These two examples use slightly different approaches to couple the local and global level. These different approaches are treated separately as necessary, but the majority of methodology discussed in this chapter is general enough to cover both examples.

The most basic FEM coupling that can be achieved is for basic mass optimization. An initial estimate of mass can be achieved by using the panel loads from FEA results and performing panel optimization on each panel independently. This approach only requires one-directional coupling, passing the loads from FEA to the panel optimizer. The next level of sophistication is to iterate with FEA to converge the load path. Each time panel optimization is performed, the FEM is updated with the optimum design, and FEA is rerun, repeating until converged. This approach requires bi-directional coupling because loads are passed from FEA to the panel optimizer, and updated stiffnesses are passed from the panel optimizer to the FEM . A further level of sophistication is to add constraints at the FEM level, which also requires bi-directional coupling. The examples presented in Chapters 7 and 8 fall into this category.

The global FEM /FEA based constraints mentioned above can come from a variety of sources. One example is aeroelasticity constraints. These can be in the form of required global stiffness (such as a required bending stiffness at specific locations in a wing), deflection

limits (such as maximum wing tip deflection or twist), or natural frequency limits. The first two are typical of static aeroelasticity constraints, and the third is from dynamic aeroelasticity.

Another type of common global structural constraints are for resistance to global buckling. Global buckling is dependent on the overall stiffness of a FEM , thus requiring constraints on global stiffness to achieve a desired buckling eigenvalue (as determined by FEA). Global buckling constraints are typically more challenging to satisfy than local buckling constraints, which can be checked analytically.

To support the objectives discussed above, this chapter first presents the bi-level optimization approach used for the FEM -based examples given in this research. This includes a description of the data transfer needed between the local and global level, as well as the algorithms used at each level. Next, methodology is presented to handle control of stiffness distributions at the global level, necessary to meet stiffness-based constraints as discussed above. The last section in this chapter provides a description of how FEM stiffness is updated from panel optimization results, which is necessary for bi-direction FEM coupling.

6.1 Bi-Level Optimization Approach

As discussed in Section 2.5, bi-level optimization is usually required any time global constraints are considered in structural optimization with a FEM . The problem naturally decomposes into a local and global level. The "local" level is synonymous with panel-based optimization, where loads and geometry are assumed to be constant over the area of the panel. The independent variables at the local level are usually panel design dimensions (thickness, flange width, etc). The "global" level refers to the FEM as a whole. Independent variables at the global level can vary depending on the global objective. Usually, FEM stiffness is controlled at the global level for the purpose of meeting deflection and global buckling constraints.

The general interaction between the local and global level has been discussed previously in 2.5. The intent of this section is to describe the optimization that drives the flow chart presented in Figure 20 in Section 2.5.

The bi-level process as a whole is controlled by the global optimizer. The objective of the global optimizer is to minimize total mass of the structure (FEM). The global optimizer must also satisfy all stiffness constraints imposed on the structure. For each step taken by the global optimizer, local optimization must be performed for each panel. The two cannot be performed independently because values selected for the global variables must be enforced at the local level. For example, if a stiffness distribution is prescribed at the global level, each local optimization is constrained to produce a stiffness which matches the global distribution at the location of the panel.

Figure 100 illustrates the data exchanged between the local and global optimization. Conceptually, Figure 100 is similar to the process presented previously in Figure 20 of Section 2.5. The new representation given in Figure 100 is focused on showing how the actual code architecture is set up to execute the bi-level optimization. The main difference from Figure 20 is that the feedback and feed-forward loops have been simplified to only those relevant to the code used to run the optimization. Additionally, the load extraction process is identified because it is an important part of the bi-level architecture. Lastly, the local optimization identified in Figure 100 is the stiffness-based optimization developed in Chapter 3, rather than optimization in the physical domain as shown in Figure 20.

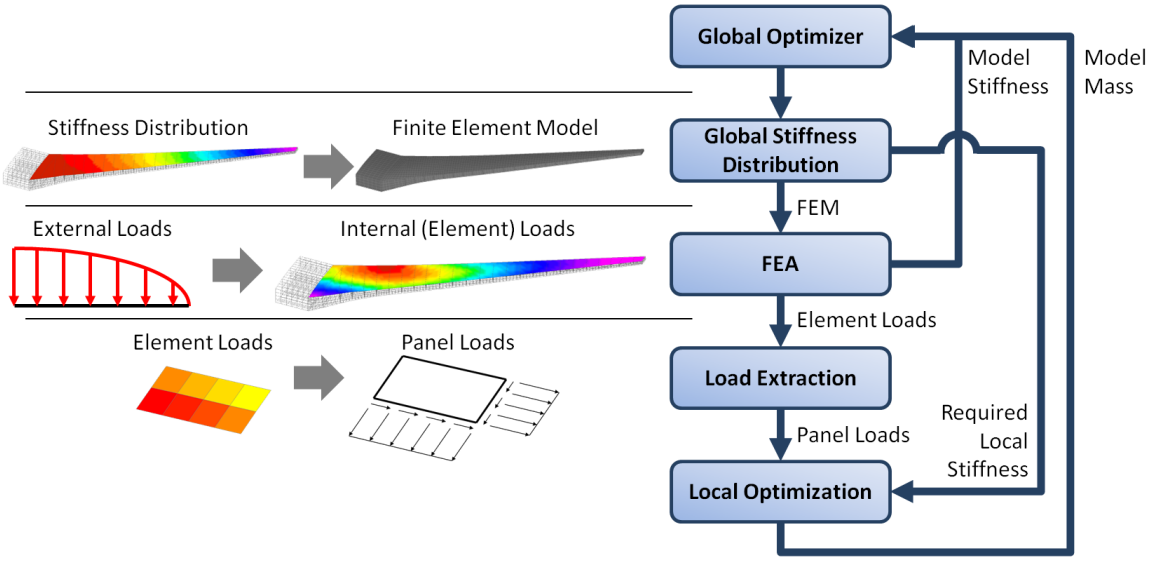

Figure 100: Outline of Iteration Process for Structural Optimization with a FEM

The first step of the process is for the global optimizer to establish a global stiffness distribution. This can be accomplished in a variety of ways, depending on the selected global variables and the chosen method for controlling the distribution. This topic is discussed in detail in the next section. Once the global stiffness distribution is specified, it is combined with the geometry mesh to establish the FEM . External loads are then applied to the FEM to derive the internal loads in each element. For each panel, the element loads are used to build equivalent panel loads, which are assumed to be uniform over the area of the panel. For the applications considered in this research, the panel loads are calculated from the area-weighted average of the elements. With these panel loads, as well as the local required stiffness value (specified from the global level), panel optimization is performed. Optimization of all the panels in the structure establishes the total structural mass, which is passed back to the global level. Additionally, resulting global stiffness information is passed back to the global level. This can be in the form of displacements, cross-sectional stiffnesses, or eigenvalues in the case of global buckling.

Having introduced the overall flow of the optimization process, the following two subsections describe the actual optimization algorithm used within the two levels of the bi-level environment.

6.1.1 Global Optimization Algorithm

The global optimizer essentially drives the entire process; each step taken by the global optimizer dictates loads and stiffnesses used by the local optimizer. The global optimizer uses a Compass Search algorithm [113], selected for its simplicity and easy customization. The objective of the FEM -based optimizations performed in this research is primarily to demonstrate ability to integrate the novel panel optimization, so simplicity is preferred over performance at the global level. Another key feature necessary for the global optimizer is to be able to control step size, which is difficult to do with more advanced gradient-based methods. Step size control is necessary because the nature of the optimization requires each iteration to initially use loads from the previous iteration. Thus, step size must be kept relatively small to avoid convergence issues.

Note that the Compass Search algorithm is not considered to be among the fastest optimization algorithms available, but was only chosen for its ease of implementation. The focus of the FEM -based examples in this research is not to demonstrate the global optimization algorithm, but instead to demonstrate the implementation of the rapid local optimization discussed previously.

The Compass Search algorithm works by checking one direction at a time, until a feasible point is found with a lower total mass than the current point. A "direction" is defined as a positive or negative change to a single variable. The optimizer then steps to this new point and repeats the process. Figure 101 provides an example of iterations performed by this algorithm in a design space with two variables.

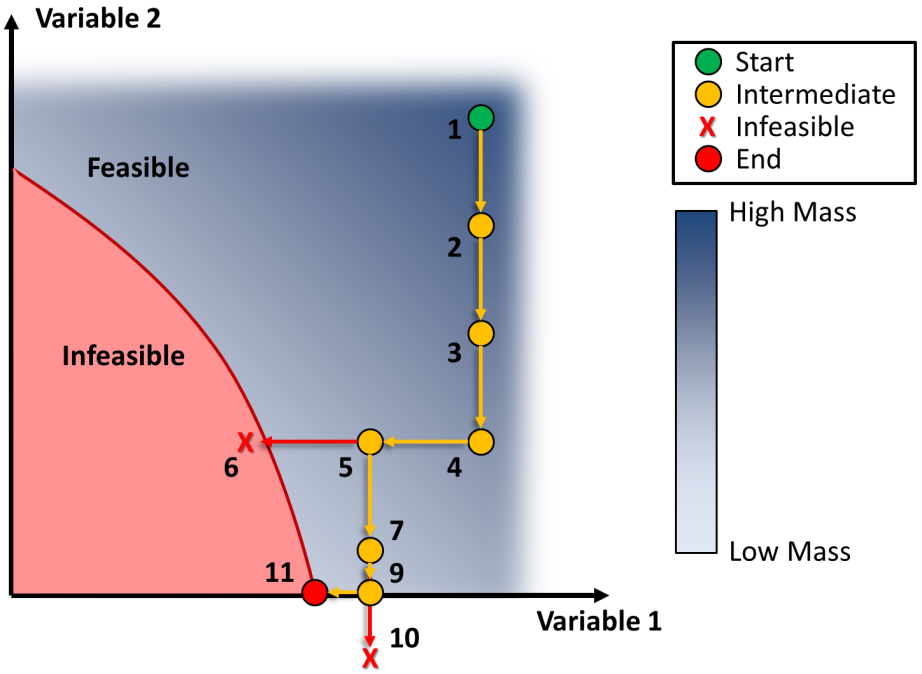

Figure 101: Example Iterations of Compass Search Algorithm

For each design point checked, the optimizer generates a set of control points that are used to create a unique stiffness distribution over the structure. This distribution is used to generate a new FEM and run FEA to get new loads. Then the local optimizer is run to determine the mass of the panels. To do this, the local optimizer finds a combination of panel stiffness terms that correspond to a panel that has minimum mass while still satisfying local failure criteria.

6.1.2 Local Optimization Algorithm

The algorithm used at the local level has been previously developed in extensive detail in Chapter 3. In particular, Section 3.6 describes how the optimization is performed. Thus, the process will not be described again here in detail. To recap, the local optimization uses a linearized representation of failure criteria in the stiffness domain which is solved by the Simplex Algorithm.

6.2 Controlling Global Stiffness Distribution

This section describes the approach taken in this research to drive global stiffness distributions over a structure. The most basic approach possible for defining the distribution is to simply have a global variable for every single panel that defines the required stiffness of that panel. However, this approach is cumbersome because it requires a large number of global variables (200 panels equals 200 global variables). An additional drawback is that significant discontinuities can occur in the stiffness distribution unless there are constraints which limit the relative difference in stiffness between adjacent panels.

Considering the drawbacks described above, a different approach was selected to drive the global stiffness distributions for the examples presented in this research: use of polynomial functions. A polynomial function provides significantly better characteristics in the two categories described above. The shape of the function can be controlled by a small number of variables. The exact number of control points depends on desired order of the function. Higher order functions allow more fluctuations in the stiffness distribution over the structure, but also require more control points. An additional benefit of using polynomial functions is that they always provide a smooth and continuous stiffness distribution. This increases the likelihood that the stiffness distribution can be related to a manufacturable design; structures are usually not constructed with large discontinuities in skin or stiffener design.

The two subsections below describe the specific ways in which polynomial functions were used to control the global stiffness distribution over the FEMs in the two optimization examples presented in Chapters 7 and 8. Application of the algebraic surface is different

between the two examples due to a difference in goals.

6.2.1 Setup for I-Stiffened Panel Optimization

This section describes how polynomial functions are used to drive the global stiffness distribution for the metallic wing box optimization with I-stiffened panels. Aside from the polynomial function, the remainder of the setup for this optimization is described in Chapter 7.

In the example optimization with the metallic wing box, the global-level constraint is to meet a target wing tip displacement. The most mass-efficient way to control the deflection of the tip of a wing box is through the span-wise stiffness of the top and bottom skin. In shell structures like a wing box, the axial stiffness (A_{11}) of the top and bottom of the structure have the greatest influence on the vertical bending stiffness of the structure as a whole (for a fixed airfoil thickness). Thus, the axial stiffness of the top and bottom skin of the wing box are controlled at the global level. This is similar to the approach used by S. Ragon [80] to control the vertical displacement of a wing.

Controlling A_{11} on the top and bottom skin is done with a two-dimensional polynomial function. Instead of having to specify a value for A_{11} at every single panel, five control points are used to define a distribution for the A_{11} values across the upper and lower surface of the wing box. This approach was also used by Wrenn et al. [89], except the polynomial function was one-dimensional and the independent variable was skin thickness, not stiffness.

The wing box FEM used in Chapter 7 has over 100 panels each on the top and bottom skins. An obvious advantage is gained by having an order of magnitude reduction in number of design variables at the global level. Without the polynomial function, the number of global variables would be equal to the total (top and bottom) number of panels (234). With the polynomial function, the number of global variables is equal to the total (top and bottom) number of control points for the functions (10).

A visualization of this polynomial distribution approach is shown in Figure 102. The polynomial function for A_{11} of the upper and lower skins is represented by the shaded surfaces. The five control points are indicated by the red circles on the edges of the surface

and each panel centroid is indicated by the black circles on the shaded surfaces.

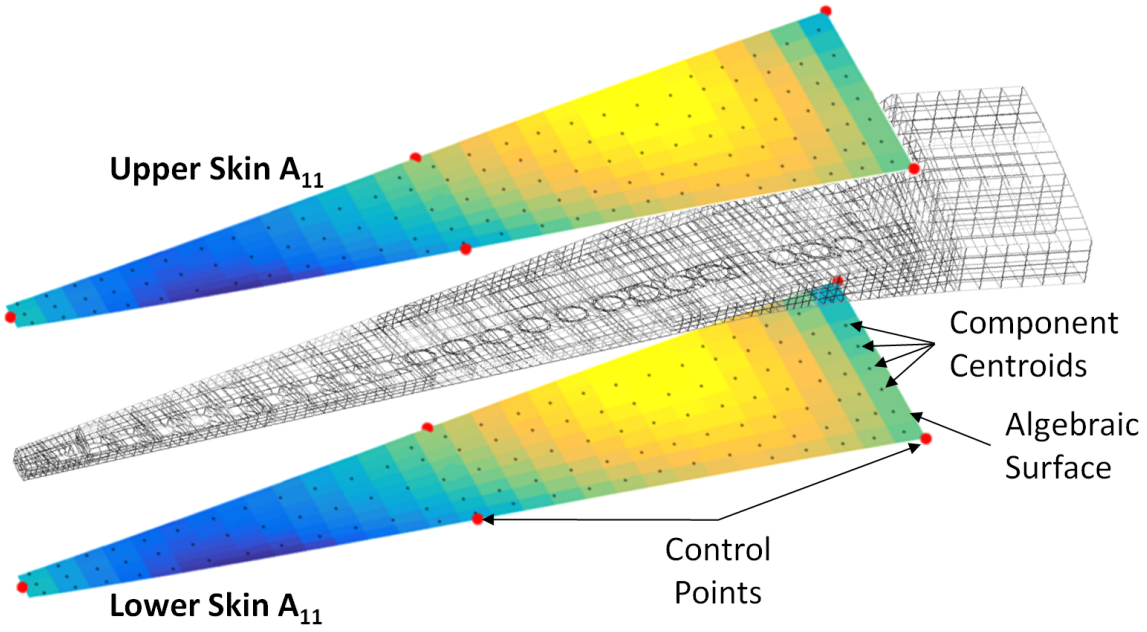

Figure 102: Stiffness Distribution Manipulation for Global Optimization

In each iteration, the A_{11} value is specified at the five control points. These values are used to determine the coefficients of the function given in Equation 63 via the matrix inversion shown in Equation 64.

$$A_{11} = R_0 + R_1 u + R_2 v + R_3 uv + R_4 v^2 \tag{63}$$

$$\begin{bmatrix} R_0 \\ R_1 \\ R_2 \\ R_3 \\ R_4 \end{bmatrix} = \begin{bmatrix} 1 & u_1 & v_1 & u_1 v_1 & v_1^2 \\ 1 & u_2 & v_2 & u_2 v_2 & v_2^2 \\ 1 & u_3 & v_3 & u_3 v_3 & v_3^2 \\ 1 & u_4 & v_4 & u_4 v_4 & v_4^2 \\ 1 & u_5 & v_5 & u_5 v_5 & v_5^2 \end{bmatrix}^{-1} \begin{bmatrix} A_{11}^{(1)} \\ A_{11}^{(2)} \\ A_{11}^{(3)} \\ A_{11}^{(4)} \\ A_{11}^{(5)} \end{bmatrix} \tag{64}$$

In Equation 64, the A_{11} function coefficients (R_i) are determined from the location of the control points. The location of the i^{th} control point for the function is defined by u_i and v_i, which are 2D chord-wise and span-wise coordinates, respectively. These quantities are used to form a 5x5 matrix, based on the form of Equation 63. The matrix is inverted, and multiplied with the vector of $A_{11}^{(i)}$ values for the control points. This calculation is

performed in each iteration of the global optimization, every time the stiffness distribution on the skins is updated.

Once the (R_i) values are defined for the current iteration, the global A_{11} distribution is fully defined. This is the point where the process interfaces with the local level. Using a list of the u_i and v_i for panel centroids, the A_{11} function is evaluated to determine the value at each panel.

For each panel, the A_{11} value defined at the global level becomes a constraint on the local optimization. The local optimizer is restricted to finding panel designs which exactly satisfy the specified A_{11} value. The methodology described in Chapter 3 is highly suitable for this task because the local optimization is formulated in terms of panel stiffness, which includes A_{11} . Thus, handling the panel A_{11} constraint is as simple as pre-substituting a design variable before the local optimization is performed. This is a contrast to a traditional local design environment, where the local optimization is in terms of physical dimensions and A_{11} is an output instead of an input. There is more complexity in a traditional local optimization because there is no way to guarantee that the A_{11} constraint will be met in every single iteration.

These topics are discussed in further detail in Chapter 7, where the optimization example with a metallic I-stiffened panel is presented.

6.2.2 Setup for Unstiffened Laminate Optimization

The global stiffness distribution setup for the unstiffened laminate optimization example is slightly different than the one described above. Primarily, the demonstration with the composite skin uses three variables at the global level instead of just one. One of the goals for the composite wing demonstration is to control the laminate definition of the skin at a global level. This requires three variables to define the number of 0° , 90° , and 45° plies. As discussed previously in Section 5.1.2.1, a unique parametrization was selected to facilitate control of three global variables using polynomial functions.

The challenge with controlling multiple global variables with polynomial functions is that it is difficult to constrain the relative values of the global variables. As an example,

consider the case where skin thickness (t), percent 0° plies (P_0), and percent 45° plies (P_{45}) were selected as the global variables. The variables P_0 and P_{45} must always have values which together sum up to be less than or equal to 80% (so that the remaining 20% can be 45° plies, the minimum allowed by the layup rules). However, P_0 and P_{45} can individually range between 20% and 60%, meaning that the sum $\leq$ 80% constraint is not necessarily satisfied automatically. This can occur when using polynomial functions to drive the variable distributions because it is not possible to always ensure that the constraint is satisfied everywhere on the structure.

To illustrate the problem described above, Figure 103 shows a distribution of percent 0° and percent 90° plies over a flat plate, dictated by a polynomial function using five control points (plotted as black circles). In both of these plots, the distribution of plies obeys the min/max bound of 20%/60%. However, the sum of these two distributions violates the 80% rule mentioned above. Although the 80% rule is satisfied at the control point locations, there are still portions of the flat plate which violate the rule. Figure 103 shows these regions with a red color gradient.

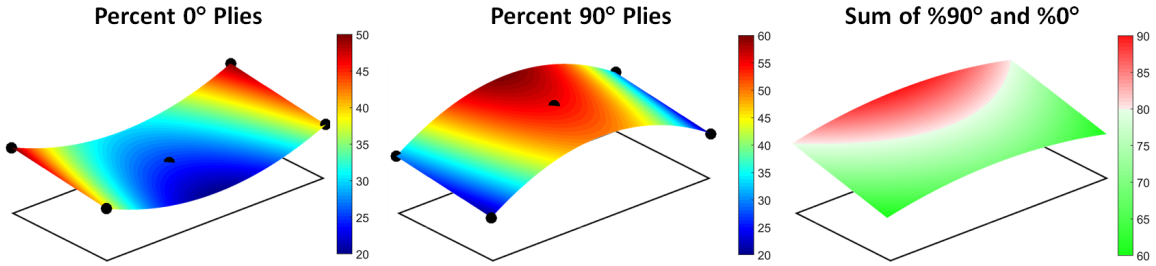

Figure 103: Example of Unsatisfactory Interaction Between Global Variables Driven by Polynomial Functions

Fortunately, these errors are avoidable by using the r-s parametrization presented in Section 5.1.2.1. This parametrization allows for ply percentages to be defined without having to deal with constraints on the relative values of the parameters. Figure 104 demonstrates this capability with the same flat plate example used above, except that the ply percentages are prescribed with the r-s parametrization. The summation of the ply percentages in Figure 104 shows that they add up to 100% in every part of the panel.

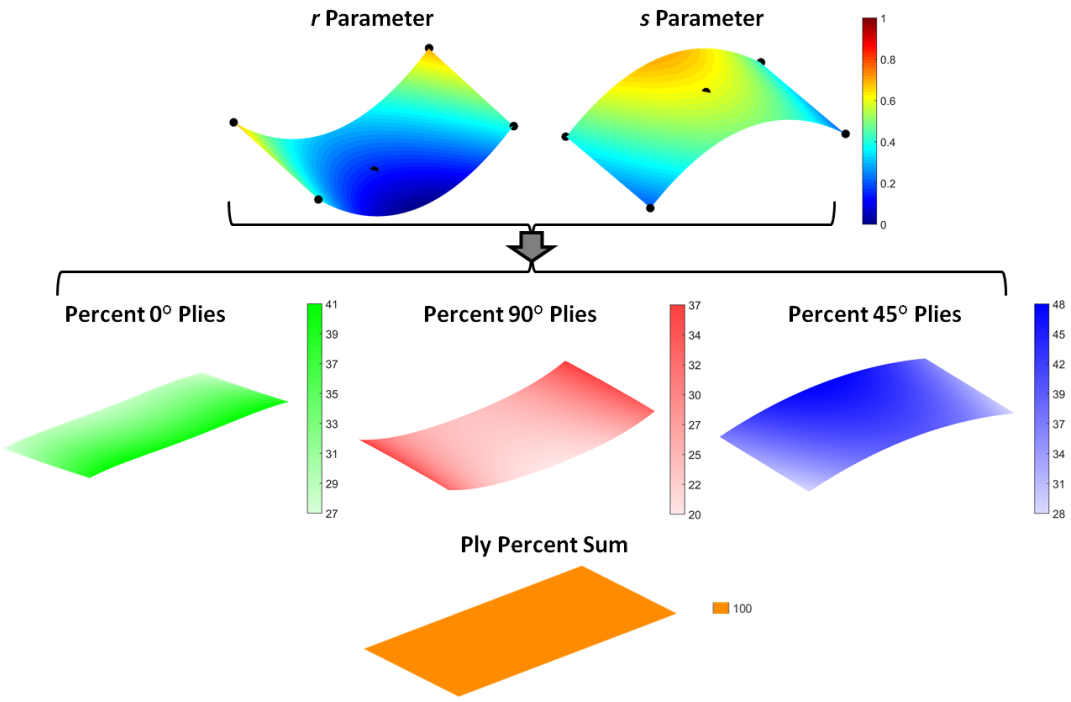

Figure 104: Example of Satisfactory Interaction Between Global Variables Using the *r*-*s* Parametrization

The demonstration in Figure 104 shows that the *r*-*s* parametrization can be effectively used in a global design environment where stiffness distributions of a composite laminate are described with a polynomial function. This parametrization is used at the global level of a composite wing skin optimization in Chapter 8.

6.3 Calculation of Full Stiffness Matrix

This section describes the final component of FEM interfacing needed to perform the global-local iterations as described in Section 6.1. This final component is calculation of the full stiffness matrix for the stiffened panels considered in this research. This is needed after local optimization has been performed for each panel and the FEM needs to be updated to get a new load path and displacement for the next iteration.

The stiffness variables as described in Section 5.1.2 for each panel type form only a small portion of the stiffness matrix needed for input to the FEM . To have a proper smeared stiffness representation of panels in the FEM , a total of 18 unique stiffness terms are needed. Although some of these can be eliminated due to assumptions made about

the panel geometry, it is necessary to develop techniques to estimate the remainder of the terms.

This challenge arises in any optimization environment that iterates with a reduced set of variables, but still has analyses that require the original set of variables. For example, the laminate stiffness trace method developed by S. Tsai [114], [115] faces a similar problem because a single value, the matrix trace (sum of the diagonal terms), is used to represent the [A], [B], and [D] matrices. The method takes advantage of the invariant property of the stiffness matrix trace to simplify the selection of optimum materials and laminate definitions considering failure criteria and stiffness requirements. After an appropriate layup pattern is selected, the optimum trace value is used to scale existing [A], [B], and [D] matrices such that they are representative of the optimum trace value.

Unfortunately, Tsai's approach is not applicable for the problem at hand because it requires a discrete set of [ABD] terms to initialize the optimization. This is not suitable for the current stiffened panel methodology because it uses a continuous optimization approach.

Thus, a new approach is needed to estimate the remaining stiffness terms. The selected approach is to perform regression of the unknown stiffness terms against the known stiffness terms. This regression is quite similar to that described in Section 3.3.4 for the failure criteria. The difference here is that the dependent variables are the unknown stiffness terms, and the panel loads are not included. However, the regression uses the same data set generated for the RSEs of Section 3.3.4. The general form of the stiffness prediction equation is shown in Equation 65.

$$[ABD]_{unknown} = f([ABD]_{variables}) \tag{65}$$

The subsections below describe specific details for developing these relations for the two panel concepts used in FEM examples in Chapters 7 and 8. Each panel has a unique set of equations that describe the unknown stiffness terms as a function of the terms that were used in the panel optimization.

6.3.1 Metallic I-Stiffened Panel

As discussed in Section 3.2.2, some of the 18 [ABD] terms are zero for the metallic I-stiffened panel due to its geometry. The remaining non-zero terms are A_{11}, A_{12}, A_{22}, A_{33}, B_{11}, B_{12}, B_{22}, B_{33}, D_{11}, D_{12}, D_{22}, D_{33}. Of these terms, A_{11}, A_{22}, A_{33}, D_{11}, and D_{22} are known because they are variables in the panel optimization, and are defined once the optimization is performed. Thus, the remaining terms must be predicted through regression of these known terms. The resulting equations for these terms are given below. Note that there is no requirement for these equations to be linear because they are only used to post-process the results of the optimization, and are not needed within the linear optimization presented in Chapter 3. The equations given for the unknown [ABD] terms were constructed from 2nd and 3rd order polynomials.

$$A_{12} = 0.009915 + 0.3403A_{22} \tag{66}$$

$$\begin{aligned} B_{11} = {} & -2.613 \cdot 10^{-15}A_{11}^3 - 3.778 \cdot 10^{-14}A_{11}^2A_{22} + 1.096 \cdot 10^{-13}A_{11}^2A_{33} \\ & - 3.809 \cdot 10^{-8}A_{11}^2 + 2.757 \cdot 10^{-7}A_{11}A_{22} + 1.212 \cdot 10^{-8}A_{11}A_{33} - 8.319 \cdot 10^{-15}A_{11}D_{11}^2 \\ & + 1.274 \cdot 10^{-7}A_{11}D_{11} + 1.72 \cdot 10^{-10}A_{11}D_{22}^2 - 1.545 \cdot 10^{-5}A_{11}D_{22} + 0.385A_{11} \\ & + 2.657 \cdot 10^{-12}A_{22}^2D_{22} - 4.107 \cdot 10^{-8}A_{22}^2 + 1.76 \cdot 10^{-10}A_{22}A_{33}D_{22} - 2.273 \cdot 10^{-6}A_{22}A_{33} \\ & + 1.981 \cdot 10^{-8}A_{22}D_{11} - 1.975 \cdot 10^{-9}A_{22}D_{22}^2 - 0.0001317A_{22}D_{22} + 0.5896A_{22} + 2.361 \cdot 10^{-10}A_{33}^2D_{22} \\ & + 3.168 \cdot 10^{-6}A_{33}^2 + 2.446 \cdot 10^{-14}A_{33}D_{11}^2 - 2.919 \cdot 10^{-12}A_{33}D_{11}D_{22} - 5.031 \cdot 10^{-7}A_{33}D_{11} \\ & - 9.193 \cdot 10^{-9}A_{33}D_{22}^2 - 0.0009848A_{33}D_{22} - 4.002A_{33} + 1.87 \cdot 10^{-15}D_{11}^3 - 2.498 \cdot 10^{-8}D_{11}^2 \\ & + 5.876 \cdot 10^{-12}D_{11}D_{22}^2 + 5.461 \cdot 10^{-6}D_{11}D_{22} + 0.2935D_{11} + 9.442 \cdot 10^{-8}D_{22}^3 + 0.009723D_{22}^2 \\ & + 855.4D_{22} + 3.362 \cdot 10^5 \end{aligned} \tag{67}$$

$$\begin{aligned} B_{12} = {} & 1.181 \cdot 10^{-9}A_{11}A_{22} - 1.417 \cdot 10^{-14}A_{11}A_{33}D_{22} - 3.733 \cdot 10^{-9}A_{11}A_{33} \\ & + 2.898 \cdot 10^{-8}A_{11}D_{22} + 0.000283A_{11} + 7.103 \cdot 10^{-14}A_{22}^3 - 8.536 \cdot 10^{-13}A_{22}^2A_{33} \\ & - 1.272 \cdot 10^{-12}A_{22}^2D_{22} + 4.882 \cdot 10^{-8}A_{22}^2 + 2.387 \cdot 10^{-12}A_{22}A_{33}^2 - 1.078 \cdot 10^{-11}A_{22}A_{33}D_{22} \\ & - 6.838 \cdot 10^{-10}A_{22}A_{33} + 9.121 \cdot 10^{-11}A_{22}D_{22}^2 + 4.451 \cdot 10^{-5}A_{22}D_{22} - 0.04451A_{22} \end{aligned}$$

$$- 1.713 \cdot 10^{-12} A_{33}^3 + 3.965 \cdot 10^{-11} A_{33}^2 D_{22} - 3.387 \cdot 10^{-7} A_{33}^2 - 1.188 \cdot 10^{-15} A_{33} D_{11} D_{22}$$
$$+1.245 \cdot 10^{-11} A_{33} D_{11} - 1.704 \cdot 10^{-10} A_{33} D_{22}^2 - 0.0001199 A_{33} D_{22} + 0.1166 A_{33} + 1.052 \cdot 10^{-9} D_{11} D_{22}$$
$$- 1.102 \cdot 10^{-5} D_{11} - 4.21 \cdot 10^{-10} D_{22}^3 - 0.0001512 D_{22}^2 + 5.838 D_{22} + 174 \quad (68)$$

$$B_{22} = 3.47 \cdot 10^{-9} A_{11} A_{22} - 4.164 \cdot 10^{-14} A_{11} A_{33} D_{22} - 1.097 \cdot 10^{-8} A_{11} A_{33}$$
$$+ 8.517 \cdot 10^{-8} A_{11} D_{22} + 0.0008316 A_{11} + 2.087 \cdot 10^{-13} A_{22}^3 - 2.508 \cdot 10^{-12} A_{22}^2 A_{33}$$
$$- 3.737 \cdot 10^{-12} A_{22}^2 D_{22} + 1.435 \cdot 10^{-7} A_{22}^2 + 7.014 \cdot 10^{-12} A_{22} A_{33}^2 - 3.167 \cdot 10^{-11} A_{22} A_{33} D_{22}$$
$$- 2.01 \cdot 10^{-9} A_{22} A_{33} + 2.68 \cdot 10^{-10} A_{22} D_{22}^2 + 0.0001308 A_{22} D_{22} - 0.1308 A_{22} - 5.035 \cdot 10^{-12} A_{33}^3$$
$$+ 1.165 \cdot 10^{-10} A_{33}^2 D_{22} - 9.954 \cdot 10^{-7} A_{33}^2 - 3.492 \cdot 10^{-15} A_{33} D_{11} D_{22} + 3.657 \cdot 10^{-11} A_{33} D_{11}$$
$$- 5.006 \cdot 10^{-10} A_{33} D_{22}^2 - 0.0003524 A_{33} D_{22} + 0.3427 A_{33} + 3.091 \cdot 10^{-9} D_{11} D_{22} - 3.238 \cdot 10^{-5} D_{11}$$
$$- 1.237 \cdot 10^{-9} D_{22}^3 - 0.0004444 D_{22}^2 + 17.16 D_{22} + 511.2 \quad (69)$$

$$B_{33} = 3.863 \cdot 10^{-14} A_{11}^2 D_{22} - 5.972 \cdot 10^{-10} A_{11}^2 - 2.915 \cdot 10^{-9} A_{11} A_{22}$$
$$- 1.149 \cdot 10^{-12} A_{11} A_{33} D_{22} + 1.528 \cdot 10^{-9} A_{11} A_{33} - 7.509 \cdot 10^{-15} A_{11} D_{11} D_{22} + 1.161 \cdot 10^{-10} A_{11} D_{11}$$
$$+ 8.042 \cdot 10^{-12} A_{11} D_{22}^2 + 1.136 \cdot 10^{-6} A_{11} D_{22} + 0.005337 A_{11} + 1.117 \cdot 10^{-13} A_{22}^3$$
$$- 1.276 \cdot 10^{-12} A_{22}^2 A_{33} - 2.272 \cdot 10^{-12} A_{22}^2 D_{22} + 4.82 \cdot 10^{-8} A_{22}^2 + 3.187 \cdot 10^{-12} A_{22} A_{33}^2$$
$$- 1.492 \cdot 10^{-11} A_{22} A_{33} D_{22} + 5.005 \cdot 10^{-7} A_{22} A_{33} + 1.973 \cdot 10^{-10} A_{22} D_{22}^2 + 6.81 \cdot 10^{-5} A_{22} D_{22}$$
$$- 0.132 A_{22} - 2.33 \cdot 10^{-12} A_{33}^3 + 2.211 \cdot 10^{-11} A_{33}^2 D_{22} - 5.524 \cdot 10^{-7} A_{33}^2$$
$$+ 4.795 \cdot 10^{-15} A_{33} D_{11} D_{22} - 9.827 \cdot 10^{-13} A_{33} D_{11} + 4.339 \cdot 10^{-10} A_{33} D_{22}^2 - 5.826 \cdot 10^{-5} A_{33} D_{22}$$
$$+ 0.04909 A_{33} + 3.601 \cdot 10^{-16} D_{11}^2 D_{22} - 5.567 \cdot 10^{-12} D_{11}^2 + 1.775 \cdot 10^{-13} D_{11} D_{22}^2$$
$$+ 1.543 \cdot 10^{-8} D_{11} D_{22} - 0.0003456 D_{11} - 4.798 \cdot 10^{-9} D_{22}^3 - 0.001439 D_{22}^2 - 84.11 D_{22} + 2.893 \cdot 10^4$$
(70)

$$D_{12} = -0.00002158 + 0.3403 * D22 \quad (71)$$

$$D_{33} = 8.384 \cdot 10^{-15} A_{11}^2 D_{22} - 1.296 \cdot 10^{-10} A_{11}^2 - 4.726 \cdot 10^{-10} A_{11} A_{22}$$
$$- 2.071 \cdot 10^{-13} A_{11} A_{33} D_{22} + 2.926 \cdot 10^{-10} A_{11} A_{33} - 1.029 \cdot 10^{-15} A_{11} D_{11} D_{22} + 1.591 \cdot 10^{-11} A_{11} D_{11}$$
$$+ 1.647 \cdot 10^{-12} A_{11} D_{22}^2 + 1.821 \cdot 10^{-7} A_{11} D_{22} + 0.001119 A_{11} + 1.359 \cdot 10^{-15} A_{22}^3$$

$$- 8.108 \cdot 10^{-14} A_{22}^2 A_{33} + 9.709 \cdot 10^{-9} A_{22}^2 + 1.386 \cdot 10^{-13} A_{22} A_{33}^2 - 4.91 \cdot 10^{-12} A_{22} A_{33} D_{22}$$
$$+ 1.571 \cdot 10^{-7} A_{22} A_{33} + 3.604 \cdot 10^{-11} A_{22} D_{22}^2 + 1.287 \cdot 10^{-5} A_{22} D_{22} - 0.03074 A_{22}$$
$$+ 1.865 \cdot 10^{-12} A_{33}^2 D_{22} - 1.58 \cdot 10^{-7} A_{33}^2 - 1.718 \cdot 10^{-16} A_{33} D_{11} D_{22} + 2.656 \cdot 10^{-12} A_{33} D_{11}$$
$$+ 1.768 \cdot 10^{-10} A_{33} D_{22}^2 + 3.767 \cdot 10^{-6} A_{33} D_{22} - 0.01015 A_{33} + 4.817 \cdot 10^{-17} D_{11}^2 D_{22}$$
$$- 7.446 \cdot 10^{-13} D_{11}^2 + 3.608 \cdot 10^{-9} D_{11} D_{22} - 5.577 \cdot 10^{-5} D_{11} - 1.33 \cdot 10^{-9} D_{22}^3 - 0.0003905 D_{22}^2$$
$$- 28.92 D_{22} + 8966 \quad (72)$$

These estimation equations correspond to the trends that can be observed in the scatter plots of Figure 164 in Appendix A. The regression sorts out which of the known variables correlates best (having low scatter in Figure 164) with the unknown [ABD] terms. Using this approach the unknown [ABD] terms can be accurately estimated. Figure 105 displays the error distributions for each of these terms. Note that the accuracy for A_{12} and D_{12} is not plotted because these two terms are linearly proportional to A_{22} and D_{22}, respectively, and thus can be predicted with 100% accuracy.

6.3.2 Unstiffened Laminate

The regression process described above is also used to generate [ABD] estimation equations for the unstiffened composite laminate. The only difference is in the independent variables. For this panel concept, the known variables are t, r, s, D_{11}, and D_{22}. In addition to the terms that were estimated for the previous panel concept, A_{11}, A_{22}, and A_{33} must be included because they were not used as optimization variables for the unstiffened panel. The terms D_{13} and D_{23} must also be estimated because they are non-zero for the unstiffened laminate. Fortunately, all of the [B] matrix terms are zero because the laminates used for optimization are all balanced and symmetric. The equations for estimating the remaining terms are shown below.

$$A_{11} = 6.968 \cdot 10^6 trs - 6.968 \cdot 10^6 tr - 5.192 \cdot 10^6 ts + 1.273 \cdot 10^7 t - 29.61 r^3$$
$$+ 3.933 \cdot 10^{-5} r^2 D_{11} - 5.16 \cdot 10^{-5} r^2 D_{22} + 45.76 r^2 + 7.64 rs + 1.934 \cdot 10^{-11} r D_{11} D_{22}$$
$$- 4.162 \cdot 10^{-5} r D_{11} + 4.886 \cdot 10^{-5} r D_{22} - 20.86 r - 4.312 s - 9.621 \cdot 10^{-12} D_{11} D_{22} + 1.097 \cdot 10^{-5} D_{11}$$

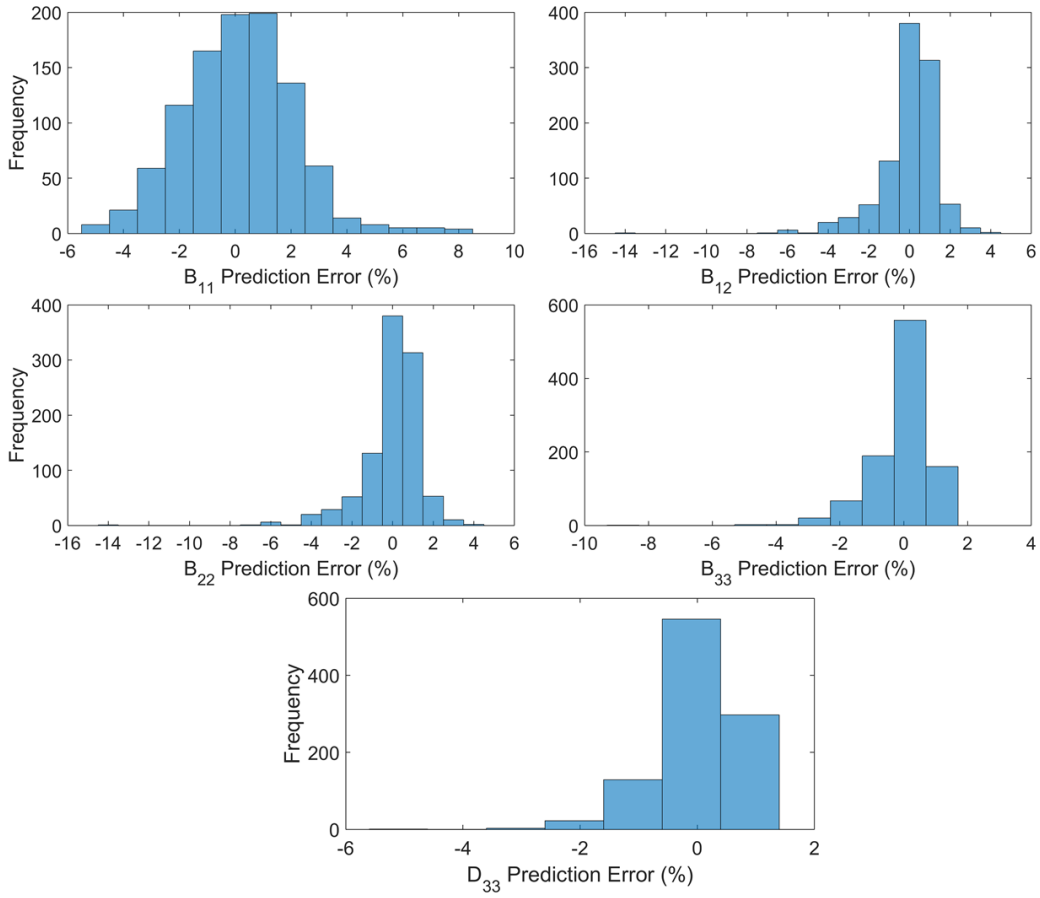

Figure 105: Prediction Error for B_{11}, B_{12}, B_{22}, B_{33}, and D_{33}

$$- 1.154 \cdot 10^{-5} D_{22} + 2.79 \quad (73)$$

$$A_{12} = 4.106t^3 - 23.72t^2 + 1.708 \cdot 10^6 ts - 1.073 \cdot 10^{-5} tD_{11} - 1.074 \cdot 10^{-5} tD_{22}$$
$$+ 1.327 \cdot 10^6 t - 1.438s^2 + 1.065s + 2.055 \cdot 10^{-5} D_{11} + 2.056 \cdot 10^{-5} D_{22} - 0.4535 \quad (74)$$

$$A_{22} = -6.968 \cdot 10^6 trs + 6.968 \cdot 10^6 tr + 1.775 \cdot 10^6 ts + 5.763 \cdot 10^6 t + 30.12r^3$$
$$- 4.194 \cdot 10^{-5} r^2 D_{11} + 5.057 \cdot 10^{-5} r^2 D_{22} - 46.07r^2 - 7.882rs - 1.931 \cdot 10^{-11} rD_{11} D_{22}$$
$$+ 4.42 \cdot 10^{-5} rD_{11} - 4.785 \cdot 10^{-5} rD_{22} + 20.79r + 3.874s + 9.605 \cdot 10^{-12} D_{11} D_{22} - 1.161 \cdot 10^{-5} D_{11}$$
$$+ 1.129 \cdot 10^{-5} D_{22} - 2.646 \quad (75)$$

$$A_{33} = -20.48t^2 + 1.708 \cdot 10^6 ts - 8.976 \cdot 10^{-6} tD_{11} - 8.989 \cdot 10^{-6} tD_{22}$$

$$+ 1.397 \cdot 10^{6} t - 1.318 s^{2} + 0.9481 s + 2.003 \cdot 10^{-5} D_{11} + 2.004 \cdot 10^{-5} D_{22} - 0.4074 \quad (76)$$

$$D_{12} = 8.812 \cdot 10^{5} t^{3} + 0.09932 t^{2} - 0.008681 ts - 0.02142 t + 0.02309 r^{2} s - 0.008236 r^{2}$$
$$+ 3.626 \cdot 10^{-7} rsD_{11} - 3.645 \cdot 10^{-7} rsD_{22} - 0.02273 rs - 1.344 \cdot 10^{-7} rD_{11} + 1.351 \cdot 10^{-7} rD_{22}$$
$$+ 0.008104 r - 7.469 \cdot 10^{-14} sD_{11} D_{22} - 1.307 \cdot 10^{-7} sD_{11} + 2.333 \cdot 10^{-7} sD_{22} + 0.004188 s$$
$$+ 1.136 \cdot 10^{-13} D_{11} D_{22} - 0.5 D_{11} - 0.5 D_{22} - 5.003 \cdot 10^{-5} \quad (77)$$

$$D_{33} = 8.87 \cdot 10^{5} t^{3} + 0.1247 t^{2} + 1.095 \cdot 10^{-12} tD_{11}^{2} - 1.676 \cdot 10^{-12} tD_{11} D_{22}$$
$$- 6.588 \cdot 10^{-8} tD_{11} + 1.094 \cdot 10^{-12} tD_{22}^{2} - 6.572 \cdot 10^{-8} tD_{22} - 0.03607 t - 1.21 \cdot 10^{-8} rsD_{11}$$
$$+ 1.212 \cdot 10^{-8} rsD_{22} - 2.833 \cdot 10^{-6} rs + 4.485 \cdot 10^{-9} rD_{11} - 4.493 \cdot 10^{-9} rD_{22} + 1.05 \cdot 10^{-6} r$$
$$+ 6.017 \cdot 10^{-9} sD_{11} - 6.028 \cdot 10^{-9} sD_{22} + 1.409 \cdot 10^{-6} s - 1.337 \cdot 10^{-19} D_{11}^{3} - 7.909 \cdot 10^{-13} D_{11}^{2}$$
$$+ 1.418 \cdot 10^{-12} D_{11} D_{22} - 0.5 D_{11} - 1.334 \cdot 10^{-19} D_{22}^{3} - 7.907 \cdot 10^{-13} D_{22}^{2} - 0.5 D_{22} + 0.002333 \quad (78)$$

The terms D_{13} and D_{23} are not included in the prediction equations above because accurate estimation could not be achieved with the regression approach. These two terms describe the bending moments M_x and M_y caused by twisting of the laminate. The terms D_{13} and D_{23} are heavily dependent on the stacking sequence of the laminate and thus are difficult to estimate from the limited number of variables used to describe the laminate. Fortunately, the twisting loads are very low in the application demonstrated in this research, and in most acreage applications of composite laminate in aerospace structures. In cases where twisting moment was not low, it would be necessary to include another term in the panel variables to describe this stiffness.

The remaining [ABD] terms calculated by the equations above were all able to be accurately calculated; all have 100% accuracy.

CHAPTER VII

OPTIMIZATION OF A METALLIC WING BOX

The objective of this chapter is to demonstrate that the stiffened panel optimization methodology developed in this research can be integrated with a FEM -based design environment. This is achieved by setting up the panel methodology in a bi-level optimization environment with a metallic wing box. To simulate the presence of static aeroelasticity constraints, a maximum wing tip deflection constraint was imposed on the optimization. The objective of the optimization was to find a stiffness distribution on the structure that met the wing tip deflection constraint ($\delta_{T,req}$) while minimizing mass (m) of the wing box top and bottom skin.

The wing box optimization was performed with the bi-level strategy presented in Chapter 6. At the global level, the longitudinal stiffness of the skins was controlled to achieve a desired wing tip deflection. At the local level, the mass of the wing box skins was minimized while simultaneously achieving the longitudinal stiffnesses prescribed at the global level. Successful optimization of the wing box skins is demonstrated in this chapter, proving the viability of the stiffness-based panel optimization approach developed in this research.

7.1 Description of Model

The model used for the optimization demonstration in this chapter is a wing box structure similar to that of a Boeing 737. The wing box provides the primary load path for the wing as well as necessary stiffness for the structure. The wing box is shown overlaid on a 737 planform in Figure 106.

7.1.1 Geometry and Mesh

The overall dimensions of the wing box as well as the internal structure are given in Figure 107. The FEM mesh for the wing box is also shown in Figure 107. Average element size of the mesh is 6 inches. The wing box has a forward and rear spar and 27 ribs. The leading

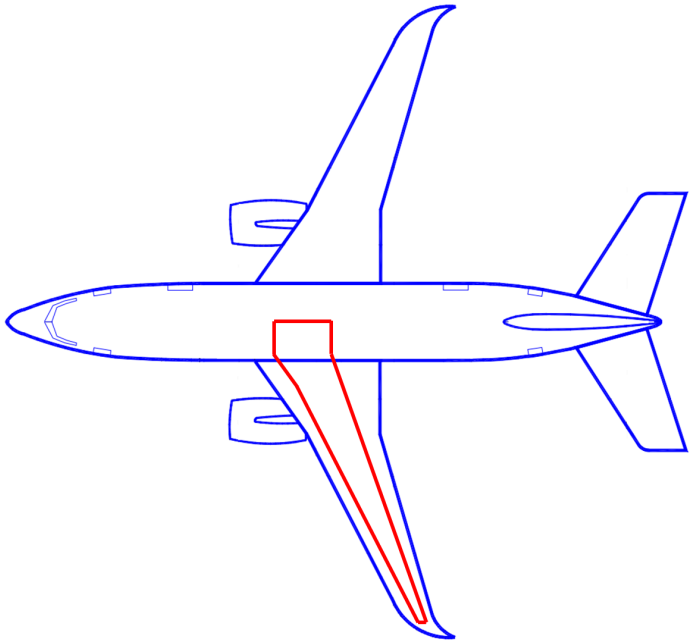

Figure 106: Outline of Wing Box on 737-300 Planform (Adapted from Reference [18])

edge of the wing is not included in the model because it is usually not a load-bearing structure on commercial aircraft wings, and thus is not designed as an integral part of the wing box structure. Additionally, trailing edge features (flaps, ailerons) are not included on this model because they are also designed separately.

In addition to the features described above, the skins of the wing box have attached stiffeners to provide additional strength and stability to the structure. The wing box FEM in this study uses a "smeared" modeling approach for the top and bottom skins. In conceptual design, smeared panels are typically used because of their design flexibility. For smeared panels, the analysis of the skin+stiffener combination is performed analytically instead of using a separate mesh geometry to represent each part of the panel. For this example, all of the skin stiffeners are represented analytically. This allows for the dimensions of the stiffened panel to be modified without having to generate a new FEM mesh. Figure 108 shows equivalent smeared and discrete cross-sections of the wing box.

On the wing skins, the smeared panels are broken up in the span-wise direction by the ribs. Area between the ribs is referred to as a "bay." Within each bay, the skin panels are sub-divided in the chord-wise direction to provide additional flexibility in the optimization.

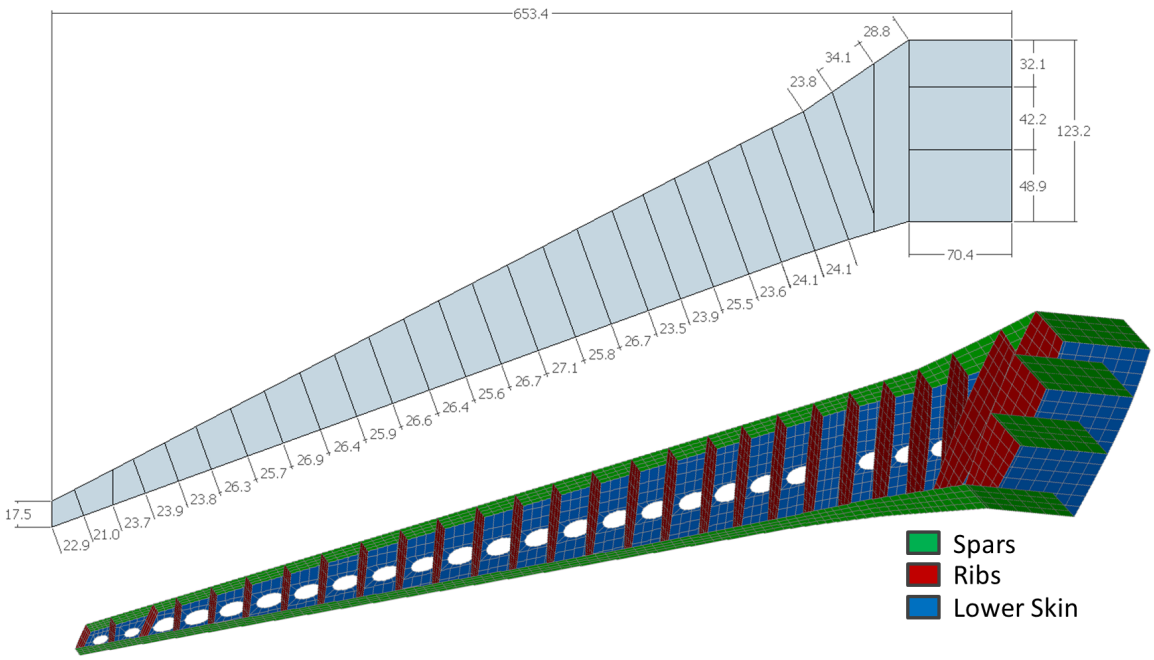

Figure 107: Dimensions and Mesh of Wing Box Structure

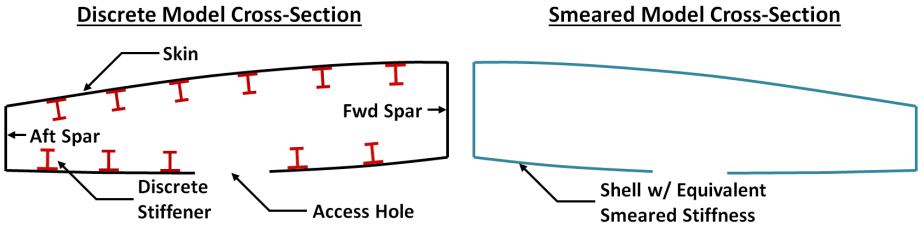

Figure 108: Equivalent Smeared and Discrete Cross-Sections

The smeared panel breakdown for the top and bottom skins is shown in Figure 109.

7.1.2 Load Cases

For conceptual design, typically around 5-10 load cases are used to size the structure. For the final detailed design of an aircraft, over 10,000 load cases are often considered, but 90% of the structure is usually driven by 5-10 critical load cases. For an aircraft wing box of the kind considered in this here, common load cases used for conceptual sizing are: +2.5g pull-up, -1.0g pull-down, taxi bump loads, 2-point braked roll, and maximum aileron deflection (see Section 2.2). Of these five, only the +2.5g pull-up load case was chosen for demonstration purposes. To demonstration the significance of the +2.5g load case, Figure

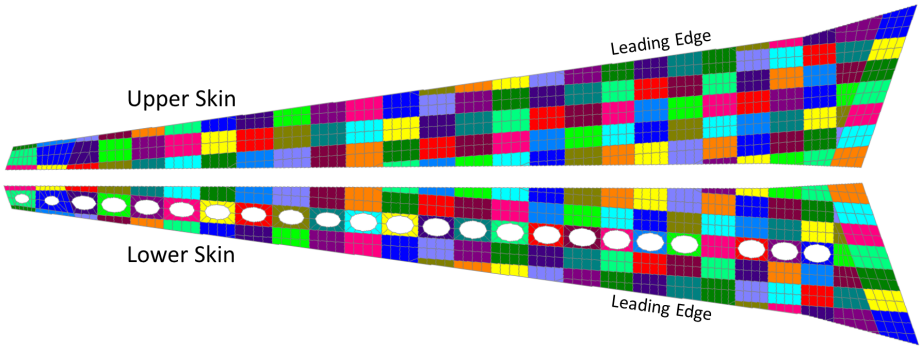

Figure 109: Wing Box Skin Component Definition

110 shows a plot of the controlling load cases for a baseline sizing using all five load cases. The figure shows that a significant portion of the structure is sized according to the +2.5g load case. Although the methodology is capable of efficiently handling multiple load cases, the +2.5g case was used for simplicity.

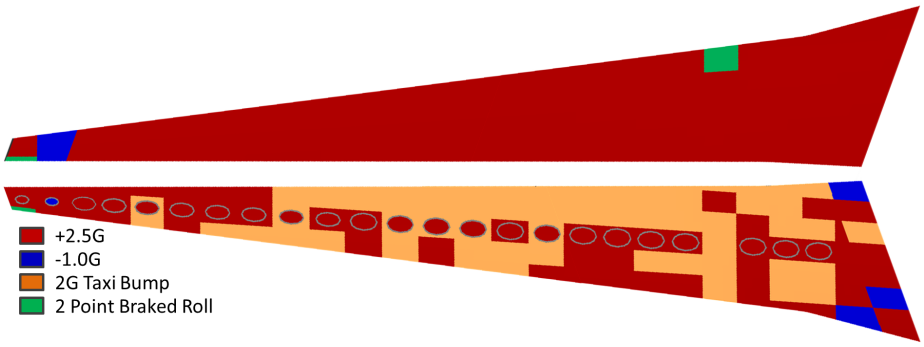

Figure 110: Controlling Load Cases for Wing box FEM

The +2.5g pull-up load case was determined with the discrete load approach described in Section 2.2. The resulting distribution of lift, drag, and pitching moment is plotted in Figure 111. Each of these discrete loads is applied at a rib location.

After applying these external loads to the FEM , a FEA was used to calculate the internal element loads of the structure. Plots of the element N_x, N_y, and N_{xy} are given in Figures 112 through 114. Plots of the bending moments M_x, M_y, and M_{xy} are given in Appendix H. The bending moments are not used by the optimization methodology presented in this research, but are still included to show that their relative magnitude is low enough to be

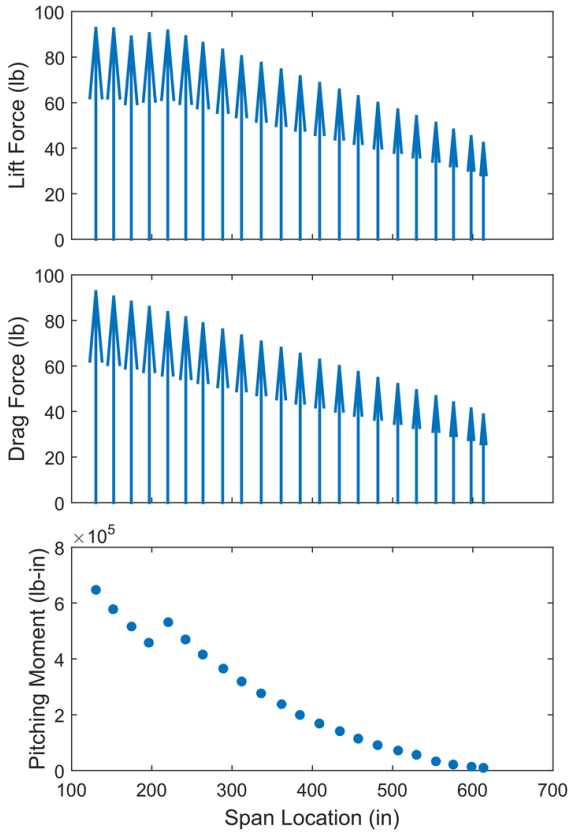

Figure 111: Discrete Loads Applied to Wing box FEM for +2.5g Load Case

neglected (failure criteria are no longer driven by bending loads). Additionally, note that the element loads presented in this section are for the baseline wing box design. The distribution of load varies during the optimization because the stiffness of the FEM is modified during iterations, and the FEA is rerun.

The final aspect of the loads to consider is which $N_x - N_y$ quadrants the panel loads occupy. Figure 115 shows that the majority of the panel loads fall into either the +/+ or -/- load quadrant. This is useful for understanding the expected accuracy of the panel optimization by comparing to the accuracy results presented in Section 4.2.

7.1.3 Optmization Setup

This optimization example with the 737-similar wing box uses the bi-level optimization process described previously in Section 2.5 and 6.1 and the global stiffness control approach described in Section 6.2.1. As introduced in Section 6.2.1, the global level of the optimization

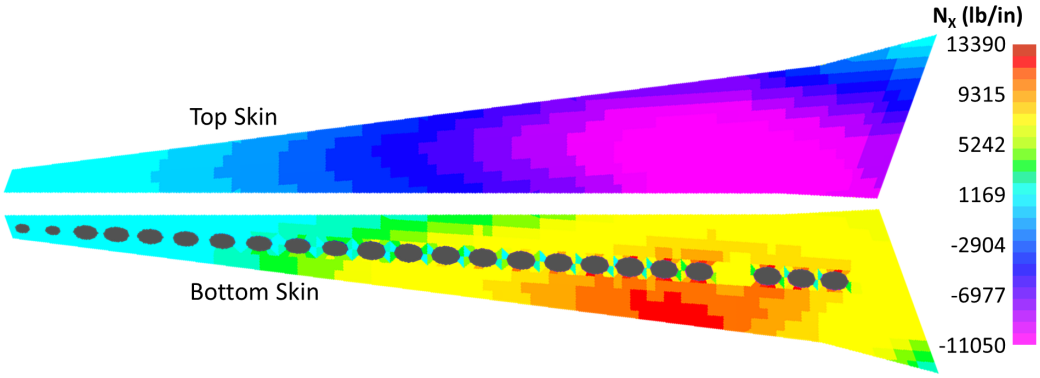

Figure 112: Baseline Internal Element N_x for +2.5g Load Case

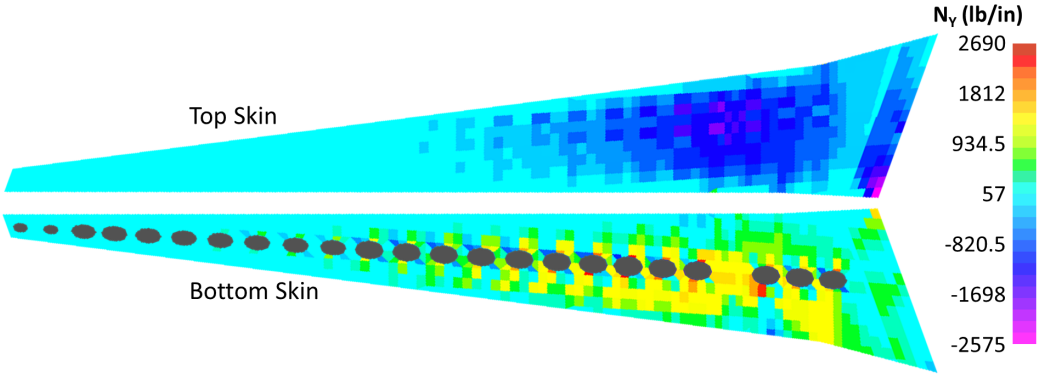

Figure 113: Baseline Internal Element N_y for +2.5g Load Case

controls axial membrane stiffness of the skin panels, A_{11}. This global variable was selected because one of the constraints of the optimization is to meet a required wing tip deflection ($\delta_{T,req}$). The axial (span-wise) membrane stiffness of the skins has a significant amount of control over the vertical deflection of the wing tip deflection. This is because adding material to the top and bottom skins is the most mass-efficient way of adding bending stiffness to the wing box. For the optimization presented in this chapter, the tip displacement requirement was set at 54.5 inches. This value was chosen to force the tip displacement to be a driving requirement in the optimization.

Additionally, A_{11} is closely related to the mass of the metallic I-stiffened panel, as described in Section 3.5.2. Mass must be minimized at the global level in the optimization. The formal problem statement for the new wing box optimization at the *global level* is given

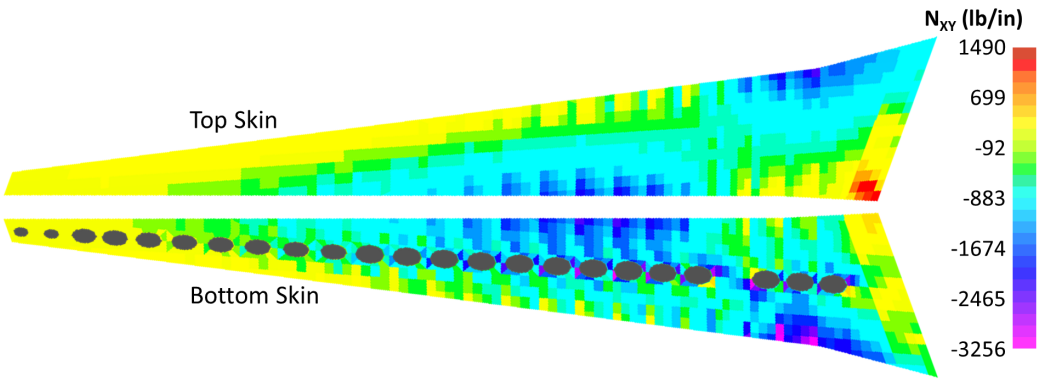

Figure 114: Baseline Internal Element N_{xy} for +2.5g Load Case

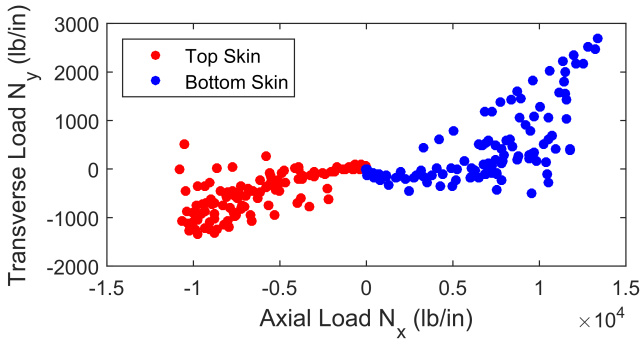

Figure 115: Scatter Plot of Axial and Transverse Running Load for 737-Similar Wing Box Skin Loads

in Equation 79.

$$\{A_{11}\} \text{ for min } m_{skins} = f(A_{11}) \text{ s.t. } \begin{cases} \delta_T \leq \delta_{T,req} \end{cases} \tag{79}$$

Similar to the global level, the objective of the local optimization is to minimize mass (m_{panel}). This optimization is a function of the remaining panel stiffness terms that were not specified at the global level (A_{22} , A_{33} , etc.). The local optimization is subject to the constraint that the A_{11} term must match the value specified from the global level ($A_{11,global}$). Finally, the local optimization must also produce designs which satisfy the panel failure criteria. This is denoted by the metric ϕ, which is less than or equal to zero when all of the criteria are met. The formal optimization statement for the local level is given in Equation

80.

$$\{A_{11}, A_{22}, A_{33}, D_{11}, D_{22}\} \text{ for min } m_{panel} = f(A_{22}, A_{33}, D_{11}, D_{22}) \text{ s.t. } \begin{cases} A_{11} = A_{11,global} \\ \phi(\vec{x}) \leq 0 \end{cases} \tag{80}$$

Once the local optimization is performed for each panel, the sum of the panel masses determines the optimum structural mass for the given global stiffness distribution. Then the global stiffness distribution is updated (using methodology described in Section 6.3.1), FEA is re-run to obtain a new load path, and the process repeats. This continues until a global stiffness distribution is determined for the top and bottom skin which satisfies the global deflection constraint with the lowest possible stiffened panel mass.

7.2 Baseline Optimization

Two baseline optimizations were performed to establish a point of comparison for the results from the stiffness based optimization. The first optimization establishes an absolute minimum mass by not including a global wing tip displacement constraint. The second optimization does include the tip displacement requirement and is used to compare to later results. HyperSizer was used to generate the baseline designs. In both baseline optimizations, all failure criteria listed in Table 1 of Section 2.6.1.5 were used. The optimization was performed on the top and bottom skins of the wing box.

7.2.1 Optimization without Tip Displacement Constraints

The first baseline optimization is used to establish an absolute minimum mass for the top and bottom skins. This was done by leaving out the wing tip displacement requirement and simply optimizing each panel to meet the failure criteria. The resulting mass is 728 lbm for the top skin and 512 lbm for the bottom skin. Wing tip deflection for this baseline optimization is 87.94 inches, which is greater than the 54.5 inch requirement used in the next baseline optimization. Thus, a substantial amount of mass will must be added to lower the wing tip deflection to meet the requirement.

7.2.2 Optimization Including Tip Displacement Constraints

In the next baseline design, the upper and lower skins were optimized with a traditional sizing approach in HyperSizer to meet the wing tip deflection requirement. HyperSizer has a specific tool, HyperFEA, which allows iteration with FEA to meet FEA-based requirements (deflection, global buckling, etc). This tool was used to develop a comparative design that enforces a wing tip deflection constraint of 54.5 inches. The final stiffness distribution from HyperFEA is given in Figure 116. HyperFEA produced a final mass of 1454 lbm for the top skin and 1021 lbm for the bottom skin (2475 lbm total) in four iterations, shown in Figure 117.

As expected, the wing box skin mass from this optimization is considerably higher than the first baseline optimization because of the wing tip displacement requirement. The mass resulting from this baseline result will be compared to the stiffness-based optimization results discussed in the following sections.

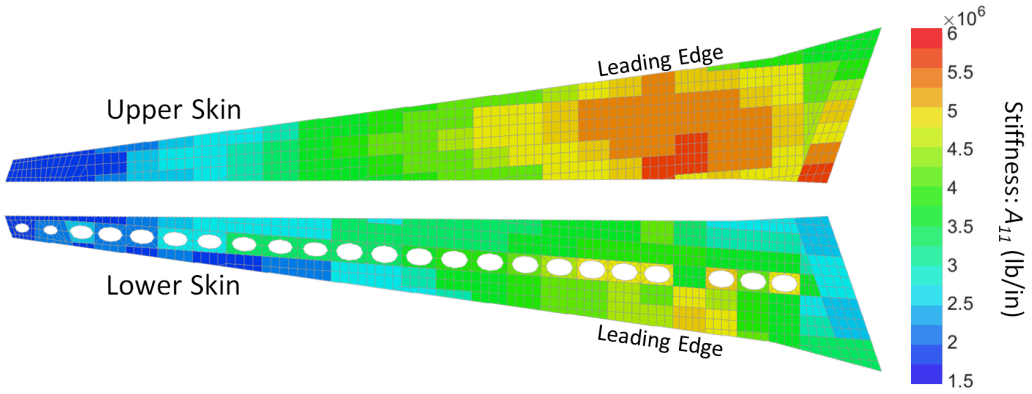

Figure 116: Final A_{11} Distribution From HyperSizer Optimization

7.3 Stiffness-Based Optimization

This section presents the optimization results using the methodology developed in this research for the metallic I-stiffened panel, discussed in Chapter 3, and the bi-level optimization strategy presented in Section 6.1. The first set of results presented are from an optimization that uses only two control points at the global level, forcing a linear distribution of A_{11} over the top and bottom skins of the wing box. The second set of results uses five control

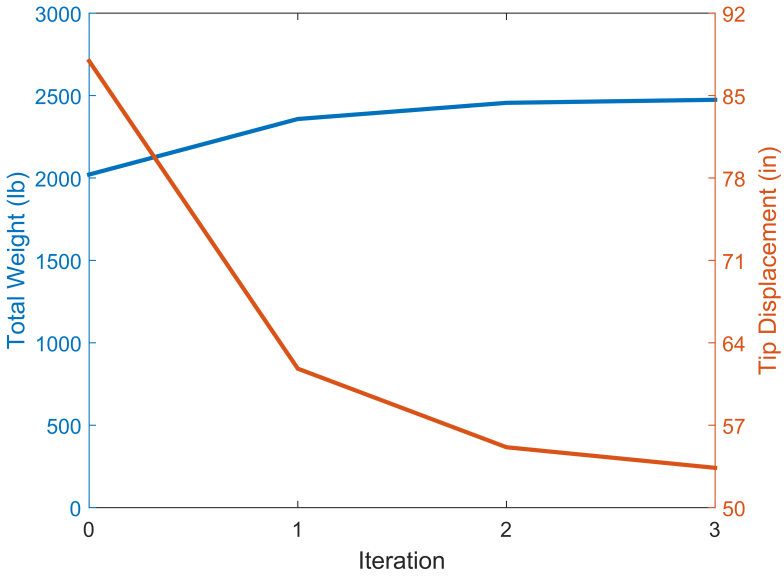

Figure 117: HyperFEA Iterations for Baseline Design

points at the global level, allowing for the A_{11} distribution to be quadratic in the span-wise direction and linear in the chord-wise direction. Next, the optimum quadratic distribution of A_{11} (using five control points) is applied to an optimization in the physical domain to ensure that the final stiffness distribution is realistic. The final set of results is an example application of the methodology that leverages its high optimization efficiency.

7.3.1 Linear Global Stiffness Distribution

The first optimization with the wing box used a linear stiffness distribution on the top and bottom skin. This linear distribution uses the same control point approach described in Section 6.2.1, but used only two control points instead of five. These control points were placed at the root and tip of the wing skins. Thus, a total of only four global variables were needed to run the optimization. The bi-level optimization was performed as described in Section 6.1.

With fewer design variables, this optimization needed the fewest iterations to converge. However, there was a small sacrifice in final mass because the optimizer was not able to tune the stiffness distribution in the chord-wise direction due to the form of the parametric surface (span-wise linear). The structure converged to 2400 lb in 22 iterations, as shown in

Figure 118.

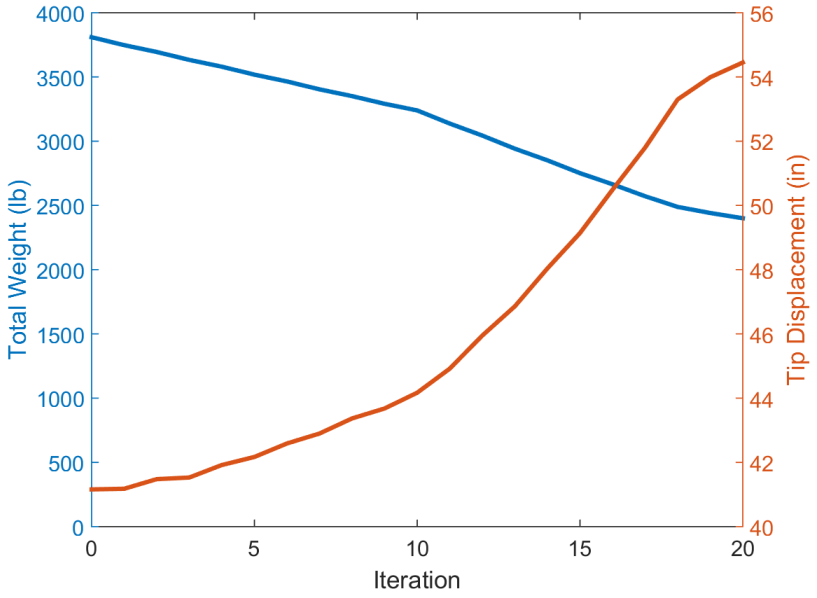

Figure 118: Optimization Convergence with Two Control Points

Because there are only two global variables for the top and bottom skin, progression through the global design space can be tracked in a 2D plot. This helps demonstrate how the global optimizer iterates toward the final solution. The two plots in Figure 119 track the iterations for the top and bottom skin. The x-axis gives the A_{11} value specified at the root control point and the y-axis gives A_{11} for the wing tip control point. All control points start off at the maximum allowed value. Both plots display isolines of the total assembly mass corresponding to the combination of root and tip A_{11}. These isolines are linear because the global A_{11} distribution is linear.

The optimization approach described in Section 6.1 is evident in Figure 119. Starting from the highest allowed A_{11} for all control points, the optimizer alternates between reducing the root and tip values until reaching convergence. In each step, the optimizer always moves to a point with a lower mass. Convergence occurs when mass can no long be reduced without violating the wing tip displacement constraint or local failure criteria.

The final stiffness distribution for the top and bottom skins is given in Figure 120. These distributions correspond to the final control point values in Figure 119. Interestingly, the

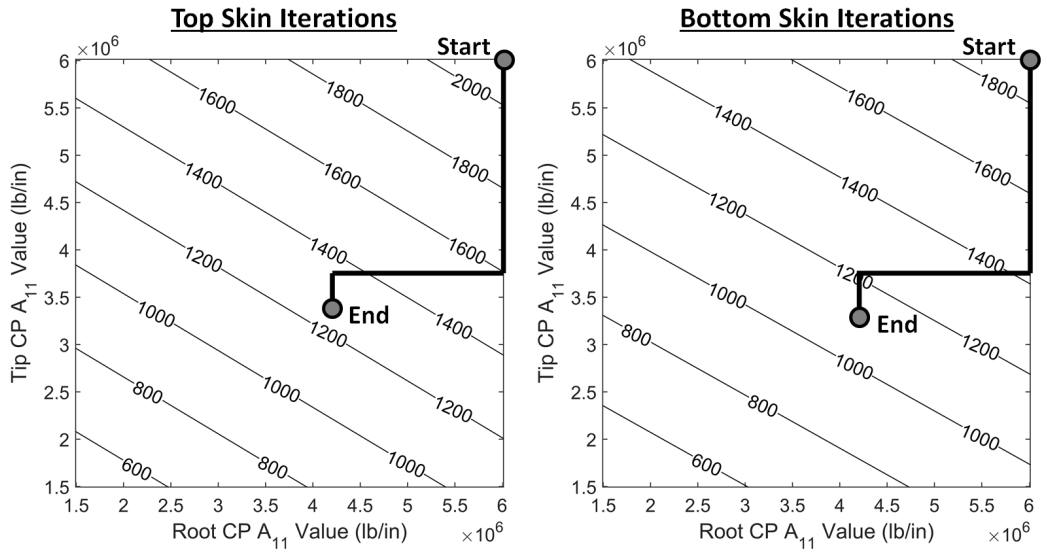

Figure 119: Iteration History for the Two CP Approach with Assembly Mass (lbm) Isolines

A_{11} distribution is nearly flat on both the top and bottom of the wing box, at a value of approximately 3.5e6 lb/in. This is likely due to the enforced linearity of the distribution. The panels toward the wing tip are narrower, so increasing their required stiffness has less impact on total mass. This drove the solution to have abnormally high stiffness at the wing tip to compensate for the inefficiency of the linear stiffness distribution, thus giving a mostly flat solution.

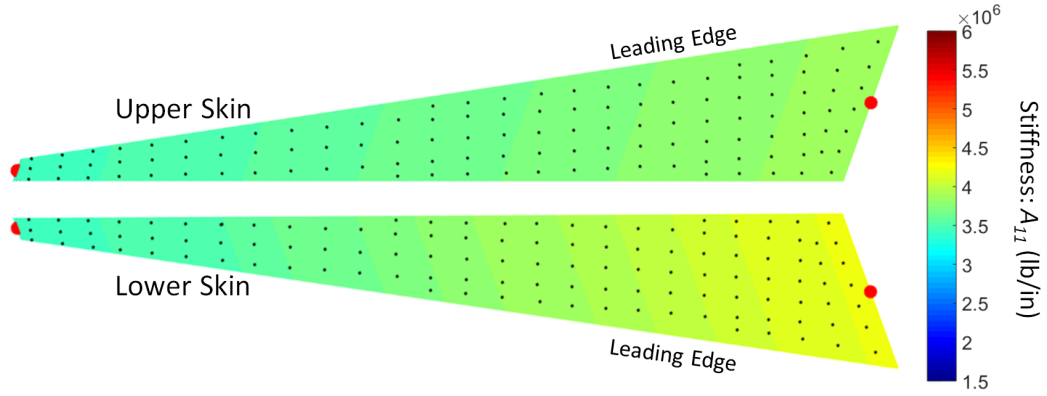

Figure 120: Final A_{11} Distribution with Two Control Points

7.3.2 Quadratic Global Stiffness Distribution

The second optimization performed with the wing box uses five control points to produce an A_{11} distribution at the global level, directly applying the methodology described in Section 6.2.1. The bi-level optimization was performed as described in Section 6.1.

The solution with five control points took longer to converge but was able to find a lower mass solution than with two control points. The iteration history of this optimization is shown in Figure 121. The iterations follow a similar trend to the two control point solution, except that the target tip displacement was met before minimum mass is achieved. The tip displacement oscillated near the required value as the optimizer continued to remove mass from the structure.

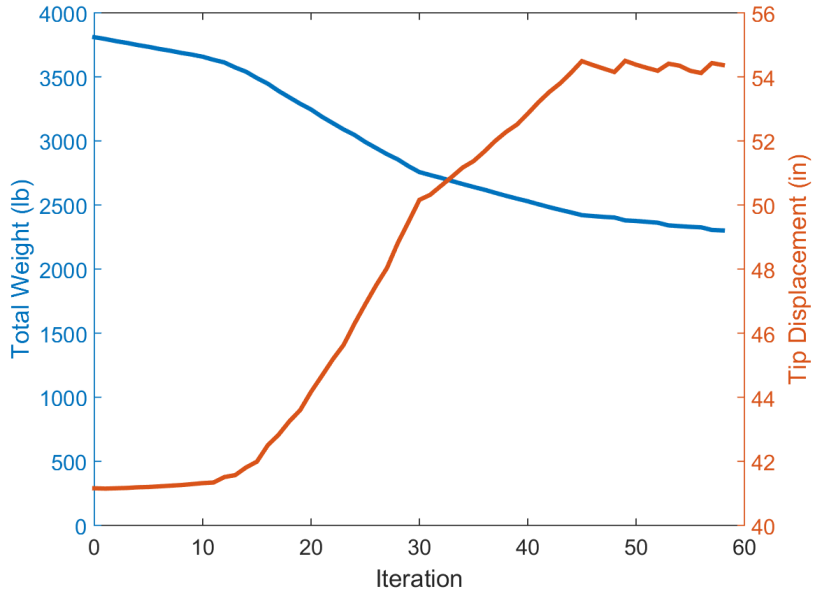

Figure 121: Optimization Convergence with Five Control Points

This solution took 59 iterations to converge, 2.7 times as many as the two control point solution. This roughly corresponds to the 2.5 times increase in the number of design variables. This linear behavior in the relationship between number of iterations and number of design variables is to be expected for the compass search optimization algorithm. The final mass was 2302 lbm, achieved by 79 analysis calls.

The final stiffness distribution for the top and bottom skins is given in Figure 122. Due

to the flexibility of the parametric surface with five control points, the A_{11} distribution was able to be tuned in both the chord-wise and span-wise direction to achieve minimum mass while also meeting the tip deflection requirement. The distribution has significant chord-wise variation near the root of the wing, and also an overall nonlinear decrease from root to tip, typical of a wing of this type.

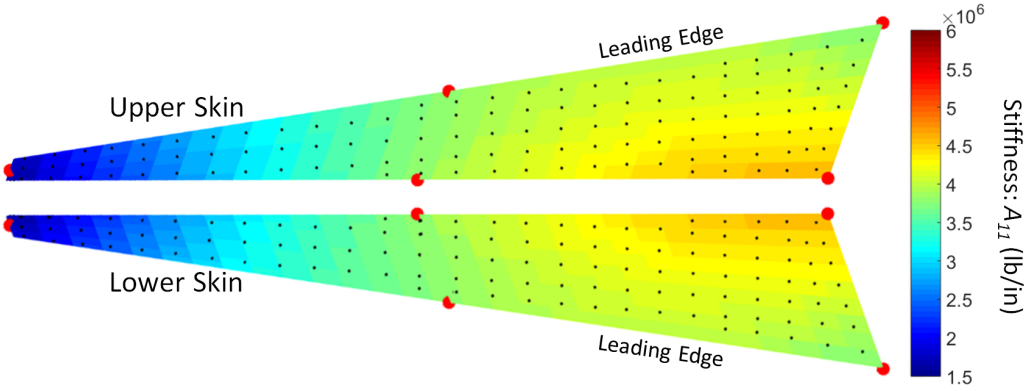

Figure 122: Final A_{11} Distribution with Five Control Points

7.3.3 Reverse Mapping to Physical Domain

The reverse mapping performed here is not as rigorous as the approach described in Section 3.9. The goal of the reverse mapping from Section 3.9 was to define a physical design from the *full* stiffness definition (A_{11},A_{22},A_{33},D_{11},D_{22}). The goal of the reverse mapping presented in the current section is simply to verify that the optimum quadratic A_{11} distribution determined previously is physically feasible. This was accomplished by assigning the A_{11} distribution in HyperSizer as a constraint for each panel. The A_{11} value for each panel was determined by extracting the A_{11} at the panel centroid from the final parametric distribution given in Figure 122. Finally, HyperSizer optimized each panel by determining physical dimensions which minimize mass and satisfy all failure criteria.

HyperSizer was able to find dimensions for each panel that satisfy the A_{11} distribution dictated by the stiffness-based methodology. Thus, the stiffness-based optimization methodology is an accurate representation of the detailed panel optimization performed by HyperSizer. The total mass reported by HyperSizer for the A_{11} distribution is 2381

lbm, which is only 3% different from the mass reported in Section 7.3.2. Additionally, the margins of safety reported by HyperSizer for the failure criteria were all positive, indicating that the optimum A_{11} is physically feasible given the applied loads.

7.3.4 Summary of Results

Tables 32 and 33 summarize the masses and run times from each of the optimization approaches described above and provide the % difference from the baseline. Compared to the baseline optimization, both solutions from the linear optimization approach produce a lower mass in substantially less run time. The optimization with five control points was able to achieve a slightly lower mass due to greater flexibility of the A_{11} distribution. However, this came at the cost of run time because more iterations were required to handle the increased number of global variables.

Note that the improvement in efficiency of the bi-level optimization over the baseline optimization is not as large as reported in Section 4.4 at the panel level. This is because the global-level optimization algorithm (discussed in Section 6.1) was designed for demonstration purposes and requires a higher number of global iterations than the baseline. However, the overall objective of this chapter was to demonstrate that the novel panel optimization methodology could be coupled with a FEM -based environment, not to demonstrate a novel global-level algorithm. To this end, the results presented in this section show successful completion of this objective because of the small difference between the baseline mass and the bi-level optimization mass.

A second note to make about efficiency pertains to the reverse mapping to the physical domain (last entry of Table 33). This process is slower than the bi-level optimization because it requires running HyperSizer to achieve the final physical designs. However, the reverse mapping only needs to be run once at the very end of a conceptual design to transition into preliminary and detailed design. Thus, the run time for reverse mapping does not negatively impact the overall capability of the conceptual optimization methodology presented in this research.

Table 32: Summary of Masses and Run Times for 737-Similar Wing Box Skin Optimization

Optimization	Top Skin Mass (lbm)	Top Skin % Diff.	Bottom Skin Mass (lbm)	Bottom Skin % Diff.
HyperSizer, Baseline	1454	0	1021	0
Bi-Level Optimization, 2 CPs	1239	-14.8	1161	13.7
Bi-Level Optimization, 5 CPs	1229	-15.5	1073	5.1
HyperSizer, Reverse Mapping	1271	-12.6	1110	8.7

Table 33: Summary of Masses and Run Times for 737-Similar Wing Box Skin Optimization (cont.)

Optimization	Total Mass (lbm)	Total Mass % Diff.	Run Time (min)	Run Time % Diff.	Run Time Factor Diff.
HyperSizer, Baseline	2475	0	480	0	0
Bi-Level Optimization, 2 CPs	2400	-3	15	-96.9	32x Faster
Bi-Level Optimization, 5 CPs	2302	-7	50	-89.6	10x Faster
HyperSizer, Reverse Mapping	2381	-3.8	120	NA	NA

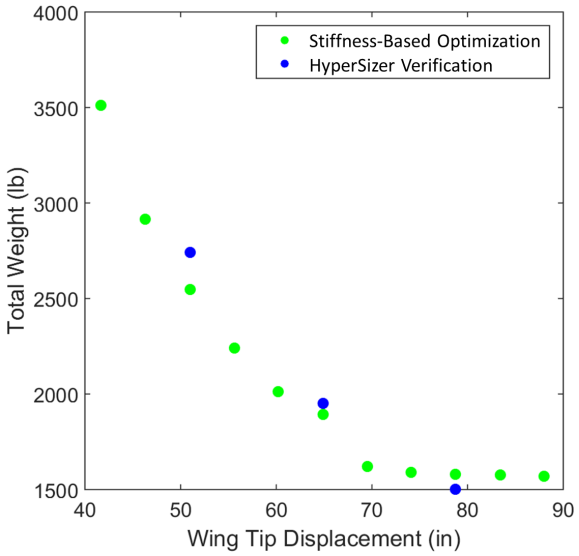

Figure 123: Curve of Wing Skin Mass versus Wing Tip Displacement

7.3.5 Example of Possible Trade Studies

The efficiency made possible by the new panel optimization methodology implemented in this research enables stiffness-based studies to be performed quickly for conceptual design purposes. The example used here is the generation of a curve that displays total mass as a function of required tip displacement, shown in Figure 123. The stiffness-based optimization

was run with five control points for each wing tip displacement value shown in Figure 123. This entire curve was generated in approximately the same amount of time as a single run with traditional sizing in HyperSizer. For comparison, three required tip deflections were run in HyperSizer and overlaid on the stiffness-based points, showing the accuracy of the approach. Note that the masses begin to plateau beyond 70 inches of required tip displacement as the skins become controlled more and more by failure criteria rather than stiffness requirements.

The mass versus tip displacement curve is just one possible application of the rapid stiffness-based optimization. Any process which requires a particular stiffness distribution over the structure (most aeroelastic applications) can be handled with the techniques presented in this research. The global optimization could easily be modified to constrain the wing deformation to a required bending or twisting profile along the span of the wing.

CHAPTER VIII

OPTIMIZATION OF A COMPOSITE WING

This chapter demonstrates application of the stiffness-based linear optimization methodology for FEM integration with a composite structure. The demonstration is performed on the wing structure of the F-86 Sabre Jet. The F-86 is a single-seater subsonic fighter jet that was developed shortly after World War II by North American Aviation, shown in Figure 124. This vehicle was chosen because it has been retired for long enough that data such as structural mass, load envelopes, internal structure, etc. are widely available. Although the original F-85 wing structure was constructed of aluminum, performing a composite re-design holds academic value for maximizing mass savings over the baseline design.

Figure 124: F-86D "Sabre Dog" [19]

The goal of this example optimization is to demonstrate that the stiffness-based methodology is capable of interfacing with a FEM using composite materials. The optimization was simplified relative to the example performed in Chapter 7 by removing the wing tip

displacement constraint. The result is that the number of iterations is reduced to two. This simplification was made to avoid demonstrating the iteration capability twice.

In the sections below, the geometry, mesh, and optimization setup of the FEM are described. Next, the results of baseline optimizations performed in HyperSizer are presented. The baseline optimization was first performed with aluminum to ensure that the techniques applied in this research produce a structural mass similar to what has been documented in previous literature. The second baseline optimization was also performed in HyperSizer, this time with a composite material to establish a point of comparison for the new methodology. The final section contains the results of performing optimization with the linear stiffness-based methodology presented in this research, and is compared to the baseline composite mass from HyperSizer.

8.1 Description of Model and Optimization

The portion of the F-86 structure used in the optimization demonstration is shown in Figure 125.

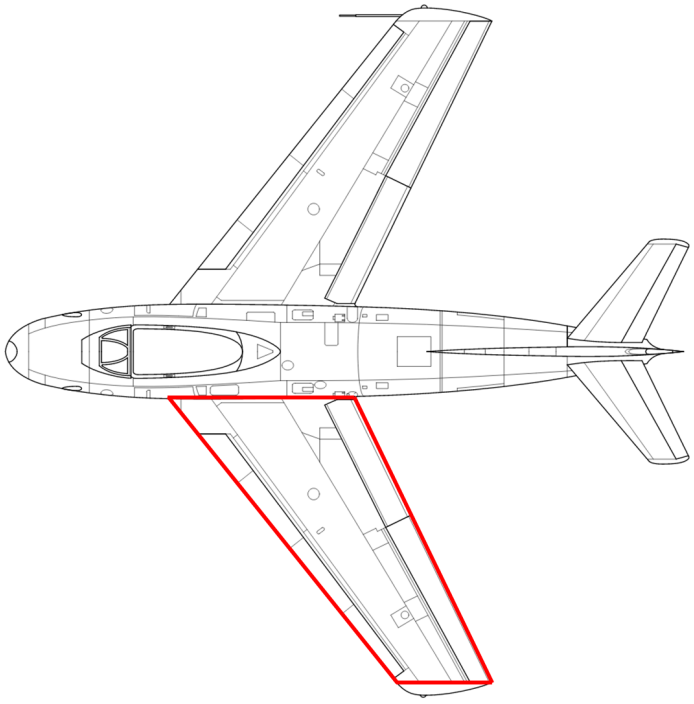

Figure 125: Portion of F-86 Planform Used for Optimization Example (Adapted from [20])

The primary difference between this wing structure and the one presented in Chapter 7 is that it is designed for high-speed flight and therefore has a much lower thickness-to-chord ratio than the 737 wing box. The result is that the internal wing structure must be configured differently to support the high-g maneuvers required of a fighter jet. The low thickness of the wing means that there is not room for attached stiffeners on the skin to provide additional stiffness. Thus, the ribs and spars must be placed close together to provide the necessary strength and structural stability. These features are identified in the next section.

8.1.1 Geometry and Mesh

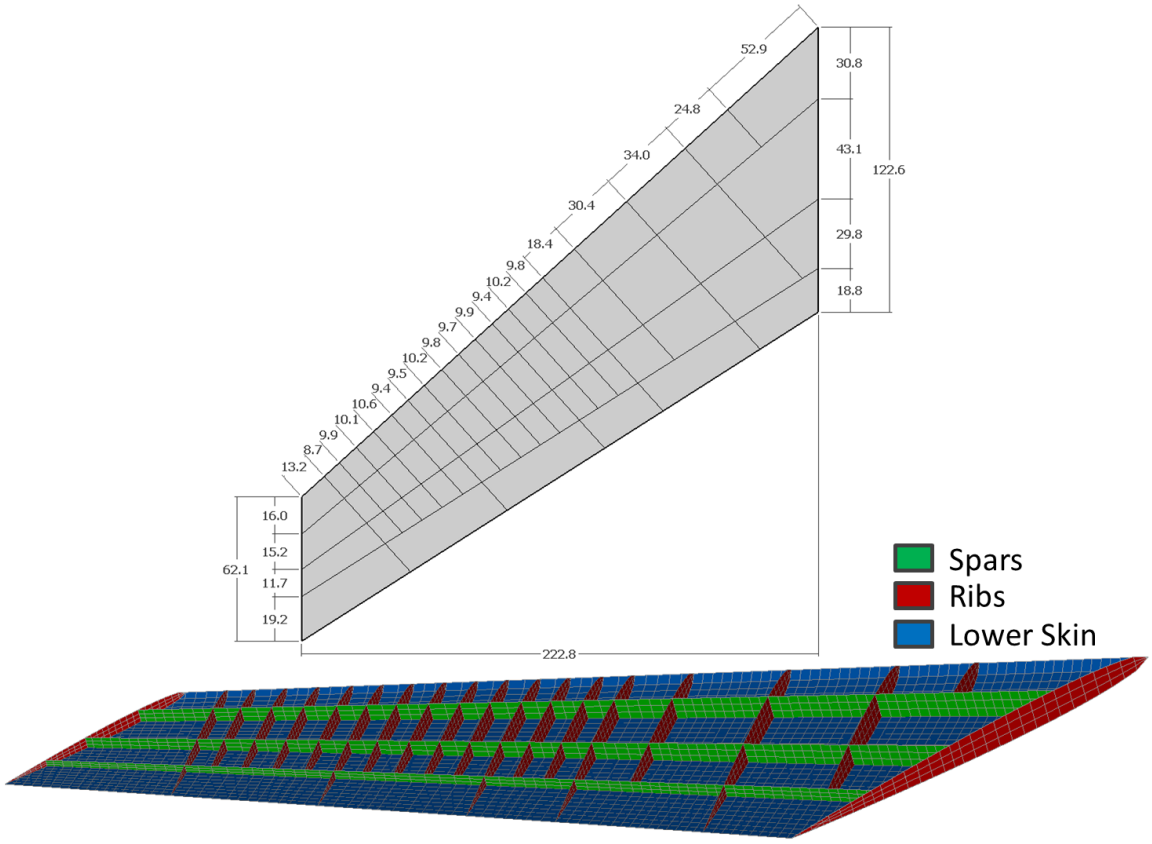

Figure 126: Dimensions (in) of F-86 Wing Internal Structure and Wing Mesh

The overall dimensions of the wing structure are given in Figure 126. These dimensions were established from the baseline model in A. Sirirojvisuth's work [116]. The wing has a total of 18 ribs and 3 spars, and uses a NACA 0009 airfoil at the root and a NACA 0008

airfoil at the wing tip [117]. The FEM mesh was created with Loft, a meshing software developed by L. Eldred at NASA Langley. The mesh is fairly coarse, as is common for conceptual FEMs ; average element size is 3.7 inches. This mesh is shown in Figure 126.

The boundaries of the panels in the FEM are defined by the internal structure of the wing. The ribs break up the panels in the span-wise direction and the spars separate the panels in the chord-wise direction. The resulting panel definition for the top and bottom skin are shown in Figure 127, with a total of 55 panels for each skin. The section of skin aft of the rear spar is not considered in the optimization because this is a part of the flaps and ailerons, which are typically designed and manufactured as a separate part. These panels are grayed out in Figure 127.

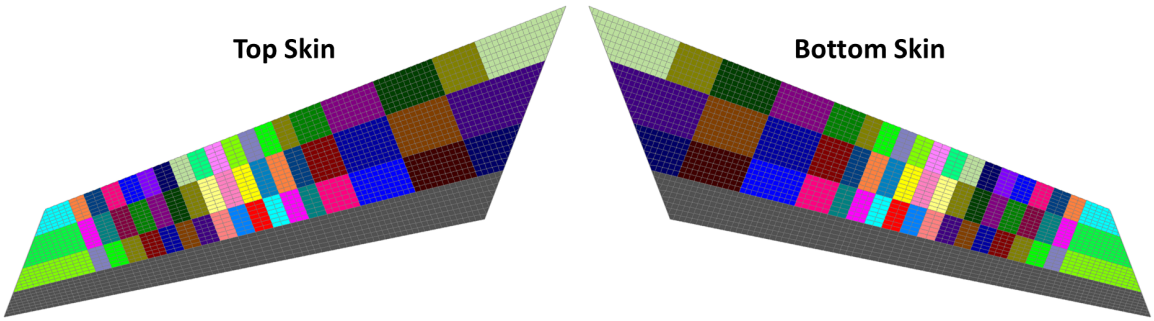

Figure 127: Wing Skin Panels for F-86 Wing Skin Optimization

Similar to the previous optimization example, the panels use a smeared stiffness representation in the FEM . The difference here is that the panel concept is a simple solid laminate instead of an I-stiffened panel as was used in the previous example. Thus, the geometry of the smeared model and the actual model are very similar. This representation depicted in Figure 128.

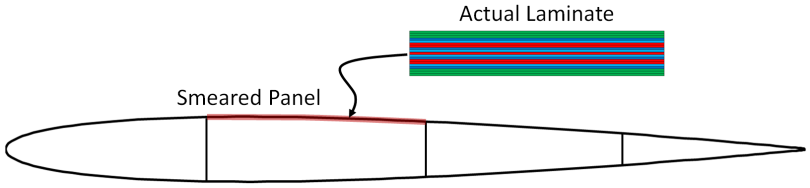

Figure 128: Smeared Stiffness Panel for F-86 Wing Skin

The implication of this design approach is that the only geometry variable is the thickness of the skins in each panel. For metallic construction, skin thickness is the only design variable. With a composite design, the design variables also include ply angles and stacking sequence of the plies.

8.1.2 Load Cases

Similar to the metallic wing box example, only a high-g pull-up maneuver load case is considered for the F-86 example. The methodology presented in this research is capable of handling multiple load cases, as discussed in Section 3.6.3, but only one is considered for simplicity. The load case is a 7-g pullup maneuver at a vehicle mass halfway between empty mass and maximum takeoff mass. This load case was taken from the V-n diagram (pictured in Figure 129) found in the F-86 flight manual [21].

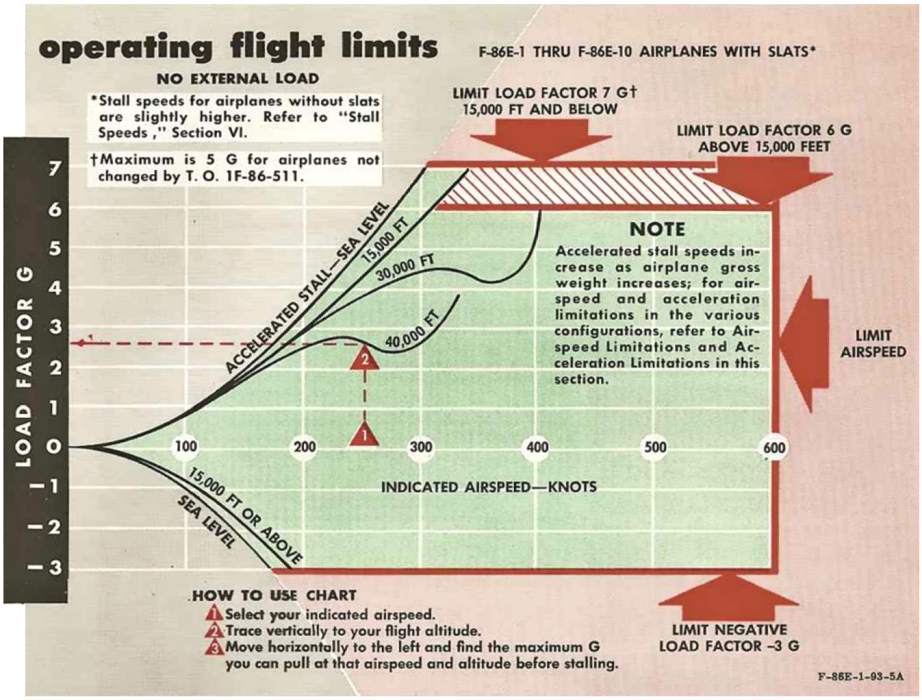

Figure 129: F-86 V-n Diagram [21]

The continuous pressure distribution approach presented in Section 2.2 was used to generate loads for the F-86 7-g pullup case. The software JavaFoil [118] was used to determine the pressure distribution over the F-86 wing airfoil. The resulting pressure distribution is

plotted in Figure 130.

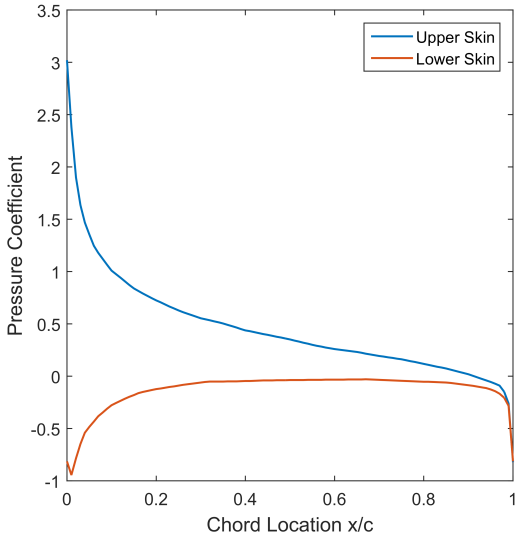

Figure 130: Distribution of Pressure Coefficient Over F-86 Airfoil

This pressure distribution was scaled in the span-wise direction to account for 3D wing effects. The selected span-wise distribution is shaped to account for the significant amount of sweep on the F-86 wing, as described in Reference [119]. This distribution is shown in Figure 131.

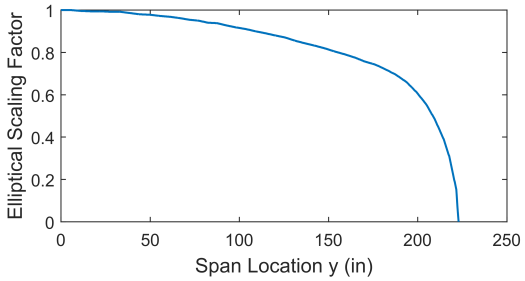

Figure 131: Distribution of Lift Scale Factor Over F-86 Wing Span

The full definition of the pressure distribution on the upper and lower skins is produced by the combination of the two distributions above. The plot of pressure coefficient over the area of the wing is given in Figure 132. Note that these pressures are plotted with respect to the airfoil normal vectors, which point outward from the airfoil. This gives mostly positive

values on the upper skin and mostly negative values on the lower skin.

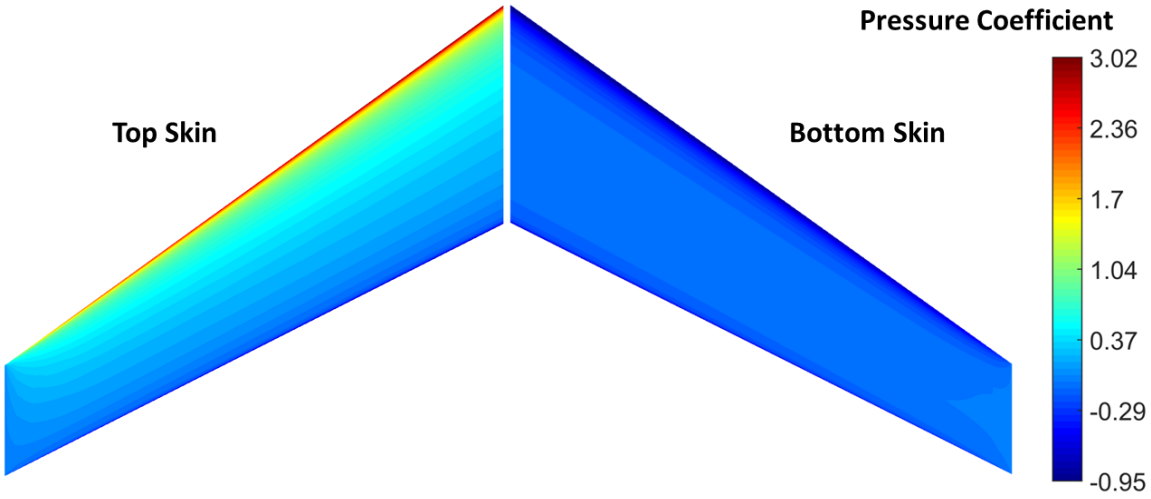

Figure 132: Distribution of Pressure Coefficient Over F-86 Wing Skins

Mapping the pressure distribution in Figure 132 to the upper and lower skins in the FEM provided the external load definition for this load case. Additionally, an acceleration load of 7gs was applied in the -Z (downward) direction to provide the appropriate inertial relief on the wing. The resulting in-plane element running loads (N_x, N_y, N_{xy}) calculated by FEA are given in Figures 133 through 135.

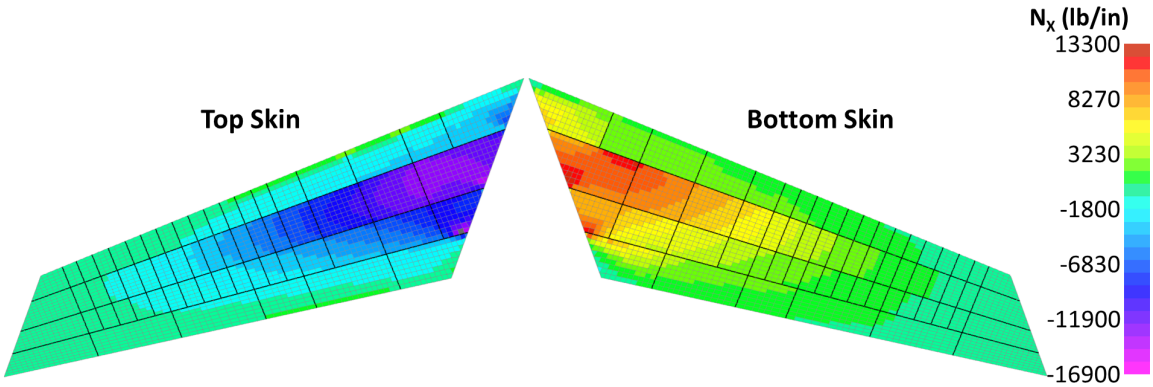

Figure 133: Span-Wise Running Load (N_x) in F-86 Wing, per Element

Bending moments are not included here because they are not considered by the panel optimization methodology presented in this research. However, they are provided in Appendix I to verify that their relative magnitude is small enough to be neglected in the

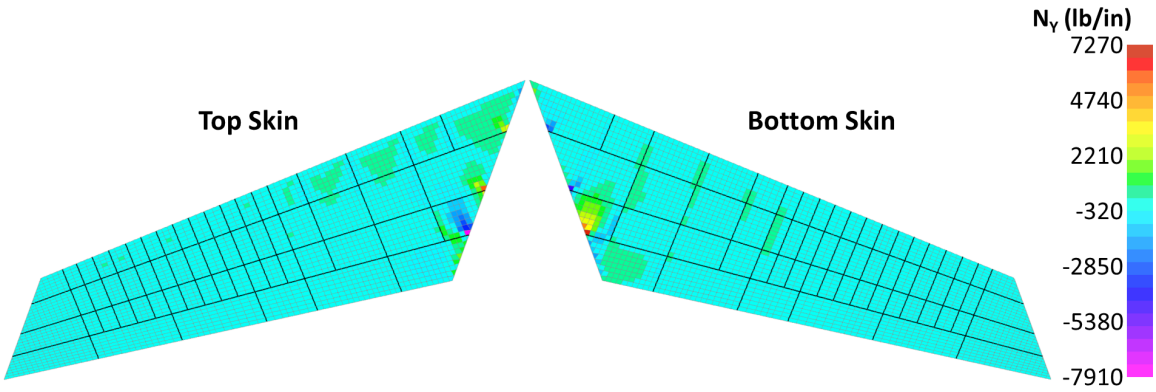

Figure 134: Chord-Wise Running Load (N_y) in F-86 Wing, per Element

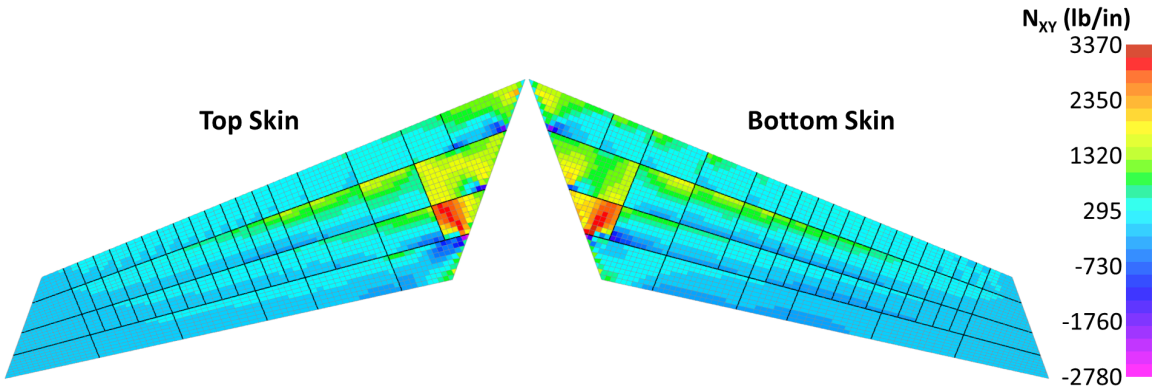

Figure 135: Shear Running Load (N_{xy}) in F-86 Wing, per Element

optimization.

The loads used for sizing are determined by the area-weighted average of the loads in every element in each panel. These panel loads are given in Figure 197 through 199 of Appendix I. Additionally, the value of N_x and N_y are plotted for all panels in Figure 136. This scatter plot can be used to identify how many panels fall into each of the load quadrants. This information is useful to identify which failure criteria RSEs were used from Section 5.1.4.1.

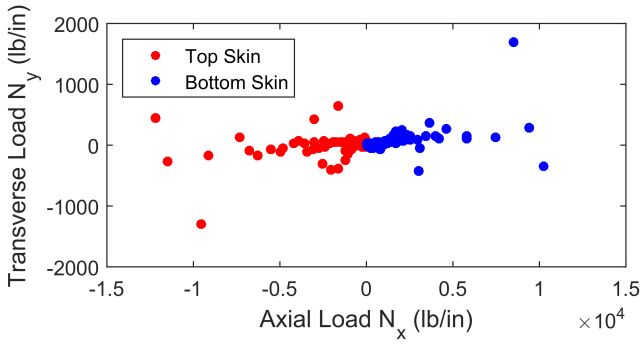

Figure 136: Scatter Plot of Axial and Transverse Running Load for F-86 Wing Skin Loads

8.1.3 Optimization Setup

Optimization of the F-86 wing is performed with a bi-level approach. The approach uses the global-level FEM interfacing described in Section 6.2.2, where variable distributions are described at the global level using polynomial functions. At the local level, mass optimization is performed using the stiffness-based methodology adapted for composite laminates with design variables t, r, s, D_{11}, and D_{22}, as described in Chapter 5. The overall integration of these global and local capabilities is described below.

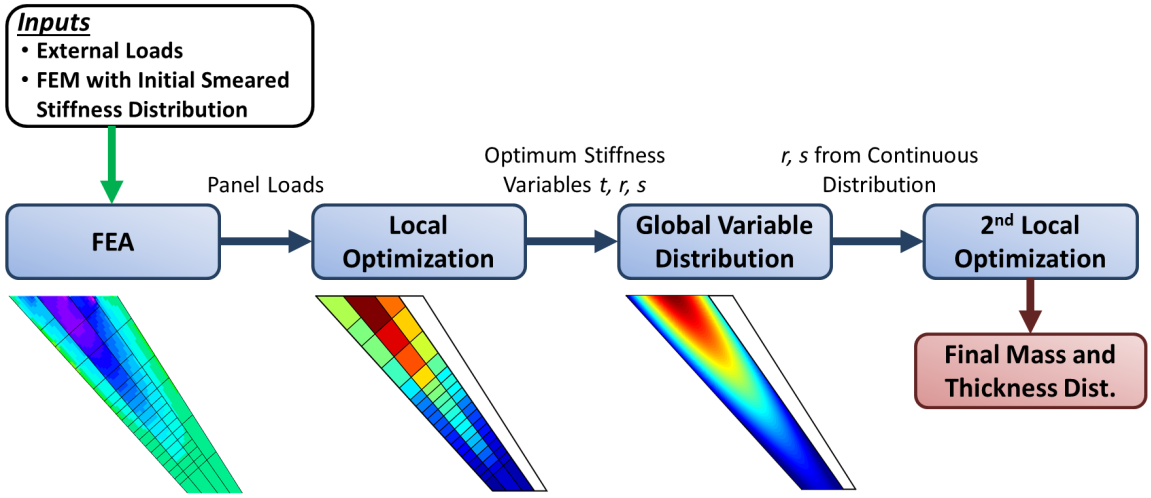

Figure 137: Bi-Level Optimization Process for the Composite F-86 Wing Example

The optimization process for the F-86 wing is more simple than the process presented for the 737 wing because a wing tip deflection constraint is not being considered. This

significantly reduces the number of iterations with FEA needed to converge on a solution. In the resulting bi-level optimization environment, the global level is really only needed to enforce a continuous distribution of the design variables because there are no global level stiffness constraints. Because there are no global constraints, there is no need to control the variable distributions at the global level. The continuous variable distributions are instead generated by a regression of the local optimization results. The process for optimization of the F-86 wing is outlined in Figure 137. The process shown in Figure 137 is essentially a subset of the more complex FEM iteration process presented in Figure 20 of Section 2.5. The flow chart was rearranged to provide a more clear visualization of the simplified process for the F-86 wing example.

The process described in Figure 137 starts with a FEM that has an initial smeared stiffness distribution and applied external loads. Internal element loads are produced from analyzing the FEM , which are then used to derive the equivalent uniform loads for each panel. Next, local optimization is performed with the panel loads and buckling spans extracted from the model. Optimized skin variables are passed to the global level, where a smooth, continuous distribution is generated from regression of the variables against the panel centroid locations. The final step is to perform a 2nd optimization for each panel, this time assigning the parameters r and s based on the value of the continuous distribution at the panel centroid. This 2nd optimization produces the final mass of the structure, as well as the final skin thickness distribution.

Translating the process described above into a formal global optimization statement, the objective is to minimize the mass (m) of the upper and lower skin while constraining the composite laminate variables t, r, and s to fall on a continuous polynomial function (f_t, f_r, f_s) over the area of the wing. This optimization statement is given in Equation 81.

$$\{t, r, s\} \text{ for min } m = f(t) \text{ s.t. } \begin{cases} t \in f_t(x, y, xy, x^2, y^2) \\ r \in f_r(x, y, xy, x^2, y^2) \\ s \in f_s(x, y, xy, x^2, y^2) \end{cases} \tag{81}$$

At the local level, the optimization statement has a similar form to the one presented

for the metallic wing box. The objective is to minimize the mass of the panel subject to the constraint that the variables t, r, and s match the values specified at the global level at the location of the panel ($t_{G,i}$, $r_{G,i}$, $s_{G,i}$). Additionally, the panel is constrained to pass all applied failure criteria ($\phi_{ij} \leq 0$) This optimization statement is given in Equation 82. Optimization at the panel level uses all five variables presented in Chapter 5 for the composite laminate.

$$\{t, r, s, D_{11}, D_{22}\} \text{ for min } UM = f(t) \text{ s.t. } \begin{cases} t = t_{G,i} \\ r = r_{G,i} \\ s = s_{G,i} \\ \phi_{ij} \leq 0 \end{cases} \tag{82}$$

8.2 Baseline Optimization

The first objective of the baseline optimization is to establish a metallic structural mass to verify that the general optimization approach for the F-86 is correct. Additionally, comparing the metallic structure mass to previous literature establishes the validity of the applied loads. The second objective is to use the same FEM to perform a baseline optimization with a composite tape material. The results from this optimization establish a point of comparison for the results from the stiffness-based methodology presented in this research. Both baseline optimizations were performed in HyperSizer.

8.2.1 Aluminum Design

For this baseline optimization, all parts of the wing structure were considered, including the skin, ribs, and spars. The structure was sized using Aluminum 7075, properties listed previously in Table 9. All of the failure criteria listed previously in Table 1 of Section 2.6.1 were applied in the optimization, which includes both strength and stability analyses. A minimum gauge of 0.04 inches was enforced to keep the aluminum from sizing down to an un-manufacturable thickness.

The plots in Figure 138 and 139 show the margins of safety on the skins, ribs, and spars. The majority of the margins are close to zero, indicating that HyperSizer was able

to achieve a local optimum on these panels. A number of panels on the lower skin, as well as the ribs and spars have margins significantly greater than zero. This indicates portions of the structure that are lightly loaded and therefore encounter the min gauge constraint during sizing.

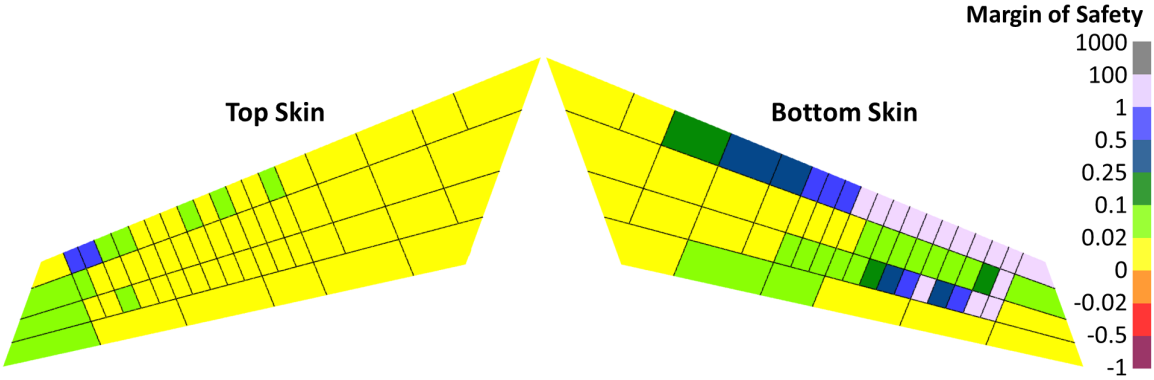

Figure 138: Margins of Safety for F-86 Baseline Optimized Aluminum Wing Skins

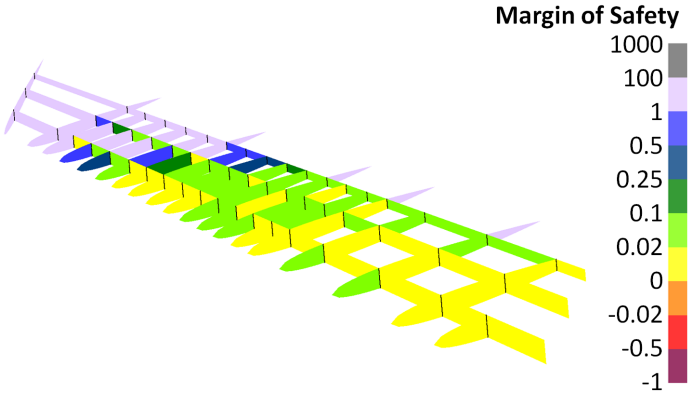

Figure 139: Margins of Safety for F-86 Baseline Optimized Aluminum Wing Spars and Ribs

Material thickness as optimized by HyperSizer is shown in Figure 140 and 141 for the skins, spars, and ribs. The upper skin has the thickest panels at the root due to the high compressive loads here. Although the loads in the upper and lower skin are relatively similar in magnitude, the compression in the upper skin requires significantly greater thickness to resist local buckling of the panel. In both the upper and lower skin, min gauge is encountered towards the tip of the wing. An interesting feature of the material thickness result is that

the structure developed natively developed a wing box-like construction with the 1st and 2nd spars and the skin between these two spars. This is the thickest part of the airfoil, so it is more mass efficient to put material in that area to increase the overall stiffness of the wing. Another note to make about this result is that the skin between the 1st and 2nd spar is substantially thicker than the spars themselves, lending to an I beam-like construction.

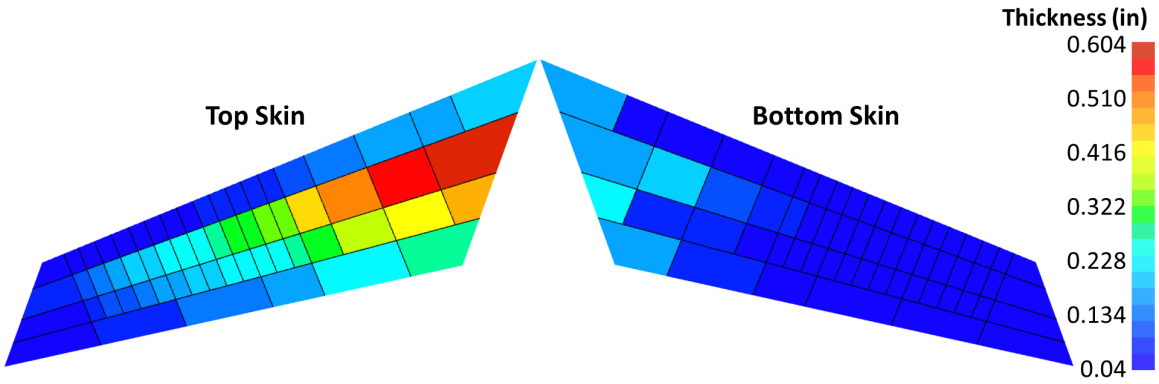

Figure 140: Material Thickness for F-86 Baseline Optimized Aluminum Wing Skins

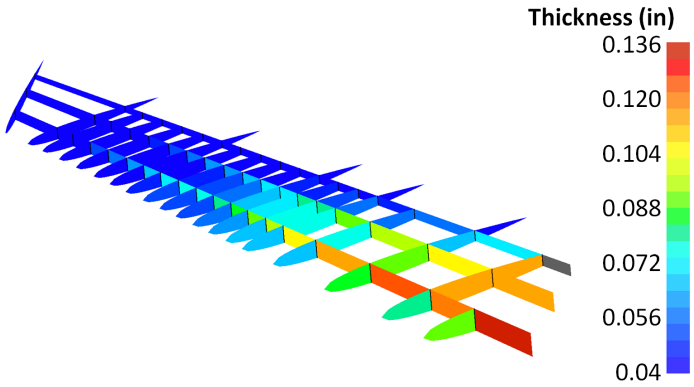

Figure 141: Material Thickness for F-86 Baseline Optimized Aluminum Wing Spars and Ribs

The total optimized mass for the wing FEM is 763.9 lbm. Note that this mass is for only the left wing of the vehicle. Both wings combined would have a mass of 1528 lbm. This result is comparable to the 1643 lbm reported by A. Sirirojvisuth for the exact same structure [116]. The 7% under-prediction is likely due to the fact that only a +7g pull-up maneuver was used here for sizing. The addition of a negative-g pull-down load case would cause the lower skin to size up, raising the wing structural mass slightly. Overall,

the optimized mass is close enough to the mass found in literature to consider the analyses used in this research to be viable.

The last piece of information to draw from these results is the mass of the portion of wing skins considered for comparison to the stiffness-based methodology. The mass of the wing skin subsection shown in Figure 127 is 439.3 lbm for the upper skin and 134.1 lbm for the lower skin. This will be compared to results in later sections.

8.2.2 Composite Design

For the composite baseline optimization, only the subsection of the upper and lower skins shown in Figure 127 is considered. The baseline optimization was performed in HyperSizer using a composite tape material (properties are listed in Table 22 of Chapter 5). This material has a minimum gauge of 8 plies (0.044 inches). Margins of safety from the composite optimization are shown in Figure 142. Due to the higher strength of the composite material compared to aluminum, more of the panels size to min gauge, causing margins to be greater overall on the wing skin. Additionally, the composite skin thickness is forced to have discrete steps due to the thickness of each ply, whereas the thickness of the aluminum can vary continuously. This also causes the margins to be higher than those on the aluminum skin.

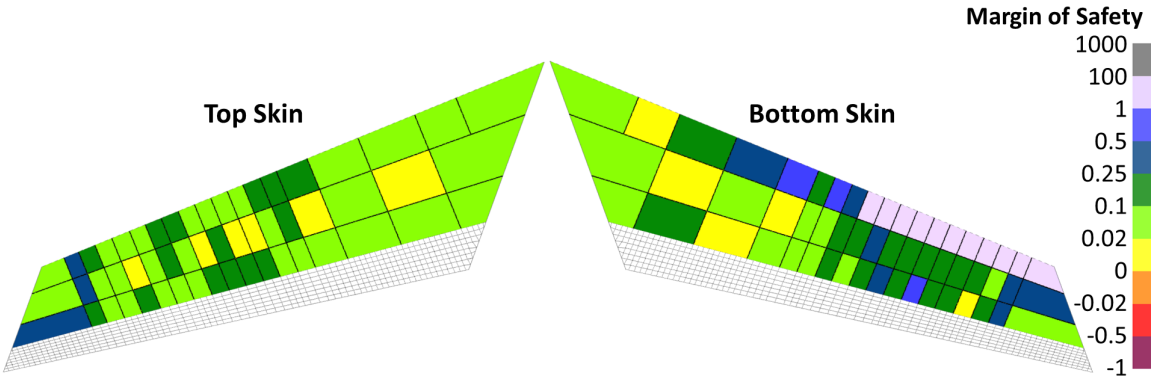

Figure 142: Margins of Safety for F-86 Baseline Optimized Composite Wing Skins

Thickness of the baseline composite skin, as well as percentage of 0° , 45° , and 90° plies are shown in Figures 143 through 146. Thickness of the composite skin design follows a pattern similar to that of the aluminum skins. The maximum thickness (top skin at

the wing root) for the composite is actually slightly higher than for aluminum. Although the composite tape material by itself is nearly twice as stiff as the aluminum in the fiber direction, the final laminates require a significant number of 45° and 90° plies at the wing root to support the N_y and N_{xy} loads in this area. Thus, the laminate ends up being slightly thicker than the aluminum to provide sufficient bending stiffness to resist panel buckling in this high-compression area.

Ultimately, the composite design is still much lighter than the aluminum because the density of the composite material is less than the aluminum. The composite upper skin section has a mass of 279.2 lbm and the lower skin section has a mass of 85.55 lbm. Compared to the aluminum design, the skins are 36% lighter.

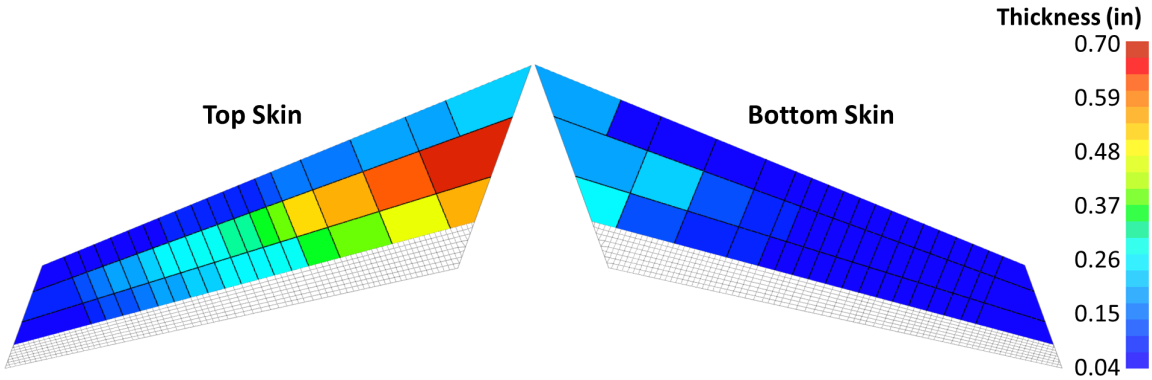

Figure 143: Material Thickness for F-86 Baseline Optimized Composite Wing Skins

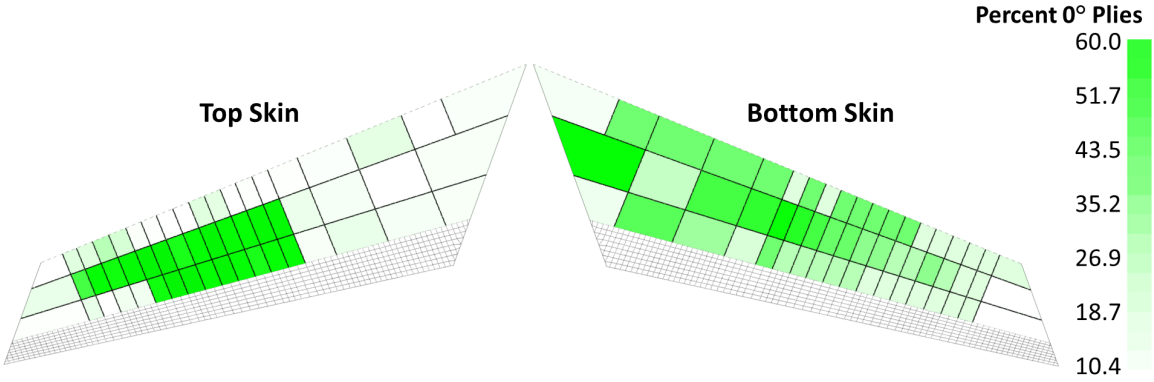

Figure 144: Percent 0° Plies for F-86 Baseline Optimized Composite Wing Skins

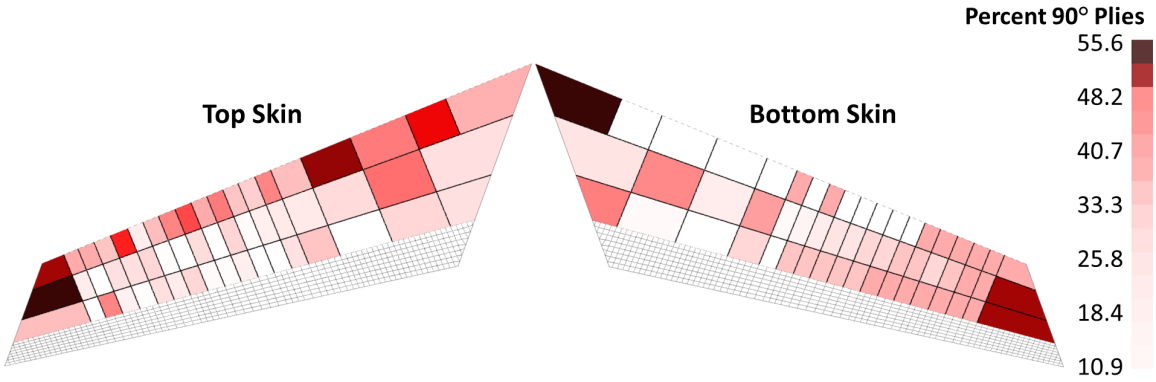

Figure 145: Percent 90° Plies for F-86 Baseline Optimized Composite Wing Skins

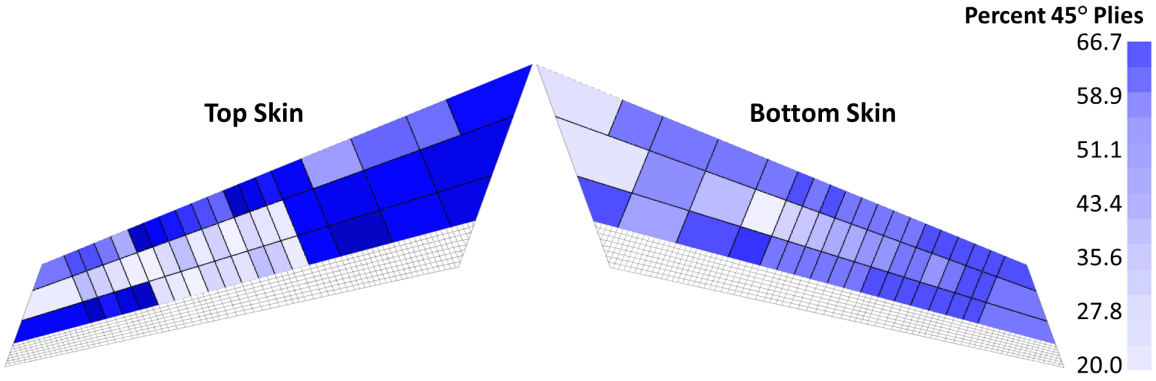

Figure 146: Percent 45° Plies for F-86 Baseline Optimized Composite Wing Skins

8.3 Stiffness-Based Optimizaiton

The final section in this chapter contains the results produced by the bi-level optimization of the F-86 wing skins using composites and the stiffness-based methodology developed in this research. The results are presented in the order in which they were described in Figure 137 of Section 8.1.3. The first set of results are from the initial panel-based optimization, with no continuity enforced between panels. Next, the results are given from enforcing global continuity of the variables. The last set of results come from mapping the optimized variables in the stiffness domain back to the physical domain to check final margins and mass.

8.3.1 Initial Optimization Results

As described in Section 8.1.3, the first pass of the process was to perform optimization on a per-panel basis, with no global linking between panels. The variable results for t, r, and s are shown in Figures 147, 148, and 149 respectively. These results correspond to a top skin mass of 307.0 lbm (10% greater than baseline) and 90.71 lbm (6.1% greater than baseline). Along with the close match in total structural mass, the distribution of skin thickness also closely matches that found in Figure 143 for the baseline composite design. This low error indicates that the first pass of the stiffness-based optimization establishes a good starting point for the composite wing skin design.

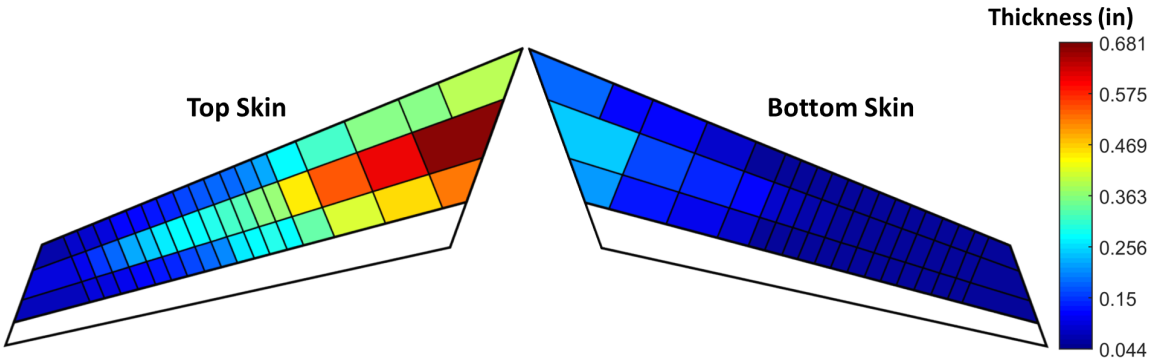

Figure 147: Per-Panel Skin Thickness from Stiffness-Based Linear Optimization

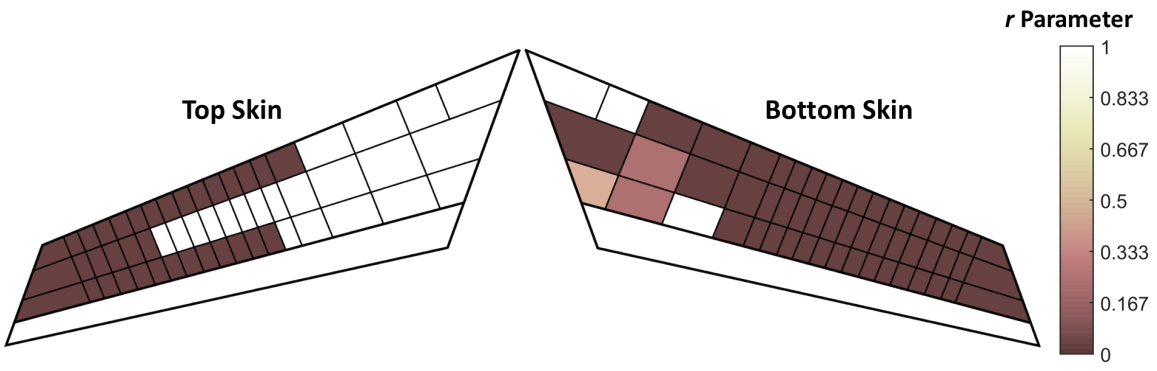

Figure 148: Per-Panel Skin r Parameter from Stiffness-Based Linear Optimization

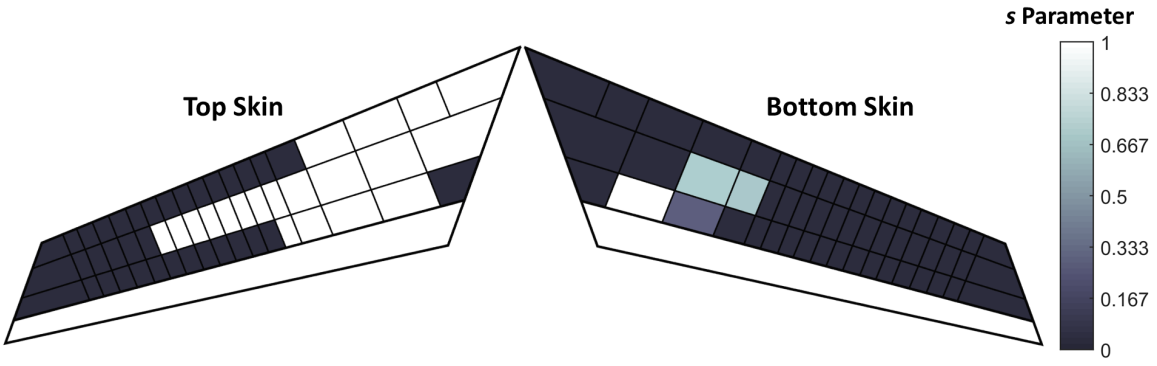

Figure 149: Per-Panel Skin s Parameter from Stiffness-Based Linear Optimization

8.3.2 Enforcing Global Variable Distributions

The second part of the process was to perform regression of the laminate variables t, r, and s calculated above. This enforces a continuous distribution of these variables over the wing skins by creating a polynomial representation of these three variables. Next, a second pass of stiffness-based sizing was run to establish the final values for all five of the laminate variables. The values of t, r, and s for each panel were dictated by the global polynomial functions and enforced as constraints at the panel level, as described by Equation 82.

Once the final continuous distributions of r and s were established, they were mapped back to a definition of ply percentages (P_0, P_{90}, P_{45}). This was done by evaluating the ply percentages from the value of r and s at every point on the wing skin, using the relationship defined in Section 5.1.2.1 and also illustrated in Figure 104 of Section 6.2.2.

The final continuous distributions of wing skin thickness and ply percentages are given

in Figures 150 through 153. Additionally, a contour map of skin thickness is given in Figure 154. These contours represent notional optimum ply shapes, with each blue line indicating where five ply drops occur. Overall, the results from the final pass of the optimization are

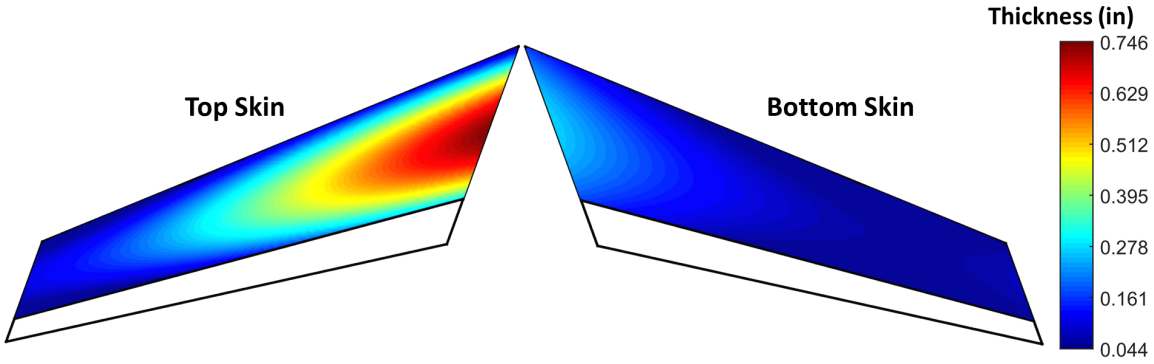

Figure 150: Continuous Skin Thickness Distribution from Stiffness-Based Linear Optimization

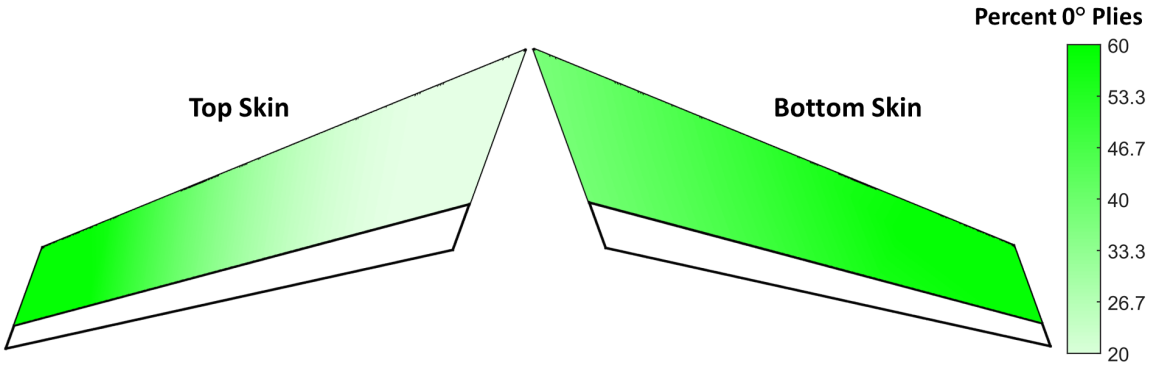

Figure 151: Continuous 0° Ply Distribution from Stiffness-Based Linear Optimization

quite similar to the baseline results, indicating validity of the approach. This optimization produced a top skin mass of 307.2 lbm and a bottom skin mass of 91.1 lbm. This is only slightly higher than the first optimization, indicating that the panel methodology was able to enforce the continuous polynomial-based distribution of r and s over the wing skins without incurring a significant mass penalties

An additional benefit of these results is that the variable distributions are smooth and continuous, ultimately leading to a more manufacturable design. In the next section, these results will be mapped to the physical domain to show that the stiffness-based optimization

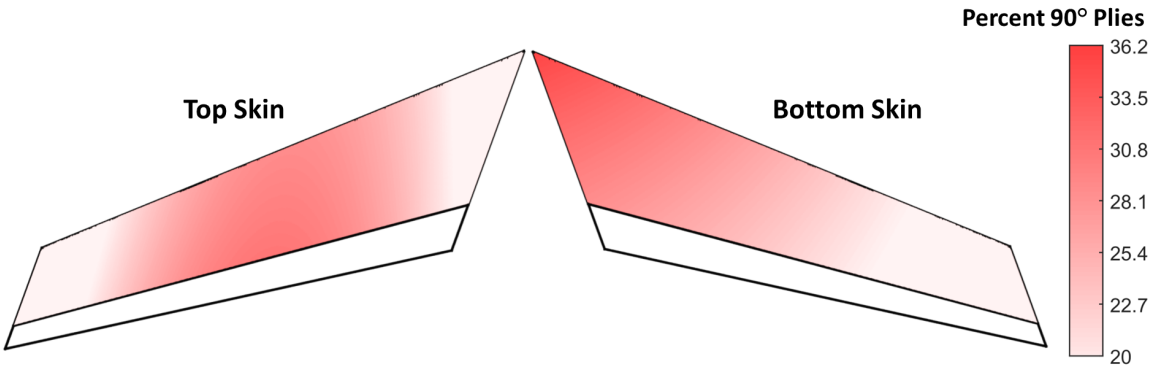

Figure 152: Continuous 90° Ply Distribution from Stiffness-Based Linear Optimization

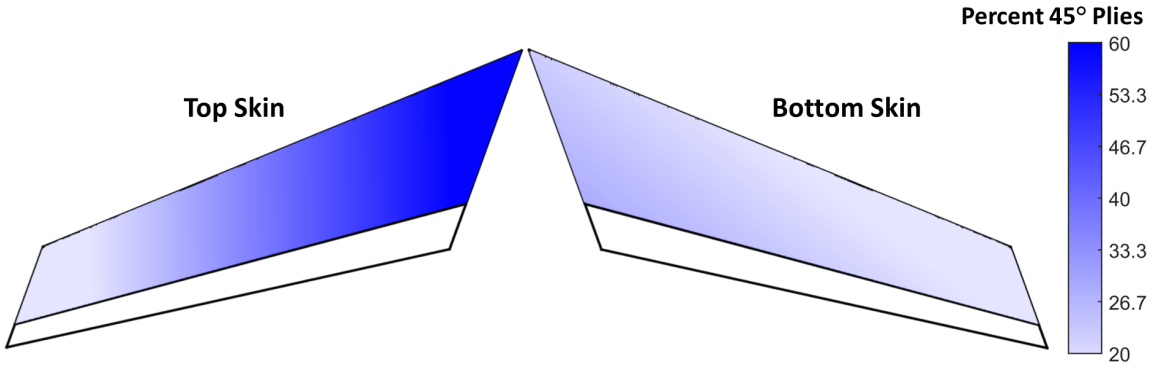

Figure 153: Continuous 45° Ply Distribution from Stiffness-Based Linear Optimization

process produces viable designs.

8.3.3 Reverse Mapping to Physical Domain

Having completed the optimization in the stiffness domain, the last step is to map the results back to the physical domain. This is done to ensure that the optimization performed in the stiffness domain produces a realistic final design. Reverse mapping for the composite laminate is achieved through a process similar to the one establish for the metallic I-stiffened panel, described in Section 3.9. However, this reverse mapping is more simple because there are significantly fewer geometry variables. Because the process is more simple, there is no need to perform a sub-optimization to complete the process, as was required for the metallic I-stiffened panel. The reverse mapping process for a single panel is outlined in Figure 155.

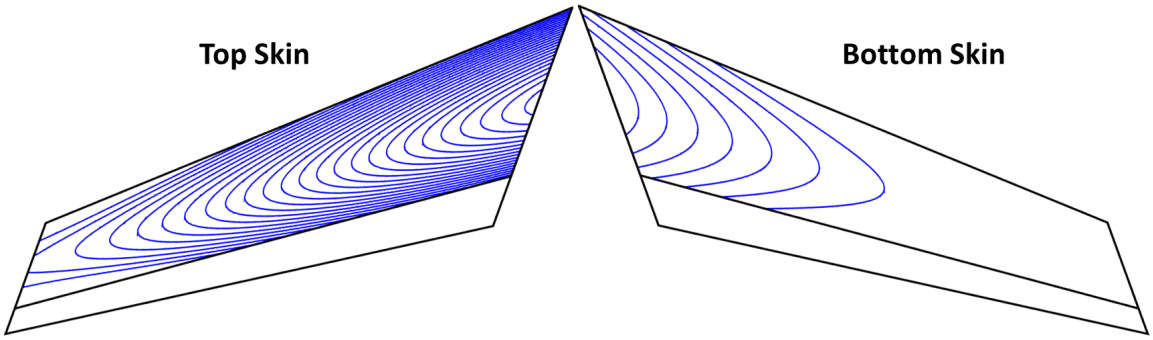

Figure 154: Contour Curves of Skin Thickness Distribution

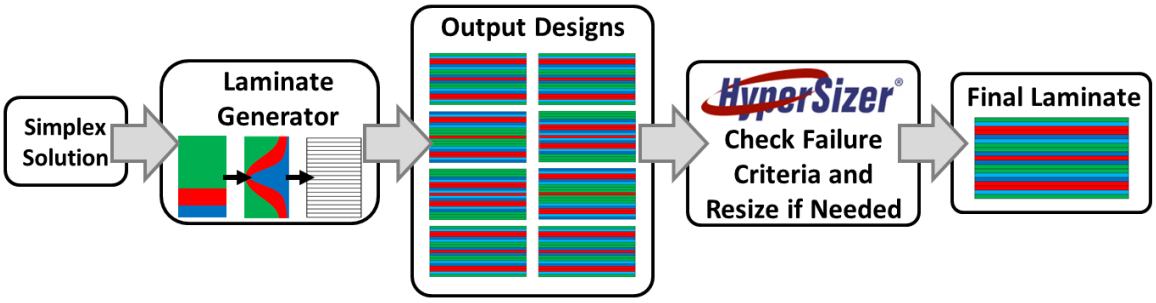

Figure 155: Reverse-Mapping Process for Unstiffened Composite Laminate Panel

The process starts with the stiffness-based solution for the panel, which consists of laminate thickness, parameters r and s (mapped to %0° , %45° , %90°), and bending stiffnesses D_{11} and D_{22}. With this information, laminates are generated using the capability presented in Section 5.1.3.1. These laminates include slight permutations of laminate thickness and ply percentages so that a range of up to 150 laminates can be generated for each panel. These output laminates are then assigned to the corresponding panel in HyperSizer, where the failure criteria are run for each panel to determine if the design is viable, and to perform any final re-sizing if necessary. This determines the final laminate for the panel.

Figure 156 shows the final thickness of the reverse-mapped design in the physical domain. The top skin has a mass of 295.7 lbm and the bottom skin has a mass of 90.67 lbm, for a combined value of 386.4 lbm. This is a 5.9 % difference from the baseline optimization, indicating validity of the approach.

Figures 157 through 159 show the corresponding ply percentages. These distributions are substantially smoother and more continuous than the baseline distributions presented

in Section 8.2.2. The distributions could be improved further by taking a mass penalty to further improve continuity, if desired. For composite structures, continuity of design features usually corresponds to better manufacturability. Trading manufacturability against mass is a common design practice.

These results complete the optimization process for the F-86 wing skins. The next section summarizes the masses from each step of the process and also compares the run times needed for each step.

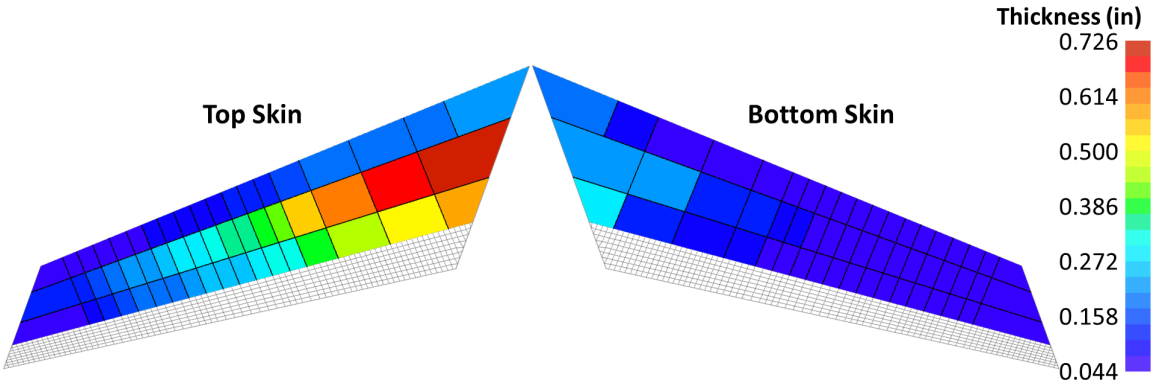

Figure 156: Skin Thickness of Final Reverse-Mapped Design in the Physical Domain

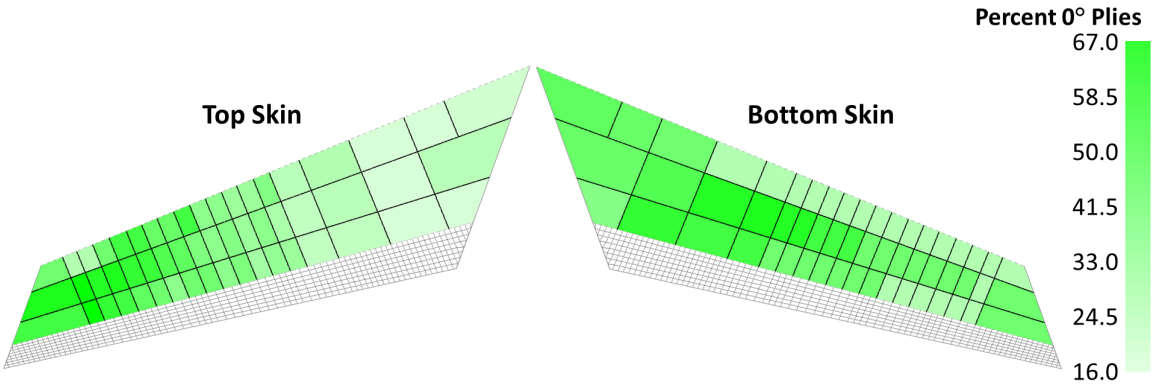

Figure 157: Percent 0° Plies of Final Reverse-Mapped Design in the Physical Domain

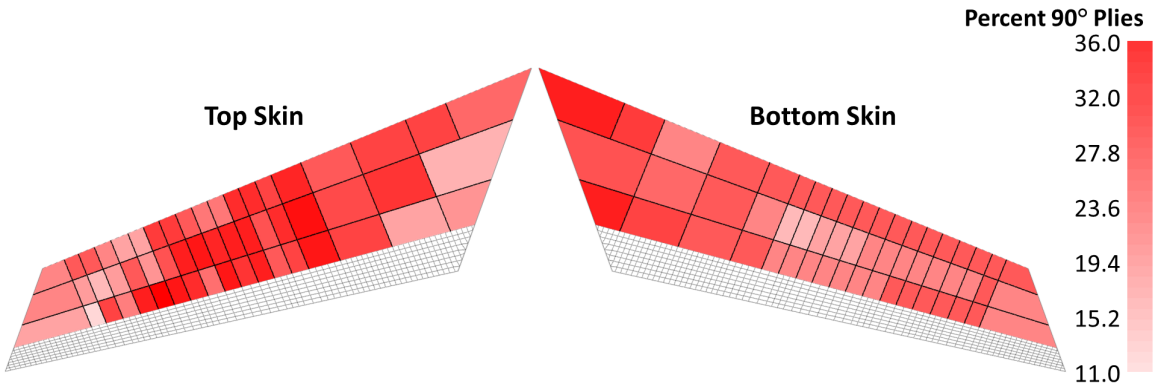

Figure 158: Percent 90° Plies of Final Reverse-Mapped Design in the Physical Domain

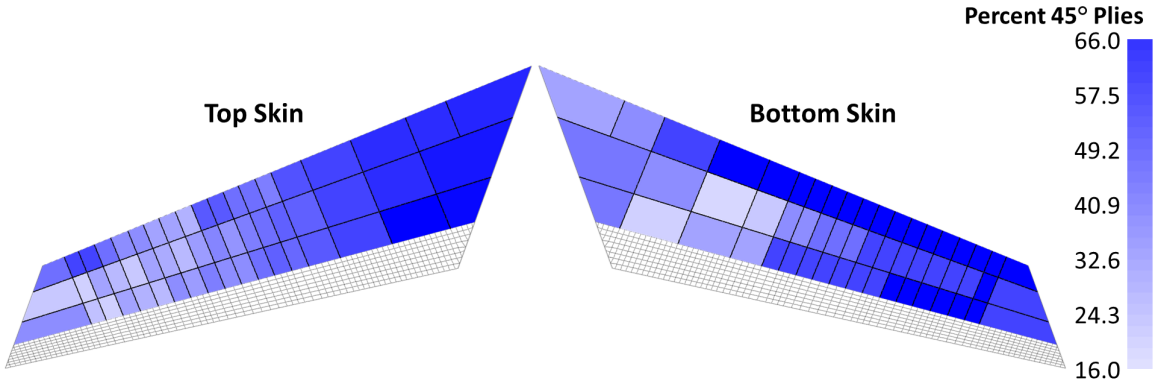

Figure 159: Percent 45° Plies of Final Reverse-Mapped Design in the Physical Domain

8.3.4 Summary of Results

Table 34 and 35 summarize the mass optimization results for the composite F-86 wing skins and the percent difference from the baseline. The difference in mass between the baseline and linear optimization can be attributed to two sources. The first is the optimization error discussed in Section 5.4 for the composite laminate. The mass difference found in Table 34 is within the range of error found for the panel optimization. The second possible source of the difference in mass is due to the polynomial functions applied at the global level for the variables r, s, and t. Although the polynomial functions give a smooth and continuous variable distribution, they cause the mass of the structure to go up because the global design freedom is reduced. As mentioned previously, this is not necessarity a defect of the optimization because it improves manufacturability of the structure.

Table 34: Summary of Masses and Run Times for F-86 Wing Skin Optimization

Optimization	Top Skin Mass (lbm)	% Diff.	Bottom Skin Mass (lbm)	% Diff.
HyperSizer, Baseline	279.2	0	85.55	0
Linear Optimization, 1st Pass	307.0	10	90.71	6.1
Linear Optimization, 2nd Pass	307.2	10	91.10	6.5
HyperSizer, Reverse Mapping	295.7	5.9	90.67	6.0

Table 35: Summary of Masses and Run Times for F-86 Wing Skin Optimization (cont.)

Optimization	Total Mass (lbm)	% Diff.	Run Time (s)	% Diff.
HyperSizer, Baseline	364.8	0	221	0
Linear Optimization, 1st Pass	397.7	9.0	21.1	-90
Linear Optimization, 2nd Pass	398.3	9.1	14.9	-93
HyperSizer, Reverse Mapping	386.4	5.9	30	-86.4

The mass of the final step in the process, reverse mapping to the physical domain, is slightly closer to the original baseline value. This difference can be attributed to the small amount of error that exists in the stiffness domain.

In terms of optimization efficiency (shown in Table 35), the linear optimization provides a substantial improvement over the baseline. The total run time for the linear optimization is 36 seconds for both the 1st and 2nd pass required to complete the process. This is 83% faster than the baseline optimization. This result is comparable to the efficiency gains presented in Section 5.5 because a similar number of panel optimizations are performed in the baseline and linear approach.

Overall, the results presented here show that the stiffness-based panel optimization meets the objective of this chapter, successfully demonstrating ability to couple with a FEM -based design environment using composite materials. The approach developed in this research is capable of finding an accurate solution in substantially less time than traditional optimization approaches.

CHAPTER IX

CONCLUSIONS AND FUTURE WORK

This chapter closes out the dissertation by providing conclusions of the results presented and also providing discussion on future avenues to investigate with the methodology developed in this research.

9.1 Conclusions

The research question that formed the premise of this research was to determine if a stiffened panel optimization environment could be constructed to provide significant improvement in efficiency over existing methods, retain the accuracy of higher-fidelity physics-based structures tools, and also have low offline run-time requirements. These characteristics are necessary for the structures discipline to function well in a multi-discipline optimization environment. Four objectives were created to form a hypothesis for addressing this research question (outlined in Section 1.2). A discussion of these objectives and how they were met is given below.

The study was initiated by first examining how existing tools could be used to expedite stiffened panel design. Of particular interest was the application of a design of experiments and response surface equations to the stiffened panel design environment to provide a surrogate model for the panel failure criteria. This allowed for a rapid gradient-based optimizer to be implemented for stiffened panel design. The optimizer had a run time of 3 seconds for an example metallic I-stiffened panel loaded in compression. This compares favorably to a traditional optimization performed in HyperSizer, which requires a run time of 247 seconds to produce the same level of mass accuracy.

Although the improvement in efficiency listed above is substantial, there is still a desire for further improvement to make the panel optimization more suitable for multi-discipline integration. This formed the second research objective, which was accomplished through a novel change of variables in the stiffened panel optimization problem, mapping from the

physical domain to the stiffness domain. The mapping allowed for accurate linearization of the stiffened panel design space. By linearizing the design space, the Simplex Algorithm was able to be used for optimization, vastly improving efficiency of the process. With this methodology, the stiffened panel optimization run time was reduced to 0.13 seconds.

To ensure that the new methodology retains most of the accuracy of higher-fidelity approaches, thorough validation was performed. The validation was accomplished by comparing the new stiffness-based optimization environment to the traditional optimization tool HyperSizer in three areas of accuracy. The first comparison demonstrated that the linearized design space provides accurate representations of panel failure criteria with error less than 10%. The second comparison verified that the stiffness-based optimization methodology is able to produce an optimum panel with average mass error less than 10%. The third comparison verified ability to determine if a stiffness constraint imposed on the optimization can be correctly identified as feasible or infeasible (necessary for iterating with FEA). This was done with error less than 4%.

The third research objective was to demonstrate generality of the panel methodology by applying it to composite panels. This was done with two panel types: an unstiffened laminate and an I-stiffened panel. The application to composites panels was developed in a very similar manner to that of the metallic panel, with a few modifications needed to handle the increased complexity of the material. Accuracy of the failure criteria and mass optimization was also verified, showing similar amount of error to the metallic panels.

To meet the final objective of the research, the stiffness-based optimization methodology was applied to two FEM -based design environments. The first example was with a metallic wing box structure. The objective of this optimization was to minimize the mass of the I-stiffened skins while meeting a wing tip deflection requirement. This was achieved by controlling the longitudinal stiffness of the skin panels at the global level. The methodology was ultimately able to achieve a lower total mass than the baseline optimization from HyperSizer (2302 versus 2475 lbm) in a fraction of the run time (50 versus 480 minutes).

The second FEM -based example used a composite wing structure. In this optimization, mass of the wing was minimized by controlling the distribution of skin thickness and

ply counts at the global level with a continuous polynomial. The mass of the wing skins optimized with the stiffness-based methodology closely matched the baseline design from HyperSizer (9.1% error), indicating validity of the approach. The stiffness-based optimization ran in 14.9 seconds, which is significantly faster than the 221 seconds of the HyperSizer optimization.

Overall, the content discussed above demonstrates completion of the objectives set forth for this research. The new stiffened panel methodology has been shown to be highly efficient, accurate, general enough for application to composites, and capable of coupling with an FEM -based design environment. Thus, the methodology is well suited to serve the purpose of integrating with a large-scale multi-discipline environment, as described in the motivation for the research.

9.2 Future Work

This section presents several topics that warrant consideration but were not on the critical path to complete the objectives set forth for this research. These are recommended to be a part of future work for this research.

9.2.1 Piece-Wise Linear Constraints for Simplex

One of the main contributors to the error present in the solutions produced by the linear optimization is the linear constraints necessary for domain mapping. These were needed to properly map from the physical domain to the stiffness domain (introduced in Section 3.4, error discussed in section 4.2.3). These stiffness domain constraints are needed to ensure that design points selected in the stiffness domain can feasibly be mapped back to the physical domain. The challenge is that the boundary of the domain can be nonlinear, as shown in Figure 160. This does not pose a problem when the boundary is *convex* because multiple linear constraints can be used to to approximate the boundary. However, a *concave* boundary can only be approximated with segments of a linear constraint. These two concepts are depicted in Figure 160.

The traditional Simplex Algorithm used for linear optimization applied in the current research is not capable of handling piecewise linear constraints. For this reason, nonlinear

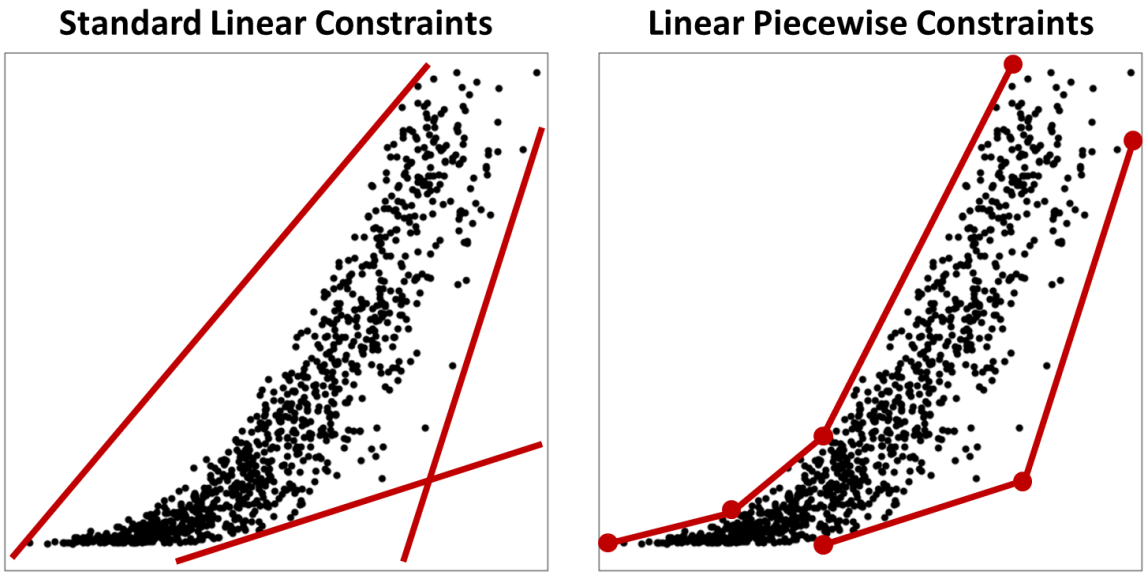

Figure 160: Use of Piecewise Linear as Domain Constraints

boundaries could only be represented precisely if they were convex. However, extensions of the Simplex Algorithm have been made in recent years to handle piecewise linear constraints. The approaches by Wolf [120] and Fourer [121] both address this challenge. Implementing these approaches in the present research would improve representation of the domain boundaries, thus improving optimization accuracy. This task was not addressed in the current work due to the substantial programming effort required.

9.2.2 Application to Other Stiffener Concepts

To further demonstrate the generality of the methodology developed in this research, the next step would be to apply it to other panel concepts such as those shown in Figure 27 in Section 2.6.1. The hat-stiffened panel is an obvious choice for application of this methodology because of its widespread use through fuselages and barrel sections of launch vehicles.

9.2.3 Internal Structural Arrangement Studies

As discussed in Section 2.3, studies of internal structural arrangement are a critical part of conceptual design. This pertains to finding optimum placement of primary structural features such as ribs, spars, frames, and bulkheads. Determining the optimum internal

arrangement requires iterating through many configurations and performing detailed structural design with each. This process can be performed efficiently by applying the panel optimization techniques in the current research.

To demonstrate applicability to internal arrangement studies, a global optimization environment would be set up to automatically examine different arrangements. This could potentially be accomplished by generating a FEM that contains every possible structural member to be considered. An example of this setup is shown in Figure 161 for a supersonic wing. The wing FEM contains a large number of ribs and spars which could be turned "on" or "off" by the global optimizer. For each configuration considered by the optimizer, FEA would be run to determine the internal load distribution and to evaluate constraints such as wing tip deflection and global buckling. The methodology developed in this research would be used drive the global optimization to meet global constraints as well as perform the panel optimization for each configuration.

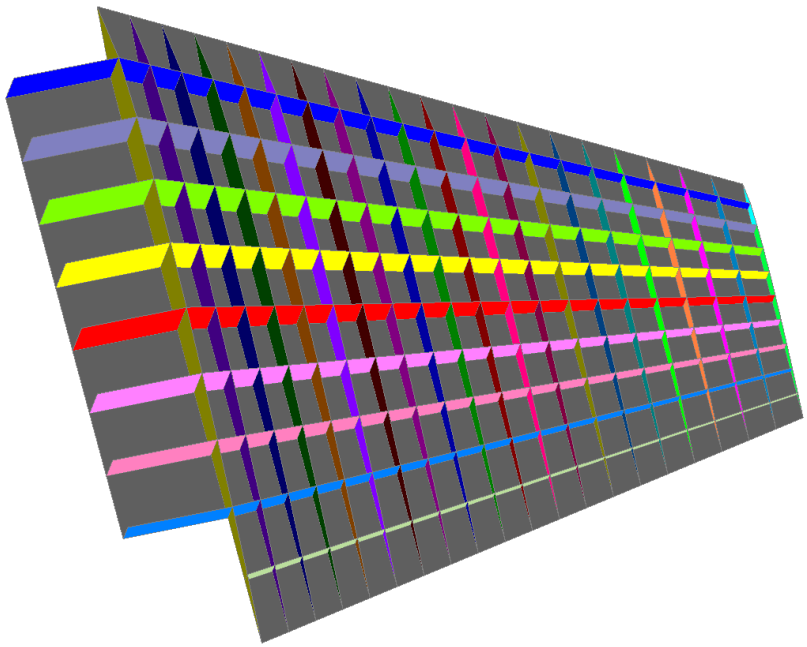

Figure 161: Supersonic Wing Setup for Optimization of Rib and Spar Arrangement

In addition to the simple bi-directional arrangement study shown in Figure 161, variation in rib and spar orientation could also be added to the mix. As has been demonstrated in References [9] and [10], rib and spar orientation can have a significant impact on deflection

and twist of a wing box, as well as aeroelastic performance. The references showed that rib and spar orientation can be tailored to meet these constraints with a more mass-optimal solution than traditional rib and spar orientation. However, these studies were performed on an academic rectangular wing box. The approach has yet to be demonstrated in the literature with a realistic wing model. This gap in literature could be filled by applying the optimization approaches discussed above to the X-29 wing. The X-29 is shown in Figure 162.

Figure 162: X-29 Experimental Flight Vehicle [22]

The X-29 wing is a good demonstration model because it presents a challenging aeroelastic design problem. Due to the forward-swept configuration of the X-29 wing, divergence is possible in high-g maneuvers. The forward-swept geometry inherently causes the wing to twist to a higher angle of attack when the wing loading is increased. This problem was handled in the X-29 design with tailored composites which twist forward when the wing deflects upward [44]. However, the mass of the wing could be reduced by studying non-traditional rib and spar orientations as discussed above. These studies could be performed efficiently by applying the composite panel design methodology presented in this research. Figure 163 displays potential internal arrangements to be explored for the X-29 wing box.

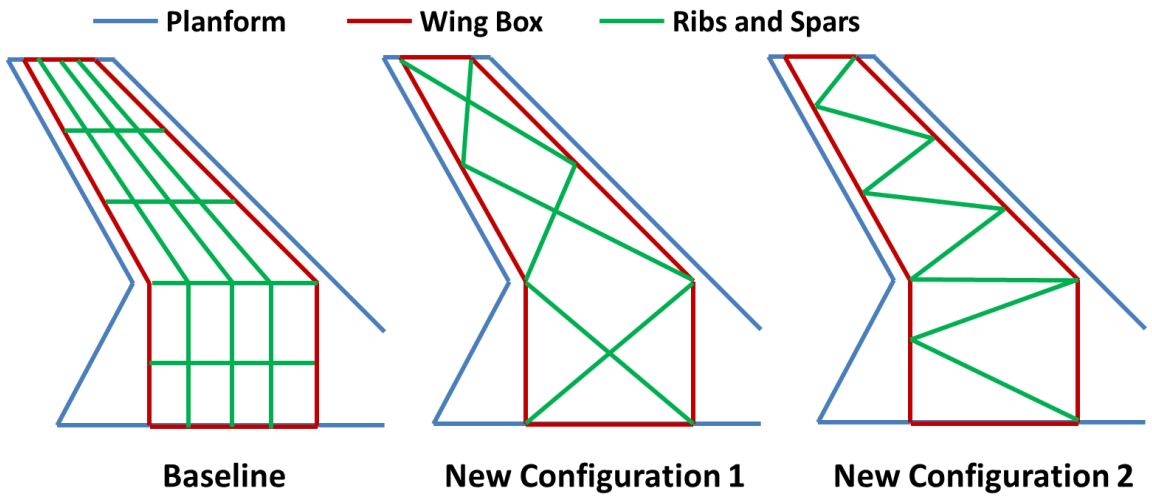

Figure 163: Internal Arrangements of the X-29 Wing Box to be Studied

9.2.4 Consideration of Aeroelasticity

Aeroelasticity consists of the study of interaction between the aerodynamics and structures discipline, and is thus a subset of the broad multi-discipline environment introduced in Section 2.1. This section identifies some of the challenges that exist when considering aeroelasticity during design, from the perspective of the structures discipline. These challenges could potentially be addressed by the methodology developed in the current research.

As identified by Collar's triangle [122], elastic forces are one of the three primary contributors to aeroelastic analyses, along with aerodynamic forces and inertial forces. When aeroelastic tailoring is performed on a structure, mass optimization becomes a sub-discipline that must be run each time a new configuration is explored and new external loads are generated [39]. For this reason, it is desirable to have a simplified structural analysis tool with low run times that is closely coupled with the global stiffness distribution of the structure. To achieve these analysis characteristics, many aeroelastic tailoring studies work with structural models whose only design variable is skin thickness [39],[123] to improve run time. However, this is an academic simplification and would not work in an actual manufactured aerospace structure where there are other variables such as stiffener design and spacing, all of which have a bearing on global stiffness.

Thus, a methodology that could fully capture the impact of stiffened panel dimensions

while also having low run times would be valuable for aeroelastic tailoring studies. This further re-iterates the need to have a fast, simplified structural sizing environment that captures the coupling between local and global stiffness.

This need becomes more critical when the internal arrangement of structures is considered in conjunction with aeroelastic tailoring [9],[124]. Internal arrangement in aerospace structures refers to the placement of significant structural members such as the ribs and spars in a wing or the ring frames in a fuselage or rocket body. For each arrangement of these structural members that is explored, the entire structure (external panels plus internal structure) must be sized with the applied external loads. Because of the large number of arrangements that are explored in aeroelastic tailoring, the run time of the structural sizing tool is critical to the success of the optimization. Similar to the discussion on conceptual design, it is important to capture the influence of local panel designs on global stiffness and load distribution.

Typically, aeroelastic requirements are given as deflection and twist limits [125],[126],[127], or as a stiffness distribution over a structure [128],[129]. The presented research is highly capable of handling these requirements at a native level due to the use of a stiffness-based design approach. Thus, a future application of the current methodology would be to perform aeroelastic tailoring, or optimize a structure in the presence of aeroelastic constraints.

APPENDIX A

DESIGN VARIABLE INTERACTIONS

This appendix contains scatter plots that demonstrate the interactions between stiffness terms for metallic and composite stiffened panels. The scatter plots data points were generated in the physical domain for regression (for failure criteria RSEs), and were then mapped to the stiffness domain.

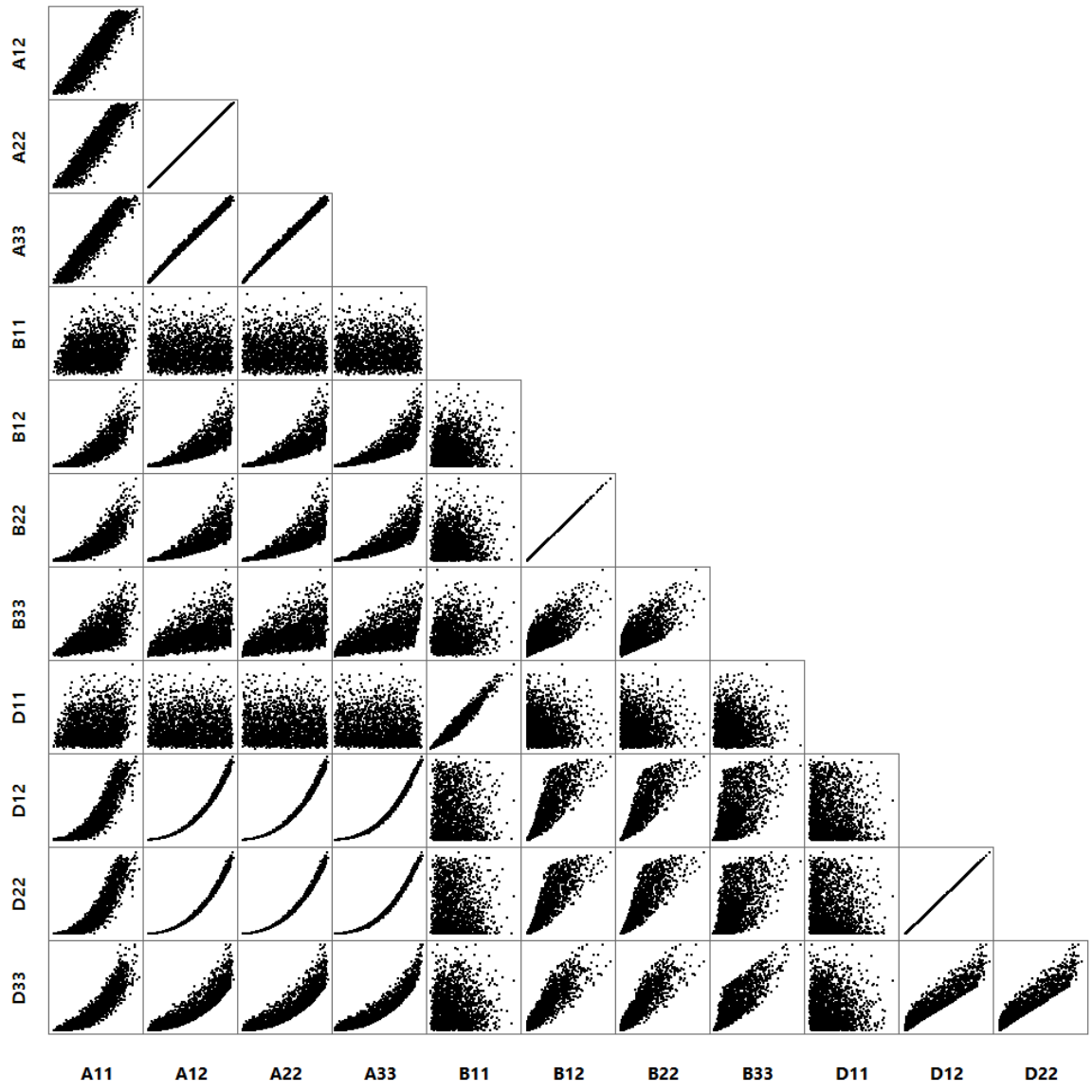

Figure 164: ABD Term Interactions for Metallic I-Stiffened Panel

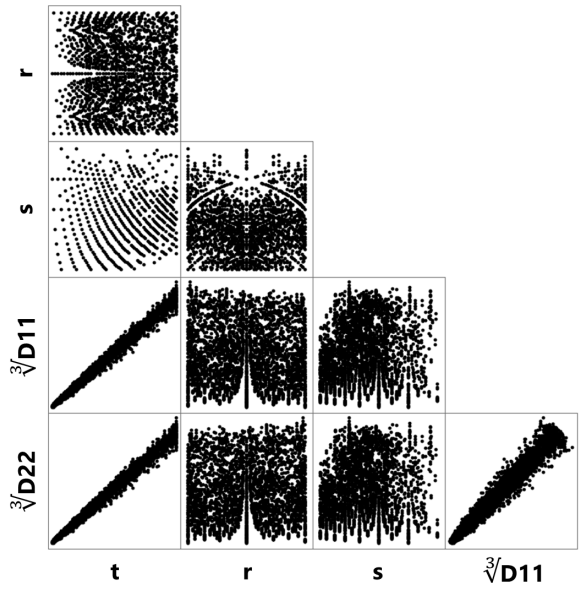

Figure 165: ABD Term Interactions for Composite Unstiffened Laminate

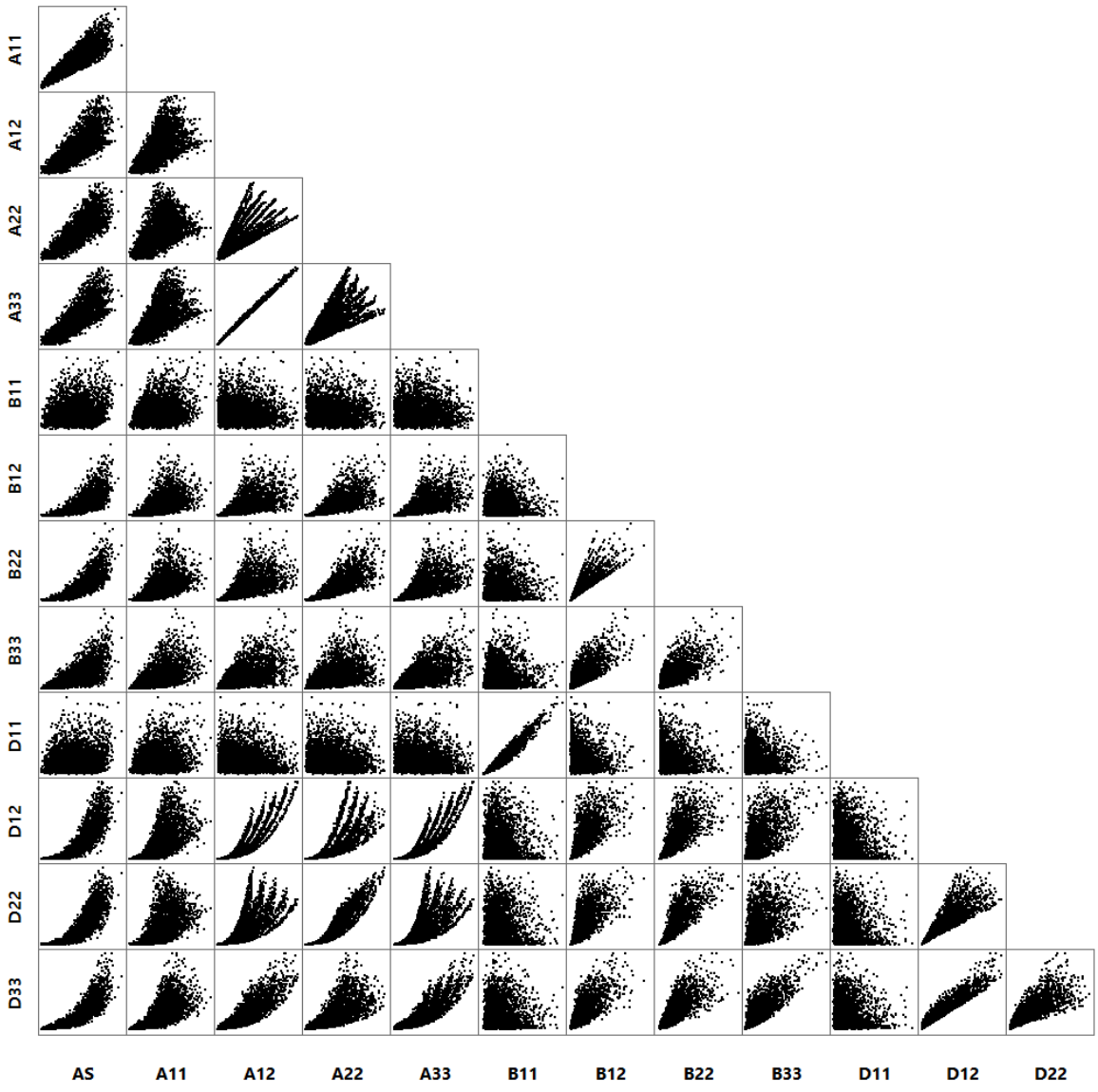

Figure 166: ABD Term Interactions for Composite I-Stiffened Panel

APPENDIX B

RELATIVE SIGNFICANCE OF RSE TERMS

The tables in this appendix contains two statistics metrics relevant to reducing the number of terms in the RSEs. The values in Table 36 and 37 correspond to the panel buckling failure criteria RSE for $-N_x$, $-N_y$ loading.

Table 36: t-Ratios and p-Values for Terms in the $-N_x$, $-N_y$ Panel Buckling RSE

Term	t-Ratio	p-Value	Term	t-Ratio	p-Value
$N_x \cdot N_y$	34.67	< 0.0001	$N_x \cdot N_x \cdot D_{11}$	3.84	< 0.0001
$N_x \cdot N_y \cdot N_y$	16.6	< 0.0001	$N_y \cdot D_{11}$	1.93	0.0534
$N_x \cdot N_x \cdot N_y$	14.03	< 0.0001	$N_x \cdot N_x \cdot A_{11}$	-1.86	0.0633
$N_x \cdot a$	-12.41	< 0.0001	$N_y \cdot N_y \cdot A_{22}$	1.85	0.064
$N_y \cdot N_y$	11.99	< 0.0001	$b \cdot D_{22}$	1.82	0.0691
$N_x \cdot D_{11}$	10.6	< 0.0001	$N_y \cdot N_y \cdot b$	-1.81	0.0704
$N_x \cdot N_y \cdot D_{11}$	9.89	< 0.0001	$N_y \cdot N_y \cdot A_{33}$	-1.74	0.0812
$N_x \cdot N_x$	9.33	< 0.0001	$a \cdot a \cdot D_{11}$	-1.72	0.0857
$N_x \cdot N_y \cdot a$	-7.65	< 0.0001	$b \cdot b$	1.71	0.0867
a	-7.51	< 0.0001	$N_x \cdot N_{xy} \cdot N_{xy}$	-1.7	0.0894
$N_y \cdot A_{11}$	7.3	< 0.0001	$b \cdot b \cdot D_{22}$	1.55	0.1213
N_y	6.64	< 0.0001	$N_y \cdot N_y \cdot N_{xy}$	-1.53	0.1262
$N_y \cdot a$	-5.95	< 0.0001	$N_x \cdot a \cdot D_{22}$	-1.52	0.129
$N_y \cdot D_{22}$	-4.8	< 0.0001	$a \cdot a \cdot A_{11}$	1.5	0.1332
$N_y \cdot A_{22}$	4.7	< 0.0001	$N_y \cdot a \cdot A_{33}$	1.5	0.1345
$N_y \cdot A_{33}$	-4.69	< 0.0001	$a \cdot b \cdot A_{22}$	1.46	0.1443
D_{11}	4.67	< 0.0001	$N_y \cdot N_{xy} \cdot N_{xy}$	-1.43	0.1529
$a \cdot A_{11}$	-4.53	< 0.0001	$a \cdot a \cdot D_{22}$	1.43	0.1534
$a \cdot a$	4.28	< 0.0001	$N_x \cdot b \cdot b$	1.4	0.1622
N_x	3.86	< 0.0001	$N_x \cdot a \cdot a$	1.36	0.1752

Table 37: t-Ratios and p-Values for Terms in the $-N_x$, $-N_y$ Panel Buckling RSE (Cont.)

Term	t-Ratio	p-Value	Term	t-Ratio	p-Value
$N_y \cdot b \cdot D_{22}$	2.01	0.0443	$b \cdot b \cdot A_{11}$	0.92	0.3589
$N_y \cdot D_{11}$	1.93	0.0534	$N_x \cdot b \cdot A_{33}$	-0.91	0.3617
$N_x \cdot N_x \cdot A_{11}$	-1.86	0.0633	$N_x \cdot b \cdot D_{22}$	0.9	0.3664
$N_y \cdot N_y \cdot A_{22}$	1.85	0.064	$a \cdot a \cdot a$	0.86	0.3911
$b \cdot D_{22}$	1.82	0.0691	$N_y \cdot N_y \cdot D_{11}$	0.85	0.3928
$N_y \cdot N_y \cdot b$	-1.81	0.0704	A_{22}	0.85	0.3931
$N_y \cdot N_y \cdot A_{33}$	-1.74	0.0812	$b \cdot A_{33}$	-0.83	0.4055
$a \cdot a \cdot D_{11}$	-1.72	0.0857	$N_x \cdot N_{xy} \cdot D_{11}$	0.83	0.406
$b \cdot b$	1.71	0.0867	$N_y \cdot b$	-0.77	0.4422
$N_x \cdot N_{xy} \cdot N_{xy}$	-1.7	0.0894	$a \cdot b \cdot D_{11}$	0.75	0.4529
$b \cdot b \cdot D_{22}$	1.55	0.1213	$N_x \cdot N_{xy} \cdot A_{33}$	0.75	0.4545
$N_y \cdot N_y \cdot N_{xy}$	-1.53	0.1262	$N_{xy} \cdot N_{xy} \cdot D_{22}$	0.74	0.4566
$N_x \cdot a \cdot D_{22}$	-1.52	0.129	$N_x \cdot N_x \cdot D_{22}$	-0.73	0.4673
$a \cdot a \cdot A_{11}$	1.5	0.1332	$a \cdot a \cdot A_{22}$	-0.72	0.4687
$N_y \cdot a \cdot A_{33}$	1.5	0.1345	$b \cdot b \cdot A_{22}$	-0.72	0.4737
$a \cdot b \cdot A_{22}$	1.46	0.1443	$N_y \cdot N_y \cdot a$	0.71	0.4788
$N_y \cdot N_{xy} \cdot N_{xy}$	-1.43	0.1529	$N_y \cdot N_{xy} \cdot b$	0.68	0.4955
$a \cdot a \cdot D_{22}$	1.43	0.1534	$N_{xy} \cdot N_{xy} \cdot A_{22}$	0.66	0.5102
$N_x \cdot b \cdot b$	1.4	0.1622	$b \cdot A_{11}$	0.65	0.5184
$N_x \cdot a \cdot a$	1.36	0.1752	$N_y \cdot N_{xy} \cdot a$	0.65	0.5187
$N_x \cdot N_{xy} \cdot D_{22}$	1.33	0.1834	$a \cdot D_{22}$	-0.62	0.5365
$N_{xy} \cdot a \cdot D_{22}$	1.32	0.1873	$N_{xy} \cdot N_{xy} \cdot A_{33}$	-0.58	0.5595
$b \cdot b \cdot b$	1.32	0.1879	$N_{xy} \cdot b \cdot D_{22}$	0.57	0.5662
$N_x \cdot a \cdot A_{22}$	-1.29	0.1956	$a \cdot b \cdot D_{22}$	-0.57	0.5663
$N_{xy} \cdot a \cdot D_{11}$	1.22	0.2242	A_{33}	-0.56	0.5744
$N_x \cdot A_{33}$	1.2	0.2306	$N_x \cdot b \cdot D_{11}$	-0.53	0.5973
$N_{xy} \cdot b \cdot b$	1.18	0.2381	$N_x \cdot N_x \cdot b$	-0.51	0.6127
$N_x \cdot N_{xy} \cdot A_{22}$	-1.17	0.243	$N_{xy} \cdot b \cdot A_{11}$	-0.5	0.6185
$a \cdot b \cdot A_{33}$	-1.12	0.2618	$N_y \cdot b \cdot D_{11}$	-0.5	0.6198
$N_x \cdot a \cdot A_{33}$	1.12	0.2643	$N_x \cdot N_y \cdot A_{11}$	-0.49	0.6212
$N_{xy} \cdot a$	1.11	0.2684	$N_{xy} \cdot a \cdot A_{33}$	-0.47	0.6353
$N_y \cdot a \cdot a$	-1.1	0.2713	$N_{xy} \cdot N_{xy} \cdot N_{xy}$	-0.46	0.6441
$N_y \cdot a \cdot A_{22}$	-1.09	0.2768	$N_{xy} \cdot a \cdot A_{22}$	0.46	0.6453
$N_x \cdot N_y \cdot A_{22}$	1.08	0.2816	$N_y \cdot b \cdot A_{22}$	-0.45	0.6507
$N_x \cdot N_x \cdot A_{22}$	1.04	0.2968	$b \cdot b \cdot D_{11}$	-0.44	0.6628
$N_x \cdot b \cdot A_{11}$	0.98	0.3254	$N_{xy} \cdot a \cdot b$	-0.43	0.665
$a \cdot D_{11}$	0.97	0.3312	$a \cdot b \cdot A_{11}$	0.4	0.6884
$N_{xy} \cdot N_{xy} \cdot a$	0.95	0.3417	$b \cdot D_{11}$	0.39	0.6929
$a \cdot a \cdot b$	-0.95	0.3424	$N_y \cdot N_{xy} \cdot A_{11}$	0.39	0.7
$N_{xy} \cdot N_{xy} \cdot D_{11}$	-0.95	0.3443	$N_y \cdot b \cdot A_{11}$	0.35	0.7241

Table 38: t-Ratios and p-Values for Terms in the $-N_x$, $-N_y$ Panel Buckling RSE (Cont.)

Term	t-Ratio	p-Value	Term	t-Ratio	p-Value
$N_x \cdot b \cdot A_{22}$	0.35	0.7251	$N_y \cdot b \cdot b$	0.18	0.8579
$a \cdot b \cdot b$	-0.34	0.735	$N_x \cdot N_{xy} \cdot A_{11}$	-0.15	0.8809
b	0.34	0.7373	$N_{xy} \cdot N_{xy} \cdot A_{11}$	-0.15	0.8826
$N_{xy} \cdot N_{xy}$	-0.33	0.7392	$N_x \cdot b$	0.14	0.8886
$N_y \cdot N_{xy} \cdot A_{33}$	-0.33	0.7411	$N_y \cdot b \cdot A_{33}$	-0.13	0.8941
$N_{xy} \cdot A_{22}$	-0.32	0.7473	$N_y \cdot a \cdot D_{22}$	-0.13	0.898
$N_x \cdot N_y \cdot D_{22}$	-0.32	0.7513	$N_y \cdot N_{xy} \cdot D_{22}$	0.13	0.8992
$N_y \cdot N_{xy} \cdot D_{11}$	0.31	0.757	$N_{xy} \cdot N_{xy} \cdot b$	0.12	0.9011
$N_{xy} \cdot b$	0.31	0.7591	$N_{xy} \cdot a \cdot a$	-0.12	0.9029
$N_{xy} \cdot b \cdot A_{22}$	0.28	0.776	D_{22}	-0.11	0.9085
$N_{xy} \cdot a \cdot A_{11}$	-0.27	0.7855	$N_x \cdot N_x \cdot A_{33}$	0.11	0.9092
N_{xy}	0.26	0.7957	$N_y \cdot N_{xy} \cdot A_{22}$	0.11	0.915
$N_{xy} \cdot D_{11}$	0.26	0.7974	$b \cdot b \cdot A_{33}$	0.1	0.9184
$N_x \cdot A_{22}$	0.25	0.8016	$a \cdot b$	-0.1	0.9187
$N_x \cdot a \cdot A_{11}$	-0.24	0.8093	$N_{xy} \cdot b \cdot D_{11}$	0.1	0.9193
$N_{xy} \cdot b \cdot A_{33}$	-0.24	0.8119	$N_{xy} \cdot D_{22}$	-0.1	0.9218
$N_{xy} \cdot A_{11}$	0.23	0.8202	$N_{xy} \cdot A_{33}$	0.09	0.9268
$N_x \cdot N_{xy} \cdot a$	0.21	0.8331	$b \cdot A_{22}$	0.09	0.9271
$N_x \cdot N_{xy} \cdot b$	0.21	0.8338	$a \cdot a \cdot A_{33}$	-0.05	0.9582
$N_x \cdot a \cdot b$	0.21	0.8345	$N_x \cdot N_y \cdot A_{33}$	0.05	0.9588

APPENDIX C

RESPONSE SURFACE EQUATIONS FOR FAILURE CRITERIA

C.1 RSEs for Metallic I-Stiffened Panel

The following sections list RSEs generated for the metallic I-Stiffened Panel. The +/- and -/+ load quadrants are left out for brevity.

C.1.1 X-Tension, Y-Tension Load Quadrant RSEs

Below are the RSEs for the $+N_x$, $+N_y$ load quadrant. The equations are for facesheet local buckling 83, facesheet material failure 84, bonded combo material failure 85, and spacing span local buckling 86

$$\begin{aligned}
\phi = {} & 8.179 \cdot 10^{-12} N_x N_{xy} D_{22} - 1.268 \cdot 10^{-7} N_x N_{xy} \\
& - 5.982 \cdot 10^{-10} N_x a D_{22} + 9.271 \cdot 10^{-6} N_x a + 1.547 \cdot 10^{-11} N_x b A_{22} \\
& - 4.068 \cdot 10^{-11} N_x b A_{33} - 2.808 \cdot 10^{-6} N_x b - 1.045 \cdot 10^{-9} N_x A_{22} + 2.746 \cdot 10^{-9} N_x A_{33} \\
& - 5.887 \cdot 10^{-9} N_x D_{22} + 0.0002808 N_x + 1.375 \cdot 10^{-10} N_y N_{xy} N_{xy} + 3.333 \cdot 10^{-9} N_y N_{xy} b \\
& - 3.647 \cdot 10^{-13} N_y N_{xy} A_{11} + 5.994 \cdot 10^{-11} N_y N_{xy} D_{22} - 5.432 \cdot 10^{-8} N_y N_{xy} \\
& + 9.682 \cdot 10^{-8} N_y a b - 6.536 \cdot 10^{-6} N_y a - 1.057 \cdot 10^{-5} N_y b + 9.026 \cdot 10^{-10} N_y A_{11} \\
& - 1.483 \cdot 10^{-7} N_y D_{22} - 0.000551 N_y + 2.192 \cdot 10^{-9} N_{xy} N_{xy} N_{xy} \\
& - 3.974 \cdot 10^{-12} N_{xy} N_{xy} A_{11} - 4.826 \cdot 10^{-9} N_{xy} N_{xy} D_{22} - 3.228 \cdot 10^{-6} N_{xy} N_{xy} \\
& + 1.698 \cdot 10^{-5} N_{xy} a a - 0.0008149 N_{xy} a + 1.497 \cdot 10^{-11} N_{xy} b D_{11} + 2.58 \cdot 10^{-10} N_{xy} b D_{22} \\
& - 6.764 \cdot 10^{-5} N_{xy} b + 2.149 \cdot 10^{-8} N_{xy} A_{11} - 1.01 \cdot 10^{-9} N_{xy} D_{11} \\
& + 2.365 \cdot 10^{-5} N_{xy} D_{22} - 0.01263 N_{xy} - 0.04202 a a + 1.894 \cdot 10^{-5} a b b - 0.003041 a b \\
& + 4.486 \cdot 10^{-6} a D_{22} + 2.066 a - 0.0004545 b b - 1.161 \cdot 10^{-7} b A_{22} + 3.051 \cdot 10^{-7} b A_{33} \\
& - 3.704 \cdot 10^{-8} b D_{11} - 6.385 \cdot 10^{-7} b D_{22} + 0.2614 b - 2.885 \cdot 10^{-5} A_{11} + 7.834 \cdot 10^{-6} A_{22} \\
& - 2.059 \cdot 10^{-5} A_{33} + 2.5 \cdot 10^{-6} D_{11} - 0.02908 D_{22} + 14.61 \qquad (83)
\end{aligned}$$

$$\phi = 5.777 \cdot 10^{-8} N_x N_x N_{xy} + 2.311 \cdot 10^{-5} N_x N_x$$
$$+ 7.22 \cdot 10^{-8} N_x N_y N_y + 1.649 \cdot 10^{-7} N_x N_y N_{xy} + 6.001 \cdot 10^{-10} N_x N_y A_{11}$$
$$- 4.473 \cdot 10^{-10} N_x N_y A_{22} - 0.002652 N_x N_y - 2.405 \cdot 10^{-10} N_x N_{xy} A_{11} - 0.001408 N_x N_{xy}$$
$$- 3.097 \cdot 10^{-6} N_x A_{11} + 4.177 \cdot 10^{-6} N_x A_{22} + 10.02 N_x - 1.893 \cdot 10^{-8} N_y N_y N_y - 0.0002509 N_y N_y$$
$$- 3.029 \cdot 10^{-7} N_y N_{xy} N_{xy} - 0.001097 N_y N_{xy} - 0.003465 N_y ab + 5.178 \cdot 10^{-8} N_y a A_{11}$$
$$- 7.164 \cdot 10^{-8} N_y a D_{11} + 0.2697 N_y a - 4.418 \cdot 10^{-8} N_y b A_{33} + 2.95 \cdot 10^{-7} N_y b D_{22} + 0.1177 N_y b$$
$$- 5.744 \cdot 10^{-6} N_y A_{11} + 3.355 \cdot 10^{-6} N_y A_{22} + 2.982 \cdot 10^{-6} N_y A_{33}$$
$$+ 1.719 \cdot 10^{-6} N_y D_{11} - 1.992 \cdot 10^{-5} N_y D_{22} + 16.85 N_y - 8.617 \cdot 10^{-7} N_{xy} N_{xy} N_{xy}$$
$$+ 0.009514 N_{xy} N_{xy} - 2.519 \cdot 10^{-8} N_{xy} b A_{33} + 0.02231 N_{xy} b + 1.803 \cdot 10^{-6} N_{xy} A_{11}$$
$$+ 1.701 \cdot 10^{-6} N_{xy} A_{33} - 3.352 \cdot 10^{-7} N_{xy} D_{11} - 0.0002012 N_{xy} D_{22} - 7.599 N_{xy} + 17.32 ab$$
$$- 0.0002589 a A_{11} + 0.0003582 a D_{11} - 1348 a + 0.0002957 b A_{33} - 0.001475 b D_{22} - 654.7 b + 0.02944 A_{11}$$
$$- 0.07852 A_{22} - 0.01996 A_{33} - 0.007768 D_{11} + 1.998 D_{22} - 5201 \quad (84)$$

$$\phi = 3.075 \cdot 10^{-12} N_x N_x N_x - 5.881 \cdot 10^{-12} N_x N_x N_y$$
$$- 1.699 \cdot 10^{-11} N_x N_x N_{xy} + 4.261 \cdot 10^{-12} N_x N_x D_{22} + 6.436 \cdot 10^{-8} N_x N_x$$
$$+ 4.019 \cdot 10^{-11} N_x N_y N_y - 9.207 \cdot 10^{-11} N_x N_y N_{xy} - 1.41 \cdot 10^{-14} N_x N_y D_{11}$$
$$+ 3.21 \cdot 10^{-12} N_x N_y D_{22} - 4.232 \cdot 10^{-7} N_x N_y + 9.301 \cdot 10^{-12} N_x N_{xy} N_{xy}$$
$$+ 7.87 \cdot 10^{-10} N_x N_{xy} b + 1.807 \cdot 10^{-15} N_x N_{xy} D_{11} + 2.614 \cdot 10^{-11} N_x N_{xy} D_{22}$$
$$+ 6.138 \cdot 10^{-7} N_x N_{xy} + 1.614 \cdot 10^{-9} N_x a D_{22} - 2.501 \cdot 10^{-5} N_x a - 1.948 \cdot 10^{-6} N_x b$$
$$+ 6.603 \cdot 10^{-11} N_x D_{11} - 1.834 \cdot 10^{-7} N_x D_{22} + 0.001608 N_x - 2.918 \cdot 10^{-11} N_y N_y N_{xy}$$
$$+ 1.558 \cdot 10^{-12} N_y N_y A_{22} - 5.292 \cdot 10^{-12} N_y N_y A_{33} + 4.115 \cdot 10^{-7} N_y N_y$$
$$+ 1.224 \cdot 10^{-6} N_y N_{xy} + 3.323 \cdot 10^{-9} N_y A_{11} - 1.813 \cdot 10^{-8} N_y A_{22}$$
$$+ 5.003 \cdot 10^{-8} N_y A_{33} + 1.058 \cdot 10^{-10} N_y D_{11} - 2.407 \cdot 10^{-8} N_y D_{22} - 0.003506 N_y$$
$$- 6.976 \cdot 10^{-8} N_{xy} N_{xy} - 5.902 \cdot 10^{-6} N_{xy} b - 1.988 \cdot 10^{-10} N_{xy} A_{11}$$
$$+ 3.68 \cdot 10^{-9} N_{xy} A_{22} - 1.093 \cdot 10^{-8} N_{xy} A_{33} - 1.355 \cdot 10^{-11} N_{xy} D_{11}$$
$$- 1.961 \cdot 10^{-7} N_{xy} D_{22} - 0.00442 N_{xy} - 1.21 \cdot 10^{-5} a D_{22} + 0.1876 a + 0.01461 b - 2.371 \cdot 10^{-5} A_{11}$$

$$+ 3.702 \cdot 10^{-5} A_{22} - 9.079 \cdot 10^{-5} A_{33} - 4.953 \cdot 10^{-7} D_{11} + 0.001136 D_{22} + 18.25 \quad (85)$$

$$\begin{aligned}
\phi = & -2.526 \cdot 10^{-11} N_x N_y N_{xy} + 3.671 \cdot 10^{-13} N_x N_y D_{22} \\
& + 5.682 \cdot 10^{-8} N_x N_y + 1.816 \cdot 10^{-12} N_x N_{xy} A_{22} - 6.142 \cdot 10^{-12} N_x N_{xy} A_{33} \\
& + 7.33 \cdot 10^{-15} N_x N_{xy} D_{11} + 2.625 \cdot 10^{-11} N_x N_{xy} D_{22} + 5.796 \cdot 10^{-7} N_x N_{xy} \\
& + 2.439 \cdot 10^{-10} N_x a D_{22} - 3.78 \cdot 10^{-6} N_x a - 4.494 \cdot 10^{-9} N_x A_{22} + 1.52 \cdot 10^{-8} N_x A_{33} \\
& - 1.814 \cdot 10^{-11} N_x D_{11} - 7.266 \cdot 10^{-8} N_x D_{22} - 0.001315 N_x + 3.47 \cdot 10^{-8} N_y N_{xy} a \\
& - 4.538 \cdot 10^{-9} N_y N_{xy} b + 1.868 \cdot 10^{-13} N_y N_{xy} A_{11} + 5.277 \cdot 10^{-14} N_y N_{xy} A_{22} \\
& + 6.878 \cdot 10^{-13} N_y N_{xy} A_{33} - 3.785 \cdot 10^{-11} N_y N_{xy} D_{22} - 1.174 \cdot 10^{-6} N_y N_{xy} \\
& - 8.588 \cdot 10^{-5} N_y a + 1.123 \cdot 10^{-5} N_y b - 4.624 \cdot 10^{-10} N_y A_{11} - 1.306 \cdot 10^{-10} N_y A_{22} \\
& - 1.702 \cdot 10^{-9} N_y A_{33} + 9.092 \cdot 10^{-8} N_y D_{22} + 0.002949 N_y + 1.544 \cdot 10^{-9} N_{xy} N_{xy} N_{xy} \\
& - 1.078 \cdot 10^{-7} N_{xy} N_{xy} a + 9.072 \cdot 10^{-9} N_{xy} N_{xy} b - 8.767 \cdot 10^{-12} N_{xy} N_{xy} A_{11} \\
& + 8.122 \cdot 10^{-13} N_{xy} N_{xy} D_{11} + 8.485 \cdot 10^{-6} N_{xy} N_{xy} - 4.111 \cdot 10^{-5} N_{xy} aa \\
& + 1.93 \cdot 10^{-10} N_{xy} a A_{22} - 8.048 \cdot 10^{-10} N_{xy} a A_{33} + 0.002562 N_{xy} a + 1.036 \cdot 10^{-7} N_{xy} bb \\
& - 3.62 \cdot 10^{-5} N_{xy} b + 4.201 \cdot 10^{-8} N_{xy} A_{11} - 1.851 \cdot 10^{-8} N_{xy} A_{22} \\
& + 6.194 \cdot 10^{-8} N_{xy} A_{33} - 4.065 \cdot 10^{-9} N_{xy} D_{11} - 7.665 \cdot 10^{-9} N_{xy} D_{22} - 0.0942 N_{xy} + 0.1018 aa \\
& + 1.638 \cdot 10^{-5} abb - 0.002212 ab - 6.245 \cdot 10^{-7} a A_{22} + 2.244 \cdot 10^{-6} a A_{33} \\
& - 1.829 \cdot 10^{-6} a D_{22} - 5.432 a - 0.0006496 bb + 0.0871 b - 5.028 \cdot 10^{-5} A_{11} + 4.934 \cdot 10^{-5} A_{22} \\
& - 0.0001594 A_{33} + 5.085 \cdot 10^{-6} D_{11} + 7.664 \cdot 10^{-5} D_{22} + 150.6 \quad (86)
\end{aligned}$$

C.1.2 X-Compression, Y-Compression Load Quadrant RSEs

Below are the RSEs for the $-N_x$, $-N_y$ load quadrant. The equations are for panel buckling 87, crippling 88, facesheet local buckling 89, facesheet material failure 90, and spacing span local buckling 91

$$\begin{aligned}
\phi = & -2.047 \cdot 10^{-14} N_x N_y A_{11} + 1.628 \cdot 10^{-15} N_x N_y D_{11} \\
& - 6.863 \cdot 10^{-9} N_x N_y + 2.151 \cdot 10^{-11} N_x a D_{11} - 6.728 \cdot 10^{-5} N_x a + 2.316 \cdot 10^{-7} N_x b
\end{aligned}$$

$$+ 5.067 \cdot 10^{-10} N_x A_{11} - 1.849 \cdot 10^{-9} N_x A_{33} - 5.935 \cdot 10^{-10} N_x D_{11} + 0.001018 N_x$$

$$+ 3.03 \cdot 10^{-11} N_y N_y N_y + 6.022 \cdot 10^{-8} N_y N_y a + 4.756 \cdot 10^{-13} N_y N_y A_{11}$$

$$- 1.855 \cdot 10^{-12} N_y N_y A_{22} + 3.496 \cdot 10^{-12} N_y N_y A_{33} + 2.916 \cdot 10^{-14} N_y N_y D_{11}$$

$$- 1.46 \cdot 10^{-6} N_y N_y + 1.484 \cdot 10^{-9} N_y N_{xy} a - 7.71 \cdot 10^{-14} N_y N_{xy} D_{11}$$

$$+ 2.056 \cdot 10^{-7} N_y N_{xy} + 4.031 \cdot 10^{-11} N_y a D_{11} + 1.154 \cdot 10^{-8} N_y a D_{22}$$

$$+ 2.902 \cdot 10^{-5} N_y a + 2.987 \cdot 10^{-9} N_y bb - 4.032 \cdot 10^{-7} N_y b + 2.803 \cdot 10^{-9} N_y A_{11}$$

$$- 1.039 \cdot 10^{-8} N_y A_{22} + 1.958 \cdot 10^{-8} N_y A_{33} - 4.227 \cdot 10^{-10} N_y D_{11}$$

$$- 2.832 \cdot 10^{-7} N_y D_{22} - 0.005554 N_y + 4.155 \cdot 10^{-6} N_{xy} a - 2.159 \cdot 10^{-10} N_{xy} D_{11}$$

$$+ 0.0005757 N_{xy} + 2.91 \cdot 10^{-9} aa A_{11} + 9.113 \cdot 10^{-9} aa D_{11} - 0.03914 aa$$

$$+ 1.168 \cdot 10^{-8} ab D_{22} - 0.0001807 ab - 1.397 \cdot 10^{-7} a A_{11} - 1.983 \cdot 10^{-7} a D_{11}$$

$$+ 3.151 \cdot 10^{-5} a D_{22} + 1.597 a - 0.0001974 bb + 7.038 \cdot 10^{-7} b D_{22} + 0.01142 b + 4.73 \cdot 10^{-6} A_{11}$$

$$- 1.454 \cdot 10^{-5} A_{22} + 1.261 \cdot 10^{-5} A_{33} - 6.529 \cdot 10^{-7} D_{11} - 0.0007056 D_{22} - 14.67 \quad (87)$$

$$\phi = -2.132 \cdot 10^{-10} N_x N_x b + 4.56 \cdot 10^{-15} N_x N_x D_{11}$$

$$+ 1.258 \cdot 10^{-10} N_x N_x - 8.135 \cdot 10^{-11} N_x N_y N_y - 5.625 \cdot 10^{-14} N_x N_y A_{11}$$

$$+ 3.885 \cdot 10^{-15} N_x N_y D_{11} - 5.275 \cdot 10^{-7} N_x N_y - 2.87 \cdot 10^{-12} N_x a A_{11}$$

$$+ 1.841 \cdot 10^{-12} N_x a D_{11} + 2.806 \cdot 10^{-5} N_x a + 1.755 \cdot 10^{-10} N_x b D_{22} - 5.296 \cdot 10^{-6} N_x b$$

$$- 1.406 \cdot 10^{-10} N_x A_{11} + 9.038 \cdot 10^{-11} N_x D_{11} - 1.185 \cdot 10^{-8} N_x D_{22} - 0.001891 N_x$$

$$+ 2.903 \cdot 10^{-8} N_y N_y a - 2.68 \cdot 10^{-12} N_y N_y A_{22} + 7.528 \cdot 10^{-12} N_y N_y A_{33}$$

$$- 1.698 \cdot 10^{-6} N_y N_y - 9.071 \cdot 10^{-12} N_y N_{xy} D_{22} + 1.403 \cdot 10^{-7} N_y N_{xy}$$

$$+ 1.573 \cdot 10^{-6} N_y ab + 5.641 \cdot 10^{-5} N_y a - 3.774 \cdot 10^{-5} N_y b - 1.433 \cdot 10^{-9} N_y A_{11}$$

$$- 1.501 \cdot 10^{-8} N_y A_{22} + 4.215 \cdot 10^{-8} N_y A_{33} + 3.108 \cdot 10^{-11} N_y D_{11}$$

$$+ 8.924 \cdot 10^{-8} N_y D_{22} - 0.007794 N_y - 2.54 \cdot 10^{-8} N_{xy} D_{22} + 0.0003928 N_{xy} + 0.004403 ab$$

$$+ 4.977 \cdot 10^{-7} a A_{11} - 1.445 \cdot 10^{-6} a A_{33} - 1.098 \cdot 10^{-7} a D_{11} + 0.4798 a$$

$$+ 3.809 \cdot 10^{-8} bb D_{22} - 0.0006792 bb + 8.793 \cdot 10^{-9} b A_{22} - 9.37 \cdot 10^{-9} b D_{11}$$

$$- 3.421 \cdot 10^{-6} b D_{22} - 0.04985 b - 2.39 \cdot 10^{-5} A_{11} - 2.161 \cdot 10^{-5} A_{22} + 9.369 \cdot 10^{-5} A_{33}$$

$$+ 3.074 \cdot 10^{-6} D_{11} + 0.0004509 D_{22} - 2.276 \quad (88)$$

$$\begin{aligned}\phi = {} & -7.714 \cdot 10^{-14} N_x N_x A_{33} + 6.829 \cdot 10^{-8} N_x N_x \\ & - 6.277 \cdot 10^{-8} N_x N_y - 1.234 \cdot 10^{-9} N_x A_{33} + 0.0006872 N_x + 2.794 \cdot 10^{-11} N_y N_y N_y \\ & + 2.347 \cdot 10^{-7} N_y N_y - 0.0006109 N_y - 5.691 \cdot 10^{-6} A_{11} - 4.937 \cdot 10^{-6} A_{33} + 15.89 \end{aligned} \quad (89)$$

$$\begin{aligned}\phi = {} & -2.962 \cdot 10^{-11} N_x N_x N_{xy} + 2.94 \cdot 10^{-6} N_x N_x \\ & + 9.374 \cdot 10^{-10} N_x N_y N_{xy} - 5.975 \cdot 10^{-6} N_x N_y + 2.736 \cdot 10^{-12} N_x N_{xy} A_{11} \\ & - 4.899 \cdot 10^{-11} N_x N_{xy} A_{22} + 1.151 \cdot 10^{-10} N_x N_{xy} A_{33} + 7.55 \cdot 10^{-6} N_x N_{xy} \\ & + 2.929 \cdot 10^{-8} N_x A_{11} + 1.099 \cdot 10^{-7} N_x A_{22} - 4.783 \cdot 10^{-7} N_x A_{33} \\ & + 3.831 \cdot 10^{-6} N_x D_{22} - 0.01993 N_x + 2.73 \cdot 10^{-10} N_y N_y D_{22} + 6.179 \cdot 10^{-6} N_y N_y \\ & + 1.216 \cdot 10^{-11} N_y N_{xy} A_{11} - 1.825 \cdot 10^{-5} N_y N_{xy} - 3.01 \cdot 10^{-8} N_y A_{11} - 4.725 \cdot 10^{-9} N_y D_{11} \\ & + 2.449 \cdot 10^{-6} N_y D_{22} + 0.02943 N_y + 4.233 \cdot 10^{-9} N_{xy} N_{xy} N_{xy} \\ & - 2.609 \cdot 10^{-11} N_{xy} N_{xy} A_{11} - 1.158 \cdot 10^{-10} N_{xy} N_{xy} A_{33} - 5.423 \cdot 10^{-12} N_{xy} N_{xy} D_{11} \\ & + 0.0001833 N_{xy} N_{xy} - 7.248 \cdot 10^{-6} N_{xy} bb + 9.855 \cdot 10^{-9} N_{xy} b D_{22} + 0.000826 N_{xy} b \\ & + 1.789 \cdot 10^{-7} N_{xy} A_{11} - 1.14 \cdot 10^{-6} N_{xy} A_{22} + 2.729 \cdot 10^{-6} N_{xy} A_{33} \\ & + 2.684 \cdot 10^{-8} N_{xy} D_{11} + 1.594 \cdot 10^{-5} N_{xy} D_{22} - 0.4461 N_{xy} + 0.0001066 aa D_{22} - 1.648 aa \\ & - 0.005115 a D_{22} + 79.11 a + 0.01794 bb - 7.45 \cdot 10^{-9} b D_{11} - 2.439 \cdot 10^{-5} b D_{22} - 2.021 b \\ & - 0.0001194 A_{11} + 0.001803 A_{22} - 0.007591 A_{33} - 4.595 \cdot 10^{-5} D_{11} + 0.1193 D_{22} + 19.16 \end{aligned} \quad (90)$$

$$\begin{aligned}\phi = {} & -5.196 \cdot 10^{-11} N_x N_y N_y - 3.465 \cdot 10^{-7} N_x N_y \\ & - 2.836 \cdot 10^{-6} N_x aa + 2.203 \cdot 10^{-9} N_x a D_{22} + 0.0001108 N_x a - 5.286 \cdot 10^{-8} N_x D_{22} - 0.001588 N_x \\ & - 3.838 \cdot 10^{-13} N_y N_y A_{11} + 8.124 \cdot 10^{-7} N_y N_y + 1.451 \cdot 10^{-7} N_y N_{xy} - 2.149 \cdot 10^{-9} N_y A_{11} \\ & + 3.967 \cdot 10^{-9} N_y A_{22} - 1.326 \cdot 10^{-8} N_y A_{33} + 0.003885 N_y + 0.0004064 N_{xy} - 1.172 \cdot 10^{-7} aa A_{11} \\ & + 2.087 \cdot 10^{-7} aa A_{33} + 0.2203 aa + 1.584 \cdot 10^{-8} ab A_{22} - 4.365 \cdot 10^{-8} ab A_{33} - 0.001078 ab \end{aligned}$$

$$+ 5.623 \cdot 10^{-6} a A_{11} - 1.069 \cdot 10^{-6} a A_{22} - 7.07 \cdot 10^{-6} a A_{33} + 1.762 \cdot 10^{-5} a D_{22}$$

$$- 10.7a - 3.801 \cdot 10^{-7} b A_{22} + 1.048 \cdot 10^{-6} b A_{33} + 0.02586 b$$

$$- 7.049 \cdot 10^{-5} A_{11} + 4.43 \cdot 10^{-5} A_{22} - 1.903 \cdot 10^{-5} A_{33} - 0.0005804 D_{22} + 146.6 \quad (91)$$

C.2 RSEs for Composite I-Stiffened Panel

The following sections list all of the RSEs generated for each load quadrant for the composite I-Stiffened Panel.

APPENDIX D

BOUNDARIES FOR STIFFNESS DOMAIN

This appendix contains the boundaries on the stiffness domain generated for the metallic and composite I-stiffened panels, as well as the composite laminate. The plots indicate where the manually generated boundaries fall relative to the regression points generated for the panels.

D.1 Stiffness Boundaries for Metallic I-Stiffened Panel

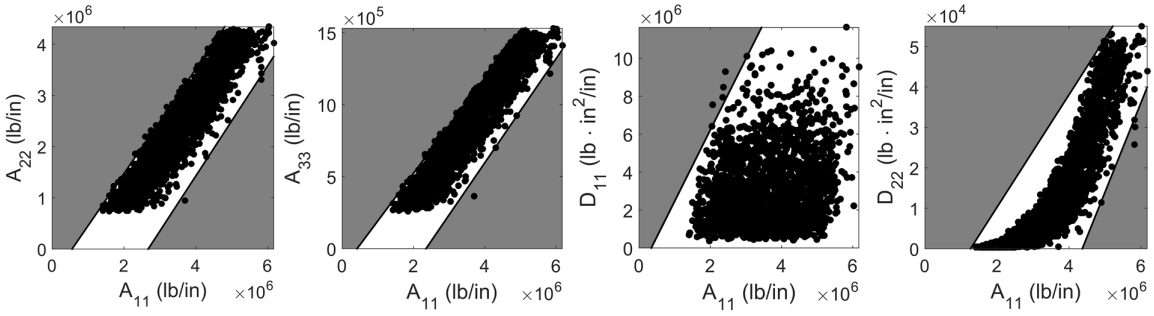

Figure 167: Variable Interaction Constraints for Metallic I-Stiffened Panel

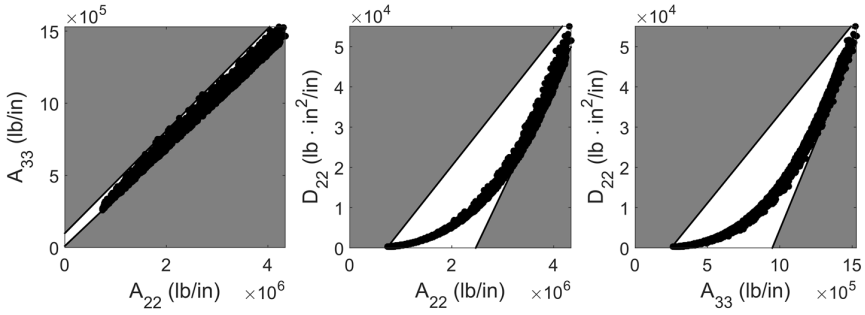

Figure 168: Variable Interaction Constraints for Metallic I-Stiffened Panel (cont.)

Equations 92 and 93 give the left and right boundaries for the A_{22} vs A_{11} plot, respectively.

$$A_{22} - 1.0196 \cdot A_{11} + 5.6440 \cdot 10^5 \leq 0 \tag{92}$$

$$1.0754 \cdot A_{11} - A_{22} - 2.8766 \cdot 10^6 \leq 0 \tag{93}$$

Equations 94 and 95 give the left and right boundaries for the A_{33} vs A_{11} plot, respectively.

$$A_{33} - 0.3311 \cdot A_{11} + 1.3833 \cdot 10^5 \leq 0 \tag{94}$$

$$0.3613 \cdot A_{11} - A_{33} - 8.4809 \cdot 10^5 \leq 0 \tag{95}$$

Equation 96 gives boundaries for the D_{11} vs A_{11} plot.

$$D_{11} - 3.7570 \cdot A_{11} + 1.2951 \cdot 10^6 \leq 0 \tag{96}$$

Equations 97 and 98 give the left and right boundaries for the D_{22} vs A_{11} plot, respectively.

$$D_{22} - 0.0139 \cdot A_{11} + 1.7598 \cdot 10^4 \leq 0 \tag{97}$$

$$0.0221 \cdot A_{11} - D_{22} - 9.6708 \cdot 10^4 \leq 0 \tag{98}$$

Equations 99 and 100 give the left and right boundaries for the A_{33} vs A_{22} plot, respectively.

$$A_{33} - 0.3548 \cdot A_{22} - 9.9031 \cdot 10^4 \leq 0 \tag{99}$$

$$0.3327 \cdot A_{22} - A_{33} + 1.1421 \cdot 10^4 \leq 0 \tag{100}$$

Equations 101 and 102 give the left and right boundaries for the D_{22} vs A_{22} plot, respectively.

$$D_{22} - 0.0160 \cdot A_{22} + 1.1665 \cdot 10^4 \leq 0 \tag{101}$$

$$0.0267 \cdot A_{22} - D_{22} - 6.5917 \cdot 10^4 \leq 0 \tag{102}$$

Equations 103 and 104 give the left and right boundaries for the D_{22} vs A_{33} plot, respectively.

$$D_{22} - 0.0442 \cdot A_{33} + 1.0976 \cdot 10^4 \leq 0 \tag{103}$$

$$0.0877 \cdot A_{33} - D_{22} - 8.3136 \cdot 10^4 \leq 0 \tag{104}$$

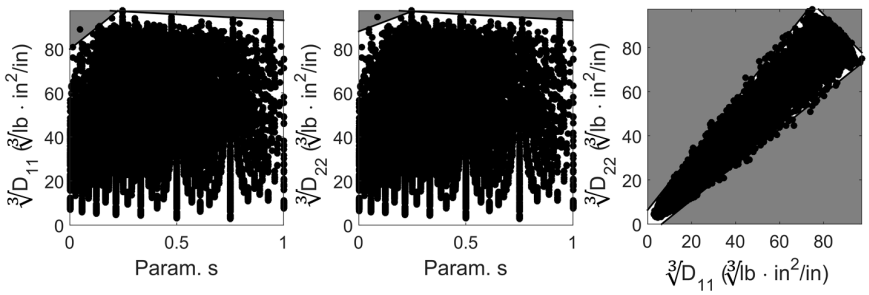

Figure 169: Variable Interaction Constraints for Composite Unstiffened Laminate (cont.)

D.2 Stiffness Boundaries for Composite Unstiffened Laminate

Equations 105 and 106 give the boundaries for the t versus $\sqrt[3]{D_{11}}$ plot (Figure 96 in Section 5.3.1).

$$-98.15t + \sqrt[3]{D_{11}} - 3.037 \leq 0 \tag{105}$$

$$76.86t - \sqrt[3]{D_{11}} - 2.543 \leq 0 \tag{106}$$

Equations 107 and 108 give the boundaries for the t versus $\sqrt[3]{D_{22}}$ plot (Figure 96 in Section 5.3.1).

$$-98.15t + \sqrt[3]{D_{22}} - 3.037 \leq 0 \tag{107}$$

$$76.86t - \sqrt[3]{D_{22}} - 2.543 \leq 0 \tag{108}$$

Equation 109 gives the boundary for the r versus $\sqrt[3]{D_{11}}$ plot (Figure 96 in Section 5.3.1).

$$12.26r + \sqrt[3]{D_{11}} - 100.8 \leq 0 \tag{109}$$

Equation 110 gives the boundary for the r versus $\sqrt[3]{D_{22}}$ plot (Figure 96 in Section 5.3.1).

$$-12.29r + \sqrt[3]{D_{22}} - 88.49 \leq 0 \tag{110}$$

Equations 111 and 112 give the boundaries for the s versus $\sqrt[3]{D_{11}}$ plot (Figure 169).

$$-77.24s + \sqrt[3]{D_{11}} - 79.92 \leq 0 \tag{111}$$

$$5.312s + \sqrt[3]{D_{11}} - 98.31 \leq 0 \tag{112}$$

Equations 113 and 114 give the boundaries for the s versus $\sqrt[3]{D_{22}}$ plot (Figure 169).

$$-36.59s + \sqrt[3]{D_{22}} - 87.96 \leq 0 \tag{113}$$

$$5.312s + \sqrt[3]{D_{22}} - 98.31 \leq 0 \tag{114}$$

Equations 115, 116, and 117 give the boundaries for the $\sqrt[3]{D_{11}}$ versus $\sqrt[3]{D_{22}}$ plot (Figure 169).

$$-1.246\sqrt[3]{D_{11}} + \sqrt[3]{D_{22}} - 6.375 \leq 0 \tag{115}$$

$$0.8023\sqrt[3]{D_{11}} - \sqrt[3]{D_{22}} - 5.115 \leq 0 \tag{116}$$

$$\sqrt[3]{D_{11}} + \sqrt[3]{D_{22}} - 175 \leq 0 \tag{117}$$

D.3 Stiffness Boundaries for Composite I-Stiffened Panel

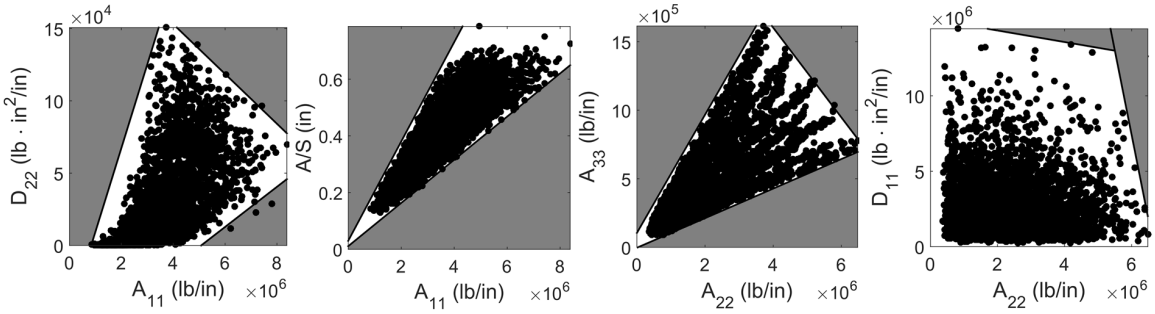

Figure 170: Variable Interaction Constraints for Composite I-Stiffened Panel

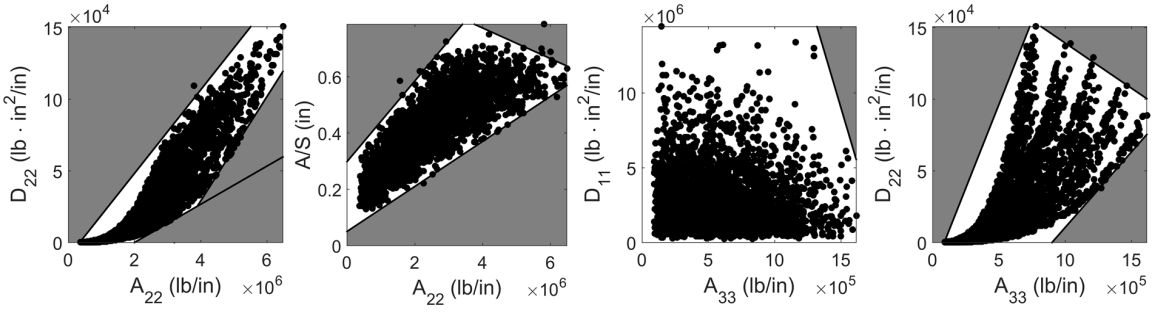

Figure 171: Variable Interaction Constraints for Composite I-Stiffened Panel (cont.)

Equations 118, 119, and 120 give the boundaries for the A_{11} versus A_{22} plot (Figure 97 in Section 5.3.2).

$$-2.301A_{11} + A_{22} + 6.917 \cdot 10^5 \leq 0 \tag{118}$$

$$0.4375A_{11} - A_{22} - 1.15 \cdot 10^6 \leq 0 \tag{119}$$

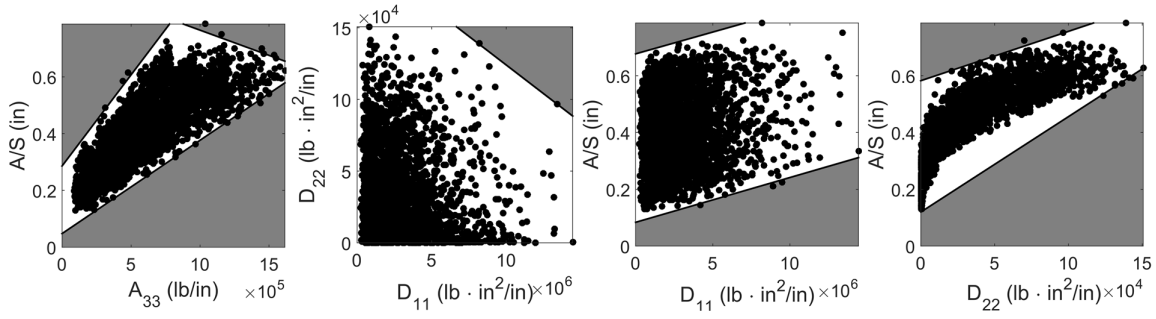

Figure 172: Variable Interaction Constraints for Composite I-Stiffened Panel (cont.)

$$0.8235A_{11} + A_{22} - 9.947 \cdot 10^6 \leq 0 \tag{120}$$

Equations 121, 122, and 123 give the boundaries for the A_{11} versus A_{33} plot (Figure 97 in Section 5.3.2).

$$-0.4193A_{11} + A_{33} + 1.368 \cdot 10^5 \leq 0 \tag{121}$$

$$0.1104A_{11} - A_{33} - 2.532 \cdot 10^5 \leq 0 \tag{122}$$

$$0.2873A_{11} + A_{33} - 3.186 \cdot 10^6 \leq 0 \tag{123}$$

Equations 124 and 125 give the boundaries for the A_{11} versus D_{11} plot (Figure 97 in Section 5.3.2).

$$-5.572A_{11} + D_{11} + 2.715 \cdot 10^6 \leq 0 \tag{124}$$

$$5.292A_{11} - D_{11} - 3.745 \cdot 10^7 \leq 0 \tag{125}$$

Equations 126, 127, and 128 give the boundaries for the A_{11} versus D_{22} plot (Figure 170).

$$-0.05793A_{11} + D_{22} + 4.855 \cdot 10^4 \leq 0 \tag{126}$$

$$0.01388A_{11} - D_{22} - 7.051 \cdot 10^4 \leq 0 \tag{127}$$

$$0.01724A_{11} + D_{22} - 2.221 \cdot 10^5 \leq 0 \tag{128}$$

Equations 129 and 130 give the boundaries for the A_{11} versus A/S plot (Figure 170).

$$-1.75 \cdot 10^{-7}A_{11} + A/S - 0.03 \leq 0 \tag{129}$$

$$7.612 \cdot 10^{-8}A_{11} - A/S + 0.01104 \leq 0 \tag{130}$$

Equations 131, 132, and 133 give the boundaries for the A_{22} versus A_{33} plot (Figure 170).

$$-0.4308A_{22} + A_{33} - 1.062 \cdot 10^5 \leq 0 \tag{131}$$

$$0.1078A_{22} - A_{33} - 2581 \leq 0 \tag{132}$$

$$0.3267A_{22} + A_{33} - 2.909 \cdot 10^6 \leq 0 \tag{133}$$

Equations 134 and 135 give the boundaries for the A_{22} versus D_{11} plot (Figure 170).

$$0.383A_{22} + D_{11} - 1.511 \cdot 10^7 \leq 0 \tag{134}$$

$$11.18A_{22} + D_{11} - 7.45 \cdot 10^7 \leq 0 \tag{135}$$

Equations 136, 137, and 138 give the boundaries for the A_{22} versus D_{22} plot (Figure 171).

$$-0.02917A_{22} + D_{22} + 1.003 \cdot 10^4 \leq 0 \tag{136}$$

$$0.03636A_{22} - D_{22} - 1.164 \cdot 10^5 \leq 0 \tag{137}$$

$$0.01333A_{22} - D_{22} - 2.667 \cdot 10^4 \leq 0 \tag{138}$$

Equations 139, 140, and 141 give the boundaries for the A_{22} versus A/S plot (Figure 171).

$$-1.433 \cdot 10^{-7}A_{22} + A/S - 0.2983 \leq 0 \tag{139}$$

$$8 \cdot 10^{-8}A_{22} - A/S + 0.05 \leq 0 \tag{140}$$

$$5.429 \cdot 10^{-8}A_{22} + A/S - 0.99 \leq 0 \tag{141}$$

Equation 142 gives the boundary for the A_{33} versus D_{11} plot (Figure 171).

$$30A_{33} + D_{11} - 5.4 \cdot 10^7 \leq 0 \tag{142}$$

Equations 143, 144, and 145 give the boundaries for the A_{33} versus D_{22} plot (Figure 171).

$$-0.2341A_{33} + D_{22} + 2.054 \cdot 10^4 \leq 0 \tag{143}$$

$$0.1056A_{33} - D_{22} - 9.5 \cdot 10^4 \leq 0 \tag{144}$$

$$0.06316A_{33} + D_{22} - 2.024 \cdot 10^5 \leq 0 \tag{145}$$

Equations 146, 147, and 148 give the boundaries for the A_{33} versus A/S plot (Figure 172).

$$-6.429 \cdot 10^{-7}A_{33} + A/S - 0.2857 \leq 0 \tag{146}$$

$$3.29 \cdot 10^{-7}A_{33} - A/S + 0.04774 \leq 0 \tag{147}$$

$$1.778 \cdot 10^{-7}A_{33} + A/S - 0.9422 \leq 0 \tag{148}$$

Equation 149 gives the boundary for the D_{11} versus D_{22} plot (Figure 172).

$$0.008D_{11} + D_{22} - 2.04 \cdot 10^5 \leq 0 \tag{149}$$

Equations 150 and 151 give the boundaries for the D_{11} versus A/S plot (Figure 172).

$$-1.538 \cdot 10^{-8}D_{11} + A/S - 0.6769 \leq 0 \tag{150}$$

$$1.574 \cdot 10^{-8}D_{11} - A/S + 0.08389 \leq 0 \tag{151}$$

Equations 152 and 153 give the boundaries for the D_{22} versus A/S plot (Figure 172).

$$-1.739 \cdot 10^{-6}D_{22} + A/S - 0.5826 \leq 0 \tag{152}$$

$$3.36 \cdot 10^{-6}D_{22} - A/S + 0.12 \leq 0 \tag{153}$$

APPENDIX E

PREDICTION ACCURACY PLOTS FOR FAILURE CRITERIA

This appendix contains plots of the failure criteria RSE prediction metric ϕ versus the three membrane components of load N_x , N_y , N_{xy} for a set of random data points. Only the -N_x , -N_y and +N_x , +N_y load regimes are shown for brevity. The term ϕ is negative when the panel is predicted to pass and positive when the panel is predicted to fail. The four categories found in each plot are described in Section 4.1.

E.1 Plots for the Metallic I-Stiffened Panel

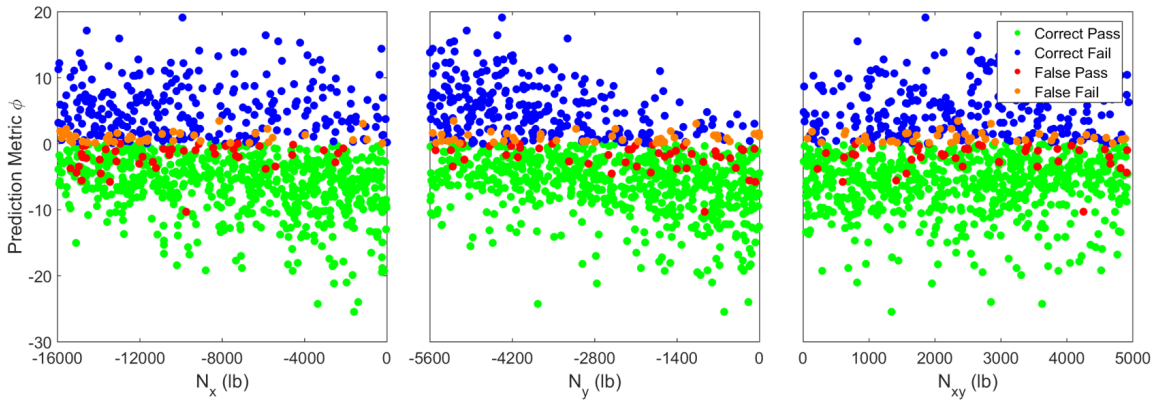

Figure 173: Panel Buckling Metric for -N_x , -N_y Load Condition

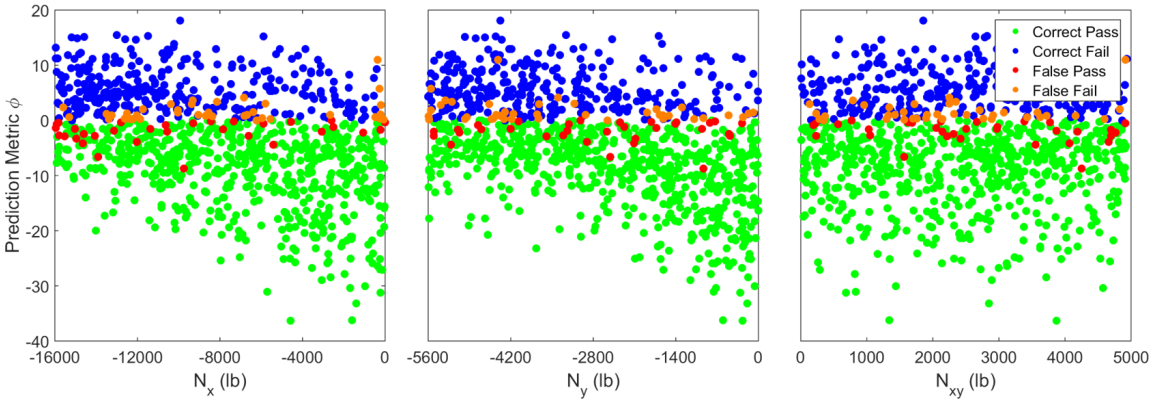

Figure 174: Crippling Metric for -N_x , -N_y Load Condition

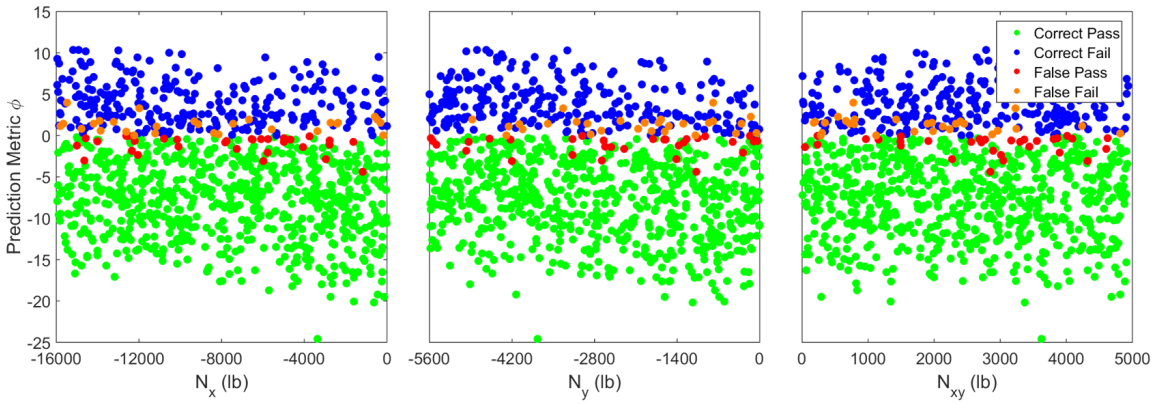

Figure 175: Facesheet Local Buckling Metric for -N_x , -N_y Load Condition

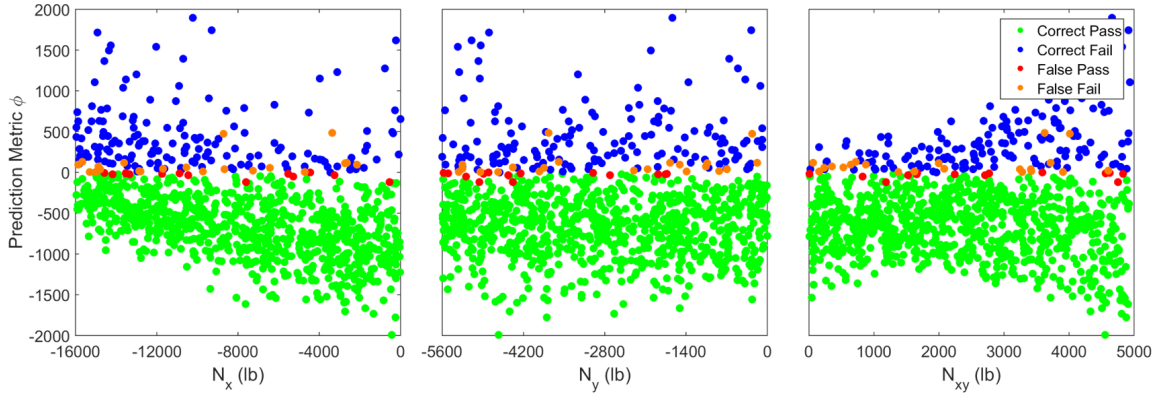

Figure 176: Facesheet Material Failure Metric for -N_x , -N_y Load Condition

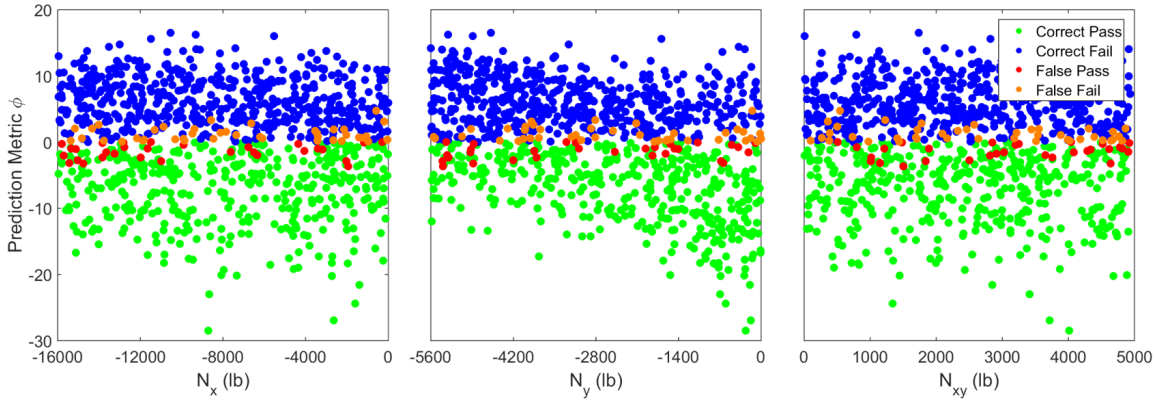

Figure 177: Spacing Span Local Buckling Metric for -N_x , -N_y Load Condition

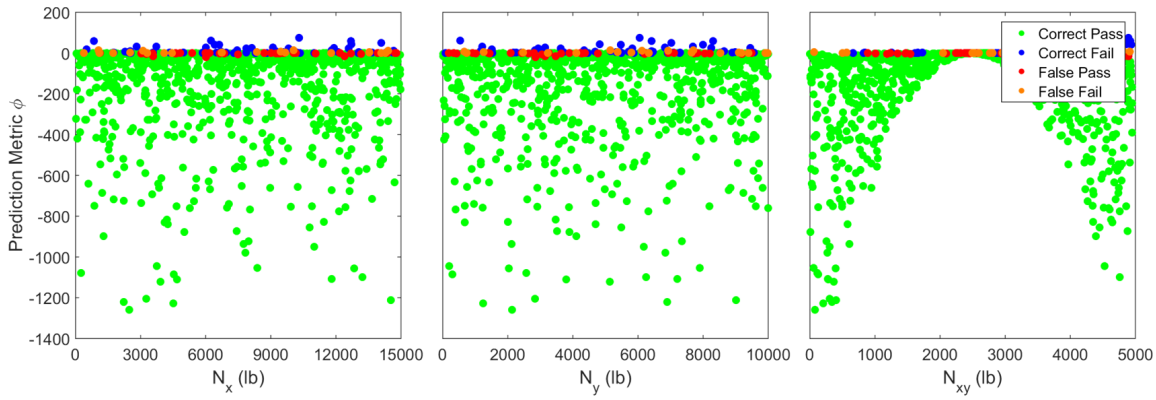

Figure 178: Facesheet Local Buckling Metric for $+N_x$, $+N_y$ Load Condition

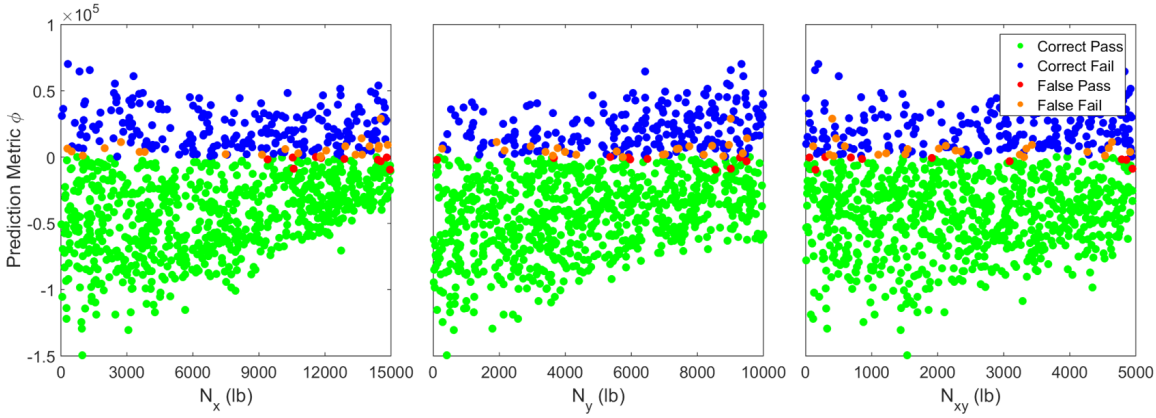

Figure 179: Facesheet Material Failure Metric for $+N_x$, $+N_y$ Load Condition

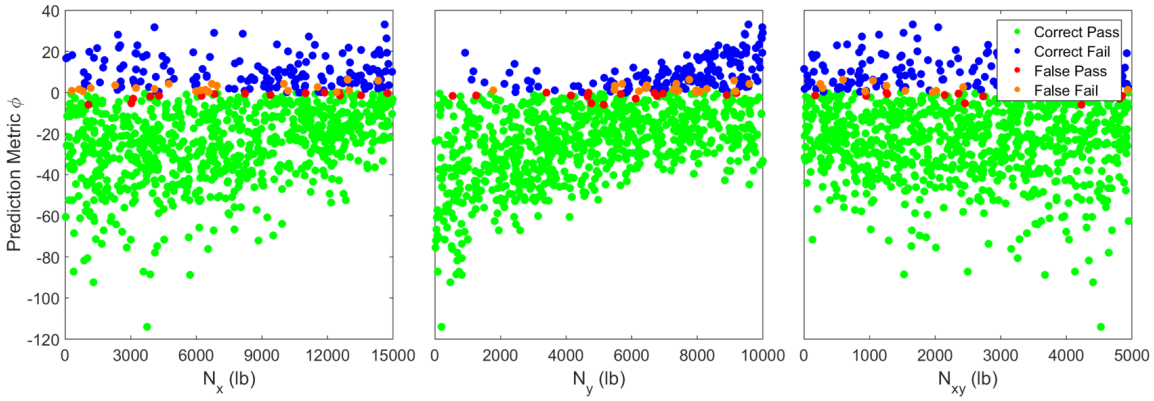

Figure 180: Bonded Combo Material Failure Metric for $+N_x$, $+N_y$ Load Condition

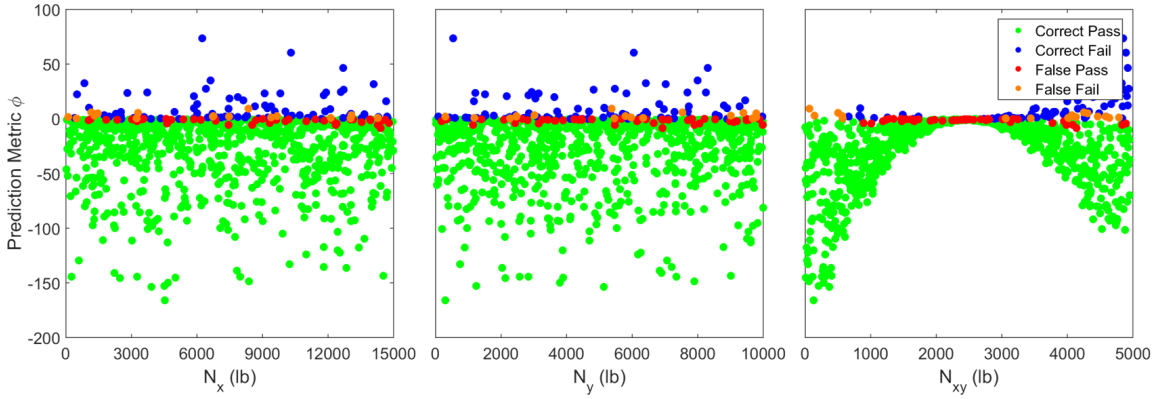

Figure 181: Spacing Span Local Buckling Metric for $+N_x$, $+N_y$ Load Condition

APPENDIX F

DISTRIBUTION OF ERROR IN OPTIMIZED MASS FOR METALLIC I-STIFFENED PANEL

This chapter contains distributions and scatter plots of the optimized mass error at random combinations of panel load (N_x , N_y , N_{xy}) and buckling spans (a, b). The error describes the difference between unit mass determined by the stiffness-based optimization and the HyperSizer optimization, as described in Section 4.2.

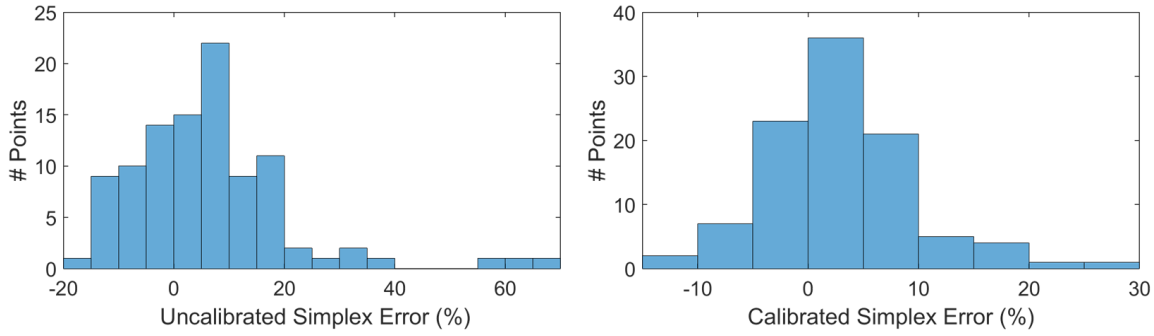

Figure 182: Mass Error Distributions: $+N_x/+N_y$ Quadrant

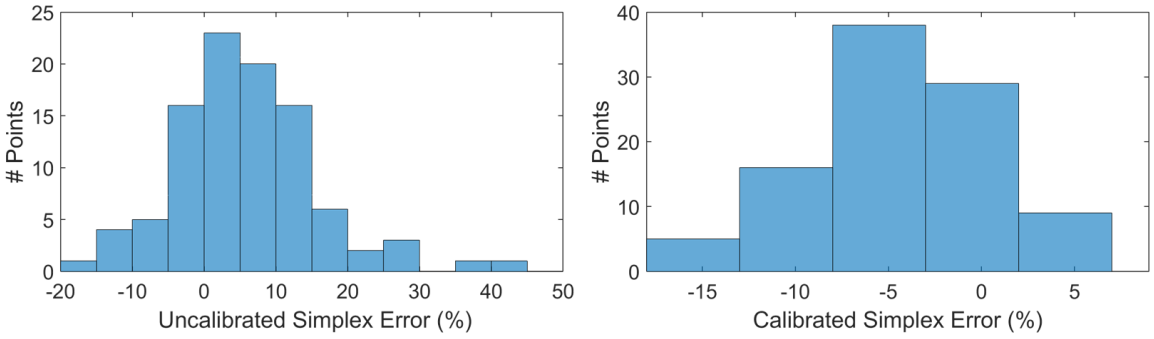

Figure 183: Mass Error Distributions: $-N_x/-N_y$ Quadrant

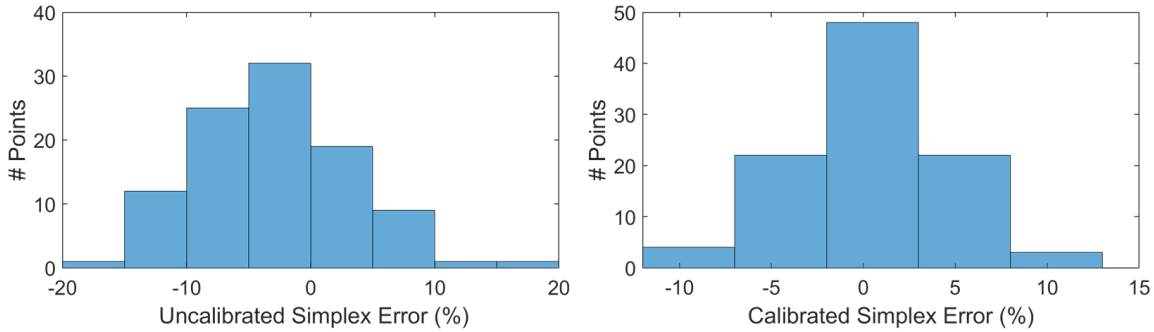

Figure 184: Mass Error Distributions: $+N_x/-N_y$ Quadrant

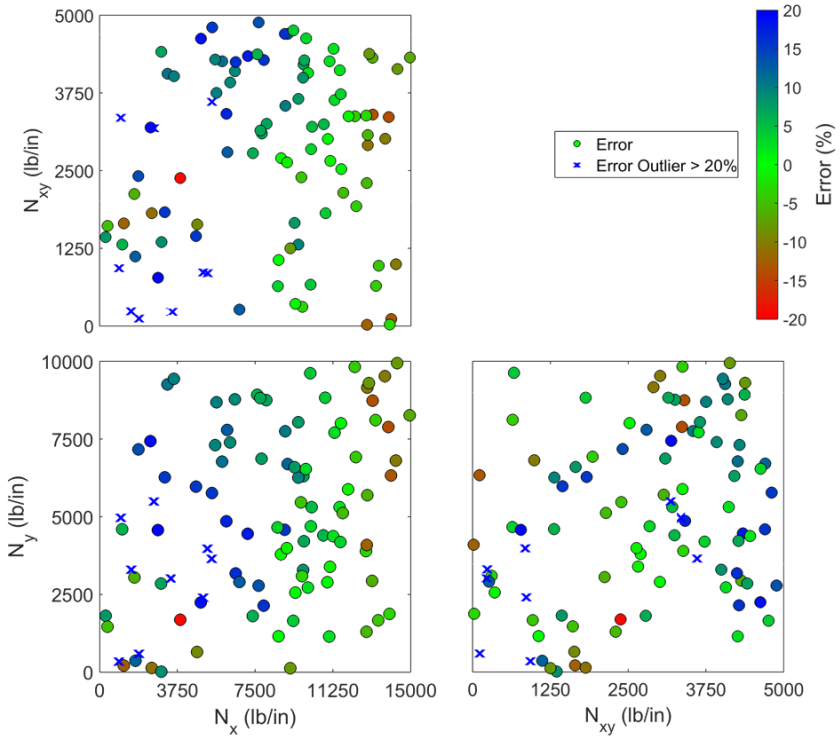

Figure 185: Uncalibrated Mass Error for Random Load and Span: $+N_x/+N_y$ Quadrant

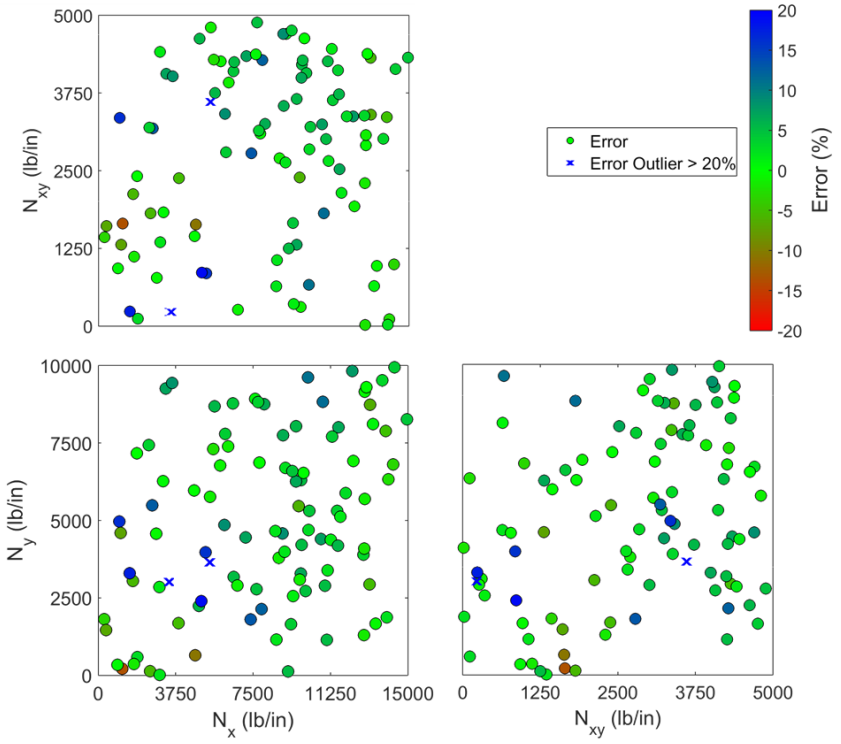

Figure 186: Calibrated Mass Error for Random Load and Span: $+N_x/+N_y$ Quadrant

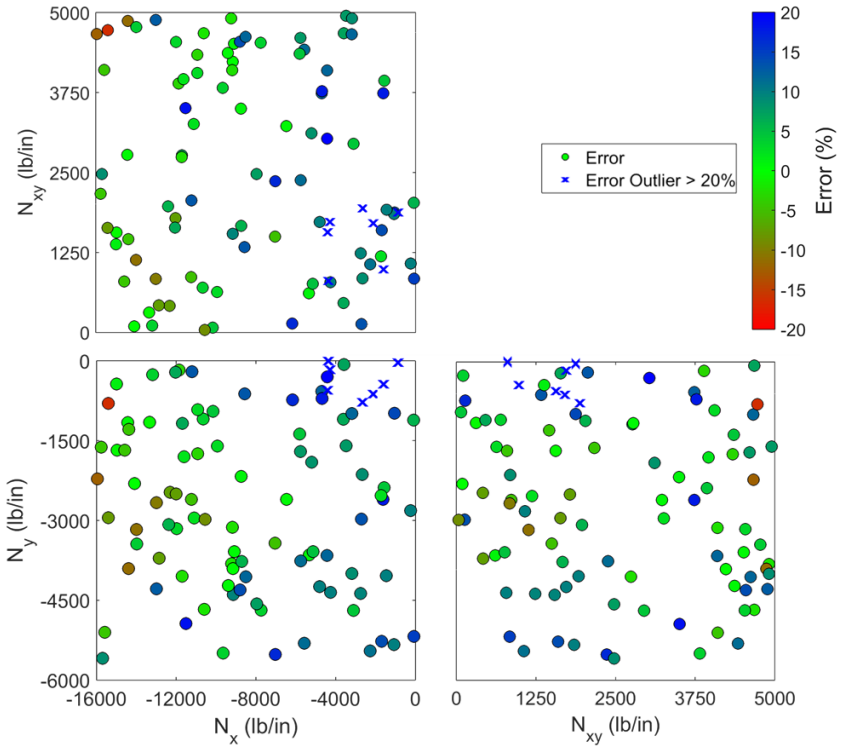

Figure 187: Uncalibrated Mass Error for Random Load and Span: $-N_x/-N_y$ Quadrant

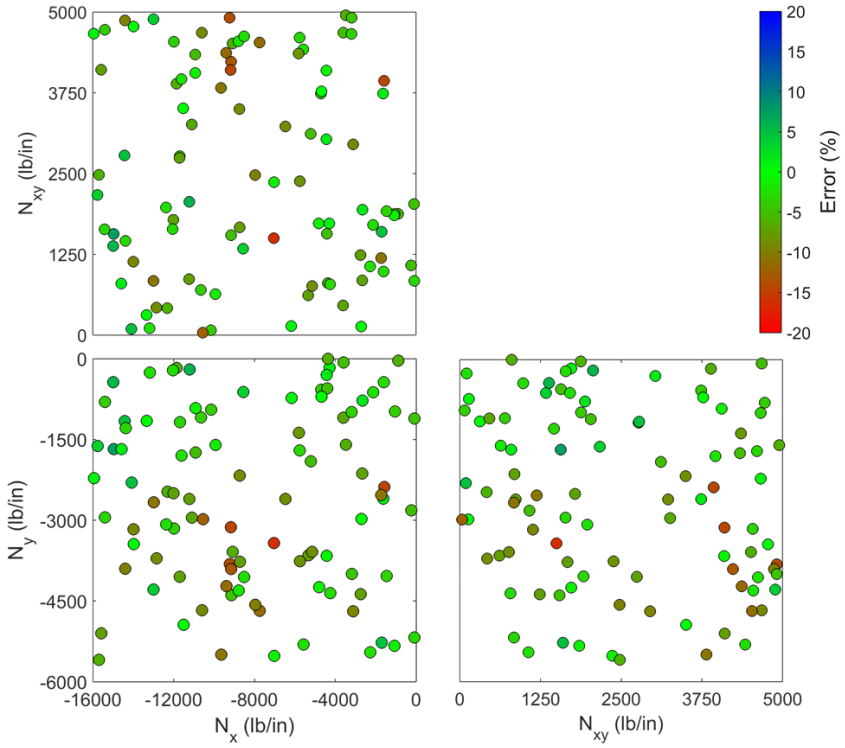

Figure 188: Calibrated Mass Error for Random Load and Span: $-N_x/-N_y$ Quadrant

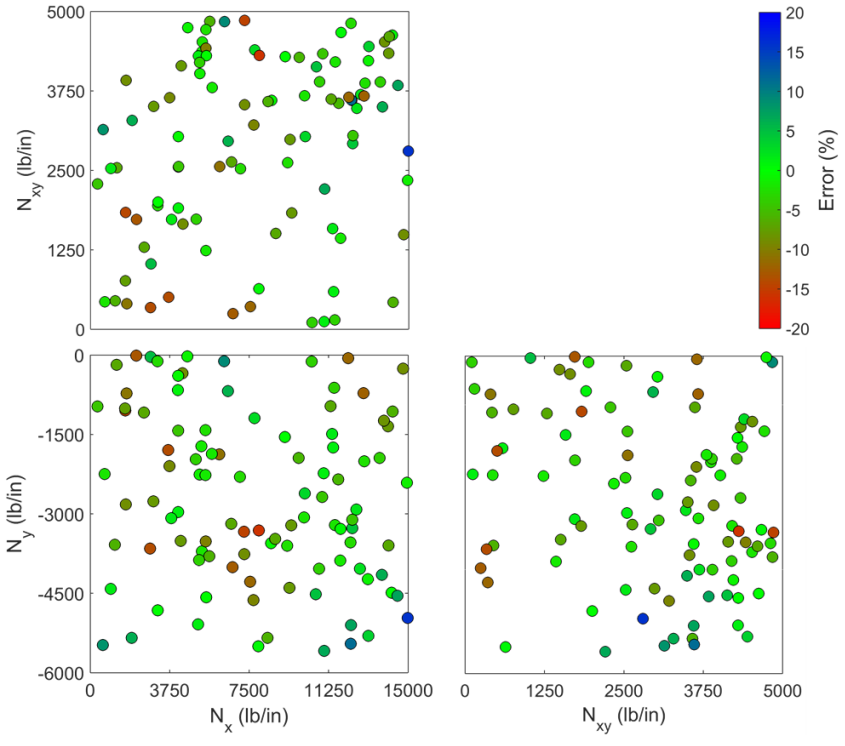

Figure 189: Uncalibrated Mass Error for Random Load and Span: $+N_x/-N_y$ Quadrant

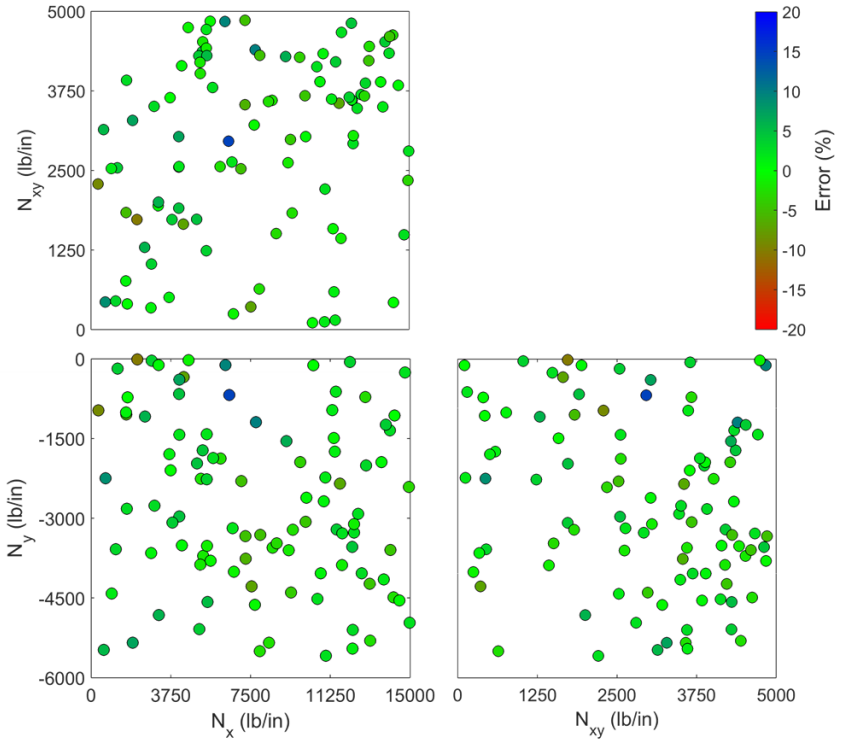

Figure 190: Calibrated Mass Error for Random Load and Span: $+N_x/-N_y$ Quadrant

APPENDIX G

FAILURE CRITERIA FOR COMPOSITE STIFFENED PANELS

This appendix contains the failure criteria used in the optimization of the composite stiffened panel presented in Chapter 5. The sections of each table represent the groups that correspond to a single failure criteria.

Table 39: Failure Criteria Used for Composite Stiffened Panel Optimization

Object	Type	Analysis Name
Panel	Buckling	Uniaxial and Biaxial, Simple BC Shear, Simple BC Uniaxial and Biaxial with Shear Interaction, Simple BC Column with Transverse Shear Flexibility, Simple BC
Panel	Crippling	Composite Crippling (Mil Handbook 17) Johnson-Euler Buckling Interaction
Stiffener	Buckling	Argyris, Flexural Torsional
Facesheet	Material	Strength, Max Strain, x-Direction Strength, Max Strain, y-Direction Strength, Max Strain, xy-Direction Strength, Max Stress, x-Direction Strength, Max Stress, y-Direction Strength, Max Stress, xy-Direction Strength, Tsai-Hill Interaction Strength, Tsai-Wu Interaction Strength, Tsai-Hahn Interaction Strength, Hoffman Interaction
Facesheet	Local Buckling	Biaxial Shear Biaxial and Shear Interaction
Bonded Combo	Material	Strength, Max Strain, x-Direction Strength, Max Strain, y-Direction Strength, Max Strain, xy-Direction Strength, Max Stress, x-Direction Strength, Max Stress, y-Direction Strength, Tsai-Hill Interaction Strength, Tsai-Wu Interaction Strength, Tsai-Hahn Interaction Strength, Hoffman Interaction

Table 40: Failure Criteria Used for Composite Stiffened Panel Optimization (Cont.)

Spacing Span	Local Buckling	Biaxial Shear Biaxial and Shear Interaction
Web	Material	Strength, Max Strain, x-Direction Strength, Max Strain, y-Direction Strength, Max Strain, xy-Direction Strength, Max Stress, x-Direction Strength, Max Stress, y-Direction Strength, Max Stress, xy-Direction Strength, Tsai-Hill Interaction Strength, Tsai-Wu Interaction Strength, Tsai-Hahn Interaction Strength, Hoffman Interaction
Web	Local Buckling	Biaxial Biaxial and Shear Interaction
Bottom Flange	Material	Strength, Max Strain, x-Direction Strength, Max Strain, y-Direction Strength, Max Strain, xy-Direction Strength, Max Stress, x-Direction Strength, Max Stress, y-Direction Strength, Max Stress, xy-Direction Strength, Tsai-Hill Interaction Strength, Tsai-Wu Interaction Strength, Tsai-Hahn Interaction Strength, Hoffman Interaction
Bottom Flange	Local Buckling	Biaxial Biaxial and Shear Interaction

APPENDIX H

ELEMENT BENDING MOMENTS FOR F-86 WING IN 7G PULL-UP

This appendix contains bending moments from the 737-similar wing box example presented in Chapter 7.

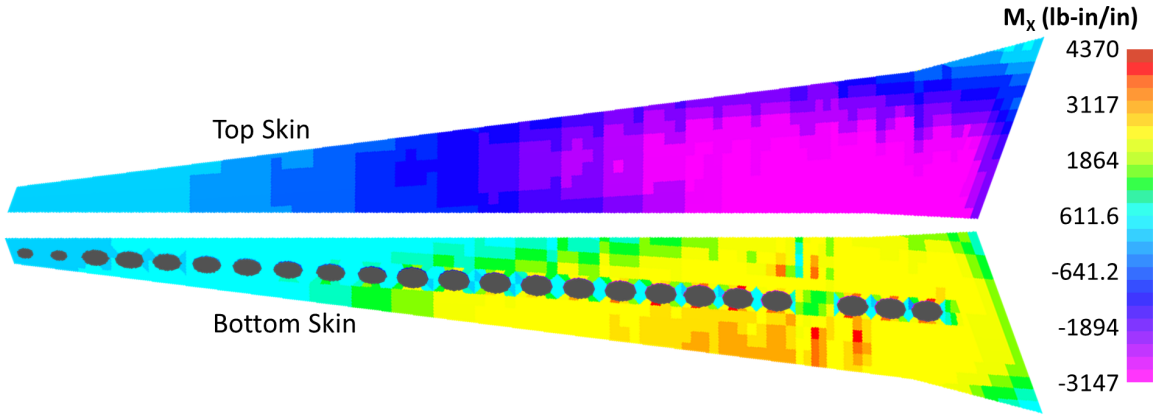

Figure 191: Baseline Internal Element M_x for +2.5g Load Case

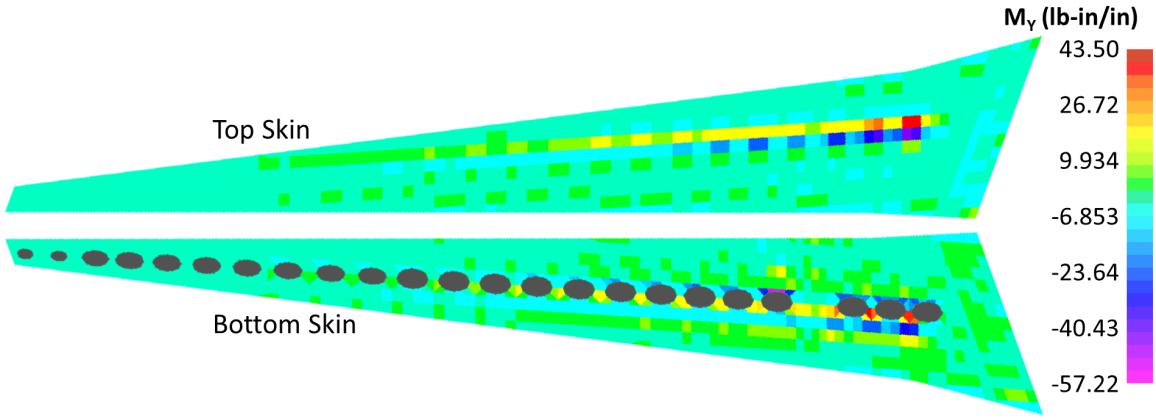

Figure 192: Baseline Internal Element M_y for +2.5g Load Case

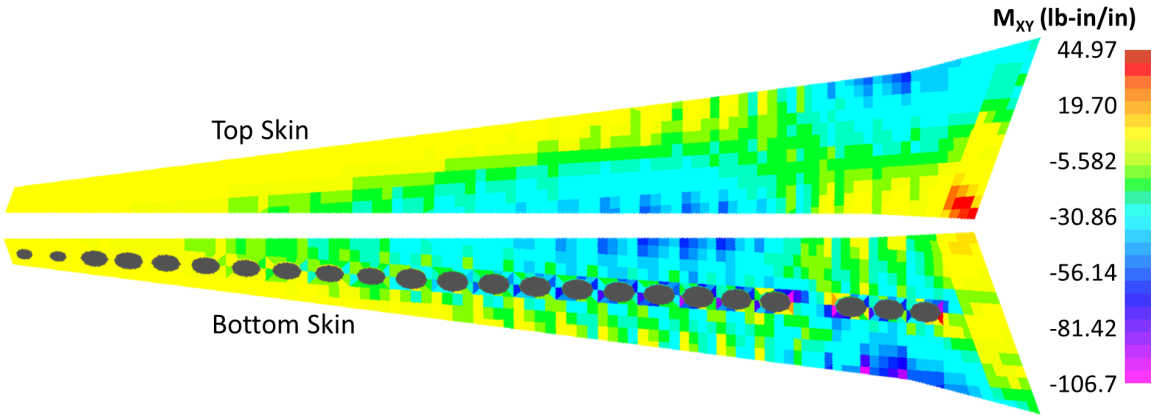

Figure 193: Baseline Internal Element M_{xy} for +2.5g Load Case

APPENDIX I

F-86 INTERNAL LOADS PLOTS

This appendix contains additional load plots from the F-86 wing example presented in Chapter 8.

I.1 Element Bending Moments for F-86 Wing in 7g Pull-Up

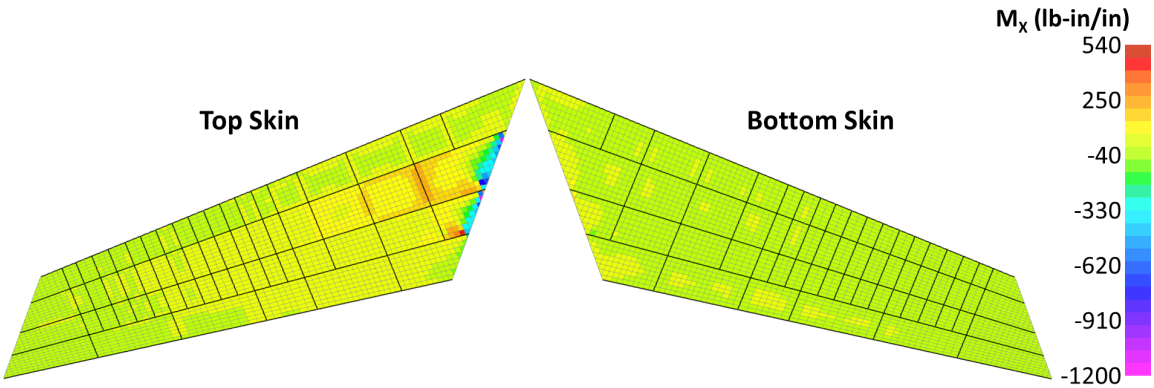

Figure 194: Running Load x-Moment in F-86 Wing, per Element

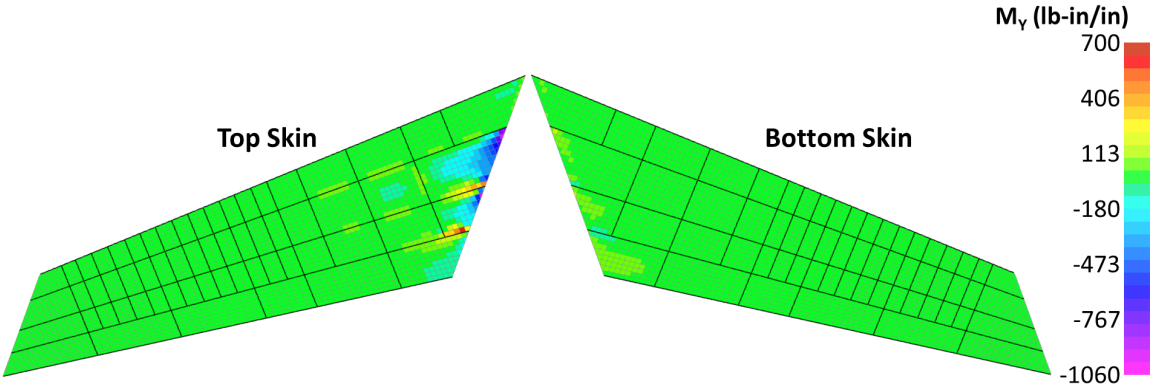

Figure 195: Running Load y-Moment in F-86 Wing, per Element

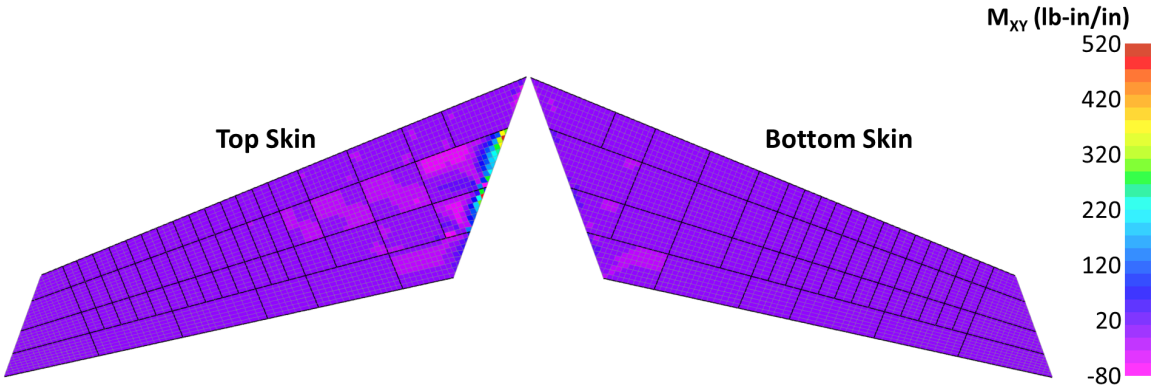

Figure 196: Running Load xy-Moment (Twist) in F-86 Wing, per Element

I.2 Averaged Panel Loads for F-86 Wing in 7g Pull-Up

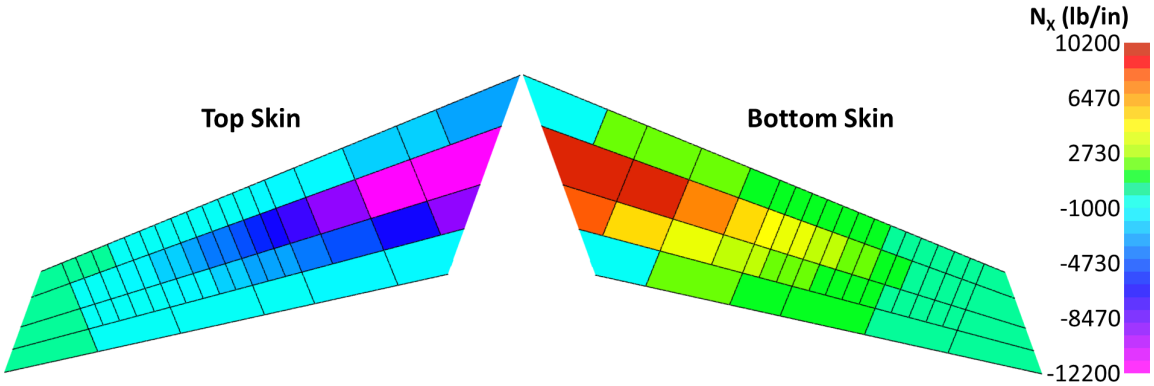

Figure 197: Span-Wise Running Load in F-86 Wing, per Panel

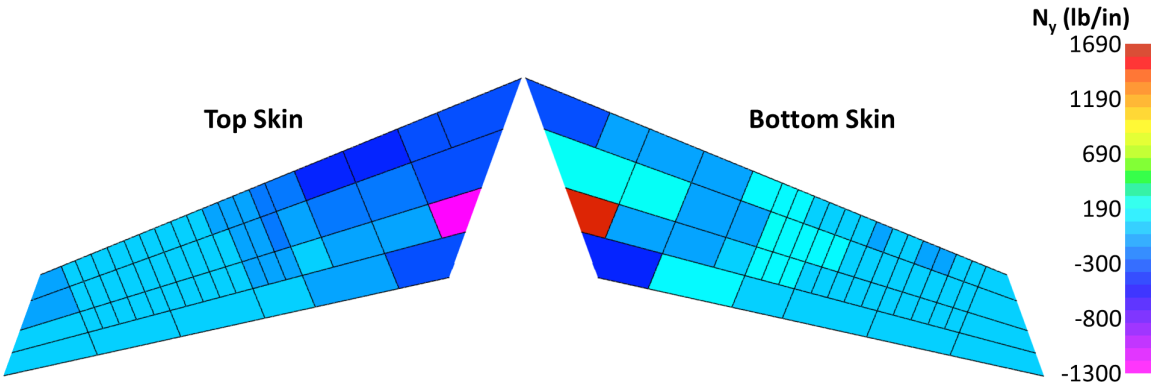

Figure 198: Chord-Wise Running Load in F-86 Wing, per Panel

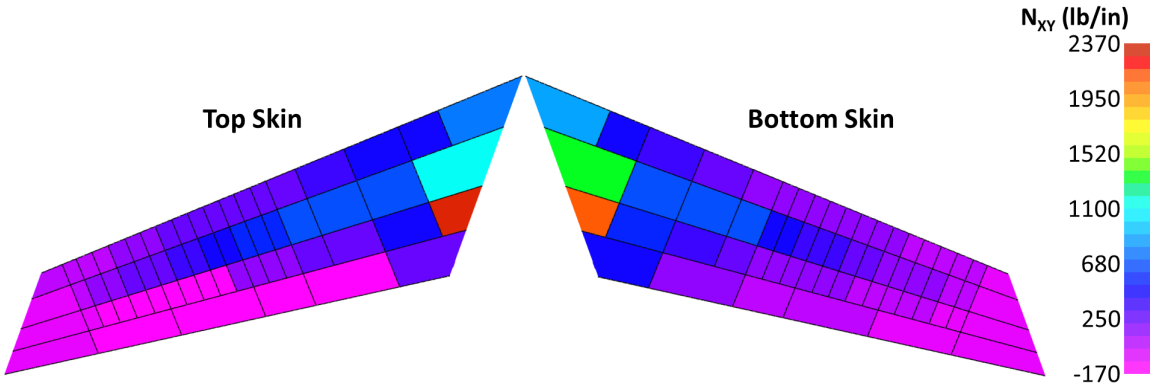

Figure 199: Shear Running Load in F-86 Wing, per Panel

REFERENCES

[1] Collier Research Corporation, "HyperSizer," 2015.

[2] Mavris, D. N., "A Paradigm Shift in Complex System Design," *Course notes from Advanced Design Methods I. Georgia Institute of Technology*, 2011.

[3] Anderson, J., *Introduction to Flight*, McGraw-Hill Education, 7th ed., 2011.

[4] Federal Aviation Administration, *PART 25AIRWORTHINESS STANDARDS: TRANSPORT CATEGORY AIRPLANES*, 2016.

[5] Airways News, "SpeciAAl Delivery Flight Event: American Airlines," *Airways News Magazine*, 2014.

[6] Hall, D., "F-16 3D Technical Cutaway," 2016.

[7] Collier, C., Ainsworth, J., Yarrington, P., and Lucking, R., "Ares V Interstage Composite Panel Concept and Ringframe Spacing Trade Studies," *51st AIAA/ASME/ASCE/AHS/ASC Structures, Structural Dynamics, and Materials Conference*, , No. 2010-2782, 2010.

[8] Laughlin, T. W., Corman, J. A., and Mavris, D. N., "A Parametric and Physics-Based Approach to Structural Weight Estimation of the Hybrid Wing Body Aircraft," *51st AIAA Aerospace Sciences Meeting including the New Horizons Forum and Aerospace Exposition*, No. AIAA 2013-1082, Dallas/Ft. Worth Region, TX, 2013.

[9] Harmin, M. Y., Ahmed, a. T., and Cooper, J. E., "Aeroelastic Tailoring of Metallic Wing Structures," *52nd AIAA/ASME/ASCE/AHS/ASC Structures, Structural Dynamics and Materials Conference*, No. AIAA 2011-1712, Denver, Colorado, 2011.

[10] Francois, G., Cooper, J. E., and Weaver, P. M., "Impact of the Wing Sweep Angle and Rib Orientation on Wing Structural Response for Un-Tapered Wings," *57th AIAA/ASCE/AHS/ASC Structures, Structural Dynamics, and Materials Conference*, No. AIAA 2016-0472, San Diego, CA, 2016.

[11] Southwest Research Institute, "Aircraft Structural Analysis," 2016.

[12] Dassault Systems, "Why Simulate?" 2010.

[13] NASA, "Saturn V Rocket," .

[14] Composites World, "A350 Wing Skin," .

[15] Byklum, E., Steen, E., and Amdahl, J., "A semi-analytical model for global buckling and postbuckling analysis of stiffened panels," *Thin-Walled Structures*, Vol. 42, No. 5, 2004, pp. 701–717.

[16] Collier Research Corporation, "Flexural-Torsional Buckling," *HyperSizer Help*, 2016.

[17] Collier Research Corporation, "Local Buckling," *HyperSizer Help*, Newport News, VA, 2013.

[18] Boeing Commercial Airplanes, "737 Airplane Characteristics for Airport Planning," Tech. rep., 2013.

[19] Gavin, "Starlingford Chronicles," .

[20] Kaboldy, "Orthographically projected diagram of the F-86 Sabre," .

[21] United States Air Force, *Flight Handbook USAF Series F-86E Aircraft*, 1956.

[22] NASA, "X-29 Forward Swept Wing Technology Demonstrator," 2009.

[23] Gemma, S. and Mastroddi, F., "Multi-Disciplinary and Multi-Objective Optimization of an Unconventional Aircraft Concept," *16th AIAA/ISSMO Multidisciplinary Analysis and Optimization Conference*, No. AIAA 2015-2327, Dallas, Texas, 2015.

[24] Sanders, A. D., Jenista, C. G., Arrowood, R. H., Donnan, R. A., Goodman, J. M., Gordon, S. E., Iii, T. L. M., Laughlin, B. P., and Mavris, D. N., "Multi-Disciplinary Design of a Supersonic, Long-Range, Air-Superiority Missile Through Parametric Design Space Exploration and Physics-Based Modeling," *50th AIAA/ASME/SAE/ASEE Joint Propulsion Conference*, No. AIAA 2014-3603, Cleveland, Ohio, 2014.

[25] Padula, S. L., Robinson, J. H., and Eldred, L. B., "Structural Analysis in a Conceptual Design Framework," *53rd AIAA/ASME/ASCE/AHS/ASC Structures, Structural Dynamics and Materials Conference*, No. AIAA 2012-1753, Honolulu, Hawaii, 2012.

[26] van Tooren, M. and Krakers, L., "Multi-Disciplinary Design of Aircraft Fuselage Structures," *45th AIAA Aerospace Sciences Meeting and Exhibit*, No. AIAA 2007-767, Reno, Nevada, 2007.

[27] Chaussée, J. and Dervault, F., "Knowledge Based Approach to Wing Weight and Stiffness," *54th AIAA/ASME/ASCE/AHS/ASC Structures, Structural Dynamics, and Materials Conference*, No. AIAA 2013-1678, Boston, Massachusetts, 2013.

[28] Mukhopadhyay, V., "Hybrid Wing-Body Pressurized Fuselage Modeling, Analysis, and Design for Weight Reduction," *53rd AIAA/ASME/ASCE/AHS/ASC Structures, Structural Dynamics and Materials Conference*, No. AIAA 2012-1999, Honolulu, Hawaii, 2012.

[29] Adams, D. F., "High-performance composite material airframe weight and cost estimating relations," *Journal of Aircraft*, Vol. 11, No. 12, 1974, pp. 751–757.

[30] Kelm, R., Lapple, M., and Grabietz, M., "Wing primary structure weight estimation of transport aircrafts in the pre-development phase," *54th Annual Conference of Society of Allied Weight Engineers*, No. SAWE 2283, Huntsville, Alabama, 1995.

[31] Hutchinson, V. L. and Olds, J. R., "Estimation of Launch Vehicle Propellant Tank Structural Weight Using Simplified Beam Approximation," *40th AIAA/ASME/SAE/ASEE Joint Propulsion Conference and Exhibit*, No. AIAA 2004-3661, Fort Lauderdale, FL, 2004.

[32] Garcia, J. G., Albus, J., and Reimerdes, H.-G., "Mass-estimation of Shell Structures with Elliptical Cross-section under Combined Loadings," 1998.

[33] Giles, G. L., "Equivalent Plate Modeling for Conceptual Design of Aircraft Wing Structures," *1st AIAA Aiircraft Engineering, Technology, and Operations Congress*, No. AIAA95-3945, Los Angeles, CA, 1995.

[34] Giles, G., "Design-Oriented Analysis of Aircraft Fuselage Structures," *39th AIAA/ASME/ASCE/AHS/ASC Structures, Structural Dynamics, and Materials Conference and Exhibit*, No. AIAA98-25044, Long Beach, California, 1998.

[35] Bindolino, G., Ghiringhelli, G., Ricci, S., and Terraneo, M., "Multilevel Structural Optimization for Preliminary Wing-Box Weight Estimation," *Journal of Aircraft*, Vol. 47, No. 2, 2010, pp. 475–489.

[36] Schmidt, K. and Vos, R., "A Semi-Analytical Weight Estimation Method for Oval Fuselages in Conventional and Novel Aircraft," *52nd Aerospace Sciences Meeting*, No. AIAA 2014-0026, National Harbor, Maryland, 2014.

[37] Nigam, N., Ayyalasomayajula, S., Qi, X., and Chen, P. C., "High - Fidelity Weight Estimation for Aircraft Conceptual," *16th AIAA/ISSMO Multidisciplinary Analysis and Optimization Conference*, No. AIAA 2015-3360, Dallas, Texas, 2015.

[38] Eldred, L. B., Kapania, R. K., and Barthelemy, J.-F. M., "Sensitivity analysis of aeroelastic response of a wing using piecewise pressure representation," *Journal of Aircraft*, Vol. 33, No. 4, 1996.

[39] Pak, C.-g., "Aeroelastic Tailoring Study of an N+2 Low-boom Supersonic Commercial Transport Aircraft," *16th AIAA/ISSMO Multidisciplinary Analysis and Optimization Conference*, No. AIAA 2015-2791, Dallas, Texas, 2015.

[40] Altair, "Optistruct," 2015.

[41] Altair, "Strength 2000," 2015.

[42] Ainsworth, J., Collier, C., Yarrington, P., Lucking, R., and Locke, J., "Airframe Wingbox Preliminary Design and Weight Prediction," *SAWE Annual Conference*, Virginia Beach, VA, 2010.

[43] Gern, F. H., "Finite Element Based HWB Centerbody Structural Optimization and Weight Prediction," *53rd AIAA/ASME/ASCE/AHS/ASC Structures, Structural Dynamics and Materials Conference*, No. AIAA 2012-1606, Honolulu, Hawaii, 2012.

[44] Putnam, T. W., "X-28 Flight Research Program," *AAIA/AHS/IES/SETP/SFTE/DGLR 2nd Flight Testing Conference*, No. AiAA-83-2687, Las Vegas, Nevada, 1983.

[45] Federal Aviation Administration, *Part 25 AIRWORTHINESS STANDARDS: TRANSPORT CATEGORY AIRPLANES*, 1970.

[46] Luber, W. G. and Füllhas, K., "Design loads for future fighter aircraft," *IMAC-XXI: Conference & Exposition on Structural Dynamics*, 2003.

[47] Sadraey, M., *Aircraft Performance Analysis*, VDM, 2009.

[48] Drela, M. and Youngren, H., "AVL," 2015.

[49] ANSYS, "ANSYS CFD," 2016.

[50] Autodesk, "Autodesk CFD," 2015.

[51] Raymer, D. P., *Aircraft Design: A Conceptual Approach*, American Institute of Aeronautics and Astronautics, 1992.

[52] Kuethe, A. M. and Schetzer, J. D., *Foundations of Aerodynamics*, John Wiley & Sons, Inc., 1959.

[53] Drela, M., "XFOIL," 2013.

[54] Hughes, T. J. R., *The Finite Element Method: Linear Static and Dynamic Finite Element Analysis*, Dover Publications, Inc, New York, 2000.

[55] Collier, C. S., "Stiffness, Thermal Expansion, and Thermal Bending Formulation of Stiffened, Fiber-reinforced Composite Panels," *AIAA/ASME/ASCE/AHS/ACS 34th Structures, Dynamics, & Materials Conference*, 1993.

[56] Collier Research Corporation, "Methods and Equations: FEA Loads," *HyperSizer Help*, Newport News, VA, 2013.

[57] Collier Research Corporation, "Stress Analysis," *HyperSizer Help2*, Newport News, VA, 2016.

[58] Bauchau, O. A. and Craig, J. I., *Structural Analysis With Applications to Aerospace Structures*, Springer, 1st ed., 2009.

[59] Wilkins, D. J., "Anisotropic Curved Panel Analysis," Tech. rep., 1973.

[60] Argyris, J. H., Dunne, P. C., and Scharpf, D. W., "On Large Displacement - Small Strain Analysis of Structures with Rotational Degrees of Freedom," *Computer Methods in Applied Mechanics and Engineering*, Vol. 14, 1978, pp. 401–451.

[61] DoD, "Composite Materials Handbook; Volume 3: Polymer Matrix Composites," Tech. Rep. MIL-HDBK-17-3F, 2002.

[62] Bruhn, E. F., *Analysis and Design of Flight Vehicle Structures*, Jacobs Pub, 1973.

[63] Stroud, W. J. and Agranoff, N., "Minimum-Mass Design of Filamentary Composite Panels Under Combined Loads: Design Procedure Based on Simplified Buckling Equations," Tech. Rep. NASA TN D-8257, Hampton, VA, 1976.

[64] Greenberg, S., *Class Notes: Structural Analysis Techniques for Preliminary Design of Launch Vehicle Structures*, Hampton, VA, 2013.

[65] Collier, C. S., "Structural Analysis and Sizing of Stiffened , Metal Matrix Composite Panels for Hypersonic Vehicles," *AlAA FOURTH INTERNATIONAL AEROSPACE PLANES CONFERENCE*, No. AIAA-92-5015, Orlando, FL, 1992.

[66] Stroud, W. J. and Anderson, M. S., "PASCO- Structural Panel Analysis and Sizing Code, Capability and Analytical Foundations," Tech. Rep. TM-80181, Hampton, VA, 1981.

[67] Herencia, J. E., Weaver, P. M., and Friswell, M. I., "Optimization of Long Anisotropic Laminated Fiber Composite Panels with T-Shaped Stiffeners," *AIAA Journal*, Vol. 45, No. 10, 2007, pp. 2497–2509.

[68] Bushnell, D., "PANDA2-Program for Minimum Weight Design of Stiffened, Composite, Locally Buckled Panels," *Computers & Structures*, Vol. 25, No. 4, 1987, pp. 469–605.

[69] Harrison, P., Rodolphe, L., and Haftka, R., "Design of Stiffened Composite Panels by Genetic Algorithm and Response Surface Approximations," *36th Structure, Structural Dynamics and Materials Conference*, No. AIAA-95-1163-CP, New Orleans,LA, 1995.

[70] Venkataramant, S., Haftka, R. T., and Johnson, T. F., "Design of Shell Structures for Buckling Using Correction Response Surface Approximations," *Proceedings, 7th AIAA/USAF/NASA/ISSMO Symposium on Multidisciplinary Analysis and Optimization*, No. AIAA-98-4855, 1998.

[71] Liu, B., Haftka, R. T., and Akgun, A., "Composite Wing Structural Optimization Using Genetic Algorithms and Response Surfaces," *7TH AIAA/USAF/NASA/ISSMO SYMPOSIUM ON MULTIDISCIPLINARY ANALYSIS AND OPTIMIZATION*, No. AIAA-98-4854, St. Louis, MO, 1998.

[72] Ragon, S. A., Gurdal, Z., Haftka, R. T., and Tzong, T. J., "Global-Local Structural Wing Design Using Response Surface Techniques," *38th Structure, Structural Dynamics and Materials Conference*, No. AIAA-97-1051, 1997.

[73] Powell, S. M. and Williams, F. W., "Local Postbuckling Analysis for Perfect and Imperfect Longitudinally Compressed Plates and Panels," *39th AIAA/ASME/ASCE/AHS/ASC Structures, Structural Dynamics, and Materials Conference and Exhibit*, No. AIAA-98-1770, Long Beach, California, 1998.

[74] Lillico, M., Butler, R., and Hunt, G. W., "Postbuckling of Stiffened Panels Using Strut, Strip, and Finite Element Methods," *AIAA Journal*, Vol. 41, No. 6, 2003.

[75] G. Mabson, B. Flynn, L. Ilcewicz, D. G., "The Use of COSTADE in Developing Composite Commercial Aircraft Fuselage Structures," *35th Structures, Structural Dynamics, and Materials Conference*, No. AIAA 94-1492, 1994.

[76] Myers, R. H., Montgomery, D. C., and Anderson-Cook, C. M., *Response Surface Methodology*, Wiley, Hoboken, NJ, 3rd ed., 2009.

[77] Miki, M., "Design of Laminated Fibrous Connposite Plates with Required Flexural Stiffness," *Recent Advances in Composites in the United States and Japan*, 1985, pp. 387–400.

[78] Joshi, P., Mulani, S. B., Kapania, R. K., and Shin, Y. S., "Optimal Design of Unitized Structures with Curvilinear Stiffeners using Response Surface Methodology," *49th AIAA/ASME/ASCE/AHS/ASC Structures, Structural Dynamics, and Materials Conference*, No. AIAA 2008-2304, Schaumburg, IL, 2008.

[79] Merval, A., Samuelides, M., and Grihon, S., "Application of Response Surface Methodology to Stiffened Panel Optimization," *47th AIAA/ASME/ASCE/AHS/ASC Structures, Structural Dynamics, and Materials Conference*, No. AIAA 2006-1815, Newport, Rhode Island, 2006.

[80] Ragon, S. A., Gurdal, Z., Haftka, R. T., and Tzong, T. J., "Bilevel Design of a Wing Structure Using Response Surfaces," *JOURNAL OF AIRCRAFT*, Vol. 40, No. 5, 2003, pp. 985–992.

[81] Rikards, R., Abramovich, H., Auzins, J., Korjakins, A., Ozolinsh, O., Kalnins, K., and Green, T., "Surrogate Models For Optimum Design of Stiffened Composite Shells," *Composite Structures*, Vol. 63, feb 2004, pp. 243–251.

[82] Rikards, R. and Auzins, J., "Response Surface Method in Design Optimization of Carbon Epoxy Stiffeners," *9th AIAA/ISSMO Symposium on Multidisciplinary Analysis and Optimization*, No. AIAA-2002-5654, Atlanta, Georgia, 2002.

[83] Sunny, M. R., B.Mulani, S., Sanyal, S., Pant, R. S., and Kapania, R. K., "An Artificial Neural Network Residual Kriging Based Surrogate Model for Shape and Size Optimization of a Stiffened Panel," *54th AIAA/ASME/ASCE/AHS/ASC Structures, Structural Dynamics, and Materials Conference*, No. AIAA 2013-1689, Boston, Massachusetts, 2013.

[84] Vitali, R., Haftka, R. T., and Sankar, B. V., "Correction Response Surface Approximations for Stress Intensity Factors of a Composite Stiffened Plate," *39th AIAA/ASME/ASCE/-AHS/ASC Structures, Structural Dynamics, and Materials Conference*, No. AIAA-98-2047, 1998.

[85] Vitali, R., Park, O., Haftka, R. T., Sankar, B. V., and Rose, C. A., "Structural Optimization of a Hat-Stiffened Panel Using Response Surfaces Introduction," *Journal of Aircraft*, Vol. 39, No. 1, 2002, pp. 158–166.

[86] Bindolino, G., Ghiringhelli, G., Ricci, S., and Terraneo, M., "Multilevel Structural Optimization for Preliminary Wing-Box Weight Estimation," *Journal of Aircraft*, Vol. 47, No. 2, 2010, pp. 475–489.

[87] Liu, D., Toroporov, V. V., Querin, O. M., and Barton, D. C., "Bilevel Optimization of Blended Composite Wing Panels," *Journal of Aircraft*, Vol. 48, No. 1, 2011, pp. 107–118.

[88] Ciampa, P. D., Nagel, B., and Tooren, M. V., "Global Local Structural Optimization of Transportation Aircraft Wings," *51st AIAA/ASME/ASCE/AHS/ASC Structures, Structural Dynamics, and Materials Conference*, No. AIAA 2010-3098, Orlando, Florida, 2010.

[89] Wrenn, Gregory A. and Dovi, A. R., "Multilevel Decomposition Approach to the Preliminary Sizing of a Transport Aircraft Wing," *Journal of Aircraft*, Vol. 25, No. 7, 1988, pp. 632–638.

[90] Schmit, L. a. and Mehrinfar, M., "Multilevel Optimum Design of Structures with Fiber-Composite Stiffened-Panel Components," *AIAA Journal*, Vol. 20, No. 1, 1982, pp. 138–147.

[91] Collier Research Corporation, "Effective Laminate Elastic Properties," *HyperSizer Help*, Newport News, VA, 2016.

[92] Hahn, H. T. and Tsai, S. W., *Introduction to Composite Materials*, Technomic Publishing Co, Inc., 1st ed., 1980.

[93] Todoroki, A. and Haftka, R. T., "Stacking Sequence Matching by Two-Stage Genetic Algorithm with Cansanguineous Initial Population," *38th Structures, Structural Dynamics, and Materials Conference*, No. AIAA-97-1228, 1997, pp. 1297–1302.

[94] Todoroki, A. and Haftka, R. T., "Lamination Prameters For Efficient Genetic Optimization Of The Stacking Sequences Of Composite Panels," *7TH AIAA/USAF/NASA/ISSMO SYMPOSIUM ON MULTIDISCIPLINARY ANALYSIS AND OPTIMIZATION*, No. AIAA-98-4816, 1998.

[95] Herencia, J. E., Haftka, R. T., Weaver, P. M., and Friswell, M. I., "Lay-Up Optimization of Composite Stiffened Panels Using Linear Approximations in Lamination Space," *AIAA Journal*, Vol. 46, No. 9, 2008, pp. 2387–2391.

[96] Liu, D., Toropov, V. V., Zhou, M., Barton, D. C., and Querin, O. M., "Optimization of Blended Composite Wing Panels Using Smeared Stiffnes Technique and Lamination Parameters," *51st AIAA/ASME/ASCE/AHS/ASC Structures, Structural Dynamics, and Materials Conference*, No. AIAA-2010-3079, Orlando, Florida, 2010.

[97] Ijsselmuiden, S. T., Abdalla, M. M., and Gürdal, Z., "Implementation of Strength-Based Failure Criteria in the Lamination Parameter Design Space," *AIAA Journal*, Vol. 46, No. 7, 2008, pp. 1826–1834.

[98] Collier Research Corporation, "Failure Analysis," *HyperSizer Help*, Newport News, VA, 2016.

[99] Collier Research Corporation, "Methods and Equations: Thermoelastic Stiffness Formulation," *HyperSizer Help*, Newport News, VA, 2011.

[100] Bednarcyk, B. A. and Yarrington, P. W., "Coupled Thermo-Electro-Magneto-Elastic Response of Smart Stiffened Panels," Tech. Rep. NASA/CR2009-215269, 2009.

[101] Collier Research Corporation, "Methods and Equations: Crippling of Panels and Beams," *HyperSizer Help*, Newport News, VA, 2012.

[102] Collier Research Corporation, "Methods and Equations: Plate and Shell Buckling," *HyperSizer Help*, Newport News, VA, 2010.

[103] Dickson, J. N. and Biggers, S. B., "POSTOP : Postbuckled Open- Stiffener Optimum Panels- Theory and Capability," Tech. Rep. CR-172259, 1984.

[104] SAS Institute Inc, "JMP," 2015.

[105] Freedman, D., Pisani, R., and Purves, R., *Statistics*, WW Norton & Co Inc, 3rd ed., 1997.

[106] SAS Institute Inc, "Regression Reports," 2016.

[107] Vanderplaats, G. N., *Multidiscipline Design Optimization*, Vanderplaats Research and Development, Inc, Monterey, CA, 1st ed., 2007.

[108] MathWorks, "MATLAB Documentation: linprog," Tech. rep., 2016.

[109] MathWorks, "Mathematica," 2016.

[110] Tsai, S. W., *Fundamental Aspects of Fiber Reinforced Plastic Composites*, Wiley Interscience, 1968.

[111] Tsai, S. and Hahn, H., "A General Theory for Strength of Anisotropic Materials," *Journal of Composite Materials*, Vol. 5, No. 1, 1971, pp. 58–80.

[112] Schellekens, J. J. and Borst, R. D., "The Use of the Hoffman Yield Criterion in Finite Element Anlysis of Anisotropic Composites," *Computers & Structures1*, Vol. 37, No. 6, 1990.

[113] Nocedal, J. and Wright, S., *Numerical Optimization*, Springer-Verlag, 2nd ed., 2006.

[114] TSAI, S. W., "A Miracle in Trace: Too Good to be True! But it is Truly True," *JEC Composites Magazine*, , No. February, 2016, pp. 42–44.

[115] Tsai, S. W., Arteiro, A., and Melo, J. D., "A Trace-Based Approach to Design for Manufacturing of Composite Laminates," *Journal of Reinforced Plastics and Composites*, Vol. 35, No. 7, 2016.

[116] Sirirojvisuth, A., *Development of Hybrid Lifecycle Cost Estimating Tool (HLCET) for Manufacturing Influenced Design Tradeoff*, Ph.D. thesis, Georgia Institute of Technology, 2012.

[117] NASA, "The Swept Wing Emerges," .

[118] Hepperle, M., "JavaFoil," .

[119] Kroo, I., *Class Notes from Aircraft Design: Synthesis and Analysis*, 2015.

[120] Wolf, D. D. and Smeers, Y., "The Simplex Algorithm Extended to Piecewise-Linearly Constrained Problems," Tech. rep., Bruxelles, Belgium, 2000.

[121] Fourer, R., "A Simplex Algorithm for Piecewise-linear Programming: Derivation and Proof," *Mathematical Programming*, Vol. 33, 1985, pp. 204–233.

[122] Bisplinghoff, R. L., Ashley, H., and Halfman, R. L., *Aeroelasticity*, Addison-Wesley Publishing Company, 1st ed., 1955.

[123] Weisshaar, T. A. and Lee, D. H., "Aeroelastic Tailoring of Joined-Wing Configurations," *43rd AIAA/ASME/ASCE/AHS/ACS Structures, Structural Dynamics, and Materials Conference*, No. AIAA 2002-1207, Denver, Colorado, 2002.

[124] Francois, G., Cooper, J. E., and Weaver, P. M., "Aeroelastic Tailoring using Rib/Spar Orientations : Experimental Investigation," *56th AIAA/ASCE/AHS/ASC Structures, Structural Dynamics, and Materials Conference*, No. AIAA 2015-0439, Kissimmee , Florida, 2015.

[125] Isogai, K., "Direct Search Method to Aeroelastic Tailoring of a Composite Wing under Multiple Constraints," Vol. 26, No. 12, pp. 1076–1080.

[126] Kapania, R. K. and Chun, S., "Preliminary Design of a Structural Wing-box under a Twist Constraint," *44th AIAA/ASME/ASCE/AHS Structures, Structural Dynamics, and Materials Conference*, No. AIAA 2003-2004, Norfolk, Virginia, 2003.

[127] Rohrle, H. and Mathias, D. W., "Optimization of Anisotropic Structures Considering Strength, Stiffness, and Aeroelastic Constraints," *Fourth AIAA/USAF/NASA/OAI Symposium on Multidisplinary Analysis and Optimizations*, No. AIAA 92-4796, Cleveland, Ohio, 1992.

[128] Stanford, B. K., Wieseman, C. D., Jutte, C. V., and Introduction, I., "Aeroelastic Tailoring of Transport Wings Including Transonic Flutter Constraints," *56th AIAA/ASCE/AHS/ASC Structures, Structural Dynamics, and Materials Conference*, No. AIAA 2015-1127, Kissimmee, Florida, 2015.

[129] Caixeta, P. R. and Marques, F. D., "Neural Network Metamodel-based Mdo for Wing Design Considering Aeroelastic Constraints," *51st AIAA/ASME/ASCE/AHS/ASC Structures, Structural Dynamics, and Materials Conference*, No. AIAA 2010-2762, Orlando, Florida, 2010.

VITA

August Noevere was born on September 20, 1989 in Road Town on the island of Tortola in the British Virgin Islands. He moved to Eastern North Carolina at the age of 7 for the remainder of his childhood and grew up exploring the woods and wide-open countryside. August enrolled in the Aerospace Engineering program at North Carolina State University in 2007 under the Chancellor's Leadership Scholarship. During his four years at NC State, he was on the Dean's List each semester and also the team lead for his senior design project, which was the design and construction of a 10ft UAV.

After completing his Bachelor's of Science in Aerospace Engineering in 2011, August went on to pursue his Master's and Ph.D. at the Georgia Institute of Technology. Two years after enrolling at Georgia Tech, August was awarded the NASA Space Technology Research Fellowship. During the last three years of his schooling, August has been located at the National Institute of Aerospace in Hampton, Virginia to work with researchers at the NASA Langley Research Center.

During his schooling, August also had the opportunity to experience internships with several different companies including NAVAIR, Spirit Aerosystems, MIT Lincoln Laboratory, and Collier Research Corporation.

In his free time, August enjoys getting outdoors as much as possible. During his time at NC State, he got into distance running and has since completed two marathons and numerous half marathons. In addition to running, August also enjoys cycling, kiteboarding, and hiking as much as possible.